Surface-Integrated Fluorescence Correlation Spectroscopy (SI-FCS) for the quantification of transient membrane and surface binding

Philipp Paul Blumhardt

München 2019

Surface-Integrated Fluorescence Correlation Spectroscopy (SI-FCS) for the quantification of transient membrane and surface binding

Philipp Paul Blumhardt

Dissertation
an der Fakultät für Physik
der Ludwig-Maximilians-Universität
München

vorgelegt von
Philipp Paul Blumhardt
aus Villingen-Schwenningen

München, den 15.04.2019

Dissertation eingereicht am:	15.04.2019
1. Gutachter:	Prof. Dr. Petra Schwille
2. Gutachter:	Prof. Dr. Ralf Jungmann
Tag der mündlichen Prüfung:	07.06.2019

Für Adelheid, Caterina, Jan und Joachim

KURZFASSUNG

Das Verständnis der komplexen Netzwerke bio-molekularer Wechselwirkungen benötigt die korrekte und präzise Quantifizierung von Bindungskinetiken. Besonders von Bedeutung sind Wechselwirkungen mit Membranen oder membrangebundenen Objekten, da Membranen nicht nur Bindungskinetiken beeinflussen, sondern auch in eine große Menge entscheidender zellulärer Prozesse grundsätzlich eingebunden sind, darunter Prozesse wie Zellteilung, Signaltransduktion, Endozytose, Exozytose oder Zellmigration.

Um die korrekte und präzise Quantifizierung von Bindungskinetiken zu ermöglichen, haben wir die oberflächen-integrierte Fluoreszenzkorrelationsspektroskopie (SI-FCS, engl. *surface-integrated fluorescence correlation spectroscopy*) entwickelt. Die Methode basiert auf der Autokorrelation von zeitlichen Fluoreszenzfluktuationen in einer Sequenz von Bildern, die mit Totalreflexions-Fluoreszenzmikroskopie (TIRF-Mikroskopie, engl. *total internal reflection microscopy*) aufgenommen wurden. SI-FCS kann zuverlässig die Assoziations- und Dissoziationsraten von reversiblen Liganden-Rezeptor-Bindungen bestimmen. Die DNA-Hybridisierung kurzer Einzelstränge – bei denen einer auf der Oberfläche immobilisiert ist, während sich der andere, fluoreszent markierte Strang in Lösung befindet – imitierte dabei Liganden-Rezeptor-Systeme und wurde in dieser Arbeit präzise mit SI-FCS vermessen.

Systematisch haben wir das Leistungsvermögen und die Limitierungen von SI-FCS untersucht und dabei die photo-induzierte Schädigung von immobilisierten Einzelsträngen als Einschränkung für lange Messzeiten oder hohe Ligandenkonzentrationen bestimmt. Die photoinduzierte Schädigung erfolgt dabei vorwiegend durch reaktive Sauerstoffspezies. In SI-FCS und in DNA-Hybrisierungs-basierter Hochauflösungsmikroskopie (DNA-PAINT) konnten wir diesen Effekt durch das biochemische Entfernen von Sauerstoff vermeiden. In einem parallelen Ansatz zeigen wir ein verbessertes Design für den bindenden DNA-Strang mit einem erhöhten Abstand zwischen dem fluoreszenten Farbstoff und der Bindungssequenz.

Die Bestimmung von Bindungszeiten im Millisekunden-Bereich und kürzer mit SI-FCS ist letzlich limitiert durch exakte mathematische Modelle für die Autokorrelationsfunktion, die auch die Diffusion durch das evaneszente TIRF-Feld mit einbeziehen. Basierend auf einem Fluoropolymer mit dem Brechungsindex wässriger Proben, haben wir eine Kalibierungsprobe entwickelt, mit derer die axiale Detektionswahrscheinlichkeit für Moleküle

in der TIRF-Mirkoskopie direkt bestimmt werden kann. Dabei haben wir eine tiefer in die Probe eindringende Komponente der TIRF-Anregung in der Objektiv-basierten TIRF-Mikroskopie gefunden, die bisher von der entsprechenden FCS-Theorie unberücksichtigt ist.

Schließlich haben wir die praktische Anwendung von SI-FCS auf die Untersuchung von Bindungen an Membranerezeptoren und die Verteilgung von Biomolekülen zwischen Lösung und Membran optimiert. Modelle für die Liganden-Rezeptor-Wechselwirkung in Kombination mit Diffusion auf der Membran, haben wir in einer DNA-Hybridisierungs-basierten Machbarkeitsstudie verifiziert. Des Weiteren zeigen wir ein modifiziertes Modell der Autokorrelationsfunktion für die Verteilung von Biomolekülen zwischen Lösung und Membran und untersuchen die komplexe Verteilung von Peptiden in Simulationen und Experimenten mit drei unterschiedlichen Modellmembransystemen.

ABSTRACT

Understanding the complex networks of biomolecular interactions requires the accurate and precise quantification of binding kinetics. Interactions with membranes or membrane-bound entities are of particular interest, as membranes do not only influence binding kinetics, but are fundamental to a large set of key cellular processes such as cytokinesis, signalling, endocytosis, exocytosis or cell migration.

To enable the accurate and precise quantification of binding kinetics, we developed surface-integrated fluorescence correlation spectroscopy (SI-FCS). This method is based on the autocorrelation of temporal fluorescence fluctuations from a stream of total internal reflection fluorescence (TIRF) images. SI-FCS reliably extracts the association and dissociation rates of reversible ligand-receptor binding. The DNA hybridization of short single-strands – one immobilized on the surface, the other fluorescently labeled in solution – mimicked ligand-receptor systems and was precisely quantified with SI-FCS within this work.

We systematically assessed the potential and limitations of SI-FCS and identified the photo-induced damage of immobilized single-strands as a constraint for longer measurement times and high ligand concentrations. The photo-induced damage was predominantly caused by reactive oxygen species (ROS). Not only did we show that this effect can be prevented in SI-FCS and DNA hybridization-based super-resolution microscopy (DNA-PAINT) with oxygen scavenging buffers, but we also presented an improved DNA handle design with increased distance between fluorescent dye and binding sequence.

Accessing binding times with SI-FCS in the millisecond range and below is ultimately limited by accurate autocorrelation models incorporating the diffusion through the evanescent TIRF field. Based on a fluoropolymer matching the refractive index of aqueous samples, we designed a calibration slide to directly characterize the axial molecule detection function in TIRF microscopy. We found a penetrating component to the TIRF excitation in objective-type TIRF microscopy, so far unconsidered by the respective FCS theory.

Finally, we optimized the implementation of SI-FCS for examining binding to membrane receptors and the partitioning of biomolecules to membranes. We verified models for ligand-receptor interaction in the presence of diffusion in the membrane using a DNA hybridization-based proof-of-concept system. Further, we presented a modified autocorrelation model for the partitioning to membranes and examined the complex partitioning of peptides in simulations and experiments on three different model-membrane systems.

Contents

List of Figures

List of Tables

List of Abbreviations

AFM atomic force microscopy
ALPS amphipathic lipid packing sensor
AOTF acousto optical tunable filter
APD avalanche photodiode

bimFCS binned imaging FCS
BLI bio-layer interferometry

chol-DNA docking strands bound to cholesterol at the 5'-end
CLSM confocal laser scanning microscope

DNA deoxyribonucleic acid
DNA-PAINT DNA-based point accumulation for imaging in nanoscale topography
DOPC 1,2-dioleoyl-*sn*-glycero-3-phosphocholine
DOPE 1,2-dioleoyl-*sn*-glycero-3-phosphoethanolamine
DOPG 1,2-dioleoyl-*sn*-glycero-3-phospho-(1'-*rac*-glycerol)
DPPC Dipalmitoyl-phosphatidylcholine
DPSS diode-pumped solid state
DSC differential scanning calorimetry

EM electron microscopy
EMCCD electron-multiplying charge-coupled device
ENTH epsin N-terminal homology

FCCS fluorescence cross-correlation spectroscopy
FCS fluorescence correlation spectroscopy
FRAP fluorescence recovery after photobleaching
FRET Förster resonance energy transfer

GLP-1 glucagon-like peptide-1
gp41 HIV-1 viral envelope protein
GUV giant unilamellar vesicle

HDMS Bis(trimethylsilyl)amine
HIV human immunodeficiency virus

ICS image correlation spectroscopy
iSCAT interferometric scattering
ITC isothermal titration calorimetry
ITIR-FCCS imaging total internal reflection fluorescence cross-correlation spectroscopy
ITO indium tin oxide

kICS k-space image correlation spectroscopy (ICS)

MIET metal induced engery transfer
MPER membrane proximal external region
MSP membrane scaffold protein
MST microscale thermophoresis
MTS membrane targeting sequence

NA numerical aperture
NMR nuclear magnetic resonance

PCD+PCA protocatcchuate-dioxygenase and 3,4-proto-catechuic acid
PH pleckstrin homology
PMT photomultiplier tube
PO+C pyranose oxidase and catalase
PSF point spread function
PtdIns(4,5)P_2 phosphatidylinositol (4,5)-bisphosphate

QCM quartz crystal microbalance
QCM-D quartz crystal microbalance (QCM) with parallel monitoring of the dissipative losses
qPAINT quantitative PAINT

RICS raster image correlation spectroscopy
ROI region of interest
ROS reactive oxygen species

SAF supercritical angle fluorescence
sCMOS scientifc metal-oxide semiconductor
SI-FCS surface-integrated FCS
SLB supported lipid bilayer
Snf7 amphipathic helix of the ESCRT-III Snf7 protein

SNR signal-to-noise ratio
SPR surface plasmon resonance
SPT single particle tracking
ssDNA single-stranded DNA
STED stimulated emission depletion
STICS spatiotemporal image correlation spectroscopy
SUV small unilamellar vesicle

TCEP Tris(2-carboxyethyl)phosphin
TCSPC time correlated single photon counting
TEG tetraethylene glycol
TIR total internal reflection
TIRF total internal reflection fluorescence
TIR-FCS total internal reflection fluorescence correlation spectroscopy
Trp tryptophan
Tyr tryosine

I

INTRODUCTION AND OUTLINE

Biological complexity is not only based on the vast number of specialized components, but also on the inherent non-linearity of their interactions. Non-linearity is required so that small changes on the molecular level can trigger macroscopic responses on the cellular or systemic level. Many key cellular processes depend on reversible interactions of proteins with membranes of organelles or the plasma membrane [Lemmon, 2008, Di Paolo and De Camilli, 2006, Teruel and Meyer, 2000, Groves and Kuriyan, 2010]. Not only is a plethora of enzymatic reactions localized at the membrane surface [Kleinschmidt, 2013], but it is also the location where many signals from the outside of the cell are processed and transferred to the inside in the form of ligand-receptor interactions [Pierce et al., 2002, Akira and Takeda, 2004]. The rates of ligand-receptor binding are influencing signalling cascades responsible for triggering cellular response [Feinerman et al., 2008, Govern et al., 2010]. Membranes are essential to the structural integrity of cells, forming not only a separator to the extracellular space, but also facilitate compartmentalizations into organelles and vesicles. Cellular membranes are increasingly appreciated for their complexity and physiological role [Simons and Ikonen, 1997, Loura et al., 2003, Simons and Gerl, 2010, Lingwood and Simons, 2010].

The dynamic reshaping of membranes is based on constant turnover and a large set of highly specialized proteins [McMahon and Gallop, 2005, Zimmerberg and Kozlov, 2005, McMahon and Boucrot, 2015]. Hence, the recruitment of biomolecules to membranes is a key mechanism to control the spatio-temporal organization of cells [Kretschmer and Schwille, 2016]. Similarly, the function of many membrane-related proteins can be assessed by examining their membrane interactions.

However, the modeling and theoretical understanding of complex and non-linear biological processes is ultimately limited by the precise and accurate quantification of the governing interactions. Quantification is hindered by the stochastic nature of biological systems limiting the precision of experimental assays. While bulk assays profit from an intrinsic averaging over many molecules, they are limited in deciphering the precise complexity of reaction pathways [Walter et al., 2008]. Fluorescence methods with single-molecule sensitivity, in return, allow the investigation of heterogeneity and apparent disorder on the level of individual molecules with high specificity. Without the need for external perturbations,

they can determine kinetics in quasi-equilibrium [Walter et al., 2008].

Following the concept of fluorescence correlation spectroscopy (FCS) [Magde et al., 1972], the autocorrelation function of the number and brightness of fluorescently labeled molecules within a small observation volume is determined by the dynamics that govern the fluorescence fluctuations. In the following years, FCS developed into an increasingly versatile tool to study not only molecular mobility [Aragón and Pecora, 1976, Koppel et al., 1976, Fahey et al., 1977], but also bi-molecular interactions [Kinjo and Rigler, 1995, Schwille et al., 1996, Rauer et al., 1996, Schwille et al., 1997]. Thus, kinetic parameters governing biochemical reactions can be extracted from the autocorrelation function. Focused laser excitation and tightly confined confocal detection allowed the study of individual molecules with FCS [Rigler et al., 1993, Eigen and Rigler, 1994]. More advanced FCS variants that scan the confocal detection in the sample [Berland et al., 1996] proved useful to elucidate not only mobility in the membrane [Benda et al., 2003, Ries and Schwille, 2006, Petrášek and Schwille, 2008], but also the partitioning into different membrane phases [Ries et al., 2009a] and the binding to membrane-localized receptors [Ries et al., 2009b]. Simultaneous to the advent of wide-field total internal reflection fluorescence (TIRF) microscopy [Axelrod, 1981], the pioneering works of Thompson and colleagues highlighted the potential of total internal reflection fluorescence correlation spectroscopy (TIR-FCS) to investigate surface binding [Thompson et al., 1981, Thompson, 1982, Thompson and Axelrod, 1983]. Studies on lipid mobility of the basal membrane of cells and of supported lipid bilayers (SLBs) [Tamm and McConnell, 1985] profited from the surface-selectivity of TIRF microscopy in combination with FCS [Thompson et al., 1993, Ohsugi et al., 2006]. Modern electron-multiplying charge-coupled device (EMCCD) camera technology enabled the multiplexing of FCS acquisition in multiple detection modalities [Krieger et al., 2015], including TIRF microscopy [Burkhardt and Schwille, 2006, Kannan et al., 2006, Kannan et al., 2007, Sankaran et al., 2009]. Image correlation spectroscopy (ICS) [Petersen et al., 1993, Wiseman, 2013], a closely related method, extracts molecular mobilities and has been used to investigate the binding of membrane-diffusing receptors to larger protein complexes as well as of ligands to microtubules [Brandão et al., 2014].

Within this thesis we expanded the set of correlation-based techniques to quantify reversible surface binding based on the stochastic intensity fluctuations from fluorescently labeled molecules (Chapter III). In a first proof-of-concept study, we systematically examined the potential and the limitations of our newly developed method, termed surface-integrated FCS (SI-FCS), for the quantification of the reversible attachment to surface-immobilized

deoxyribonucleic acid (DNA) origami nanostructures. The reversible hybridization of complementary single-stranded DNA (ssDNA) served as a proxy for the concept of ligand-receptor binding. We did not only quantify characteristic binding times ranging from 500 ms to 100 s, but also precisely extracted association and dissociation rates of the DNA hybridization with varying nucleotide overlaps. We demonstrated the outstanding sensitivity of this newly developed method and resolved the binding kinetics of individual species in mixed samples.

Working with high solution concentrations of labeled ssDNA, we found the SI-FCS autocorrelation curves to be influenced by the photo-induced depletion of the surface-immobilized DNA handles (Chapter IV). The effect appears similarly in super-resolution microscopy with DNA-based point accumulation for imaging in nanoscale topography (DNA-PAINT) [Jungmann et al., 2010]. Such light-induced sample alterations pose a significant limitation to SI-FCS and DNA-PAINT experiments. We identified reactive oxygen species (ROS) as the major cause of this depletion. We successfully reduced the depletion down to the detection threshold by identifying appropriate oxygen scavenging buffers. Our optimized acquisition procedure does not only enhance the accuracy of SI-FCS quantifications, but the quantitative super-resolution microscopy with DNA-PAINT alike [Jungmann et al., 2010, Jungmann et al., 2016, Schnitzbauer et al., 2017]. The enhanced sample stability extends the long-term stability of the SI-FCS acquisition, enabling longer measurements and thus the study of longer binding times.

In the studies highlighted above, the contribution to the SI-FCS autocorrelation curves from solution diffusion is most critical for the quantification of fast binding molecules. An accurate modeling of the autocorrelation function for solution diffusion requires assumptions regarding the functional shape of the fluorescence excitation profile in TIRF microscopy. Based on the limitations of previous attempts to measure the axial excitation profile, we developed a calibration slide to directly characterize the excitation profile of our objective-type TIRF microscope. We found that the profile is most accurately described by a biexponential consisting of the evanescent field expected from theory and an additional non-evanescent contribution (Chapter V).

Finally, we extended SI-FCS to quantify the binding to membranes and the interaction with membrane-bound biomolecules (Chapter VI). We determined the association and dissociation rates of ssDNA to their complementary membrane-bound DNA handles, conceptually resembling ligand binding to membrane-attached receptors. Further, we give an analytical solution for the autocorrelation function of a simple membrane attachment

without further specificity for receptors or sparse lipid-headgroups. Binding of amphipathic helices to membranes is generally more complex and can in some cases be described by a three-state model [White and Wimley, 1998, Myers et al., 2012]. Assuming a weakly bound and a strongly bound state, we examined the dependence of the autocorrelation function on the governing reaction rates in simulations. Finally, using SI-FCS we characterized the partitioning of the membrane proximal external region (MPER), a short peptide derived from human immunodeficiency virus (HIV)-1, into three different model membrane systems.

Taken together, we developed SI-FCS as a robust and precise method to quantify a variety of surface interactions including the highly relevant interaction of membrane-bound ligand-receptor pairs and the partitioning of amphipathic molecules from solution to membrane.

II

BASIC CONCEPTS: STUDYING DIFFUSION AND BINDING WITH FLUORESCENCE CORRELATION SPECTROSCOPY

II.1 Fluorescence Correlation Spectroscopy

Fluorescence correlation spectroscopy (FCS) [Magde et al., 1972, Elson and Magde, 1974, Magde et al., 1974] is an optical method to infer a set of parameters describing the dynamics of a system from the fluorescence signal fluctuations within a small detection volume. The observed fluorescence signal depends, among other factors, on the number and the brightness of emitters contained inside the volume. Furthermore, the autocorrelation of a recorded intensity trace is governed by the statistical processes leading to changes in the fluorescence signal. Typically, the investigated fluctuations are originating from molecular mobility [Magde et al., 1974, Elson and Magde, 1974, Magde et al., 1978], binding processes [Kinjo and Rigler, 1995, Schwille et al., 1996, Schwille et al., 1997, Michelman-Ribeiro et al., 2009] or photophysics [Widengren et al., 1995, Haupts et al., 1998, Widengren and Schwille, 2000, Torres and Levitus, 2007]. The underlying physical quantities are extracted from the autocorrelation function by fitting of the experimentally obtained autocorrelation curves with an appropriate model function. In most cases, FCS is combined with a focused laser beam and a confocal pinhole in the image plane, offering a small detection volume with single-molecule sensitivity [Rigler et al., 1993, Eigen and Rigler, 1994].

A number of excellent reviews describe the principles of FCS [Thompson, 1999, Petrov and Schwille, 2008, Petrášek and Schwille, 2009] and its numerous applications. While many reviews have a general scope, the reader is referred to the following non-exhaustive list of reviews for a special focus on the historical development of FCS [Webb, 2001, Elson, 2011, Rigler and Widengren, 2017], photophysics [Widengren, 2001, Rigler and Widengren, 2017], polymer physics [Woll, 2014, Papadakis et al., 2014], living cells [Bacia et al., 2006, Kim et al., 2007, Weidemann and Schwille, 2009, Weidemann et al., 2014], membrane dynamics [Kahya and Schwille, 2006] or lipid-protein interactions [Melo et al., 2014]. Investigations of bi-molecular interactions profited from the development of dual-color cross-correlation spectroscopy [Schwille et al., 1997] (reviewed in [Bacia et al., 2006, Bacia and Schwille,

2007, Nguyen et al., 2012]). A stronger focus on image-based correlation methods can be found in [Machán and Wohland, 2014, Krieger et al., 2015].

II.1.1 Focused Laser Single-point Confocal FCS

The principles of confocal microscopy are excellently described in [Pawley, 2006]. A detailed derivation of the autocorrelation function in confocal FCS is presented in [Krichevsky and Bonnet, 2002].

We define the normalized autocorrelation function based on the fluctuations $\delta F(t)$ of the fluorescence signal $F(t)$ around the mean $\langle F(t)\rangle$, as

$$\delta F(t) = F(t) - \langle F(t)\rangle \,. \tag{II.1}$$

The autocorrelation function of a stationary system is then given by

$$G(\tau) = \frac{\langle \delta F(t)\delta F(t+\tau)\rangle}{\langle F(t)\rangle^2} \tag{II.2}$$

with the brackets $\langle \ldots \rangle$ denoting the thermodynamic ensemble average and τ being the lag time of the autocorrelation function.

Based on the underlying dynamics, a model function can be derived to relate the experimentally obtained autocorrelation function to the physical parameters governing the system under investigation. A recommended, comprehensive introduction to confocal FCS was presented by Petrov and Schwille [Petrov and Schwille, 2008], including potential pitfalls and a detailed discussion of different autocorrelation model functions in combination with diffusion, chemical reactions, triplet state contributions, flow and active transport. For the purpose of this thesis, we will limit ourselves for the confocal single-point FCS to a motivation of the employed autocorrelation models. From fitting these models to the experimental autocorrelation curves, concentrations and diffusion coefficients of fluorescent dyes and dye-conjugated biomolecules may be obtained.

For the choice of the appropriate autocorrelation model, it is important to take into account the specific sample and the employed detection scheme. For the diffusion of a fluorescent tracer in three dimensions, we use

$$\text{3D diffusion:} \qquad G(\tau) = \frac{1}{N}\frac{1}{1+\frac{\tau}{\tau_D}}\frac{1}{\sqrt{1+\frac{\tau}{S^2\tau_D}}} \,. \tag{II.3}$$

Here, $\tau_D = \frac{w_{xy}^2}{4D}$ is the diffusion time and N the number of particles. Moreover, w_{xy} is the lateral extension of the detection volume, assumed as the $1/e^2$-width of a three-dimensional Gaussian volume. In practice, w_{xy} is determined by a calibration measurement with a dye of known diffusion coefficient D. The number of particles N is linked to the average concentration $\langle c \rangle$ by the effective detection volume V_{eff} as $N = \langle c \rangle V_{\text{eff}} = \langle c \rangle (\pi)^{3/2} S w_{xy}^3$. $S = w_z/w_{xy}$ is the structure parameter describing the enlargement along the optical axis and is obtained experimentally from the fit of the calibration measurement. In confocal FCS, where particles are often assumed to be point-like in an ideal solution, the dependence of the autocorrelation function on the particle number N follows from Poisson statistics [Landau and Lifshitz, 1980].

The triplet state of fluorescent molecules has an increased lifetime compared to the excited state, does not contribute to the fluorescence signal, and thus causes blinking dynamics as an additional contribution to the autocorrelation function, that can be well approximated at lower irradiances by an exponential decay [Widengren et al., 1994, Widengren et al., 1995, Petrov and Schwille, 2008]:

$$\text{3D diffusion + triplet:} \qquad G(\tau) = \frac{1}{N} \frac{1}{1 + \frac{\tau}{\tau_D}} \frac{1}{\sqrt{1 + \frac{\tau}{S^2 \tau_D}}} \left[1 + \frac{T}{1-T} \exp\left(-\frac{\tau}{\tau_T} \right) \right] . \quad \text{(II.4)}$$

Here we additionally introduced the triplet time τ_T and the triplet fraction T.

In practice, the temperature and the specific detector characteristics need to be considered to achieve accurate FCS results. The Stokes-Einstein-Smoluchowski equation describes the temperature dependence of the diffusion coefficient D of spherical objects with the hydrodynamic radius R_h in medium with the viscosity $\eta(T)$ [Einstein, 1905, von Smoluchowski, 1906, Sutherland, 1905]:

$$D = \frac{k_B T}{6\pi \eta(T) R_h} . \quad \text{(II.5)}$$

Accurate determinations of not only the diffusion coefficient, but also the extracted concentration thus critically depend on a correction of temperature differences of the respective measurement, the calibration measurement and the literature values [Petrov and Schwille, 2008].

For fluorescence detection, we employ avalanche photodiodes (APDs) as they offer high quantum yields and single-photon sensitivity. A semiconductor photodiode is operated at high reverse voltages so that photo-generated electron-hole pairs are multiplied

to avalanches of detectable electric signal. A downside of this approach is the detector dead time of roughly 100 ns, limiting the linear range of fluorescence detection to typically below 1 MHz [Schätzel, 1986]. More importantly, in APDs there is a non-zero probability that that a second ghost photon is detected a short time after the actual photon event. Splitting the fluorescence signal on two independent detectors and calculating the pseudo-cross-correlation [Arecchi et al., 1971, Burstyn and Sengers, 1983], eliminates this so-called afterpulsing. Thus, we account for the afterpulsing experimentally and use Equations II.3 or II.4 as autocorrelation model. Further, the amplitude of the autocorrelation function and thus the extracted concentration are influenced by the presence of an uncorrelated background. For low concentrations or high dark counts of the APDs a background correction of the autocorrelation amplitude should be performed (see Equation II.9 and Section II.1.3).

II.1.2 Total Internal Reflection Fluorescence Correlation Spectroscopy (TIR-FCS)

Confocal FCS routinely enables the detection of dynamics on the micro- to high millisecond time scale, often from transitions through the resolution-limited confocal detection volume. Thus, biochemical reactions have been examined by following changes in the translational diffusion coefficient of a fluorescent ligand when binding a receptor with significantly larger hydrodynamic radius [Kinjo and Rigler, 1995, Schwille et al., 1996, Dorn et al., 1998, Van Craenenbroeck and Engelborghs, 1999, Wohland et al., 1999]. This arrangement is however limited to large differences in hydrodynamic radius [Meseth et al., 1999]. Fluorescence cross-correlation spectroscopy (FCCS) elegantly circumvented this problem by observing both reaction partners in separate spectral channels [Schwille et al., 1997]. While both assays give access to equlibrium properties of the binding, the accessibility of reaction kinetics is limited. If the transitions through the detection volume are faster than the reaction kinetics (as frequently the case), the autocorrelation function will predominantly report on the fluctuations from diffusion and not on the reaction kinetics [Starr and Thompson, 2001, Michelman-Ribeiro et al., 2009]. Principally, the transit times of binding partners can be extended by enlarging the detection volume, however, this seriously restricts the accessible ligand concentration range [Laurence and Weiss, 2003].

Another option is to immobilize one binding partner within the detection volume such that the residence time in the detection volume depends on the binding kinetics [Michelman-Ribeiro et al., 2009, Bierbaum and Bastiaens, 2013]. With the introduction

of TIRF mircoscopy for the investigation of biomolecules and cells [Burghardt and Axelrod, 1981, Axelrod, 1981], Thompson, Burghardt and Axelrod recognized the potential of the tightly confined surface-illumination to investigate binding kinetics [Thompson et al., 1981]. Total internal reflection (TIR) of a laser beam reflected from a glass-water interface results in an exponentially decaying evanescent field in the sample with a decay length of typically less than 100 nm [Toomre and Manstein, 2001]. The pioneering works of Thompson and colleagues combined TIR illumination with FCS analysis. In the inital concept TIR-FCS was proposed to not only extract the kinetics of surface-immobilized ligand-receptor binding, but similarly the transport rate for surface diffusion [Thompson et al., 1981, Thompson, 1982]. A first experimental realization investigated the nonspecific reversible binding of immunoglobulin G to a protein-coated silica surface [Thompson and Axelrod, 1983].

Strikingly, it was only after the breakthrough of confocal FCS [Eigen and Rigler, 1994], nearly 20 years later, that TIR-FCS was revisited in theory and experiment. Lagerholm and Thompson addressed the effect of rebinding of ligands in specific geometries [Lagerholm and Thompson, 1998]. Hansen and Harris applied TIR-FCS to study the adsorption and desorption of small molecules (rhodamine 6G) to chromatographic surfaces [Hansen and Harris, 1998a, Hansen and Harris, 1998b].

The Thompson group further advanced TIR-FCS in the following years by providing a refined theory for the rebinding of ligands [Lagerholm and Thompson, 2000] and, most importantly, a closed-form analytic solution for the combined ligand-receptor binding and axial diffusion through the evanescent field [Starr and Thompson, 2001]. Further, they addressed the accessibility of surface densities with SI-FCS and gave practically relevant approximations to the general solution. In the following, we summarize the relevant theory for quantifying surface and membrane binding with TIR-FCS, largely based on the works by Starr and Thompson (Section II.1.3). The systematic investigation of diffusion in solution very close to a membrane further contributed to the quantitative understanding of surface-binding kinetics [Starr and Thompson, 2002].

A convincing quantification of ligand-receptor binding extracted a large set of parameters from the autocorrelation function, including the dissociation rate, surface density, solution concenration and axial diffusion rate [Lieto et al., 2003]. To circumvent the problems of high ligand concentrations (resulting in small autocorrelation amplitudes) and unspecific binding, mostly non-fluorescent ligands were mixed with a small fraction of labeled ligands. Already the initial works on TIR-FCS suggested that the properties of a

species of non-fluorescent ligands can be assessed by investigating a second labeled species competing for the same binding sites [Thompson, 1982]. Notably, this opens the possibility for TIR-FCS to quantify label-free samples in combination with some of the advantages of a highly specific fluorescent approach.

Ries and colleagues [Ries et al., 2008a] proposed an empirical extension of the autocorrelation model of Starr and Thompson [Starr and Thompson, 2001] to accurately account for the effect of lateral diffusion in a three-dimensional model in presence of fluctuations from ligand-receptor binding. Further, they contributed a refined model for the lateral diffusion for squared detection geometries.

Until then, TIR-FCS was increasingly adopted as method to study the diffusion close to surfaces [McCain et al., 2004b, Kyoung and Sheets, 2006, Kyoung and Sheets, 2008, Weger et al., 2018], flow above surfaces [Yordanov et al., 2009, Schmitz et al., 2011], binding or adsorption [McCain et al., 2004a, Sonesson et al., 2008], membrane diffusion in live cells [Ohsugi et al., 2006, Ohsugi and Kinjo, 2009], photophysics [Blom et al., 2009] and enzyme kinetics [Hassler et al., 2007].

In many of the studies mentioned above, a prism is utilized to achieve the large incident angles on the glass-water interface required for TIR. The introduction of objective-type TIRF microscopy [Stout and Axelrod, 1989] with TIR-FCS improved the compatibility with standard microscope geometries and samples [Hassler et al., 2005b, Anhut et al., 2005, Hassler et al., 2005a]. Further, the emission properties of dipoles close to dielectric surfaces [Lukosz, 1979, Enderlein, 1999] were described in their effect on the autocorrelation function [Hassler et al., 2005b, Ries et al., 2008a] and exploited for supercritical angle fluorescence correlation spectroscopy [Ries et al., 2008b]. For prism-type TIRF, the penetration depth of the evanescent TIR field was extracted from the autocorrelation function [Harlepp et al., 2004].

Further method variations included dual-color cross-correlation spectroscopy [Leutenegger et al., 2006, Yordanov et al., 2009], the combination with time correlated single photon counting (TCSPC) detection for fluorescence lifetime analysis [Weger and Hoffmann-Jacobsen, 2017, Otosu and Yamaguchi, 2018], stimulated emission depletion (STED) to decrease the lateral extension of the detection volume [Leutenegger et al., 2012], the implementation on commercial instrumentation [Yordanov et al., 2011], and the combination of confocal and TIR-FCS on one instrument [Li and Yang, 2018].

II.1.2.1 Camera-based TIR-FCS and Temporal Image Correlation Spectroscopy

Confocal FCS probes only a small volume and can therefore measure local differences of molecular dynamics, in the easiest case by sequential recording of multiple positions. Moreover, the cross-correlation of two or more spatially separated points enables not only the determination of velocity and directionality of flows, but generally enhances the spatiotemporal assessement of molecular mobility. Efforts to multiplex simultaneous spatial acquisitions were initially limited in the number of spots by the available instrumentation [Brinkmeier et al., 1999, Wachsmuth et al., 2000, Dittrich and Schwille, 2002, Gösch et al., 2004, Takahashi et al., 2005]. However, it was shown that fluctuations in the spatial domain can be examined with camera detection ICS [Petersen et al., 1993, Wang and Axelrod, 1994, Huang and Thompson, 1996].

The combination of FCS and highly sensitive EMCCD cameras enabled single-molecule sensitivity in combination with a time-resolution in the millisecond range [Burkhardt and Schwille, 2006, Kannan et al., 2006]. The group of Thorsten Wohland pioneered the development of multiplexed EMCCD camera detection for camera-based TIR-FCS to study temporal dynamics [Kannan et al., 2007, Guo et al., 2008] and extended it to the spatial domain [Sankaran et al., 2009, Bag et al., 2012]. Similarly, the group of Paul Wiseman advanced ICS to the temporal domain [Kolin et al., 2006a, Kolin et al., 2006b]. A number of specialized methods extended the FCS/ICS framework, all eventually based on the correlation of spatio-temporal fluorescence intensity fluctuations, e.g. spatiotemporal image correlation spectroscopy (STICS) [Hebert et al., 2005], raster image correlation spectroscopy (RICS) [Digman et al., 2005b, Digman et al., 2005a], k-space ICS (kICS) [Kolin et al., 2006b, Brandão et al., 2014], imaging total internal reflection fluorescence cross-correlation spectroscopy (ITIR-FCCS) [Sankaran et al., 2009], binned imaging FCS (bimFCS) [Huang and Pralle, 2011, Lim et al., 2013, Huang et al., 2015] and finally SI-FCS as presented in this thesis (Chapter III). A comparison of the individual methods is presented in [Wiseman, 2013, Bag and Wohland, 2014, Wiseman, 2015, Krieger et al., 2015].

Of special interest for the quantification of binding dynamics is the application of kICS to study not only the ligand-receptor interaction of fluorescently labeled, soluble motor proteins binding to microtubules, but also receptor-receptor docking [Brandão et al., 2014]. While the mathematical framework differs in Fourier-space (k-space), the underlying assumptions and extracted parameters are similar to SI-FCS.

II.1.3 The Autocorrelation Function in TIR-FCS

In TIR-FCS, we define the normalized autocorrelation function as in the confocal case (Equation II.2)

$$G(\tau) = \frac{\langle \delta F(t) \delta F(t+\tau) \rangle}{\langle F(t) \rangle^2} = \frac{g(\tau)}{\langle F \rangle^2} \,. \tag{II.6}$$

In the presence of an uncorrelated background, the collected fluorescence signal $F(t)$ can be expressed as the sum of the correlated signal $F'(t)$ and the background signal $B_\mathrm{g}(t)$, as

$$F(t) = \langle F(t) \rangle + \delta F(t) = \underbrace{\langle F'(t) \rangle + \delta F'(t)}_{\text{signal}} + \underbrace{\langle B_\mathrm{g}(t) \rangle + \delta B_\mathrm{g}(t)}_{\text{uncorrelated background}} \,. \tag{II.7}$$

The measured autocorrelation is then given by

$$G_\mathrm{meas}(\tau) = \frac{\langle \delta F(0) \delta F(\tau) \rangle}{\langle F \rangle^2} = \frac{\langle \delta F'(0) \delta F'(\tau) \rangle}{\left(\langle F' \rangle + \langle B_\mathrm{g} \rangle \right)^2} \,, \tag{II.8}$$

with the arbitrary start time $t = 0$ for ergodic systems and the simplified notation of the averages $\langle F(t) \rangle = \langle F \rangle$. Based on the averages of background and signal contribution, a simple correction of the amplitude can be performed by [Thompson, 1999]

$$G(\tau) = G_\mathrm{meas}(\tau) \frac{\left(\langle F' \rangle + \langle B_\mathrm{g} \rangle \right)^2}{\langle F' \rangle^2} = G_\mathrm{meas}(\tau) \frac{\langle F \rangle^2}{\left(\langle F \rangle - \langle B \rangle \right)^2} \,. \tag{II.9}$$

To simplify the notation, in the following, we assume the signal free from background $F(t) = F'(t)$ and correct the amplitude of the autocorrelation function in the last step, provided the background is known.

We follow the derivation developed by Ries and colleagues [Ries et al., 2008a], which itself is based on work by Starr and Thompson [Starr and Thompson, 2001]. The pioneering first derivation of the TIR-FCS autocorrelation function was presented by [Thompson et al., 1981]. The fluorescence signal can be calculated from the position- and time-dependent concentrations $C_i(\vec{r}, t)$, the molecule detection function $\vec{\Omega}(\vec{r})$ and the molecular brightness of the molecules. To generalize to multiple species of molecules, Ries and colleagues express the signal as the sum of n species with molecular brightness η_i [Ries et al., 2008a]. The

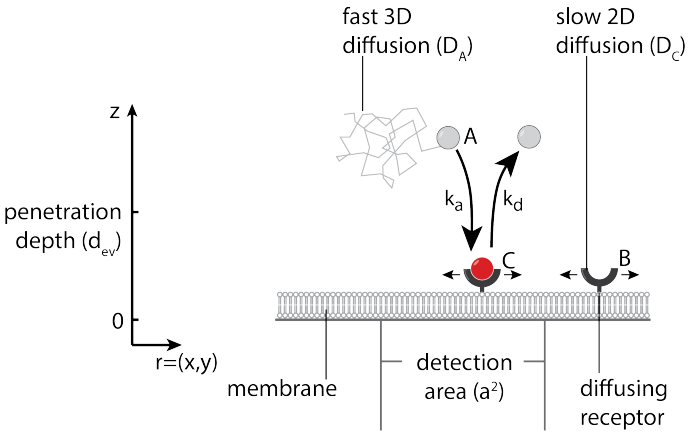

Figure II.1: Contributions of membrane binding to the TIR-FCS autocorrelation function. Fluorescently labeled molecules A diffuse in solution with the average concentration $\langle A \rangle$ and the diffusion coefficient D_{A}. Molecules contribute to the autocorrelation function as long as they reside within the squared detection area with the side length a and the TIRF excitation, characterized by the penetration depth d_{ev}. Following the reaction scheme $A + B \leftrightharpoons C$, A binds to unoccupied binding sites B, forming the complex C. The binding is characterized by the association and dissociation rate k_a and k_d, respectively. Formed complexes diffuse laterally on the membrane with the diffusion coefficient D_{C}.

collected fluorescence signal is then given as the integral

$$F(t) = \sum_{i=1}^{n} \int \mathrm{d}^3\vec{r}\, \eta_i\, \Omega(\vec{r}) C_i(\vec{r}, t)\,. \tag{II.10}$$

The correlation of a two-species system with indices i, j is given as

$$G(\tau)\langle F\rangle^2 = \sum_i \sum_j g_{ij}(\tau) \tag{II.11}$$

with

$$g_{ij}(\tau) = \eta_j \eta_j \int\int \mathrm{d}^3\vec{r}\, \mathrm{d}^3\vec{r}\,'\, \Omega(\vec{r}) \Phi_{ij}(\vec{r}, \vec{r}\,', \tau) \Omega(\vec{r}\,')\,. \tag{II.12}$$

Unfortunately, Ries and colleagues handle the molecular brightness η_i inconsistently and introduce it, what we believe incorrectly, in the concentration correlation (e.g. Equation (8) in [Ries et al., 2008a]). For convenience, we therefore set $\eta_A = \eta_C = 1$ in the following.

Further, we use the concentration correlation function

$$\Phi_{ij}(\vec{r}, \vec{r}\,', \tau) = \langle \delta C_i(\vec{r}, 0) \delta C_j(\vec{r}\,', \tau)\rangle\,. \tag{II.13}$$

The challenge is to determine the molecule detection function $\Omega(\vec{r})$ and the concentration correlation Φ_{ij} for the specific system.

Our general case is describing fluorescent molecules diffusing freely in solution (A), non-fluorescent membrane-bound receptors diffusing laterally on the membrane (B), and bound fluorescent molecules diffusing with the receptors (C) (Figure II.1). The correlation function $g(\tau)$ is then composed of a contribution from free-diffusion g_{AA}, surface-bound fluorophores g_{CC} and the cross-correlation g_{AC} as

$$G(\tau)\langle F\rangle^2 = g_{\mathrm{AA}}(\tau) + 2g_{\mathrm{AC}}(\tau) + g_{\mathrm{CC}}(\tau)\,, \tag{II.14}$$

The three components of the correlation function do not generally factorize into axial and lateral part. For the one-dimensional model a closed-form analytic solution has been found, differing signficantly from the correct three dimensional model [Ries et al., 2008a]. In the specific case of a square pinhole with a side length a and a monoexponential TIRF field with the penetration depth d_{ev}, the error in the extracted diffusion coefficient decreases with increasing pinhole size a [Ries et al., 2008a]. To our knowledge, no analytic solution has

been found describing the full three-dimensional model including binding [Thompson et al., 1981, Thompson and Axelrod, 1983, Lagerholm and Thompson, 1998, Starr and Thompson, 2001, Ries et al., 2008a]. We are therefore seeking approximations and follow the semi-empirical descriptions of the autocorrelation function for diffusion and binding dynamics presented by Ries and colleagues [Ries et al., 2008a].

II.1.3.1 Three-dimensional Autocorrelation Function for Diffusion in Absence of Binding and Observation Through a Square Pinhole

The solution for diffusion without binding has an analytic solution of special interest, as a semi-empirical solution for the case with binding can be derived from it [Ries et al., 2008a]. The diffusion coefficient is assumed to be independent from the distance to the surface [Ries et al., 2008a], which is justified for small molecules [Pero et al., 2006]. We assume a reflective surface at $z = 0$ with molecules diffusing only in the half-space $z > 0$. The concentration correlation then factorizes in lateral and axial components [Ries et al., 2008a][1]

$$\Phi_{\mathrm{AA}}(\vec{r},\vec{r}\,',z,z',\tau) = \langle A\rangle \Phi_{\mathrm{AA,xy}}(\vec{r},\vec{r}\,',\tau)\Phi_{\mathrm{AA,z}}(z,z',\tau)\,, \tag{II.15a}$$

$$\Phi_{\mathrm{AA,xy}}(\vec{r},\vec{r}\,',\tau) = \frac{1}{4D_{\mathrm{A}}\pi\tau}\exp\left(-\frac{(\vec{r}-\vec{r}\,')^2}{4D_{\mathrm{A}}\tau}\right)\,, \tag{II.15b}$$

$$\Phi_{\mathrm{AA,z}}(z,z',\tau) = \frac{1}{\sqrt{4D_{\mathrm{A}}\pi\tau}}\left(\exp\left(-\frac{(z-z')^2}{4D_{\mathrm{A}}\tau}\right)+\exp\left(-\frac{(z+z')^2}{4D_{\mathrm{A}}\tau}\right)\right)\,. \tag{II.15c}$$

Similarly, the molecule detection function factorizes into the lateral detection profile L(x,y) and the axial TIRF profile W(z), as

$$\Omega(x,y,z) = L(x,y)W(z)\,, \tag{II.16}$$

and so does the autocorrelation function [Ries et al., 2008a][2]

$$G(\tau)\langle F\rangle^2 = \langle A\rangle g_{\mathrm{xy}}(\tau)g_z(\tau)\,. \tag{II.17}$$

[1] Ries and colleagues [Ries et al., 2008a] additionally multiply equation II.15a with η_{A}. However, Φ_{AA} is a concentration correlation and the brightness is accounted for by evaluating Equation II.12 in a later step. We therefore present Equation II.15a simply as the average concentration $\langle A\rangle$ multiplied with the propagators $\Phi_{\mathrm{AA,xy}}$ and $\Phi_{\mathrm{AA,z}}$.

[2] In comparison with [Ries et al., 2008a], as in the case of Equation II.15a, we believe that the autocorrelation function should obtain a pre-factor η_{A}^2 from evaluating Equation II.12, resulting in the autocorrelation function $G(\tau)$ independent of the brightness η_{A}. In our notation, however, we set $\eta_{\mathrm{A}} = 1$.

Further, we assume the axial molecule detection to be dominated by the evanescent field of the TIRF excitation

$$W(z) = W(0)\exp(-\kappa z) \tag{II.18a}$$

$$d_{\mathrm{ev}} = \frac{1}{\kappa}\,, \tag{II.18b}$$

with d_{ev} being the penetration depth [Gingell et al., 1987]. In Chapter V (p. 91), we will discuss the molecule detection function in the special case of objective-type TIRF microscopy in detail.

The axial TIR-FCS correlation function is calculated from Equation II.15c inserted into II.12 as

$$g_{\mathrm{z}}(\tau) = \sqrt{\frac{D_{\mathrm{A}}\tau}{\pi}} - \frac{2D_{\mathrm{A}}\tau\kappa^2 - 1}{2\kappa} w\left(i\sqrt{D_{\mathrm{A}}\tau}\kappa\right)\,, \tag{II.19a}$$

$$w(i\xi) = \exp\left(\xi^2\right)\mathrm{erfc}(\xi)\,, \tag{II.19b}$$

with the monotonically decaying Faddeeva function w, a complex variant of the error function [Abramowitz and Stegun, 1965]. We neglect effects from supercritical angle fluorescence (SAF), which Ries and colleagues accounted for by an effective penetration depth [Ries et al., 2008a].

In this work, we will employ camera acquisition with the camera pixels serving as square pinholes. We will thus limit the discussion of the lateral correlation function to the case of squared detection profiles $L(x, y) = L_x(x)L_x(y)$. The detection point spread function (PSF), contributing a blur to the outlines of the rectangle, can be approximated by a Gaussian

$$\mathrm{PSF}(x - x_0) = \frac{1}{\sqrt{2\pi}\sigma}\exp\left(-\frac{(x - x_0)^2}{2\sigma^2}\right)\,. \tag{II.20}$$

The width of the PSF

$$\sigma = \sigma_0\frac{\lambda}{\mathrm{NA}}\,, \tag{II.21}$$

depends on the emission wavelength λ, the numerical aperture NA of the objective and a pre-factor $\sigma_0 = 0.21$ following theoretical considerations [Zhang et al., 2007, Ries et al., 2008a]. Notably, for camera detection, based on the noise contribution of EMCCD cameras

[Michalet et al., 2007] and experimental results [Sankaran et al., 2009, Bag et al., 2012] different values for σ_0 have been proposed. The integration profile in one dimension is given by integration along this dimension of the square with side length a, as

$$\begin{aligned} L(x) &= \frac{1}{a}\int_0^a \mathrm{PSF}(x-x_0)\mathrm{d}x_0 \\ &= \frac{1}{2a}\left(\mathrm{erf}\left(\frac{a-x}{\sqrt{2}\sigma}\right)+\mathrm{erf}\left(\frac{x}{\sqrt{2}\sigma}\right)\right). \end{aligned} \tag{II.22}$$

For large lateral extensions of the detection volume ($a \gg \sigma$), the effect of the PSF becomes negligible, equivalent to $\sigma = 0$ [Sankaran et al., 2009]. Notably, σ_0 can be extracted from a fit to the obtained autocorrelation functions if the pinhole size a and σ on the same order of magnitude [Sankaran et al., 2009, Bag et al., 2012]. As also the lateral propagator factorizes

$$\begin{aligned} \Phi_{\mathrm{AA,xy}}(\vec{r},\vec{r}',\tau) &= \Phi_{\mathrm{AA,x}}(x,x',\tau)\Phi_{\mathrm{AA,x}}(y,y',\tau), \\ \Phi_{\mathrm{AA,x}}(x,x',\tau) &= \frac{1}{\sqrt{4D_\mathrm{A}\pi\tau}}\exp\left(-\frac{(x-x')^2}{4D_\mathrm{A}t}\right), \end{aligned} \tag{II.23}$$

so does the lateral autocorrelation function

$$g_{\mathrm{xy}}(\tau) = g_{\mathrm{x}}(\tau)^2. \tag{II.24}$$

Following Equation II.12 and using Equations II.22 and II.23, the lateral autocorrelation can be calculated as

$$\begin{aligned} g_{\mathrm{x}}(\tau) &= \int_{-\infty}^{\infty}\mathrm{d}x\int_{-\infty}^{\infty}\mathrm{d}x'\, L_{\mathrm{x}}(x)\Phi_{\mathrm{AA,x}}(x,x',\tau)L_{\mathrm{x}}(x'), \\ &= \frac{2}{a^2\sqrt{\pi}}\sqrt{\sigma^2+D_\mathrm{A}\tau}\left(\exp\left(-\frac{a^2}{4(\sigma^2+D_\mathrm{A}\tau)}\right)-1\right)+\frac{1}{a}\mathrm{erf}\left(\frac{a}{2\sqrt{\sigma^2+D_\mathrm{A}\tau}}\right). \end{aligned} \tag{II.25}$$

For g_{xy} we use a more compact notation

$$g_{\mathrm{xy}}(\tau) = \frac{1}{a^2}\left(\frac{1}{\sqrt{\pi}\mu}\left(e^{-\mu^2}-1\right)+\mathrm{erf}(\mu)\right)^2, \tag{II.26a}$$

$$\mu = \frac{a}{2\sqrt{\sigma^2+D_\mathrm{A}\tau}}. \tag{II.26b}$$

It is worth noting that Ries and colleagues [Ries et al., 2008a] also present a numerical solu-

tion and an approximation for observation through a circular pinhole. Circular pinholes are relevant in the case of confocal detection with APD and circular pinholes, often realized by multimode fibers [Schneider et al., 1988, Petrov and Schwille, 2008, Ries et al., 2009b, Weidemann and Schwille, 2009, García-Sáez and Schwille, 2008, Petrášek et al., 2011]. Within this thesis, however, we limit ourselves to squared pinholes.

Notably, in the special case of lateral diffusion of molecules C on the surface and the absence of binding kinetics or diffusion in solution, Sankaran and colleagues obtain the same functional shape as in Equation II.26 [Sankaran et al., 2009]

$$G(\tau) = \frac{1}{N}\left(\frac{1}{\sqrt{\pi}\mu}\left(e^{-\mu^2}-1\right)+\mathrm{erf}(\mu)\right)^2, \tag{II.27a}$$

$$\mu = \frac{a}{2\sqrt{\sigma^2 + D_\mathrm{C}\tau}}. \tag{II.27b}$$

Moreover, Sankaran and colleagues [Sankaran et al., 2009] give a detailed derivation of Equation II.27 including the cross-correlation of two arbitrary rectangular detection regions and the contribution of flow to the correlation functions.

II.1.3.2 Theoretical Autocorrelation Function for Binding Studies with TIR-FCS

Ries and colleagues [Ries et al., 2008a] found a semi-empirical solution based on the solution for freely diffusing particles (Section II.1.3.1) and the previous works of Starr, Thompson and colleagues [Thompson et al., 1981, Starr and Thompson, 2001]. The presented solution was found to adequately describe the results of Monte Carlo simulations [Ries et al., 2008a]. As the range of simulated parameters was limited, a careful re-evaluation within the parameter range of interest might be necessary. Here, the autocorrelation functions factor in axial and lateral parts:

$$G(\tau)\langle F\rangle^2 = \langle A\rangle(g_\mathrm{AA}(\tau) + 2g_\mathrm{AC}(\tau) + g_\mathrm{CC}(\tau)) \tag{II.28a}$$

$$g_\mathrm{AA}(\tau) = g_\mathrm{AA,z}(\tau)g_\mathrm{xy}(\tau, D_\mathrm{A}) \tag{II.28b}$$

$$g_\mathrm{AC}(\tau) = g_\mathrm{AC,z}(\tau)\sqrt{g_\mathrm{xy}(\tau, D_\mathrm{A})}\sqrt{g_\mathrm{xy}(\tau, D_\mathrm{C})} \tag{II.28c}$$

$$g_\mathrm{CC}(\tau) = g_\mathrm{CC,z}(\tau)g_\mathrm{xy}(\tau, D_\mathrm{C}). \tag{II.28d}$$

The lateral correlation contribution $g_\mathrm{xy}(\tau, \{D_\mathrm{A}, D_\mathrm{C}\})$ (Equation II.26) is identical for free molecules in solution (A) and molecules bound to the surface (C), by simple replace-

ment of the diffusion coefficient. D_A and D_C are the diffusion coefficients of the three-dimensional bulk diffusion (A) and the two-dimensional surface diffusion (C), respectively.[3] The solution assumes that the lateral dimension of the system, characterized by the projected pinhole side length a, is much larger than the penetration depth of the evanescent field d_ev. The average fluorescence intensity $\langle F_i \rangle$ for the two species $i = \{A, C\}$ is related to the average particle number N_i and the average concentrations as [Starr and Thompson, 2001]:

$$\langle F_i \rangle = \eta_i N_i \,, \tag{II.29}$$

$$N_\mathrm{C} = \langle C \rangle a^2 \,, \tag{II.30}$$

$$N_\mathrm{A} = \langle A \rangle a^2 d_\mathrm{ev} \,. \tag{II.31}$$

For the expressions for the axial terms, we use

$$\sqrt{R_{1,2}} = -\frac{R_\mathrm{r}}{2\sqrt{R_\mathrm{t}}} \pm \sqrt{\frac{R_\mathrm{r}^2}{4R_\mathrm{t}} - R_\mathrm{r}} \,, \tag{II.32a}$$

$$\sqrt{R_{3,4}} = \sqrt{R_{1,2}} + \sqrt{R_\mathrm{e}} \,, \tag{II.32b}$$

with the reaction rate

$$R_\mathrm{r} = k_a \langle A \rangle + k_d \,, \tag{II.33}$$

the transport rate in solution

$$R_\mathrm{t} = D_\mathrm{A} \left(\frac{\langle A \rangle}{\beta^* \langle C \rangle} \right)^2 \,, \tag{II.34}$$

and the transport rate through the evanescent field

$$R_\mathrm{e} = \frac{D_\mathrm{A}}{d_\mathrm{ev}^2} \,. \tag{II.35}$$

[3] Please note that Ries and colleagues [Ries et al., 2008a] introduced a common pre-factor $\eta_\mathrm{A} \langle A \rangle$, here $\langle A \rangle$, in the three-dimensional solution (Equation II.28a) compared to the one-dimensional case (Equation II.14), as derived by Starr and Thompson [Starr and Thompson, 2001].

Here, we denote $\beta^* = (1 + K\langle A\rangle)^{-1}$.[4] The equilibrium constant is $K = k_a/k_d$ and thus the inverse of the dissociation constant $K_d = K^{-1} = k_d/k_a$. The axial autocorrelation functions are then given by the rather lengthy expressions [Starr and Thompson, 2001, Ries et al., 2008a] [5]

$$g_{\mathrm{CC,z}}(\tau) = \frac{\langle C\rangle\beta^*}{\langle A\rangle}\frac{\sqrt{R_1}w\left[-i\sqrt{\tau R_2}\right] - \sqrt{R_2}w\left[-i\sqrt{\tau R_1}\right]}{\sqrt{R_1}-\sqrt{R_2}}, \tag{II.36a}$$

$$g_{\mathrm{AC,z}}(\tau) = \frac{\langle C\rangle R_\mathrm{r}}{\langle A\rangle}\frac{\sqrt{R_4}w\left[-i\sqrt{\tau R_1}\right] - \sqrt{R_3}w\left[-i\sqrt{\tau R_2}\right] + \left(\sqrt{R_1}-\sqrt{R_2}\right)w\left[-i\sqrt{\tau R_\mathrm{e}}\right]}{\left(\sqrt{R_1}-\sqrt{R_2}\right)\sqrt{R_3R_4}}, \tag{II.36b}$$

$$\begin{aligned} g_{\mathrm{AA,z}}(\tau) =& d_\mathrm{ev}\sqrt{\frac{\tau R_\mathrm{e}}{\pi}} - \frac{d_\mathrm{ev}(2\tau R_\mathrm{e}-1)}{2}w\left[-i\sqrt{\tau R_\mathrm{e}}\right] - \frac{\langle C\rangle}{\langle A\rangle}\frac{R_\mathrm{r}}{\sqrt{R_1}-\sqrt{R_2}} \\ &\times\left\{\frac{\sqrt{R_1}}{R_3}\left(w\left[-i\sqrt{\tau R_1}\right] + \left(2\tau\sqrt{R_1R_\mathrm{e}} + 2\tau R_\mathrm{e} - 1\right)w\left[-i\sqrt{\tau R_\mathrm{e}}\right] - 2\sqrt{\frac{\tau R_3}{\pi}}\right)\right. \\ &\left. -\frac{\sqrt{R_2}}{R_4}\left(w\left[-i\sqrt{\tau R_2}\right] + \left(2\tau\sqrt{R_2R_\mathrm{e}} + 2\tau R_\mathrm{e} - 1\right)w\left[-i\sqrt{\tau R_\mathrm{e}}\right] - 2\sqrt{\frac{\tau R_4}{\pi}}\right)\right\}. \end{aligned} \tag{II.36c}$$

The axial autocorrelation functions $g_{ij,\mathrm{z}}(\tau)$ are thus fundamentally determined by the three rates R_r, R_t and R_e. The experimentally obtained autocorrelation $G(\tau)$ (Equation II.28a)

[4] Please note that Ries and colleagues [Ries et al., 2008a] omitted the exponent -1 in β^* with otherwise identical notation as [Starr and Thompson, 2001]. We consistently denote β as found in [Thompson et al., 1981, Starr and Thompson, 2001, Ries et al., 2008a] as $\beta^* = 1 - \beta$. Accordingly, $\beta^* = [\langle B\rangle/(\langle B\rangle + \langle C\rangle]$ and $\beta = [\langle C\rangle/(\langle B\rangle + \langle C\rangle]$ as defined in [Mücksch et al., 2018].

[5] Please note that Equation II.28a (i.e. Equation 29 in [Ries et al., 2008a]) introduced a common pre-factor $\langle A\rangle$ ($\eta_A\langle A\rangle$ in [Ries et al., 2008a]), compared to the notation of Starr and Thompson (Equation 2 in [Starr and Thompson, 2001]), whereas both denote the average concentration $\langle A\rangle = A$. This pre-factor requires the concentration correlation Φ_{ij} (Equation 45-48 in [Ries et al., 2008a]) to be divided by $\langle A\rangle$ (or $\eta_A\langle A\rangle$) compared to the solution derived by Starr and Thompson (Equations A10 in [Starr and Thompson, 2001]). Additionally, however, Ries and colleagues introduce a factor η_C and omit $\delta(\vec{r}-\vec{r}')$ in Φ_{CC} without further comment. Multiplying the δ-function, we obtain $g_{\mathrm{CC,z}}$ from $\Phi_{\mathrm{CC,z}}$ as presented by Ries and colleagues (Equations 1, 5 and 50 in [Ries et al., 2008a]). Removing the introduced η_C, the solution is consistent with Starr and Thompson (Equation A11 in [Starr and Thompson, 2001]). Consequently, we believe η_C should be removed in Equations II.36a to II.36c compared to the solution presented by Ries and colleagues. Finally, [Starr and Thompson, 2001] and [Ries et al., 2008a] inconsistently list k_d or R_r for $\Phi_{\mathrm{AC,z}}$, $\Phi_{\mathrm{AA,z}}$ $g_{\mathrm{AC,z}}$ and $g_{\mathrm{AA,z}}$.

is finally calculated by dividing by the mean fluorescence signal $\langle F\rangle^2$ with[6]

$$\begin{aligned}\langle F\rangle &= F_{\mathrm{A}} + F_{\mathrm{C}} \\ &= \left(\int \mathrm{d}x\mathrm{d}y\, L(x,y)\right)\left(\langle A\rangle \int \mathrm{d}z\, W(z) + \langle C\rangle W(0)\right) . \end{aligned} \tag{II.37}$$

Notably, the semi-empirical solution (Equation II.28) has limiting cases of special interest, depending on the ratio of the three rates (R_{r}, R_{t}, R_{e}) with significantly simplified expressions. In the reaction limit, $R_{\mathrm{r}} \ll (R_t, R_e)$ the axial autocorrelation function simplifies to a binding term

$$g_{\mathrm{CC,z}}(\tau) = \frac{\langle C\rangle\beta^*}{\langle A\rangle}\exp\left(-R_{\mathrm{r}}\tau\right) \quad (\text{for } R_{\mathrm{r}} \ll (R_{\mathrm{t}}, R_{\mathrm{e}}))\,. \tag{II.38}$$

Here, we used the identity $(\mathrm{erfc}(x) + \mathrm{erfc}(-x))/2 = 1$. The reaction rate R_{r} is the inverse of the characteristic decay time τ_c of the autocorrelation function in the reaction-limited regime ($R_{\mathrm{r}} = \tau_c^{-1}$) [Starr and Thompson, 2001]. The reaction limit is valid, if the fast diffusion in solution leads to a separation of time scales of solution diffusion and binding kinetics. Evaluating the autocorrelation on the time scale of the binding decay, the contribution of solution diffusion vanishes and can be treated as uncorrelated background (Equation II.9). The reaction limit benefits further from a large number of reaction-based fluctuations compared to number of diffusing molecules, or simply put, small solution concentrations.

Neglecting solution diffusion $(g_{\mathrm{AA}}, g_{\mathrm{AC}}) = \text{const.}$ leads to

$$G(\tau)\langle F\rangle^2 = \langle C\rangle\beta^*\,\exp\left(-R_{\mathrm{r}}\tau\right) g_{\mathrm{xy}}(\tau, D_{\mathrm{C}}) \quad (\text{for } R_{\mathrm{r}} \ll (R_{\mathrm{t}}, R_{\mathrm{e}}))\,, \tag{II.39}$$

depending only on the binding kinetics encoded in R_{r} and the lateral diffusion of bound molecules on the membrane (Equation II.26).

In this approximation molecules A in solution contribute as uncorrelated background. The total background intensity is therefore the sum of the solution contribution and other background sources $\langle F_{\mathrm{A}}\rangle + \langle B_g\rangle$. For simplicity, we assume $\langle F_{\mathrm{A}}\rangle = 0$ to obtain the autocorrelation function and later correct for the uncorrelated background. Solving for $G(\tau)$

[6]Please note that we omitted η_{A} and η_{C} for reasons explained above.

and inserting $\langle F \rangle$ (Equation II.37), we thus obtain in the reaction limit

$$G(\tau) = \frac{\beta^*}{N_\mathrm{C}} \exp\left(-R_\mathrm{r}\tau\right) g_\mathrm{xy}(\tau, D_\mathrm{C}) \quad (\text{for } \langle F_\mathrm{A} \rangle = 0)\,. \tag{II.40}$$

We will use this approximation in Chapter VI to describe the binding to sparse, laterally diffusing membrane-attached binding sites.

In case of surface-immobilized binding sites the lateral diffusion of binding sites vanishes ($g_{xy}(\tau, D_\mathrm{C}) = \text{const.}$) and thus we obtain similarly

$$G(\tau) = \frac{\beta^*}{N_C} \exp\left(-R_\mathrm{r}\tau\right) \quad (\text{for } R_\mathrm{r} \ll (R_\mathrm{t}, R_\mathrm{e}), \text{and } C \text{ surface-immobilized})\,. \tag{II.41}$$

This special case of the solution presented by Ries and colleagues [Ries et al., 2008a] was previously derived by Starr, Thompson and colleagues [Thompson et al., 1981, Starr and Thompson, 2001]. In Chapters III and IV this autocorrelation model describes adequately the hybridization of DNA oligonucleotides to surface-immobilized DNA origami nanostructures.

Finally, taking into account the influence of the background intensity on the measured amplitude of the autocorrelation, we correct the amplitudes in Equations II.40 and II.41 to obtain accurate particle numbers.

$$G(\tau) = G_\mathrm{meas}(\tau) \frac{\left(\langle F_\mathrm{A} \rangle + \langle F_\mathrm{C} \rangle + \langle B_\mathrm{g} \rangle\right)^2}{\langle F_\mathrm{C} \rangle^2} \tag{II.42}$$

This correction is important to obtain accurate concentrations and reaction rates from the experimentally obtained autocorrelation curves.

III

QUANTIFYING REVERSIBLE SURFACE BINDING VIA SURFACE-INTEGRATED FLUORESCENCE CORRELATION SPECTROSCOPY

III.1 Motivation and Summary

The interaction of ligands with their receptors is the key regulatory step for many cellular functions [Alberts, 2002, Stillwell, 2016]. Cellular signalling is activated by the specific binding to receptors localized on the membrane [Pierce et al., 2002, Groves and Kuriyan, 2010, Dustin and Groves, 2012]. One key distinction of ligand-receptor binding on membranes from the binding to receptors in solution is the concept of a surface-attached binding site. Surfaces can accelerate binding rates by a reduction of dimensionality [Adam and Delbrück, 1968, Kholodenko et al., 2000] or slow reaction speeds depending on their influence on molecular mobility and accessiblity [Jung et al., 2009].

Moreover, specific and non-specific interactions with other molecules often contribute to a complex reaction scheme that goes beyond a simple bimolecular binding. Quantifying a bimolecular interaction in a complex environment thus yields different results than the study of the same interaction studied in a minimal system [Rivas and Minton, 2018]. Complemented by surface effects and the partitioning into microcompartements, these environmental effects most likely contribute significantly to frequently obsevered discrepancy of *in vivo* and *in vitro* experiments [Rivas and Minton, 2018]. Molecular crowding and excluded volume effects are only one specific aspect, which has found increasing appreciation for its relevance for surface binding kinetics [Minton, 2001, Zhou et al., 2008, Kim and Yethiraj, 2010, Rivas and Minton, 2016]. The full information about the interaction of interest within the cellular context is only available from measurements in different environments. An accurate quantification of ligand-receptor binding thus ideally combines measurements under simplified conditions with measurements in complex media and even live cells. Such a functionality is, however, not provided by commonly used label-free surface binding assays, such as SPR, which fail to recover binding kinetics from multicomponent systems.

TIR-FCS, as pioneered by Thompson and colleagues [Thompson et al., 1981, Thompson, 1982, Thompson and Axelrod, 1983], enables in principle the quantification of reversible ligand-receptor binding [Starr and Thompson, 2001, Lieto et al., 2003] (Section II.1.2). Fluorescent labels and TIR excitation satisfy the high demands towards specificity and surface-selectivity. Moreover, the method has the potential to quantify complex systems. For example, a fluorescent species could be discerned from a non-fluorescent species when competing for the same binding site [Thompson, 1982, Lieto and Thompson, 2004]. However, TIR-FCS binding studies were limited to proof-of-concepts with photomultiplier tube (PMT)-based point detection on specialized instrumentation. The introduction of highly sensitive EMCCD cameras enabled the spatial multiplexing of membrane mobility measurements on standard TIRF microscopes that are widely available to the life science community [Kannan et al., 2006, Kannan et al., 2007, Sankaran et al., 2009], even in live cells [Bag et al., 2014, Krieger et al., 2015, Bag et al., 2016]. A first proof-of-concept in the rather complex framework of kICS highlights the potential to employ camera-based FCS for ligand-receptor interactions [Brandão et al., 2014]. We believe that TIR-FCS was practically, but not principally limited in its capability to explore binding kinetics. While binding studies with TIR-FCS relied on single-point detection and a rather complex treatment of solution diffusion, camera-based applications were mostly limited to studies of lateral diffusion. Strikingly, the potential to enhance binding studies in TIR-FCS with modern camera detection within a simple theoretical framework, stayed widely unexploited.

In this chapter, we developed a camera-based TIR-FCS routine, called SI-FCS, to quantify ligand binding to surface-immobilized receptors. In contrast to TIR-FCS, SI-FCS integrates the signal within large surface areas, extracting only the binding information, while suppressing diffusion contributions. The hybridization of short, complementary DNA oligonucleotides, as employed in DNA-PAINT microscopy, served as a model system to be studied with SI-FCS. We systematically assessed the potential and limitations of the presented approach and found measurements to be precise and highly reproducible. We thus were able to extract association and dissociation rates of the ligand-receptor interaction in agreement with previously published results.

Previous studies, especially the pioneering work by Thompson and colleagues [Thompson et al., 1981, Thompson, 1982, Thompson and Axelrod, 1983, Starr and Thompson, 2001, Lieto and Thompson, 2004], suggest that additional parameters are potentially accessible with SI-FCS, including surface densities, surface diffusion, solution diffusion and solution concentrations. Herein, we make a first important step to revisit the concept of

TIR-FCS that will result in a robust quantification of surface-bound ligand-receptor binding in a wide range of systems, enhancing the general understanding of surface-binding processes.

III.2 Contributed Publication

Quantifying Reversible Surface Binding via Surface-integrated Fluorescence Correlation Spectroscopy

Jonas Mücksch*, Philipp Blumhardt*, Maximilian T. Strauss,
Eugene P. Petrov, Ralf Jungmann, Petra Schwille

* *authors contributed equally*

published in

Nano Letters, 18(5): 3185-3192
doi:10.1021/acs.nanolett.8b00875

The following modifications have been made to the manuscript: citations and references to equations, tables and figures are displayed in a style consistent with this thesis; Supplementary Materials, Supplementary Figures S8 and S10 of the original manuscript are placed in the appendix (pp. 263ff.)

Author Contributions: J.M., P.B., R.J., and P.S. conceived the study. J.M. and P.B. designed, performed, and analyzed the experiments. M.T.S. designed and produced DNA origami samples. J.M., P.B., M.T.S., and E.P.P. performed simulations. J.M., P.B., and P.S. wrote the manuscript. All authors discussed and interpreted results. All authors revised the manuscript and have given approval to the final version of the manuscript. J.M. and P.B. contributed equally to this work.

The binding of proteins to biological surfaces, especially to membranes or membrane proteins, such as receptors, is of key importance for the function and control of many cellular processes. Thus, an accurate determination of surface binding rates and affinities is of great interest for basic research on cells and organisms, but also for biotechnological applications, often targeted toward creating and characterizing new efficient receptor ligands. Consequently, many techniques have been released for the specific task of measuring surface affinities, most prominently label-free ones such as surface plasmon resonance (SPR) [Hodnik and Anderluh, 2013, Singh, 2016] and quartz crystal microbalance (QCM) [Nielsen and Otzen, 2013, Speight and Cooper, 2012], which probe the binding of molecules to specific surfaces indirectly, through a change in resonance frequency of an electromagnetic or

acoustic reference signal upon a mass change of the surface. Other methods commonly used to characterize protein–protein or protein–ligand binding in solution, such as isothermal titration calorimetry (ITC) [Velazquez-Campoy et al., 2015, Freyer and Lewis, 2008], microscale thermophoresis (MST) [Wienken et al., 2010], or fluorescence correlation spectroscopy (FCS) [Magde et al., 1972, Eigen and Rigler, 1994, Schwille et al., 1997], pose the additional problem of solubilizing the membrane or membrane proteins, which has recently been elegantly solved by the introduction of membrane nanodiscs [Bayburt et al., 2002, Nath et al., 2007, Bayburt and Sligar, 2010]. However, the common key shortcoming of all of these well-established techniques is that they function well for irreversible reactions or for perturbed systems relaxing into equilibrium, but not in quasi-steady state, when the numbers of forward and backward reactions are more or less equilibrated and when most binding sites feature a constant turnover of binders. On the other hand, this situation is physiologically most relevant, as it is frequently found in cellular environments. In other words, direct access to the rates of reversible surface binding in unperturbed, native systems has so far hardly been possible.

In the present study, we aim to overcome this limitation of established methods for analyzing surface binding rates by presenting an elegant new way of combining FCS and surface-selective single-molecule wide-field imaging with camera detection. The high surface selectivity is achieved by a total internal reflection (TIR) scheme for excitation. The idea is to time-correlate the total fluorescence signal detected at a selectively TIR-illuminated surface, collected from all of the fluorescent single molecules that are temporarily attached. Consequently, we refer to our approach as surface-integrated FCS (SI-FCS). Touchdowns and turnovers of molecules at this surface are reflected in intensity fluctuations, which can be resolved if the surface concentration is sufficiently low. These fluctuations have so far been mainly utilized by PAINT (points accumulation for imaging in nanoscale topography) microscopy, surpassing the optical diffraction limit for image acquisition. However, as demonstrated here, the steady-state time-correlation analysis of the fluctuating fluorescence intensity also yields characteristic attachment times, from which surface binding and dissociation rates can be efficiently derived with a high statistical accuracy.

In fact, a very similar concept was already at the basis of early formulations of fluorescence correlation spectroscopy for receptor–ligand binding [Thompson et al., 1981, Thompson, 1982, Thompson and Axelrod, 1983], when Thompson and colleagues recognized that TIRF (total internal reflection fluorescence) microscopy [Axelrod, 1981, Stout and Axelrod,

1989] is well-suited to analyze signal fluctuations originating from binding events [Thompson et al., 1981, Thompson, 1982, Thompson and Axelrod, 1983]. However, before the advent of fast and highly sensitive cameras, wide-field TIRF microscopy with area detectors has not supported data acquisition with sufficiently high signal-to-noise ratios required for FCS. In the following decades, the dynamics of single molecules at surfaces have primarily been analyzed by wide-field imaging and tracking with CCD cameras [Schmidt et al., 1996]. Single-particle tracking has been used to quantify residence times in a variety of systems in vitro [Helenius et al., 2006, Loose et al., 2011] as well as in vivo [Elf et al., 2007, Gebhardt et al., 2013, Yang et al., 2004]. However, tracking of fluorophores relies on sparse and clearly distinguishable binding events, which not only leads to a limitation of accessible concentration ranges but also restricts the number of sampled binding events and, thus, the statistical accuracy and precision.

In contrast, FCS has the potential to access kinetics at regimes where single-particle events cannot be resolved by standard imaging approaches. Thus, the combination of TIR excitation with FCS, termed TIR-FCS, originally introduced by Thompson and co-workers with a wide-field prism illumination [Thompson et al., 1981], was revisited after shifting to the technically much simpler objective-based illumination [Anhut et al., 2005, Hassler et al., 2005a]. TIR-FCS has been applied to measure diffusion in membranes [Kannan et al., 2007, Ohsugi et al., 2006, Huang et al., 2015, Bag et al., 2012, Bag et al., 2014], adsorption to C-18 modified glass [Hansen and Harris, 1998b, Hansen and Harris, 1998a, Sonesson et al., 2008], and binding to surface-adsorbed proteins [Lieto et al., 2003, Hassler et al., 2007]. Camera-based FCS, as applied to study diffusion in membranes, significantly improved the multiplexing capabilities compared to confocal FCS, while making it compatible with commonly available TIRF microscopes [Kannan et al., 2007, Bag et al., 2012, Guo et al., 2008]. However, the potential originally proposed for TIR-FCS to determine the kinetic rates of transient surface binding with a high statistical accuracy has still not been experimentally confirmed, mainly due to a lack of proper detectors supporting sufficiently sensitive surface integration with a high temporal resolution.

Remarkably, modern camera technology has arrived at a level that allows one to revisit previous TIR-FCS concepts and elevate them to a level that significantly surpasses other established methods to analyze surface affinity, as demonstrated here. We apply FCS analysis to time series of integrated surface areas acquired by standard TIRF microscopes and extract kinetic information encoded in the signal fluctuations caused by reversible surface binding processes in equilibrium. We validate our approach by analyzing the DNA hy-

bridization kinetics of single-stranded DNA (ssDNA) probes to surface-immobilized DNA origami structures exposing complementary handle strands.

Conceptually, SI-FCS extracts the kinetic rates from a fluctuating signal, where the time scales of the fluctuations differentiate surface binding events from diffusion transients. Both the spatial dependence of the TIR excitation in the direction normal to the surface and the residence times of the bound molecules contribute to the discrimination of bound and unbound molecules. In essence, a bound strand stays longer in the detection volume than a freely diffusing strand. As SI-FCS only discriminates between bound and unbound states, binding kinetics can be simply determined from the fluorescence integrated over the sample surface.

To investigate whether SI-FCS has the desired ability to resolve the rates of reversible surface binding, we studied DNA hybridization kinetics in well-controllable systems. Therefore, we used the DNA origami technique [Rothemund, 2006], in which a long (typically 7249 nucleotides (nt), M13mp18 phage genome) DNA scaffold can be folded into a manifold of engineered nanostructures. We immobilized sheet-like DNA origami structures exposing 12 single-stranded DNA (ssDNA) docking handles [Schnitzbauer et al., 2017] on a passivated coverslip surface (Figure III.1a and supplementary Methods in Section A.1, p. 263). Subsequently, we added complementary imager ssDNA labeled with Cy3B, which diffused freely in solution, but occasionally bound reversibly to its complementary strand at the TIR-illuminated surface, thus producing a local burst of fluorescence to be recorded by the camera. This transient DNA hybridization is an ideal model reaction, as the binding dynamics are highly tunable through the DNA duplex length and thus stability. Therefore, we were able to vary the binding kinetics systematically to probe the performance of our SI-FCS approach.

When such experiments are performed in a regime of sparse binding events, each hybridization event manifests itself as a bright spot in the camera image. Under the right conditions, these events can be precisely localized and rendered to a super-resolved image (Figure III.1b). The localization of transient DNA hybridization events belongs to the variety of localization microscopy approaches and is termed DNA-PAINT [Jungmann et al., 2010]. Moreover, the duration of individual binding events and the time between two consecutive binding events to the same binding site can be used to estimate the association and dissociation rates [Schnitzbauer et al., 2017, Jungmann et al., 2010]. The determination of residence times with single-particle tracking is quite powerful, but it is restricted to individually discernible events, thereby limiting the range of addressable sam-

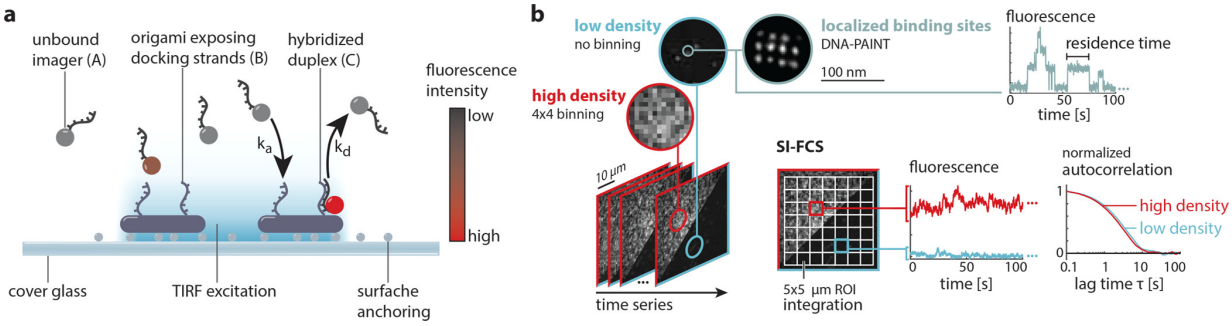

Figure III.1: Application of SI-FCS to quantify DNA hybridization kinetics. (a) Schematic of the transient binding of fluorescently labeled imager ssDNA to the complementary docking strand exposed on a surface-immobilized DNA origami. With TIR excitation, molecules in proximity to the surface, in particular bound molecules, are highlighted. (b) Image series of DNA hybridization events with low (blue) and high (red) surface densities of DNA origami structures. At extremely low densities, individual binding events can be resolved, a super-resolved DNA-PAINT image can be reconstructed, and residence times can be inferred from intensity traces. SI-FCS workflow in low- and high-density regimes (lower right): The signal is integrated over a set of ROIs, yielding an intensity trace for each ROI. From each intensity trace, an autocorrelation curve is calculated and can be fitted by a model function. Depending on the sample, the fit results may be averaged or used to generate a map of binding rates.

ples, the concentration of ligand in solution, and the statistical accuracy. Additionally, the localization of binding events requires small pixel sizes and sufficiently high signal-to-noise ratios, which constrains the achievable camera frame rate. To circumvent these limitations toward a more general applicability, we developed a time-correlation-based method, which is independent of the recognition of individual binding events.

Instead of identifying individual particles in every image, we dissect the image into regions of interest (ROIs), integrate the signal over each of these ROIs, and repeat this step for every image, therefore generating an intensity trace for each ROI (Figure III.1b). The obtained signal traces are autocorrelated in time and fitted by an appropriate model function, which for the case of simple binding and unbinding is a single exponential $G(\tau) = G_0 \exp(-\tau/\tau_c)$. (See the supplementary Theoretical Basis in Section III.2.1, p. 39.) G_0 is the amplitude of the autocorrelation function, a constant prefactor. The characteristic decay time of this exponential function is given by

$$\tau_c = (k_a \langle A \rangle + k_d)^{-1} \tag{III.1}$$

Here we introduced the association and dissociation rates k_a and k_d, and the mean con-

centration of unbound ligand $\langle A \rangle$. In the special case of hybridization studies, $\langle A \rangle$ is the concentration of free ssDNA. The functional dependency of τ_c has two major implications: First, in a low concentration regime ($\langle A \rangle \ll k_d/k_a$), τ_c equals the inverse dissociation rate, which is commonly termed the surface residence time τ_d. Second, we note that a classical titration of $\langle A \rangle$ experimentally determines the dependence of τ_c on $\langle A \rangle$. This dependence can be fitted by Equation III.1, to simultaneously obtain k_a and k_d. Finally, it is straightforward to calculate the dissociation constant $K = k_d/k_a$ from there. The capability to extract K from SI-FCS measurements is already an attractive feature of the method. The capability to directly measure the dissociation and association rates themselves makes SI-FCS even more powerful. Provided the experimental data can be supported by theoretical predictions of the binding free energy ΔG, it is possible to estimate k_a and k_d from a single measurement in the limiting case of small ligand concentration compared to the dissociation constant $\langle A \rangle \ll K$. (See the supplementary Table III.2, p. 43.)

To experimentally explore the kinetics accessible to SI-FCS, we designed four different DNA origami structures, which together with our labeled ssDNA strand form a 7, 8, 9, and 10 nt overlap, respectively. (See the supplementary Methods in Section A.1, p. 263.) All measurements were taken at a sufficiently low illumination, such that bleaching was negligible. (See the supplementary Figure III.4, p. 45.) Strikingly, the corresponding four experimental autocorrelation curves are clearly distinguishable, but even more importantly, the exponential model describes the curves adequately and unambiguously (Figure III.2a). We conclude that the proposed model, which considers only reversible binding and assumes that diffusion dynamics are equilibrated on the relevant time scale, is an appropriate choice. The shifts between the four correlation curves in Figure III.2a manifest themselves in significant differences in characteristic decay times τ_c as obtained from the individual fits. We measured decay times $\tau_c = (0.44 \pm 0.01)$ s for 7 nt, $\tau_c = (2.39 \pm 0.05)$ s for 8 nt, $\tau_c = (4.86 \pm 0.05)$ s for 9 nt, and $\tau_c = (90 \pm 7)$ s for 10 nt (supplementary Table III.2, p. 43). In all cases, the standard deviation was well below 5 % of the mean, and individual measurements for the same nt overlap were indistinguishable (supplementary Figure III.5, p. 45). The obtained characteristic decay times reflect the number and type of the base pairing. As expected, the residence time increases with an increasing nt overlap. Moreover, we observed that the relative increase of τ_c from 9 to 10 nt is by far the largest. We attribute this effect to the addition of a stronger binding GC pair from 9 to 10 nt, whereas in the other cases a weaker binding AT pair was added (supplementary Table III.2, p. 43). Having demonstrated the capability of SI-FCS to resolve differences

in the number of nucleotide overlaps, we can immediately conclude that single base pair mismatches are also resolvable. According to calculations, the free energy of DNA hybridization decreases to a larger extent by the introduction of a single base pair mismatch than by the removal of a terminal base pair [Zadeh et al., 2011].

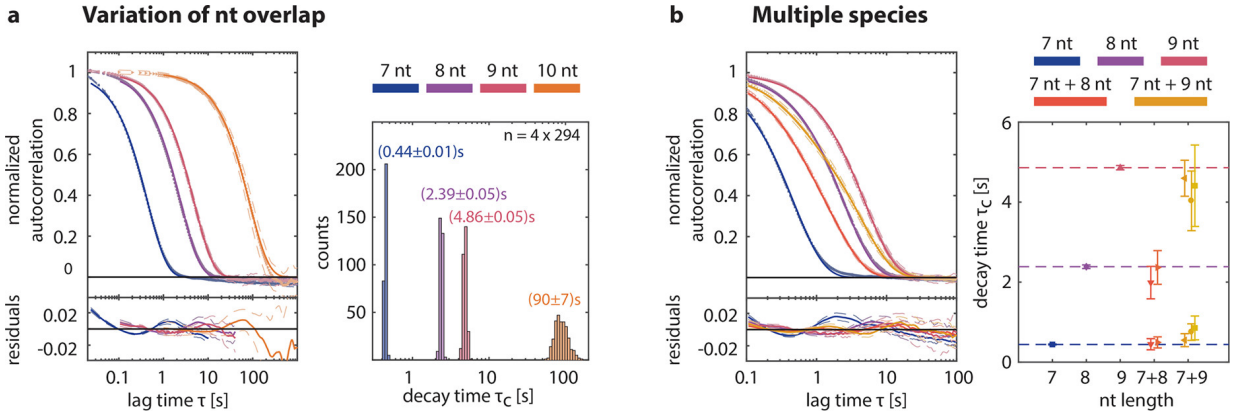

Figure III.2: Quantification of binding kinetics by SI-FCS. (a) Representative autocorrelation curves and their single-exponential fits for DNA hybridization of 7, 8, 9, and 10 nt. The different hybridization kinetics are clearly distinguishable. The obtained characteristic decay times are highly reproducible and range from 0.5 s to almost 100 s. The histograms correspond to 6 measurements per nt overlap, with 49 ROIs each. (b) Representative autocorrelation curves for mixed samples with two hybridization kinetics exhibit clear shape differences compared to single samples of 7, 8, and 9 nt, respectively. The individual decay times differ by less than a factor of 10. For mixed samples, the decay times from single sample experiments (panel a) are recovered with an error smaller than 20 %.

We performed all measurements presented in Figure III.2 with 10 nM (for 7–9 nt) or 1 nM (for 10 nt) of labeled ssDNA. The 10 nt sample has the smallest dissociation constant, which is expected to be on the order of 10–100 nM [Jungmann et al., 2010, Peterson et al., 2016]. Consequently, the condition $\langle A \rangle \ll K$ is met and the dissociation rates are estimated directly by taking the inverse of the reported characteristic decay times τ_c (supplementary Table III.2, p. 43). These estimates of k_d are comparable to previously reported rates [Peterson et al., 2016, Dupuis et al., 2013, Jungmann et al., 2016]. Small deviations can likely be attributed to the effect of different sequences and ion concentrations in the buffer, which are known to affect the formation of secondary structures. (For reviews, see refs [Woodson, 2005] and [SantaLucia and Hicks, 2004].) Moreover, we estimated the association rates based on predictions of the binding free energy ΔG (supplementary Table III.2, p. 43) [Zadeh et al., 2011]. These results are in good agreement with recently reported values [Jungmann et al., 2010, Peterson et al., 2016, Dupuis et al., 2013, Jungmann et al., 2016, Lang

and Schwarz, 2007].

To challenge the SI-FCS method even further, we performed measurements on samples with multiple species (Figure III.2b). Resolving more than one species is challenging and requires high-quality autocorrelation curves with characteristic decays on separable time scales. We combined 7 nt samples with 8 nt and 9 nt. Thus, the expected values of τ_c differ by less than an order of magnitude, which makes them intrinsically difficult to distinguish. Remarkably, the mixed samples with two kinds of binding sites show autocorrelation curves with a significantly different shape, compared to single-species samples. Consequently, it is justified to apply a biexponential fitting model, with each of the exponents reflecting one kind of binding site. Strikingly, the results from single-species measurements were recovered, although a slight bias (below 20 %) was observed. The reliability of the discrimination of two species generally depends on the relative amplitudes and the time separation of the two decays. Moreover, the signal-to-noise ratio and the correlation of the noise itself are of relevance, which makes general predictions regarding the resolvability of two species challenging.

To determine association and dissociation rates without relying on theoretical assumptions, we performed titration experiments, comprising several SI-FCS measurements with identical origami samples but varying concentrations $\langle A \rangle$ of labeled free ssDNA. Following Equation III.1, we expected that an increase in the concentration of free strands shifts the autocorrelation curve to shorter times. Indeed, our experiments on 9 and 10 nt showed this effect (Figure III.3a,b). For concentrations of free strands higher than 100 nM for 9 nt and 10 nM for 10 nt, respectively, a second component appeared at large lag times in the autocorrelation and was accounted for by a second exponential decay in the fitting model. We speculate that this second component may originate from unspecific binding. Regardless of the nature of this second component, the faster of the two decays was insensitive to changes in the fitting of the slower component. We fitted the dependence of τ_c on the concentration of free ssDNA (Figure III.3a,b) and obtained the association and dissociation constants without any further assumptions (Table III.1). The obtained dissociation rates are in line with the rates previously determined from measurements with low ligand concentrations (supplementary Table III.2, p. 43). Moreover, we calculated the binding free energy from the titration experiments and reproduced the predicted values (supplementary Table III.2, p. 43) within 10 %.

On the basis of Equation III.1, it is sufficient to perform two independent measurements at significantly different concentrations of ligand to extract k_a and k_d of a specific system.

Table III.1: Hybridization Parameters for 9 and 10 nt determined by SI-FCS and titration of free ssDNA. Errors are given by the 95 % confidence bounds of the fit.

sample	k_d [1/s]	k_a [10^6 /(Ms)]	K_d [nM]	ΔG [kJ/mol]
9 nt	0.180 ± 0.012	2.5 ± 0.5	72 ± 16	40.5 ± 0.6
10 nt	0.009 ± 0.002	2.1 ± 0.4	4.2 ± 1.8	47.5 ± 1.1

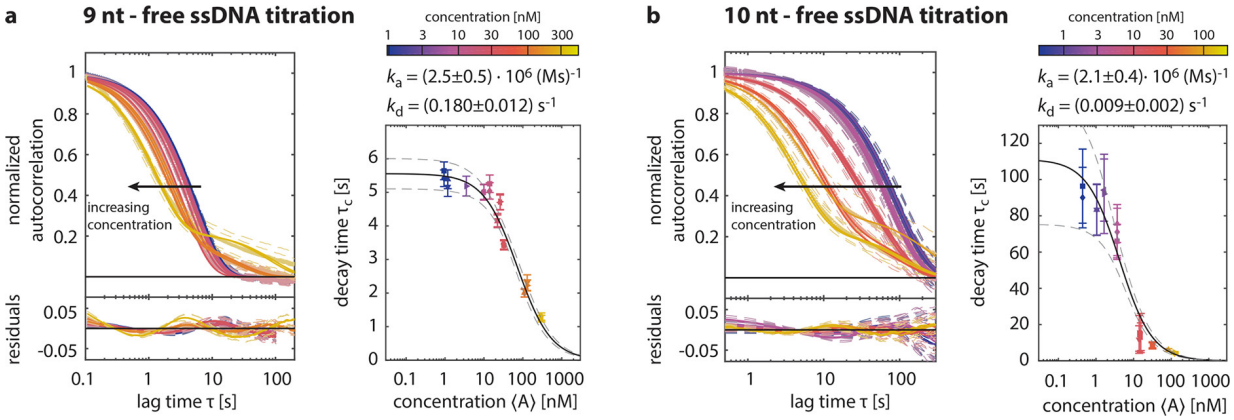

Figure III.3: Determination of association and dissociation rates by SI-FCS. (a) Autocorrelation curves for 9 nt overlap with varying concentrations of complementary ssDNA in solution, ranging from 1 nM to 300 nM. With an increase in concentration, the characteristic decay shifts to shorter times. Autocorrrelation curves for 100 nM and higher were fitted with a biexponential. (See the supplementary Methods in Section A.1, p. 263.) A fit of the characteristic decay times according to Equation III.1 yields association and dissociation constants of the binding reaction. The 95 % confidence bounds of the fit are indicated (gray dashed lines). (b) as in panel a, but with 10 nt origami and complementary ssDNA concentrations ranging from 300 pM to 100 nM. Autocorrelations for 10 nM and higher were fitted with a biexponential decay model.

Compared to a full titration series, a measurement at two concentrations saves potentially precious samples and measurement time, but comes at the cost of reduced precision. For pairs of concentrations representing sufficient intervals along the titration curve, the reaction rates for 9 and 10 nt could be recovered within 20 % accuracy. (See the supplementary Figure III.6, p. 46.)

The presented results demonstrate that dissociation and association rates of reversible binding reactions are accessible by SI-FCS. The lower limit of accessible characteristic decay times depends only on the time resolution of the camera, the fluorophore's photon budget, and the diffusion time of ligand, which in our case is considered to be much smaller than the characteristic decay time. Consequently, SI-FCS has the capability to resolve kinetics, which may be potentially too fast for SPR or QCM-D. However, it should be ensured that the time resolution, i.e., the inverse frame rate, is at least 3–10 times shorter than the characteristic decay time (confirmed by simulations, compare supplementary Figure III.7, p. 47, data not shown). On the other hand, in theory, there is no upper limit for the accessible characteristic decay times. For very large residence times, fluorophore photobleaching should be considered, but can typically be handled by identifying an appropriate regime of low irradiance, camera exposure time, and camera acquisition rate. Otherwise, the accessible characteristic decay times are only limited by the stability of the system under investigation. On the basis of a reanalysis of DNA hybridization data and Monte Carlo simulations, we determined that systematic biases stay below 10 % of the actual value, provided the total measurement times are at least a factor of 300 longer than the characteristic decay time. (See the supplementary Figure III.7, p. 47.) It should be noted that for samples with sufficiently long τ_c, the required measurement duration can exceed hours, which puts high demands on sample and microscope stability. For example, for a sample that is stable for 1 h, τ_c should not exceed 12 s. If a lower accuracy is sufficient, experiments can also be shorter; e.g., to achieve a bias below 20 %, measurements need to be only around 50 times longer than τ_c. (See the supplementary Figure III.7, p. 47.) Nonetheless, in light of potential live cell applications, the maximum accessible values of τ_c are expected to be below 10 s. On the other hand, many in vitro systems are stable over much longer times, thus providing access to slower kinetics by SI-FCS. Note that, irrespectively of the particular value of τ_c, the convergence to the true value is achieved faster than for FCS measurements of 2D diffusion with an equivalent diffusion time $\tau_D = \tau_c$.

For long time SI-FCS measurements, an important issue is the axial focus stability, which can be ensured by means of active focus stabilization, a common feature of many

commercial TIRF microscopes. In order to avoid potential artifacts, the contribution of the active stabilization system to fluorescence signal fluctuations should be negligible compared to fluctuations originating from transient binding kinetics in the sample. We found that this condition was always satisfied in all our measurements. In fact, the focus stabilization typically operated at small position adjustments in the nanometer range, whereas the method relies on the wide-field detection, where the total detected fluorescence signal is insensitive to nanometer-scale focus adjustments.

SI-FCS does not require specialized equipment but only a regular TIRF microscope, which has become standard equipment in the majority of imaging facilities. Consequently, SI-FCS is easily accessible to a broad variety of researchers. In contrast to other methods, SI-FCS is compatible with other standard light imaging modalities and does not require advanced sample preparation on specialized surfaces. On the contrary, sample preparation approaches that were developed for fluorescence imaging of surface-related processes can be applied without any alterations. Moreover, the compatibility of SI-FCS with regular TIRF or epifluorescence imaging renders it a valuable tool for quality control and sample validation inaccessible to many other methods. For example, for membrane binding kinetics, the integrity of the supported membrane can be validated by a membrane staining.

Conventional confocal FCS measurements rely on an initial calibration measurement to determine the size of the confocal detection volume. In their recent application of TIR-FCS to study lateral diffusion in a supported lipid membrane, Bag and colleagues elegantly varied the software binning during postprocessing of data to circumvent the need for any calibration [Bag et al., 2012]. In our case, SI-FCS was exclusively used to quantify binding dynamics and did not rely on any spatial information. Hence, we did not need any calibration measurement. To demonstrate this, we performed a series of measurements on one sample, altered the axial sample position in between measurements, and thereby the effective projected pixel size. Over a range of more than 3 µm, the determined characteristic decay time was constant within the errors of the measurement. (See the supplementary Figure III.8, p. 49.)

SI-FCS is an equilibrium method, which retrieves information about the nature of the system under investigation from the fluctuations in the detected fluorescence signal. This has two major implications: First, the equilibrium regime in which SI-FCS measurements are performed does not require any perturbations of the system under investigation from the outside. In particular, no pumping is needed to probe a system, nor is a constant flow of liquid above the surface required, which keeps the consumption of valuable ligand to a

minimum. Second, SI-FCS requires fluorescent labeling of the ligand, which despite the small size of chemical labels introduces an alteration to the system. On the other hand, the fluorescent label provides specificity, which allows for multiplexing through spectrally separated labels, as well as a dual-color cross-correlation option to potentially investigate cobinding and positive feedbacks [Schwille et al., 1997, Leutenegger et al., 2006, Rička and Binkert, 1989]. Moreover, the high specificity through a fluorescent label enables measurements in complex fluids. To take the latter point even further, SI-FCS is compatible with measurements on live cells [Kannan et al., 2007, Ohsugi et al., 2006], which, except for single-particle tracking, is intrinsically inaccessible to most other methods that characterize surface binding kinetics. In comparison to single-particle tracking, SI-FCS performs over a wider range of surface densities and still yields accurate results, when the surface concentration of docking sites or fluorescent probes is too high to detect them individually. (See the supplementary Figures III.9 and III.10, p. 51ff.) Moreover, the analysis of the amplitude of the autocorrelation function shows potential to obtain further insights into the surface density of the sample under investigation and will be subject to future studies.

In principle, many systems that are accessible to SPR experiments can also be quantified using SI-FCS. However, SI-FCS has the potential to also measure lateral diffusion in supported lipid bilayers and cell membranes [Thompson et al., 1981, Kannan et al., 2007, Ohsugi et al., 2006, Bag et al., 2012, Bag et al., 2014, Lim et al., 2013]. The simultaneous probing of diffusion and binding dynamics by a combination of TIR-FCS and SI-FCS would further broaden the spectrum of possible applications, ranging from membrane binding to membrane-receptor ligand interactions. Furthermore, it is worth noting that SI-FCS is in principle not limited to TIR-illumination and fluorescence detection. Any scheme rendering reversible binding as fluctuating signal separable from diffusion is compatible with surface-integrated correlation spectroscopy. Potential examples include, but are not limited to, FRET to surface-attached acceptors [Auer et al., 2017] and interferometric scattering [Piliarik and Sandoghdar, 2014].

To conclude, we quantified the association and dissociation rates of reversible surface binding by camera-based SI-FCS, which is compatible with conventional TIRF microscopes. To demonstrate the versatility of our approach, we studied the reversible hybridization kinetics of DNA as a well-controllable test system. The obtained association and dissociation rates are in agreement with previously reported results, which were obtained using different experimental methods [Jungmann et al., 2010, Peterson et al., 2016, Dupuis et al., 2013, Jungmann et al., 2016, Lang and Schwarz, 2007] and thus validate the SI-FCS ap-

proach. On the basis of the measured hybridization kinetics, we discussed the range of kinetics accessible to SI-FCS and provided a rule of thumb for the required measurement time. The small sample volumes required for SI-FCS, the potential compatibility with lateral diffusion studies and imaging modalities, and its steady-state operation without the need for external perturbations are the major advantages of the approach. We believe that the application of SI-FCS for the quantification of surface binding can make a major contribution toward understanding important biological systems on the quantitative level.

III.2.1 Supplementary Theoretical Basis: Theoretical Model for the Autocorrelation Function of a One-component Binding-unbinding Reaction Without Diffusion

Considerable effort has been previously put into the derivation or approximation of an all-embracing correlation curve, which covers lateral 2D-diffusion, 3D diffusion and reversible binding [Thompson et al., 1981, Lagerholm and Thompson, 1998, Starr and Thompson, 2001, Ries et al., 2008a]. To reduce the complexity, and as we are mainly interested in the measurement of binding kinetics, we pursue a simplified approach. We define the autocorrelation function G_{meas}, which is directly computed from acquired images, as

$$G_{\mathrm{meas}}(\tau) = \frac{\langle \delta F(0) \delta F(\tau) \rangle}{\langle F \rangle^2} \tag{III.2}$$

Here, F is the fluorescence signal, which can be decomposed into a correlated contribution $F_c(t)$ and an uncorrelated background $B_g(t)$. In a typical equilibrium system, the total fluorescence signal can be expressed in terms of its mean $\langle F \rangle$ and the fluctuations $\delta F(t)$ around this mean:

$$F(t) = \langle F \rangle + \delta F(t) = \langle F_c \rangle + \langle B_g \rangle + \delta F_c(t) + \delta B_g(t) \tag{III.3}$$

Provided that $B_g(t)$ is uncorrelated background, the computed autocorrelation function reduces to:

$$G_{\mathrm{meas}}(\tau) = \frac{\langle \delta F_c(0) \delta F_c(\tau) \rangle}{\left(\langle F_c \rangle + \langle B_g \rangle \right)^2} \tag{III.4}$$

Practically, it is rather relevant to measure the correlation curve $G_c(\tau)$ based on $\delta F_c(\tau)$ and normalize to the mean of $F_c(\tau)$. Provided that the background can be measured in a

separate blank control sample, $G_c(\tau)$ can be calculated easily [Thompson, 1999]:

$$G_c(\tau) = G_{\text{meas}}(\tau)\frac{\langle F\rangle^2}{(\langle F\rangle - \langle B_g\rangle)^2} \tag{III.5}$$

It is worth noting that the amplitude of the autocorrelation curve is decreased by uncorrelated background, but the temporal decay is not altered. In the context of the SI-FCS measurements presented here, the uncorrelated background can be not only background noise or stray light, but also the signal contribution from freely diffusing ligand. The latter can be considered as uncorrelated background if the 3D diffusion of labeled ligand through the detection volume is occurring on a much shorter timescale than the considered binding kinetics.

To obtain an expression for $G_c(\tau)$, we note that the fluorescence signal fluctuations have a contribution from freely diffusing and from bound ligand $\delta F_c \sim \delta A + \delta C$. As discussed above, only the latter is correlated on the considered timescale. Analogously, we note that $\langle F_c\rangle \sim \langle C\rangle$. Following the common scheme of derivations for FCS, we assume equivalence of the time and ensemble averages and rewrite $G_c(\tau)$ as follows:

$$G_c(\tau) = \frac{\int \mathrm{d}^3r \int \mathrm{d}^3r' \Phi_{CC}(\tau)\delta(r-r')}{\langle C\rangle^2(\int \mathrm{d}^3r)^2} \tag{III.6}$$

Here, the integrals run over the entire detection volume. To make use of Equation III.6, we aim to find an expression for δC, or the concentration correlation function

$$\Phi_{CC}(\tau) = \langle \delta C(0)\delta C(\tau)\rangle \tag{III.7}$$

The fluctuations in C are governed by binding kinetics, which we assume to be a simple bimolecular reaction of the type $A + B \leftrightharpoons C$, where A is a ligand, freely diffusing above a surface, B is an unbound receptor, which is immobilized at a surface, and C is the bound receptor-ligand-pair (see Fig. III.1a). Under the assumption that all diffusion dynamics through a considered region of interest are equilibrated, the change of the concentration of conjugates C, will be governed by a source and a sink term:

$$\frac{\mathrm{d}C}{\mathrm{d}t} = k_a AB - k_d C \tag{III.8}$$

Here, we introduced the association rate k_a and the dissociation rate k_d. Both rates fulfill

the well-known relation to the dissociation constant K_d and the mean concentrations:

$$K_d = \frac{k_d}{k_a} = \frac{\langle A\rangle\langle B\rangle}{\langle C\rangle} \tag{III.9}$$

As the total number of surface receptors $S = \langle B\rangle + \langle C\rangle = \text{const}$ is constant, it is evident that a decrease of receptor-ligand pairs will result in an increase of free receptor by the same magnitude: $\delta B = -\delta C$. Therefore, the differential equation for C is easily transformed into a differential equation for Φ_{CC}:

$$\frac{\mathrm{d}\Phi_{CC}(\tau)}{\mathrm{d}\tau} = -(k_a\langle A\rangle + k_d)\Phi_{CC}(\tau) \tag{III.10}$$

Differential equations of this kind are very well known and have the simple solution

$$\Phi_{CC}(\tau) = \Phi_0 e^{-\tau/\tau_c} \tag{III.11}$$

The obtained exponential function decays with the characteristic time constant $\tau_c = (k_a\langle A\rangle + k_d)^{-1} = (\tau_a^{-1} + \tau_d^{-1})^{-1}$, which is related to the dwell time $\tau_d = k_d^{-1}$ and the association time $\tau_a = (k_a\langle A\rangle)^{-1}$.

To obtain an expression for Φ_0, we follow the argumentation of Thompson and colleagues [Thompson et al., 1981]: First, Φ_0 needs to meet the initial condition $\Phi_{CC}(\tau = 0) = \Phi_0 = \langle \delta C^2\rangle$. This quantity is known as the variance. To find the underlying distribution, we note that for every given point in time, each surface receptor occupies one out of two states: bound to a ligand or unbound. Provided that all receptors are independent, this corresponds to a binomial distribution, which has the variance $\Phi_0 = S\beta(1-\beta)$. Here we used again the total surface concentration of receptors $S = \langle B\rangle + \langle C\rangle$, and introduced the fraction of bound receptors $\beta = \frac{\langle C\rangle}{\langle B\rangle+\langle C\rangle} = \frac{1}{1+\frac{k_d}{k_a\langle A\rangle}} = \frac{\tau_c}{\tau_a}$, which can be interpreted as the success probability of the binomial distribution. Analogously, the fraction of unoccupied receptors reads $(1-\beta) = \frac{\langle B\rangle}{\langle B\rangle+\langle C\rangle} = \frac{1}{1+\frac{k_a\langle A\rangle}{k_d}} = \frac{\tau_c}{\tau_d}$. Therefore, we obtain

$$\Phi_0 = \langle C\rangle\frac{\tau_c}{\tau_d} = \langle C\rangle(1-\beta) \tag{III.12}$$

And finally, after insertion into Equation III.6, we get an analytic expression for the auto-

correlation function of reversible binding:

$$G_c(\tau) = \frac{1}{N_C}\frac{\tau_c}{\tau_d}e^{-\tau/\tau_c} = \frac{1}{N_S}\frac{1-\beta}{\beta}e^{-\tau/\tau_c} \tag{III.13}$$

Here, we introduced the average number of bound receptors N_C and the total number of receptors N_S in the detection volume. Alternatively, Equation III.13 can be obtained as a limiting case of the advanced derivation of the full autocorrelation by Thompson and colleagues [Thompson et al., 1981]. Interestingly, the amplitude $G_0 = \lim_{\tau\to 0} G_C(\tau)$ of the correlation is not only proportional to the absolute number of occupied binding sites, but also depends on the fraction of unoccupied sites. However, if $\tau_a \gg \tau_d$, i.e. in case of low concentration of labeled ligand $\langle A\rangle \ll K_d$, the number of occupied binding sites can be obtained directly as the inverse of the correlation amplitude.

III.2.2 Supplementary Table: Free Energy of DNA Hybridization

Table III.2: Hybridization parameters for different DNA sequences with the target sequence 5'-CTAGATGTAT-3'. SI-FCS measurements were performed in a low concentration regime of labeled strands, such that the dissociation rate is directly estimated from the characteristic decay time of the autocorrelation curve $\tau_c \xrightarrow{\langle A\rangle \ll K} \tau_d = k_d^{-1}$. For each pair of sequences, the free energy ΔG of hybridization was estimated using the Nucleic Acid Package (NUPACK) [Zadeh et al., 2011] with the following settings: temperature $T = 296.15\,\mathrm{K}$, concentration of Na^+ 50 mM, concentration of Mg^{2+} 9 mM. The calculations were performed based on the parameters provided by SantaLucia [SantaLucia, 1998], which had to be adjusted for our buffer conditions. To describe our conditions best, we used the minimum concentration of Na^+ compatible with [SantaLucia, 1998], which compensates partially for the Tris in our buffer. The remaining Na^+ could be accounted for by lowering the Mg^{2+}, although the relevant equivalent amount of Mg^{2+} would be small [Owczarzy et al., 2008, von Ahsen et al., 2001, Mitsuhashi, 1996]. The dissociation constant K and the binding free energy ΔG are linked via the well-known equation $\Delta G = -RT \ln \frac{K}{K_0}$. Here, we introduced the gas constant R, the temperature T, and a reference constant $K_0 = 1\,\mathrm{M}$, which has the sole purpose to ensure that the logarithm is applied to a dimensionless quantity. Consequently, after obtaining k_d as the inverse of τ_c, the association rate is calculated as $k_a = \frac{k_d}{K_0} e^{\frac{\Delta G}{RT}}$. The obtained association rates can be regarded as estimates of the true rates. The estimated association rates are in line with values reported elsewhere [Peterson et al., 2016, Lang and Schwarz, 2007, Jungmann et al., 2010, Dupuis et al., 2013, Jungmann et al., 2016]. Moreover, all estimated association rates appear to be similar, regardless of the basepair overlap. The same observation was recently reported for 9 nt and 10 nt hybridization [Jungmann et al., 2010].

sequence $\mathbf{5' \to 3'}$	**concentration** $\langle \mathbf{A} \rangle$ **[nM]**	**overlap**	**predicted** $\mathbf{\Delta G}$ **[kJ/mol]**	**measured** $\tau_\mathbf{c}$ **[s]**	**measured** $\mathbf{k_d}$ **[1/s]**	**estimated** $\mathbf{k_a}$ $\mathbf{[10^6/(Ms)]}$
TTATACATC	10	7 nt	36.03	0.44 ± 0.01	2.272 ± 0.052	5.15 ± 0.12
TTATACATCT	10	8 nt	37.83	2.39 ± 0.05	0.418 ± 0.009	1.97 ± 0.04
TTATACATCTA	10	9 nt	41.98	4.86 ± 0.05	0.206 ± 0.002	5.23 ± 0.05
TTATACATCTAG	1	10 nt	48.98	90 ± 7	0.0111 ± 0.0009	4.84 ± 0.39

III.2.3 Supplementary Figures

Control for Photobleaching

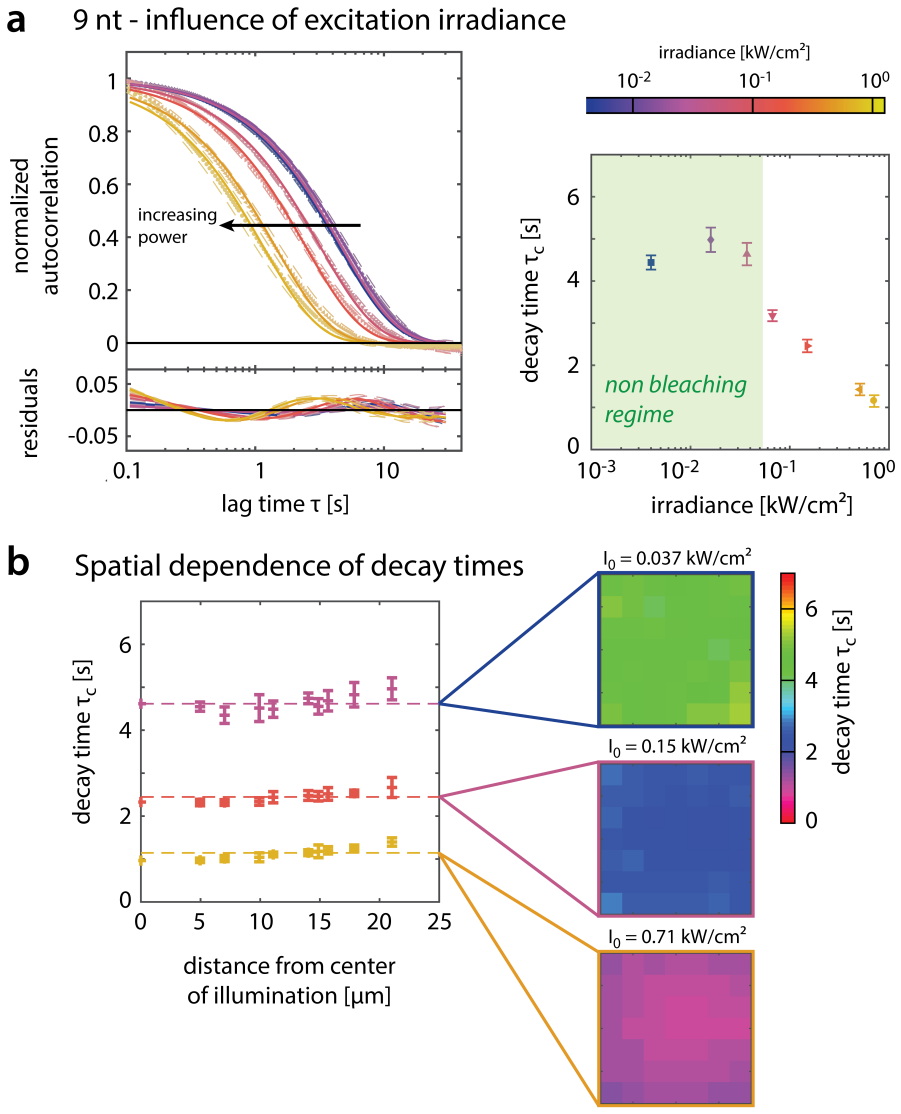

Figure III.4: caption on next page.

Figure III.4: Dependence on Excitation Power. a) Bleaching is observed as an apparent reduction of the residence time and therefore also as a reduction of τ_c. The autocorrelations were averaged over several ROIs and measured with $\langle A \rangle = 10\,\mathrm{nM}$ and 9 nt base pair overlap. We identified irradiances below $I_0 < 0.037\,\mathrm{kW/cm^2}$ to be free from bleaching. For 10 nt the residence times are significantly longer and the bleaching free regime was determined to be $I_0 < 1.6 \times 10^{-3}\,\mathrm{kW/cm^2}$, which was achieved by reducing the excitation power and the frame rate of acquisition from 85 Hz to 10 Hz (data not shown). b) The Gaussian shape of the illumination profile may induce a spatial profile of the τ_c obtained from different ROIs. For high irradiances, the apparent diffusion time is not only globally lowered due to bleaching, but also is shortest in the center of illumination. For irradiances below $I_0 < 0.037\,\mathrm{kW/cm^2}$, this spatial distribution becomes negligible.

Reproducibility of SI-FCS measurements

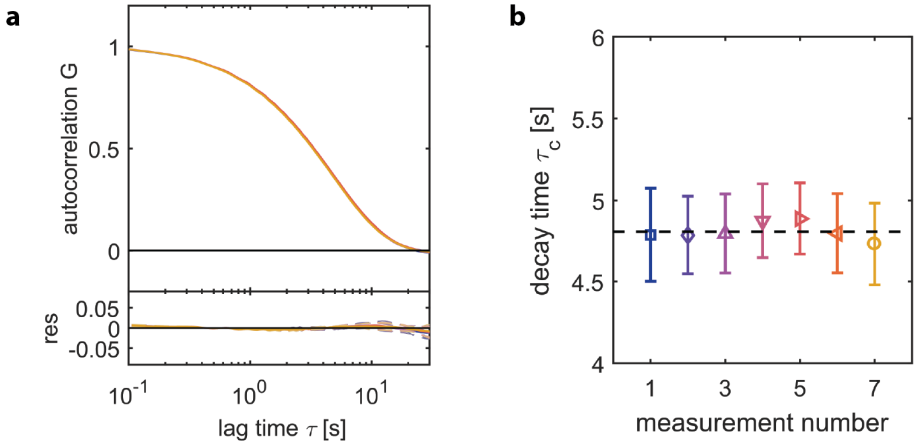

Figure III.5: Reproducibility of SI-FCS measurements. To estimate the robustness and reproducibility of this method, we repeated identical measurements on one and the same sample. When superimposing the autocorrelation curves from seven measurements on the hybridization of ssDNA with 9 nt overlap, all curves were indistinguishable (Fig. III.5a). For every measurement, the standard deviation of the characteristic decay times obtained from 49 ROIs was considerably lower than 10 % of the mean, demonstrating that consistent results are obtained over the entire field of view, independent of the local illumination profile. Moreover, the comparison of the average characteristic decay times from several independent measurements (Fig. III.5b) showed that the scatter is less than 5 % of the overall average, that is $\langle \tau_c \rangle = (4.81 \pm 0.05)\,\mathrm{s}$, with the error being the standard deviation of the seven measurements. This series of similar measurements demonstrated the excellent accuracy of SI-FCS for the determination of binding rates.

Determination of kinetic rates from two measurements

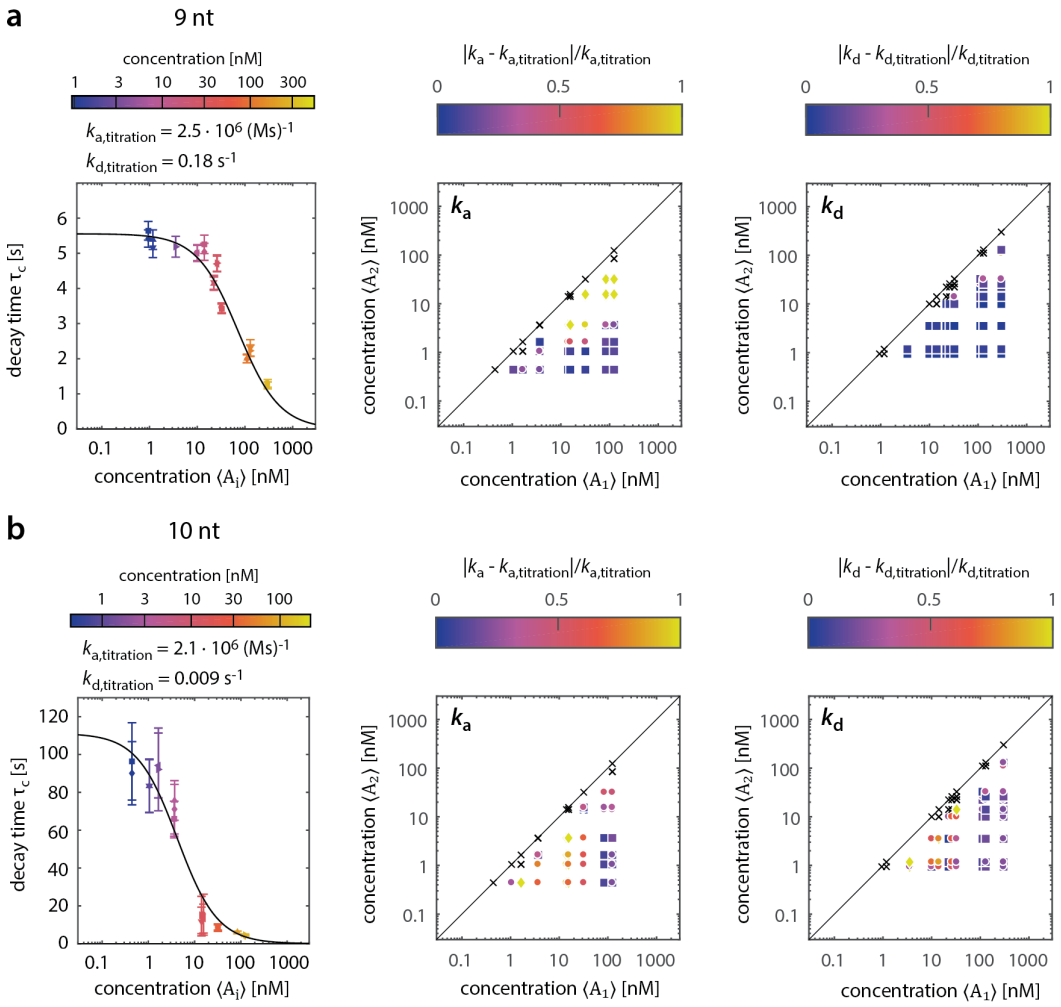

Figure III.6: Extraction of association and dissociation rates from two measurements. Based on Equation III.1 the knowledge of two points of the titration curve is in principle sufficient to determine the association rate k_a, the dissociation rate k_d and therefore also the equilibrium constant $K = k_d/k_a$. a) For 9 nt, the full titration curve (left panel), k_a (center panel) and k_d (right panel) calculated from pairs of two measurements along the titration curve. The relative difference $|k_{a/d} - k_{a/d,\text{titration}}|/k_{a/d,\text{titration}}$ is represented by the color of the points. For pairs of concentrations $(\langle A_1\rangle, \langle A_2\rangle)$ of differently dominated regimes ($k_d \ll k_a\langle A_1\rangle$ and $k_d > k_a\langle A_2\rangle$) the rates can be recovered with an error smaller than 20 % (highlighted as squares). Pairs of concentrations which were different less than a factor of two were excluded from the analysis and marked as crosses. Concentration pairs leading to a relative error of more than 100 % saturated the color scale and were marked as diamonds. b) Same as panel a), but the analysis was based on data sets from 10 nt hybridizations.

Required measurement time

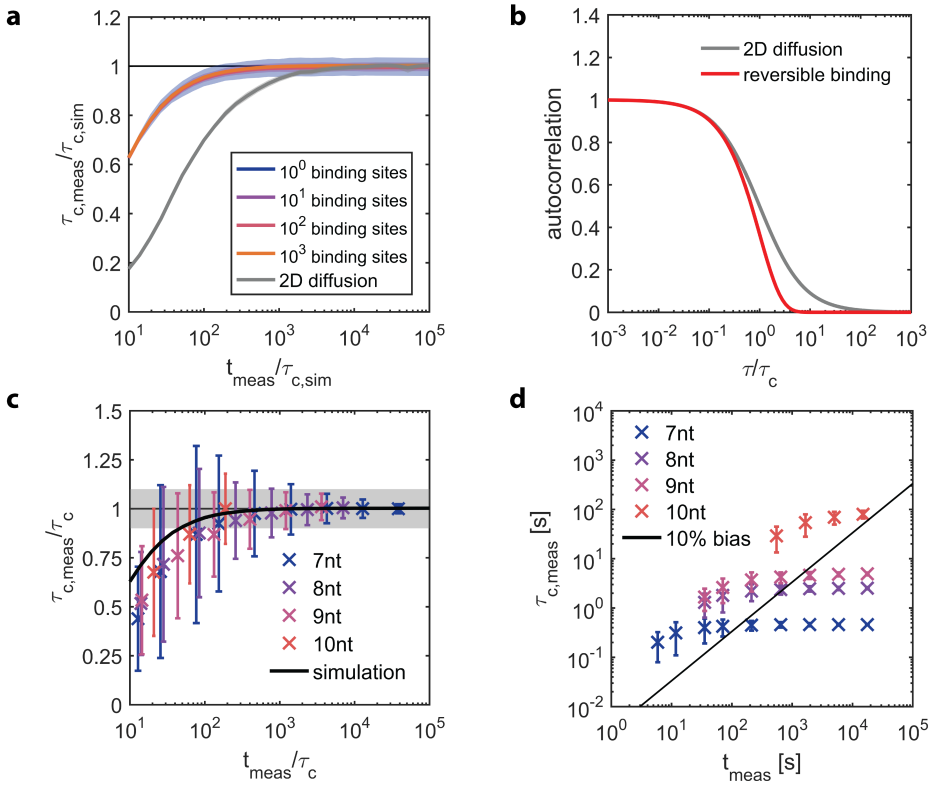

Figure III.7: Effect of the measurement time. We performed Monte Carlo simulations to evaluate the effect of the duration of individual measurements. To this end, we simulated 10 signal traces, which were 105 times longer than the characteristic decay time, fitted the resulting autocorrelation curves and related the results to the initially set characteristic decay time. To assess the effect of the measurement time but keep the statistics comparable, we cut the initial traces into shorter traces and repeated the analysis, thereby keeping constant the total number of binding events observed. For example, to analyze the case of traces, which are 103 times longer than the characteristic decay time, we split each of the 10 initial traces (105 times longer than $\tau_{c,\mathrm{sim}}$ into 100 sub-traces and subsequently computed and analyzed all resulting 1000 autocorrelation curves. Fig. III.7a shows the obtained decay time $\tau_{c,\mathrm{meas}}$ as a function of the duration of individual simulations. Both parameters are normalized to the characteristic decay time $\tau_{c,\mathrm{sim}}$ set in the simulation, which we expect to be the relevant time scale when assessing the required measurement time [Schätzel et al., 1988, Saffarian and Elson, 2003]. To avoid any effects of poor sample statistics, we repeated every simulation 10 times and varied the number of considered binding sites from 1 to 1000. The corresponding results are shown as mean (central line) plus/minus standard deviation of the ten simulations (shaded area).

caption continues on next page.

Figure III.7: cont.

No difference between the different settings is discernible and it appears that the bias from the autocorrelation (biased estimator [Schätzel, 1987, Schätzel et al., 1988]) converges to zero for sufficiently long measurements. Nonetheless, it should be noted, that the required measurement times for binding studies using SI-FCS can be long. When aiming for a bias smaller than 10 %, one should conduct measurements at least 300-fold longer than the characteristic decay time. Therefore, slow dynamics require particularly long measurement time, which makes the use of a focus stabilization system essential.
Nonetheless, for a correlation curve originating from binding and unbinding the convergence happens significantly faster than for a correlation curve originating from 2D diffusion (Fig. III.7a). The reason is the different shape of the correlation curves. For reversible binding, the autocorrelation curve decays relatively fast as a single exponential $G_C(\tau) \sim e^{-\frac{\tau}{\tau_c}}$, whereas the autocorrelation curve for 2D diffusion $G_{2D}(\tau) \sim \left(1+\frac{\tau}{\tau_D}\right)^{-1}$ has a significantly longer tail. Fig. III.7b demonstrates this effect by superimposing both autocorrelation curves with a time axis normalized to the relevant decay times τ_c and τ_D respectively.
To confirm the simulation results, we re-analyzed the measurements for 7-10 nt in a similar way as we analyzed the long simulated traces. By this, we can superimpose the simulated dependence from Fig. III.7a and the measurement results (Fig. III.7c). Strikingly, without any fitting involved, the simulation and the experimental results follow the same trend. Moreover, in this depiction, we see no difference between different nucleotides, which is expected as we normalize by τ_c. Nonetheless, we can conclude that the underlying dynamics for 7-10 nt hybridization are identical, and only occur on different time scales, which makes the depicted relation a universal concept. For short measurement times, the bias of the experimental data seems to be slightly larger than the simulation suggests, which we attribute to noise involved in the measurements. From (Fig. III.7c) we conclude that the systematic bias on the obtained characteristic decay time cannot be smaller than indicated by the simulated dependence. The bias cannot be reduced below this line, not even by an increasing number of binding events observed within the same measurement duration. The only option to reduce the systematic bias is an increased duration of the total measurement time. Furthermore, Fig. III.7c shows that an individual measurement has to be at least 300-fold longer than the characteristic decay time to achieve a bias smaller than 10 %. Based on this finding, we can replot Fig. III.7c without normalization of all times and superimpose a border, which corresponds to the 10 % systematic bias (solid line, Fig. III.7d). All points on the right hand side of this line have a bias of less than 10 %, which gives a direct and quick check for whether a particular measurement was long enough to provide the required accuracy.

SI-FCS measurements of reversible binding are calibration-free

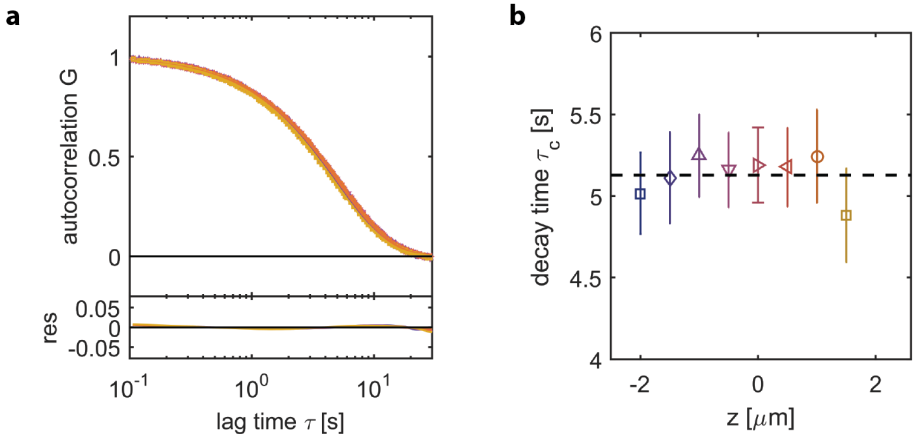

Figure III.8: SI-FCS is calibration-free and robust to defocused imaging. The calibration of the detection volume is a crucial step in confocal FCS measurements. On the other hand, camera-based SI-FCS measurements on diffusion dynamics in supported lipid bilayers have been shown to be calibration-free by variable pixel binning during post-processing of images [Bag et al., 2012]. In contrast, when looking at the reversible binding of labeled freely diffusing ligand to a surface-immobilized target, SI-FCS is intrinsically calibration-free, as it does not require any lateral spatial resolution. Here, the signal fluctuation originates from binding and unbinding events to the surface. Any changes in the lateral size of the detection volume do not qualitatively alter the underlying kinetics of the fluctuating signal. To prove this, we performed a series of measurements at different axial positions of the detection volume relative to the sample surface. This is equivalent to systematic defocusing, which varies the lateral size of the PSF. The SI-FCS experiments presented here are within reasonable limits robust to any defocusing of the sample. The situation changes when looking at lateral diffusion through a detection volume, e.g. a region of interest spanning a certain number of pixels on the camera detector. In this case, the decay of the autocorrelation curve depends on the diffusion coefficient, the size of the region of interest and the size of the PSF [Ries et al., 2008a, Bag et al., 2012]. a) Autocorrelation curves and single-exponential fits obtained from the same sample but different axial positions of the specimen. The axial positions are color coded and can be inferred from panel b). b) Characteristic decay times obtained from single-exponential fits of the SI-FCS autocorrelation functions measured for different sample positions along the optical axis.

Surface density accessible to SI-FCS

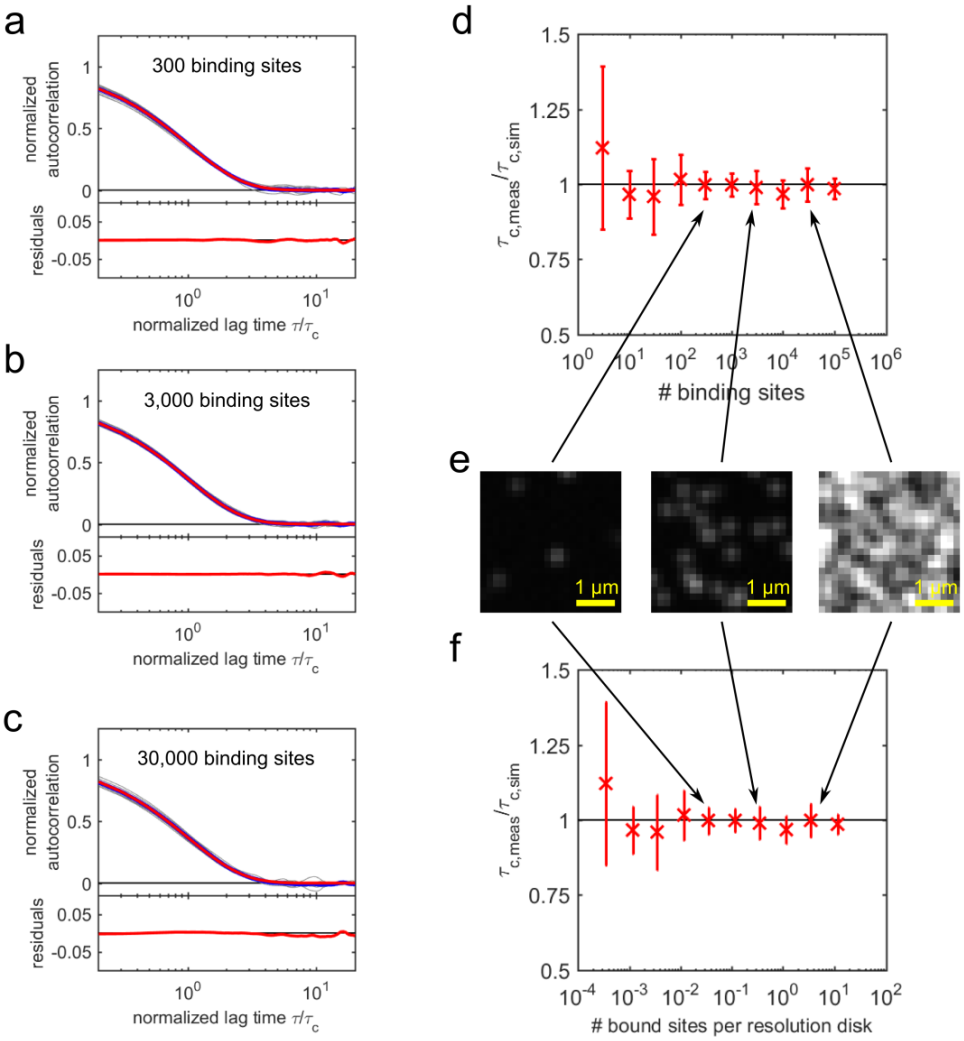

Figure III.9: caption on next page.

Figure III.9: Performance of SI-FCS at different receptor surface densities: Simulations. We simulated SI-FCS image series (see Supplementary Theoretical Basis, p. 39) using the Picasso software tool [Schnitzbauer et al., 2017]. To assess the surface densities of receptors which are compatible with SI-FCS, we started off by simulating SI-FCS measurements for 24×24 pixels ($160 \times 160\,\mathrm{nm}^2$ per pixel), with $k_d = 1/\mathrm{s}$, $k_a\langle A\rangle = 0.008/\mathrm{s}$, and 3 to 100,000 receptors in the considered area. The simulated frame rate was 10 Hz and a total of 40,000 frames was simulated for each run, corresponding to a total measurement duration $t_{\mathrm{meas}} = 4000\,\mathrm{s}$. Each simulation was performed ten times to develop a feeling for the scatter of results. Fig. III.9a-c show ten individual curves each (light grey), superimposed with their mean (blue line) and the corresponding single exponential fit (red line) from which the characteristic decay time is extracted. These curves demonstrate once more that a single exponential describes the autocorrelation curves appropriately. Second, the least from 300 binding sites on, the statistical scatter for the simulated conditions becomes small. Each individual autocorrelation curve represents on average $\beta N_S \left(k_d^{-1} + k_a^{-1}\langle A\rangle^{-1}\right) t_{\mathrm{meas}}^{-1}$ binding events (for $N_S = 300$ less than 104 events). For all receptor densities considered, we recovered the simulated characteristic decay times accurately (Fig. III.9d). With reasonable computation times (maximum number of binding sites 105), we could not find a regime where SI-FCS could not recover the simulated characteristic decay times. This is a clear advantage of SI-FCS over tracking based approaches in which the residence time is determined. Here, we are not confined to regimes where individual particles can be identified. Figures III.9e show representative simulated images for 300, 3,000 and 30,000 binding sites. Clearly, already in the case of 3,000 binding sites, a tracking based approach would suffer from misassignments during the reconstruction of tracks, leading to overestimations of residence times. We note that the number of binding sites or the surface density of binding sites are not particularly good parameters to compare the performance of SI-FCS and tracking-based estimations of the residence time. As tracking relies on the detection of individual particles, it is rather relevant to replot Fig. III.9d in terms of the occupied binding sites per resolution disk $N_b = S\beta A_{\mathrm{resolutiondisk}}$ (Fig. III.9f). Here, we used the total density of binding sites S, and the fraction of occupied binding sites $\beta = \frac{1}{1+\frac{k_d}{k_a\langle A\rangle}}$ (see Supplementary Methods in Section A.1, p. 263). As the resolution disk we define a circle with the $1/e^2$ value w_{xy} of the Gaussian-shaped PSF as radius. This equals to the assumption that two resolution limited spots can be distinguished reliably if their centers are separated by at least w_{xy}. As shown in Fig. III.9f, the SI-FCS approach reliably reproduces the simulated binding times not only in a regime where tracking-based approaches would perform, but also at surface densities of bound receptors which exceed the tracking regime by at least two orders of magnitude.

Measurements surface density

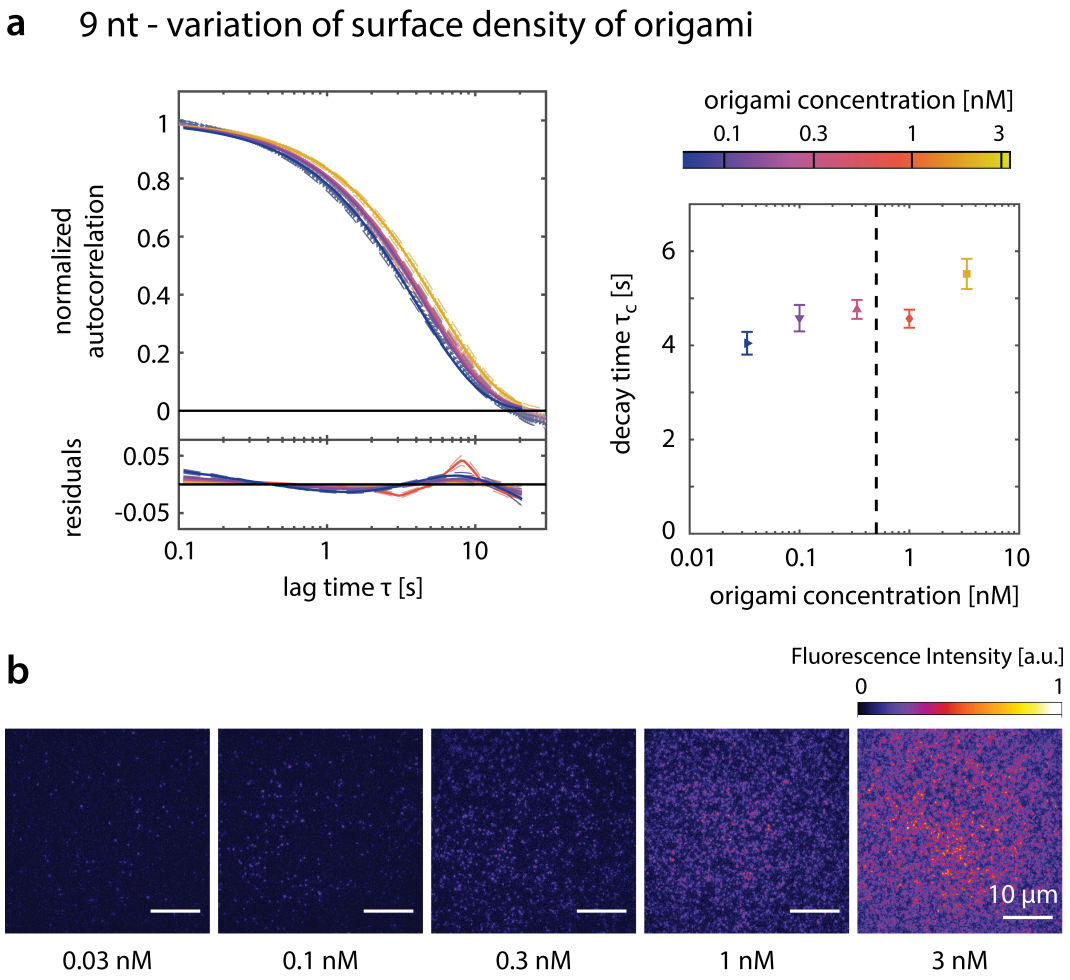

Figure III.10: Performance of SI-FCS at different receptor surface densities: Experimental data a) Autocorrelation curves obtained from five individual SI-FCS measurements of the hybridization kinetics of a 9 nt overlap. The measurements differ in the origami surface density, which is intrinsically difficult to control quantitatively. As a simple approach, we incubated the surfaces for the same time with different concentrations of DNA origami (0.03, 0.1, 0.3, 1.0, and 3 nM). SI-FCS yields reasonably consistent decay times for the range of investigated surface densities, although a slight increase is observed for very high surface densities. The dashed line corresponds to the surface concentration we used in typical SI-FCS measurements (Fig. III.2 and III.3). b) Representative images corresponding to the conditions described in a) For the lowest surface concentrations, particle tracking approaches could be potentially conducted, whereas for origami concentrations above 0.1 nM, tracking approaches would clearly fail, because individual events cannot be identified any longer. SI-FCS yielded smooth low-noise autocorrelation curves even in regimes that were clearly not accessible to tracking approaches. Time series were recorded without binning with a resolution of 256 × 256 pixel.

DNA-PAINT reconstruction of binding sites on DNA origami structures

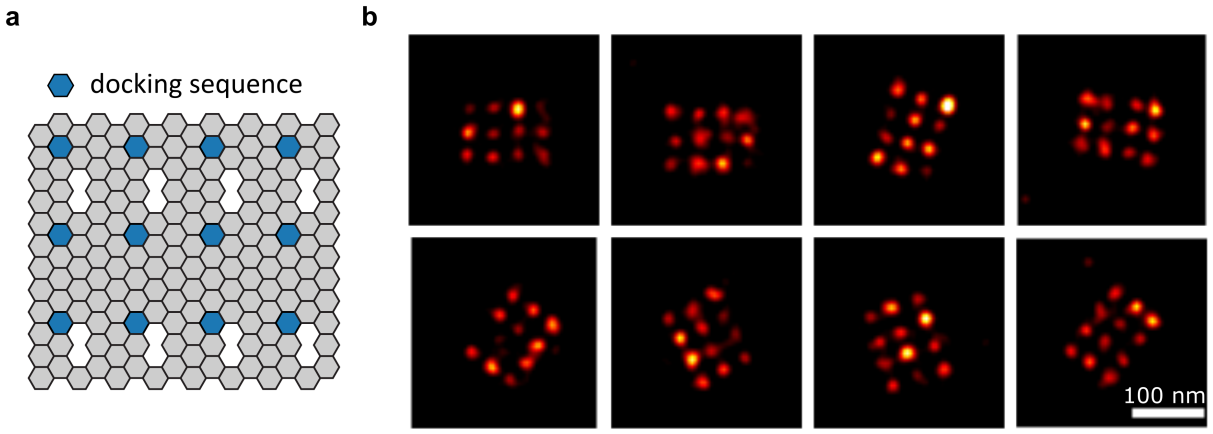

Figure III.11: Super-resolution of DNA origami exposing 12 single-stranded DNA handles. a) Schematic of the rectangular DNA origami structures, exposing 12 ssDNA handles. The image was generated with the Picasso software tool [Schnitzbauer et al., 2017]. b) Representative DNA-PAINT images of the rectangular origamis.

Effect of ROI size

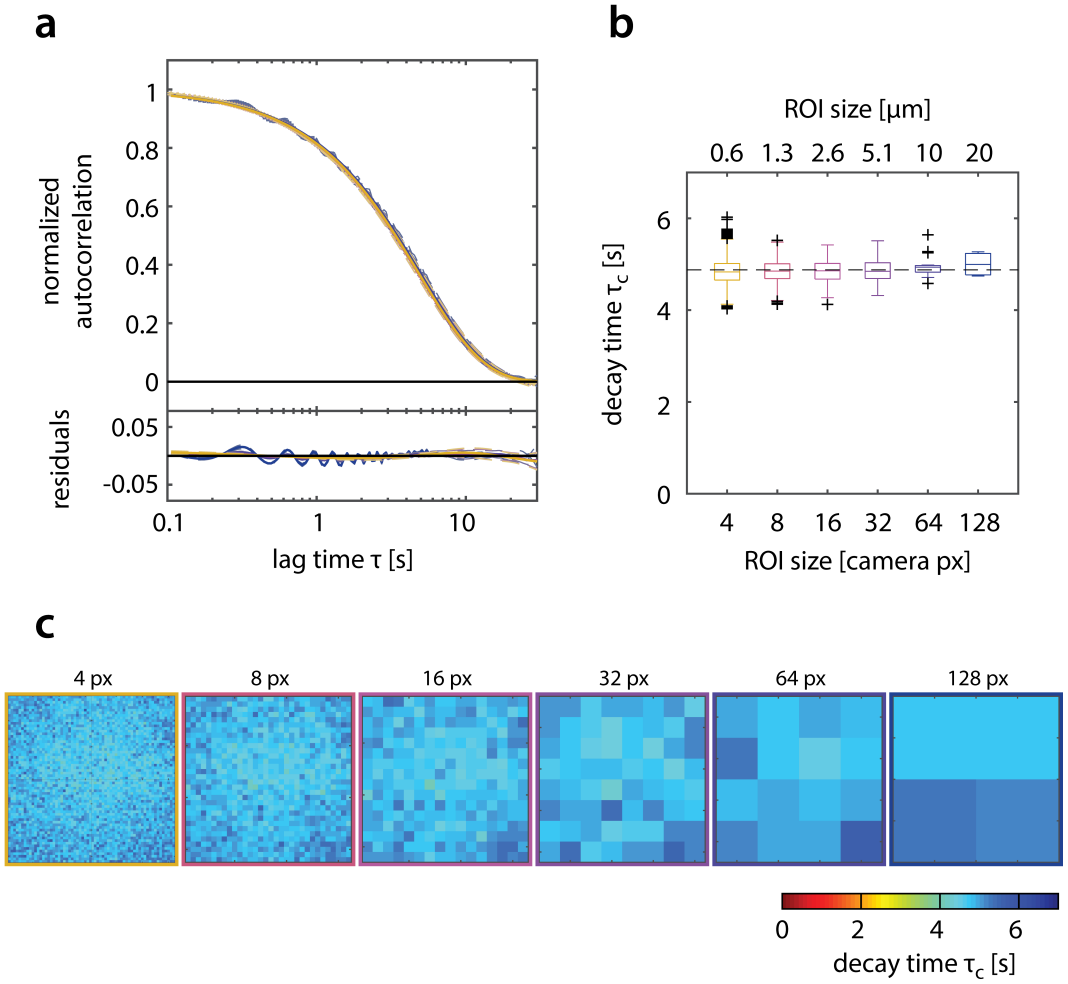

Figure III.12: caption on next page.

Figure III.12: Effect of the ROI size. a) Average normalized autocorrelation curves for 9 nt hybridization obtained for different ROI sizes are indistinguishable and are adequately described by a single exponential decay. To facilitate high frame rates, we employed 4×4 pixel (px) hardware binning during image acquisition. b) Boxplots of the obtained corresponding characteristic decay times are independent of the ROI size. The center lines mark the median. The box edges correspond to upper and lower quartile, and are extended by the whiskers marking 1.5 times the inter-quartile range. Data points outside the whiskers are marked as crosses. For small ROIs, the overall scatter is larger, as less events are sampled within an individual ROI. The average τ_c, however, is in agreement with larger ROI sizes. Theoretically, for too large ROIs, the fluctuations become less relevant, the amplitude of the autocorrelation curve approaches zero, and a fluctuation-based autocorrelation analysis becomes less reliable. For the investigated conditions, however, this regime is not reached. On the other hand, for large ROIs and small correlation amplitudes, the autocorrelation function becomes more sensitive to mechanical and laser excitation instabilities. In this particular measurement, small oscillations of the piezo controlling the TIRF angle position could be observed as oscillations for the 128 px ROIs, but not for smaller ROIs. The chosen ROI size of 31×31 px offered spatial resolution to investigate bleaching across the illumination profile, but did not affect the overall measured τ_c. c) The larger overall scatter is illustrated by generating a map of decay times. The computational effort and memory consumption increase quadratic with the ROI size or linearly with the number of ROIs. In this particular example, the measured τ_c is independent of the ROI size. It should be noted, that there may be conditions, e.g. for very high or very low densities of binding events, where this is not the case. Although we experienced that SI-FCS measurements were generally robust against the choice of the ROI, we suggest to carefully explore a range of ROI sizes during post-processing.

IV

PHOTO-INDUCED DEPLETION OF BINDING SITES IN SI-FCS AND DNA-PAINT MICROSCOPY

IV.1 Motivation and Summary

The accurate quantification of surface-binding with SI-FCS (Chapter III) requires measurement times to be at least 300 times longer than the characteristic time of binding τ_c measured by the autocorrelation function (Figure III.7, p. 47). Consequently, for long binding times of more than 100 s, as observed for the 10 nt imager (Figure III.2, p. 33), required measurement times exceed hours and raise high demands regarding the temporal stability of the sample. If sealed properly, DNA-PAINT samples [Schnitzbauer et al., 2017] offer a remarkable long-term stability, making it possible to reproduce results on the same sample over days.

However, at high concentrations of fluorescent imager strands in solution we observed an additional component in the decay of the autocorrelation function, which could not be attributed to binding kinetics (Figure III.3, p. 35). In this chapter, we systematically traced the origin of the additional contribution to a photo-induced and concentration-dependent depletion of docking handles on our DNA origami nanostructures. In the previous chapter, the time scales of the photo-induced depletion separated well from the binding kinetics, allowing kinetic parameters to be extracted from a biexponential fit. Notably, this simple treatment will fail as soon as binding kinetics and photo-induced depletion start to overlap in time, i.e. binding times increase beyond 100 s or concentrations exceed 300 nM (Figure III.3, p. 35). Moreover, this effect does not only influence the temporal decay, the shape and the amplitude of the autocorrelation function in SI-FCS, but similarly the extracted kinetics from localization based DNA-PAINT microscopy [Jungmann et al., 2010].

We successfully reduced the photo-induced depletion of binding sites by the use of oxygen-scavenging buffers or a modified design of imager strands. We compared two commonly used oxygen scavenging systems (a) pyranose oxidase and catalase (PO+C) and (b) protocatcchuate-dioxygenase and 3,4-proto-catechuic acid (PCD+PCA), finding PO+C to be favorable for SI-FCS on DNA-based samples. Not requiring additives, an increase in the

distance of fluorophore and docking strand effectively reduces the photo-induced damages in SI-FCS, but only to a minor extent in DNA-PAINT.

Our systematic study of photo-induced damages presented here is of major importance to the accurate quantification of kinetic rates and the counting of molecules with SI-FCS, DNA-PAINT and quantitative PAINT (qPAINT) [Jungmann et al., 2016].

IV.2 Contributed Publication

Photo-induced Depletion of Binding Sites in DNA-PAINT Microscopy

Philipp Blumhardt, Johannes Stein, Jonas Mücksch, Florian Stehr,
Julian Bauer, Ralf Jungmann, Petra Schwille

published in

Molecules 2018, 23(12), 3165
doi:10.3390/molecules23123165

The following modifications have been made to the manuscript: citations and references to equations, tables and figures are displayed in a style consistent with this thesis; notation mistakes fixed in the captions of Table IV.1 and Figure IV.10; Materials and Methods are placed in the Appendix (pp. 271ff.).

Author contributions: Conceptualization, P.B. and J.M.; Formal analysis, P.B., J.S., F.S. and J.B.; Funding acquisition, R.J. and P.S.; Investigation, P.B. and J.S.; Methodology, P.B., J.S., J.M. and F.S.; Project administration, P.B. and J.S.; Resources, P.B., J.S., J.M. and F.S.; Software, P.B., J.S., J.M. and F.S.; Supervision, R.J. and P.S.; Validation, P.B., J.S. and F.S.; Visualization, P.B., J.S., F.S. and J.B.; Writing—original draft, P.B.; Writing—review & editing, P.B., J.S., J.M., F.S., R.J. and P.S.

IV.2.1 Introduction

Super-resolution microscopy has greatly contributed to the study of biological specimens with resolutions down to few nanometers while retaining the high specificity of fluorescent labels [Huang et al., 2009, Baddeley and Bewersdorf, 2018, Pertsinidis et al., 2010]. The stochastic blinking of individual fluorophores enables the precise localization of molecules in various single molecule localization microscopy (SMLM) methods. In many variants of SMLM, in particular the prominent PALM [Betzig et al., 2006, Hess et al., 2006] and (d)STORM [Rust et al., 2006, Heilemann et al., 2008] the number of photons available

from permanently bound, individual fluorophores determines the achievable localization precision [Thompson et al., 2002, Deschout et al., 2014]. In particular, the spatial information from non-functional or immediately photo-bleached labels is entirely lost. In contrast, points accumulation for imaging in nanoscale topography (PAINT) [Sharonov and Hochstrasser, 2006] generates the blinking of fluorophores by reversible binding reactions. While an individual binding event is still limited by the photon-budget of the fluorescent dye, binding sites can be revisited by fresh probes and thus contribute to higher resolved images [Schnitzbauer et al., 2017]. In DNA-based PAINT (DNA-PAINT) [Schnitzbauer et al., 2017, Jungmann et al., 2010] the structure of interest is labeled with a short DNA single strand (docking strand), serving as binding site for fluorescently labeled complementary single (imager) strands. The formed duplex immobilizes the imager for the time of binding and creates a bright, localized spot on the detector, usually a sensitive camera, while freely diffusing imager strands remain blurred as a constant background intensity.

Transient binding reactions not only enable super-resolution microscopy, but their kinetics also reflect on the nature of the binding process. Under appropriate imaging conditions, the kinetics of the transient binding can be directly extracted from time traces of the localization data [Jungmann et al., 2010, Jungmann et al., 2016]. In samples with high densities of binding events, where localization fails, fluorescence correlation spectroscopy (FCS) can reliably extract binding kinetics [Lieto et al., 2003, Mücksch et al., 2018, Peng et al., 2018]. We recently showed that surface-integrated fluorescence correlation spectroscopy (SI-FCS) can determine the kinetic rates of transient DNA hybridization [Mücksch et al., 2018].

However, the advantage of DNA-PAINT in that individual binding sites are revisited is limited for long acquisitions, due to photo-induced damages, effectively creating an upper limit for the image quality. In addition, SI-FCS experiments suffer from the depletion of bindings sites, complicating the correct extraction of kinetic rates. Unwanted photo-induced effects are intrinsic to fluorescence microscopy [Diaspro et al., 2006, Ha and Tinnefeld, 2012]. Excited states of fluorescent molecules in general, but in particular long-lived triplet states, are prone to oxidation or reduction and the subsequent generation of highly reactive molecules [Ha and Tinnefeld, 2012, Eggeling et al., 1999, Eggeling et al., 1998, Eggeling et al., 2005, Widengren et al., 2007]. Triplet states have been found to play a role in photo-bleaching pathways and to promote the generation of reactive oxygen species (ROS) [Eggeling et al., 1999, Widengren et al., 2007, Wilkinson et al., 1994, Davidson, 1979, Hoogenboom et al., 2005, Vogelsang et al., 2008, Widengren and Rigler, 1996, Eggeling

et al., 2006]. ROS are not only known to bleach fluorescent dyes [Ha and Tinnefeld, 2012, Zheng et al., 2014a] and have phototoxic effects on biological samples [Dixit and Cyr, 2003, Schneckenburger et al., 2012], but also to damage DNA [Sies and Menck, 1992, Matter et al., 2018].

The damage induced by ROS is significantly reduced by the use of oxygen scavenging buffers that remove molecular oxygen from solution and thereby lower the amount of reactive oxygen species. The popular enzymatic oxygen scavenging system glucose oxidase, catalase and glucose (GO+C) [Harada et al., 1990, Benesch and Benesch, 1953] produces gluconic acid, consequently acidifying the sample. GO+C is thus not suited for long acquisitions or pH dependent systems [Shi et al., 2010, Englander et al., 1987, Kim et al., 2012]. An alternative systems is the combination of protocatechuate-dioxygenase and 3,4-protocatechuic acid (PCD+PCA) [Patil and Ballou, 2000, Aitken et al., 2008]. The oxidation of PCA produces muconic acid, but at the same time has a buffering effect around pH 8, leading to improved pH stability compared to GO+C [Swoboda et al., 2012]. More recently, pyranose oxidase, catalase and glucose (PO+C) have been reported as effective oxygen scavengers with no acidifying effect over the time span of hours [Swoboda et al., 2012]. In particular, when studying the DNA duplex formation above the melting temperature, prerequisite for DNA-PAINT imaging, the reaction kinetics are sensitive to the pH of the solution and salt concentrations [Jungmann et al., 2010].

Since molecular oxygen acts as triplet quencher, its removal increases the triplet lifetime, leading to long-lived dark states and decreased fluorescence [Ha and Tinnefeld, 2012, Widengren et al., 2007, Widengren et al., 1997]. The vitamin E analog Trolox has been found to serve as effective triplet quencher in combination with oxygen scavenging systems, resulting in comparably bright and photostable fluorescence imaging conditions [Rasnik et al., 2006, Dave et al., 2009]. In this study, we systematically investigate the stability for long acquisition time series in DNA-PAINT microscopy and SI-FCS kinetic measurements. We provide two practical solutions to the inherent problem of phototoxicity, by comparing two oxygen scavenging reagents, and by presenting a modified imager that utilizes a higher distance of fluorescent dye to docking site.

IV.2.2 Results

To systematically investigate the effect of the photo-induced depletion of binding sites, we compared DNA-PAINT super-resolution microscopy and SI-FCS kinetic measurements from samples in the presence and absence of oxygen scavenging systems. If the depletion

of binding sites is caused by ROS, oxygen scavenging buffers will lead to a longer lifetime of binding sites. Additionally, we probed whether the distance of fluorescent dye to the docking strand influences the rate of depletion. To achieve optimal resolution in SMLM, the fluorescent dye is conventionally placed in closest possible proximity to the labeling site. In DNA-PAINT, this is easily achieved by design. In many cases, including this study, the DNA origami scaffold and the fluorescent probe on the imager strand are upon binding only separated by a short spacer [Schnitzbauer et al., 2017, Jungmann et al., 2010, Jungmann et al., 2014]. This arrangement, however, also creates ROS close to the docking strand, and is therefore prone to damaging of DNA bases resulting in an increased depletion rate of binding sites. Assuming an isotropic diffusion of ROS, an increase in the distance between fluorescent dye and the docking strand ought to decrease the probability for interaction. We investigated the depletion of docking sites in the following five conditions (Figure IV.1):

1. Conventional: we used standard conditions as commonly found in DNA-PAINT super-resolution microscopy and SI-FCS measurements [Schnitzbauer et al., 2017, Mücksch et al., 2018];

2. Oxygen scavengers:

   (a) PO+C: we added PO+C as oxygen scavenging system and Trolox as triplet quencher to samples otherwise identical to (1);

   (b) PCD+PCA: as in (2a), but with PCD+PCA as oxygen scavenging system and Trolox added;

3. 18-mer spacer:

   (a) we extended the 10-nucleotide (nt) imager by an additional 18-mer double stranded spacer sequence to attach the dye at greater distance from the hybridizing docking strand, maintaining otherwise conditions as in (1);

   (b) we added PO+C as in (2a) to samples otherwise identical to (3a).

Depletion of binding sites in DNA-PAINT manifests itself in a decrease in the number of localizations with increasing measurement time (Supplementary Figure IV.5, p. 78, left panel, raw data is available as Supplementary Material, p. 278). To study the underlying effect, two processes have to be disentangled: First, the bleaching of fluorescence imager strands in solution, and second, a depletion of docking sites. The effective concentration

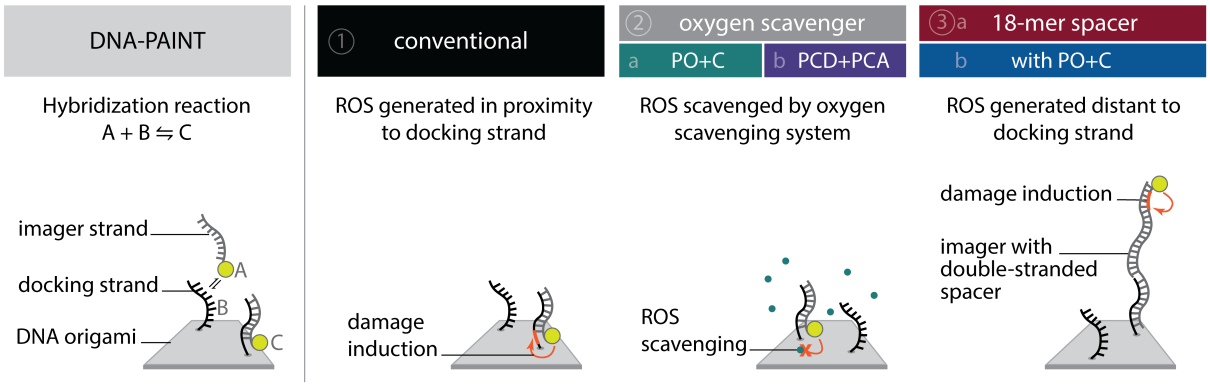

Figure IV.1: Schematic of DNA-PAINT with the binding of imager strands (A) to docking strands (B) forming the hybridized duplex (C) (left panel). Overview of the conditions to explore the photo-induced depletion of binding sites in DNA-PAINT microscopy and kinetic measurement with SI-FCS (right panel): **(1)** conventional 9 nt overlapping imager, **(2)** identical imager as in (1) but in presence of a oxygen scavenging system (**2a**: PO+C or **2b**: PCD+PCA), **(3a)** a modified imager with identical binding sequence and buffer conditions as in (1) but extended by an double-stranded spacer, increasing the distance of dye and docking strand and **(3b)** the combination of 18-mer spacer and PO+C. ROS scavenging and an increased distance of the fluorescent dye to the docking strand are ought to decrease the rate of depletion of docking sites.

of fluorescent imager strands within the total internal reflection fluorescence (TIRF) excitation volume can be assumed equilibrated with the bulk solution concentration, as the exchange rate of imager strands from solution by diffusion is about four orders of magnitude faster than the exposure time or minimum correlation time (Supplementary Figure IV.6, p. 80). Bleaching of the bulk imager solution is usually negligible in DNA-PAINT, as the reservoir of fluorophores in solution is large enough so that the concentration of fluorescent dye is not affected by imaging a small volume via TIRF illumination. Accordingly, moving the sample laterally by more than the size of the illumination fully recovers the number of initial localizations (Supplementary Figure IV.5, p. 78, right panel). Thus, photo-bleaching does not significantly affect the bulk dye concentration. The second effect, the depletion of binding sites, however, affects the surface-immobilized sample, therefore dominates in the observation region and accumulates over time.

To observe the photo-induced depletion of docking sites under conventionally used imaging conditions, we rendered super-resolved DNA-PAINT images from five subsets of one 25,000 frame or 83-min-long acquisition at a peak irradiance of $I_0 = 0.2\,\mathrm{kW/cm^2}$, allowing for the localization of individual binding sites. Depending on the particular application, DNA-PAINT experiments are conventionally performed with peak irradiances up to $6\,\mathrm{kW/cm^2}$ [Schnitzbauer et al., 2017], further enhancing the problem of photo-induced damages. The first subset, covering the first 17 min, renders a super-resolved image with the majority of docking sites visible. Due to the limited incorporation efficiency, not all docking sites are observable in the first subset [Strauss et al., 2018]. Later subsets show a decreasing number of localized binding sites, indicating that less docking strands are available for hybridization of imager strands on the DNA origami scaffold (Figure IV.2a and Supplementary Figure IV.7, p. 82). Time traces of localizations within circular areas enclosing the individual docking sites show frequent binding events in the beginning of the acquisition, but eventually turn dark during the measurement (Figure IV.2b).

We further quantitatively investigated the depletion of binding sites in DNA-PAINT microscopy by automated alignment and averaging of the acquired DNA origami nanostructures (Supplementary Figure IV.8, p. 83), as published previously [Schnitzbauer et al., 2017, Strauss et al., 2018]. The drift correction, identification and averaging of nanostructures were performed on the complete time series prior to division into the subsets. Selected individual binding sites on the averaged image were then back-translated to individual nanostructures (Picasso: 'Unfold') to analyze the intensity trace of each docking site individually. To account for rare unspecific binding events, only traces with more than

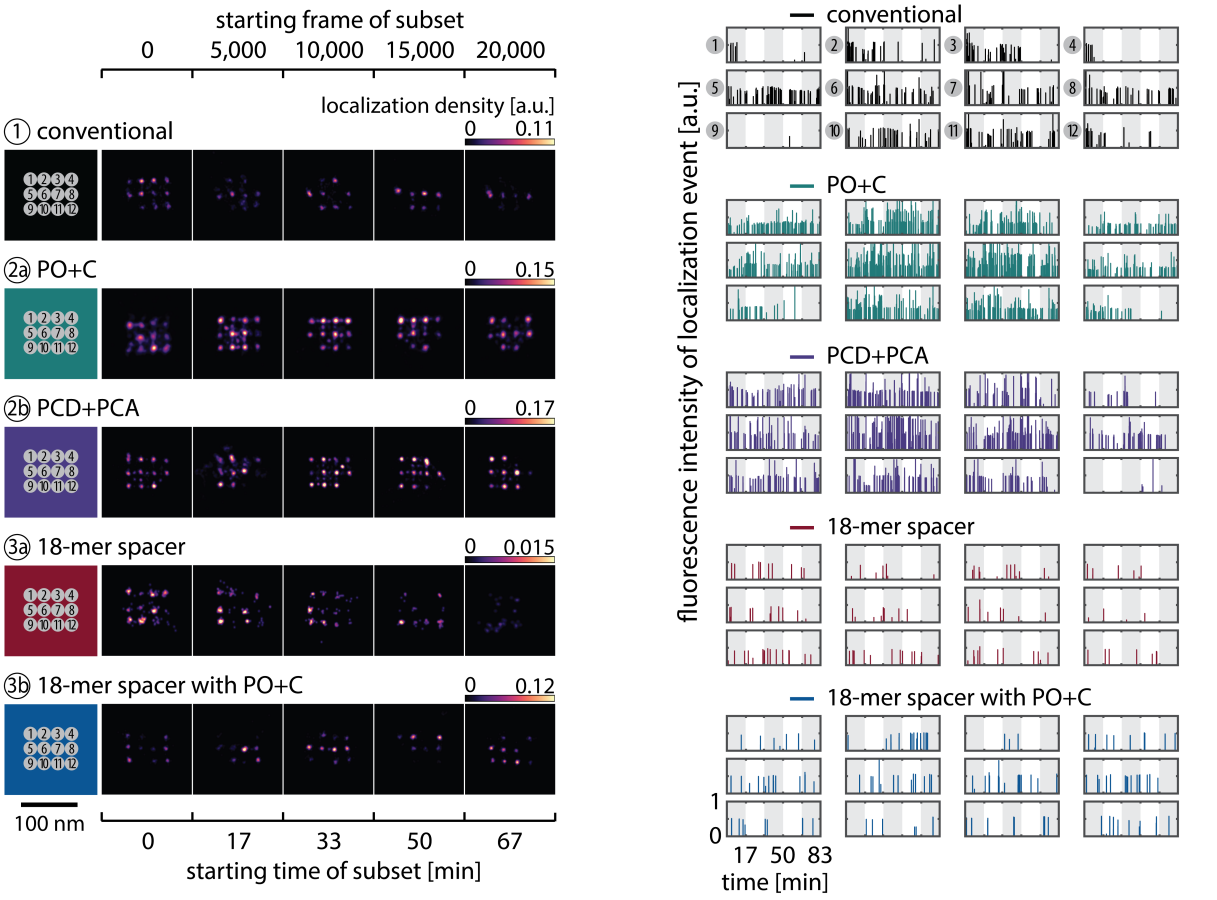

Figure IV.2: Long DNA-PAINT acquisition of DNA origami nanostructures with 12 exposed docking strands arranged in a 3×4 grid with 20 nm spacing. Five conditions are displayed: conventional imager (1, black), conventional imager with oxygen scavenging system added (2a: PO+C, turquoise; 2b: PCD+PCA, purple), imager with 18-mer spacer between docking sequence and fluorescent dye (3a, red) and the 18-mer spacer with PO+C (3b, blue). (a) Time series of representative super-resolved DNA-PAINT images, reconstructed from five subsequent 5,000 frame long subsets of a 25,000 frame long acquisition (in total 83 min). Additional examples are listed in the Appendix (Section IV.2.4, Supplementary Figure IV.7, p. 82). Scale Bar: 100 nm. (b) Time traces of localizations within circular areas picked as individual bindings sites. The alternating shade of the background indicates the five subsets. DNA-PAINT raw data is available as Supplementary Material (p. 278).

three localizations per subset were counted as active docking sites. This cutoff slightly changes the absolute numbers of active docking sites, but does not influence the qualitative shape of the observed decays. Following this analysis, roughly 10 docking sites are on average detected as active in the initial subset for the conventional imager in absence (1) and presence of oxygen scavenging buffers (2a,b) (Figure IV.3a, left panel), in agreement with previous investigations [Strauss et al., 2018]. With increasing measurement time, increasing numbers of docking sites become inactive, leaving on average six binding sites per nanostructure active, with the conventional imager at the end of the time series. In stark contrast, less than one binding site is depleted on average during the entire measurement in presence of oxygen scavenging buffers. The depletion of binding sites is limited to the irradiated sample region, and non-irradiated areas are indistinguishable from a fresh sample (Figure IV.3a, right panel). In case of the 18-mer spacer (3a,b), we observe a decreased association rate, leading not only to a lower number of localizations, but also to docking sites not being visited frequently enough to classify docking sites reliably as active within one subset. Using the whole time series to identify docking sites, the total number of active docking sites is recovered to about 10, similar to the conventional imager (Supplementary Figure IV.9, p. 84). Irrespective of the low association rate, docking sites are also depleted for the imager carrying the 18-mer spacer ($I_0 = 0.2\,\mathrm{kW/cm^2}$) (Figure IV.3a). For the combination of 18-mer spacer and oxygen scavenger PO+C (3b), we observe an increased error rate within the automated structure alignment and a slightly decreased number of active docking sites (Supplementary Figure IV.9, p. 84). As mentioned, the cut-off for unspecific binding events does not influence the qualitative shape of the decay.

Further, the depletion can also be analyzed based on the kinetics of the reoccurring binding events to individual DNA origami. We use the well-established analysis of the duration of individual binding events and the time span between two consecutive binding events, referred to as bright time τ_B and dark time τ_D, respectively [Schnitzbauer et al., 2017, Jungmann et al., 2010, Jungmann et al., 2016]. For the conventional imager strand (1), we observe an increasing dark time for later subsets, which directly reflects on the depletion of binding sites (Figure IV.3b, top). For completely depleted binding sites, the dark time becomes theoretically infinite. In practice, noise misinterpreted as localization event limits the dark times and leads to a large scatter of the distribution of dark times for later subsets. With the addition of oxygen scavenging buffers (2a,b), the average dark time appears shorter and does not show any significant dependence on the measurement time, indicating a strong reduction in the depletion of binding sites. The two oxygen

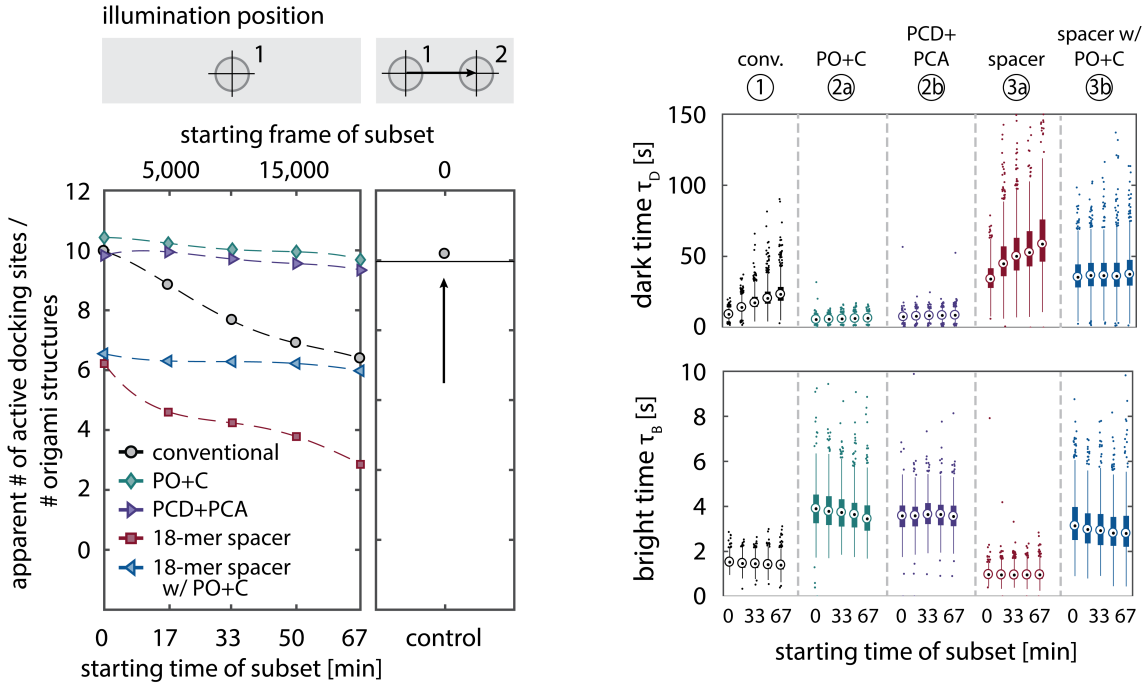

Figure IV.3: Quantitative analysis of the depletion of docking strands in DNA-PAINT super-resolution microscopy. The five conditions displayed are identical to Figure IV.2. (a) Left panel: active docking sites are counted individually on DNA origami nanostructures, based on the back-translation of the position of docking sites picked on automatically averaged nanostructures (Supplementary Figure IV.8, p. 83) and divided by the total number of identified origami structures. The dashed line is a guide to the eye. Right panel: a control of 5000 frames, equivalent to the first subset, was measured in a previously not irradiated area on the same sample and compared to the initial number of active docking sites (solid horizontal line) for the conventional condition (right panel). The total numbers of identified DNA origami nanostructures for the five conditions are: (1) 786, (2a) 824, (2b) 566, (3a) 690, (3b) 580 and 690 for the control of condition (1). (b) Box plots of the bright times τ_B and dark times τ_D for the subsets shown in (a). Circles indicate the median; bottom and top edges of the box (bold vertical lines) indicate the 25th and 75th percentiles, respectively. The whiskers extend to the data points not considered outliers (thin vertical lines); outliers are plotted individually as dots.

scavenging systems PO+C and PCD+PCA seem to perform similarly well in reduction of the depletion. For the 18-mer spacer, dark times are higher as for the conventional imager, reproducing the apparent lower association rate (Figure IV.2b and Figure IV.3b). Without oxygen scavengers (3a), an increase in dark times is observed, as depletion of binding sites is induced under the chosen irradiation conditions. Adding oxygen-scavenger to the 18-mer spacer (3b) stabilizes the dark times on the level observed in the first subset without oxygen scavengers (3a).

The bright time τ_B, in return, is stable or slightly decreases with time (Figure IV.3b, bottom). The conventional imager and the 18-mer spacer show similar bright times, shortened by the photo-bleaching of the fluorescent dye to less than 2 seconds. With the addition of oxygen scavenging buffers, the bright times increase to roughly 4 seconds, matching the values expected from SI-FCS measurements for a bleaching-free regime (Table IV.1 from SI-FCS results below). The observed slight decrease in bright time can be attributed to an artifact arising for two simultaneous binding events that are misinterpreted by the localization algorithm [Schnitzbauer et al., 2017] as one longer binding event (Supplementary Figure IV.10, p. 85). The more binding sites are accessible, the higher is the probability for two imager strands to bind simultaneously. With increasing measurement time and according depletion of binding sites, the probability to bind two imager strands decreases, and thus the bright time approaches its true value in the later subsets. The dependencies of dark and bright time on the number of docking sites per nanostructure appear similarly in simulations (Supplementary Figure IV.10b, p. 85). Experimentally, the decreasing bright time can be avoided by lower imager concentrations at the cost of extended measurement times to maintain the total amount of localizations. The increasing dark time, however, is intrinsic to the depletion of docking sites and can particularly hinder quantitative analyses based on the association rate [Jungmann et al., 2016].

Table IV.1: Binding kinetics as measured by SI-FCS titrations of the imager concentrations $\langle A \rangle$. Hybridization rates and affinity as obtained from the titrations in Figure IV.4. The errors represent the 95 % confidence bounds of the fit.

Imaging Condition	$\mathbf{k_a}$ **[10^6 /(Ms)]**	$\mathbf{k_d}$ **[1/s]**	$\mathbf{K_d}$ **[nM]**
conventional	1.49 ± 0.17	0.303 ± 0.010	200 ± 30
PO+C	1.5 ± 0.4	0.268 ± 0.017	180 ± 60
PCD+PCA	1.3 ± 0.4	0.25 ± 0.02	190 ± 70
18-mer spacer	0.59 ± 0.11	0.245 ± 0.012	420 ± 100
18-mer spacer with PO+C	0.28 ± 0.12	0.26 ± 0.02	1000 ± 500

The high irradiances necessary for precise localization of fluorophores in super-resolution microscopy lead to a high probability of photo-bleaching fluorophores while still being attached to the docking strand [Mücksch et al., 2018], thus adding an additional layer of complexity. To further separate the effect of photo-bleaching from the depletion of individual binding sites, we analyzed the hybridization kinetics in a low irradiance regime ($I_0 = 0.018\,\mathrm{kW/cm^2}$) with surface-integrated fluorescence correlation spectroscopy (SI-FCS) [Mücksch et al., 2018]. The fluctuations in fluorescence intensity of transiently hybridizing imager and docking strands are analyzed to extract the binding rates. This approach does not rely on any localization or discrimination of individual binding events and can thus be performed at orders of magnitude lower irradiances. Nonetheless, SI-FCS traces exhibit a decaying mean fluorescence intensity that is accounted for by a monoexponential detrending of the intensity trace before the autocorrelation [Mücksch et al., 2018]. The fluorescence intensity $I(t)$ of each integrated region is fitted and subsequently divided by:

$$I(t) = I_0 \exp\left(-\kappa t\right) + I_\infty\,, \tag{IV.1}$$

with the effective depletion rate κ characterizing the loss in fluorescence intensity, the amplitude I_0 and the offset I_∞ (Supplementary Figure IV.11, p. 87). For a one-component reversible binding, the SI-FCS autocorrelation function $G_\mathrm{N}(\tau)$, with the amplitude normalized to one, is an exponential function decaying with a characteristic decay time τ_c:

$$G_\mathrm{N}(\tau) = \exp\left(-\frac{\tau}{\tau_\mathrm{c}}\right). \tag{IV.2}$$

A detailed derivation of the SI-FCS autocorrelation function is found in [Mücksch et al., 2018]. The monoexponential correction (Equation (IV.1)) allows the accurate quantification of kinetics via SI-FCS, when the characteristic decay time τ_c of the autocorrelation function (ACF) is much shorter than the characteristic time of detrending ($\tau_\mathrm{c} \ll 1/\kappa$).

With higher average concentration of fluorescent imager in solution $\langle A\rangle$, the probability of docking sites to be occupied increases. In SI-FCS, an increase of imager concentration manifests itself as a decrease of the characteristic decay time τ_c, which can be expressed in terms of the association and dissociation rates k_a and k_d, respectively:

$$\tau_\mathrm{c}\left(\langle A\rangle\right) = \frac{1}{k_\mathrm{a}\langle A\rangle + k_\mathrm{d}} \tag{IV.3}$$

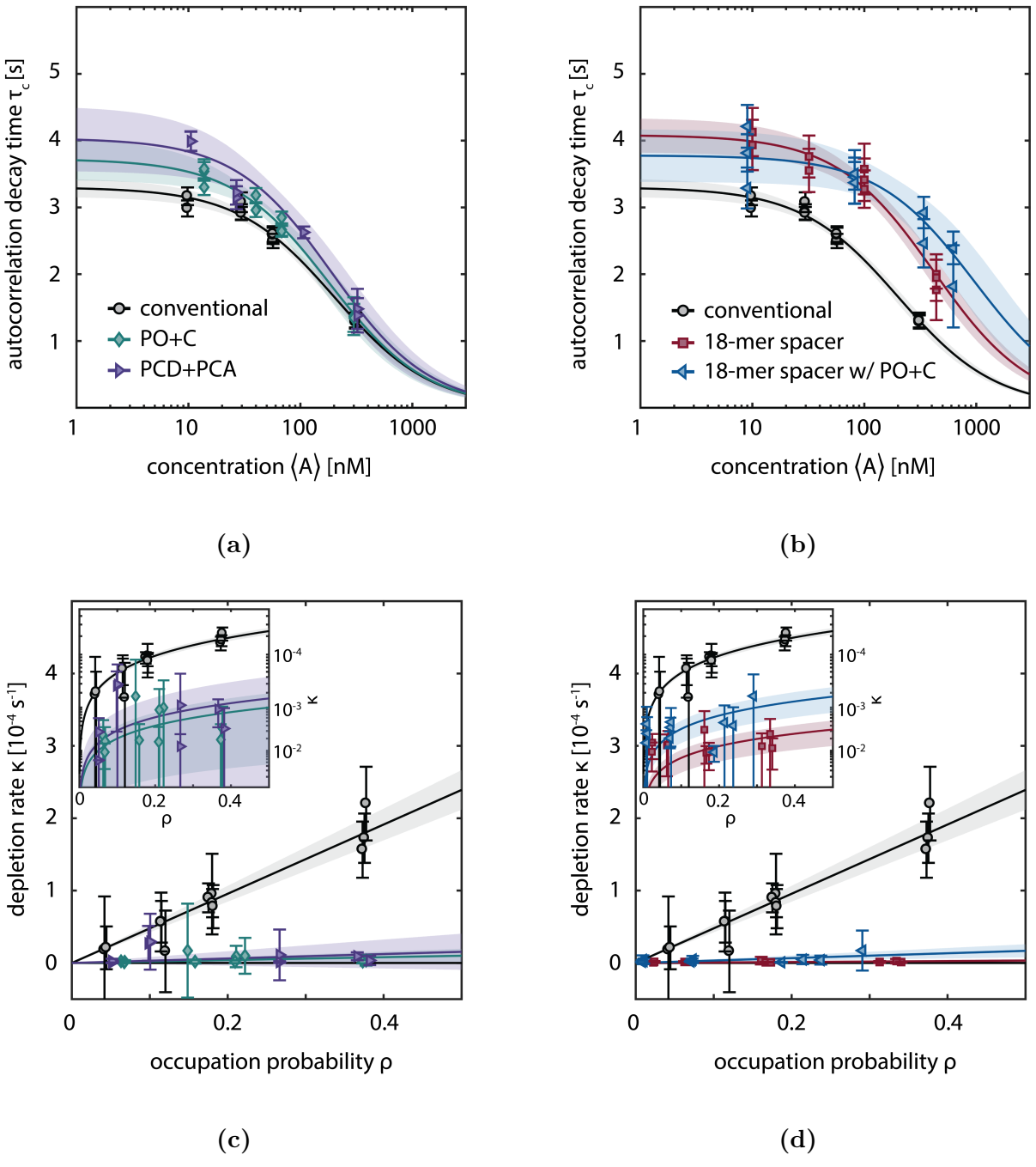

Figure IV.4: caption on next page.

Figure IV.4: Depletion of docking sites investigated by SI-FCS at low irradiance ($0.018\,\mathrm{kW/cm^2}$). (a) Titration series of the imager concentration $\langle A \rangle$ with 9 nt overlap for conventional imager strands (black), addition of oxygen scavenging system PO+C (turquoise) and PCD+PCA (purple). Data points and error bars represent mean and standard deviation from 64 regions of interest ($5.1 \times 5.1\,\mu\mathrm{m}$), respectively. Solid lines show the fit to Equation (IV.2). The 95 % functional error bounds are displayed as shaded areas. (b) As (a) but comparing the conventional imager to the 18-mer spacer (red) and 18-mer spacer with PO+C (blue). (c) The effective depletion rate κ (Equation IV.1) of docking strands depends linearly on the occupation probability ρ, which is calculated from the concentration and the kinetic rate constants according to Equation (IV.6). Solid lines show the fit to Equation (IV.4). Data points and errors are displayed as described in (a). The inset shows the depletion rate κ on a logarithmic scale. (d) Samples as in (b) displayed as in (c). SI-FCS raw data is available as Supplementary Material (p. 278).

We performed five titration series of the imager concentration $\langle A \rangle$ with otherwise identical conditions as described above: with conventional imager in absence of oxygen scavenging buffers (1), with PO+C added (2a), PCD+PCA added (2b), with the 18-mer spacer (3a), and the combination of 18-mer spacer and PO+C (3b). We obtained similar hybridization rates for conventional imager with and without oxygen scavenger system (Figure IV.4a). Comparing the conventional to the oxygen-scavenged buffer, the dissociation rate is slightly lowered ((0.303 ± 0.010)/s compared to (0.268 ± 0.017)/s, and (0.25 ± 0.02)/s for conditions (1), (2a), and (2b) respectively). This decrease is potentially caused by residual photo-bleaching of bound fluorophores, which was previously not observed when determining a bleaching-free regime by variation of the excitation power [Mücksch et al., 2018]. The imager with 18-mer spacer (3a,b) shows a decreased association rate (Figure IV.4b), in agreement with the lower binding frequency observed in DNA-PAINT traces (Figure IV.2b) and the higher dark times (Figure IV.3b). A lower association rate can be caused by different steric features of the imager, which are reflected by a larger hydrodynamic radius. We determined the translational diffusion coefficient as $(120 \pm 20)\,\mu\mathrm{m}^2/\mathrm{s}$ for the 18-mer spacer, being by a factor 1.7 smaller than the diffusion coefficient of the conventional imager (Supplementary Figure IV.6c, p. 80). We observe a difference for the association rate in absence (3a) and presence (3b) of PO+C only slightly larger than the estimated error of the measurement. The dissociation rate is similar to the conditions in presence of oxygen scavenging buffer (Table IV.1).

To investigate the effect of depletion of binding sites in SI-FCS, we compared the rate of the detrending κ (Equation (IV.1) and Supplementary Figure IV.11a, p. 87) in

absence and presence of oxygen scavenging buffers and the 18-mer spacer. If the process of depletion of docking sites is mediated by the fluorescent dye, only hybridized duplexes create damages. Therefore, κ represents an effective depletion rate, which is given by a depletion rate constant δ specific to the investigated system, lowered by multiplication with the occupation probability $\rho(\langle A \rangle)$ of docking sites:

$$\kappa(\rho) = \delta \cdot \rho(\langle A \rangle). \tag{IV.4}$$

The occupation probability ρ is intuitively accessible as the fraction of the bright time τ_B to the duration of one binding cycle, represented by the sum of bright and dark time $(\tau_\mathrm{B} + \tau_\mathrm{D})$:

$$\rho = \frac{\tau_\mathrm{B}}{\tau_\mathrm{B} + \tau_\mathrm{D}} \tag{IV.5}$$

Bright and dark times are principally accessible from low irradiance PAINT measurements, allowing for the individual detection of docking sites. High irradiances, however, as required to resolve multiple narrow spaced binding sites on one DNA origami nanostructure, reduce the bright time and hinder the direct determination of the occupation probability. Without the need for localization, ρ can be expressed in variables accessible from SI-FCS titrations, in particular the association rate $k_\mathrm{a} = 1/(\tau_D \langle A \rangle)$ and the dissociation rate $k_\mathrm{d} = 1/\tau_\mathrm{B}$, as:

$$\rho = \frac{1}{1 + k_\mathrm{d}(k_\mathrm{a}\langle A \rangle)^{-1}} \tag{IV.6}$$

Experimentally, we determine the specific depletion rate constant δ by varying the concentration $\langle A \rangle$ of fluorescent imager in solution (Equation (IV.4)). For the conventional imager (1), we confirm the linear dependence of $\kappa(\rho)$ with a slope of $\delta_\mathrm{conv} = (470 \pm 40) \times 10^{-6}/\mathrm{s}$. Strikingly, the slope δ decreases by two orders of magnitude when oxygen scavenger is added (Figure IV.4c), thus nearly eliminating the depletion of binding sites ($(20 \pm 19) \times 10^{-6}/\mathrm{s}$ and $(30 \pm 50) \times 10^{-6}/\mathrm{s}$, for PO+C and PCD+PCA, respectively). Similarly, the 18-mer spacer reduces the depletion rate to $(7 \pm 4) \times 10^{-6}/\mathrm{s}$ and $(33 \pm 18) \times 10^{-6}/\mathrm{s}$ in absence and presence of PO+C, respectively (Figure IV.4d). For the low irradiances ($I_0 = 0.018\,\mathrm{kW/cm^2}$), employed in SI-FCS, the effect of depletion of binding sites approaches zero for both oxygen scavenging systems and the 18-mer spacer. As apparent from the estimated errors of the individual measurements, the differences observed

for the close to zero depletion rates are indistinguishable within the precision of the measurement. The depletion is only distinguishable from zero at high imager concentrations (Figure IV.4b and Table IV.2).

Table IV.2: Slope of the linear fit of Equation (IV.4) to the depletion rate $\kappa(\rho)$ in Figure IV.4. The errors represent the 95 % confidence bounds of the fit.

Imaging Condition	δ **[10^{-6}/s]**
conventional	480 ± 55
PO+C	20 ± 19
PCD+PCA	30 ± 50
18-mer spacer	7 ± 4
18-mer spacer with PO+C	33 ± 18

IV.2.3 Discussion

To summarize, we have confirmed that docking strands in DNA-PAINT microscopy are depleted by irradiation with visible light in an indirect process mediated by the excitation of fluorescent dyes. DNA-PAINT microscopy with long acquisition series showed that individual docking sites get irreversibly lost in irradiated areas (Figure IV.2 and Figure IV.3). In the majority of SMLM methods, the resolution and signal-to-noise ratio (SNR) of super-resolved images are limited by the photon-budget of fluorophores irreversibly bound to labeled sites [Thompson et al., 2002,Deschout et al., 2014]. Making use of the reoccurring binding and a large reservoir of fluorescent imager, DNA-PAINT is less limited by the photo-bleaching of fluorophores to precisely localize binding sites [Schnitzbauer et al., 2017]. In this work, we showed that DNA-PAINT is ultimately limited by the eventual damage of docking sites.

We showed evidence that the depletion of docking strands of DNA origami nanostructures is caused by damages of DNA handles and can thus be distinguished from photobleaching of fluorophores (Figure IV.3). In our SI-FCS experiments, we find a linear dependence of the effective depletion rate on the presence of fluorescently labeled imager (Figure IV.4c,d). This does not only show that the depletion process is mediated by bound fluorophores, but it also indicates that direct photo-damage of DNA is negligible compared to fluorophore-mediated damages. Our experiments in oxygen scavenging buffers strongly indicate the involvement of ROS in the depletion of available docking strands. Not only do we see a significantly reduced depletion in high irradiance DNA-PAINT microscopy

($I_0 = 0.2\,\mathrm{kW/cm^2}$) (Figure IV.2 and Figure IV.3), but also in low irradiance SI-FCS measurements ($I_0 = 0.018\,\mathrm{kW/cm^2}$), we observed a close to zero depletion rate (Figure IV.4c,d and Table IV.2). The importance of ROS for photo-induced damages following fluorescence excitation has been studied not only in the context of fluorescence photobleaching [Ha and Tinnefeld, 2012, Eggeling et al., 1999, Widengren et al., 2007, Widengren and Rigler, 1996, Eggeling et al., 2006, Zheng et al., 2014a], but also photo-toxicity [Dixit and Cyr, 2003, Schneckenburger et al., 2012] and in particular DNA damage [Sies and Menck, 1992, Matter et al., 2018, Cadet and Teoule, 1978]. ROS have also been shown to contribute to photo-induced unbinding of proteins [Neumüller et al., 2010, Heinze et al., 2009]. Generally, ROS are one of the main sources for DNA damage and have been intensively investigated in relation to several kinds of cancer [Marnett, 2000, Malins et al., 2018, Paz-Elizur et al., 2003, Liou and Storz, 2010]. Our results show the cause for the depletion to be ROS generated downstream of the fluorescence excitation, diffusing to the DNA origami nanostructures and finally damaging the exposed docking stands. From our experiments, it is not possible to identify the type of created ROS, the type of induced DNA damage or the affected DNA bases. Different ROS, most prominently singlet oxygen and superoxide radicals, are supposedly formed from excited fluorescent states [Zheng et al., 2014a, Bonnett and Martinez, 2001]. The likelihood and type of induced damage is reported to be sequence dependent and enriched at duplex ends [Matter et al., 2018]. Previous studies suggest that guanine is preferentially damaged, due to its lowest redox potential among the DNA bases [Prat et al., 1998, Neeley and Essigmann, 2006, Greenberg, 2004]. Not only were oxidation products frequently found in guanine repeats [Matter et al., 2018, Prat et al., 1998], but also electron hole diffusion along the DNA leads to guanine oxidation distant from the site of single electron transfer [Hirakawa et al., 2003, Colson et al., 1992, Yun et al., 2007]. On the other hand, adenine and thymine are the predominant bases on the docking strand that are closest to the fluorescent dye upon imager binding. Thus, most likely, a variety of damage types is induced simultaneously.

The probability of a ROS to reach a docking site by 3D diffusion scales with the squared distance between both, assuming a much longer free path length of the ROS [Ogilby, 2010, Redmond and Kochevar, 2007]. Accordingly, a larger spacing between docking strands and fluorophores reduced the depletion of binding sites (Figure IV.4b) at low irradiances ($0.018\,\mathrm{kW/cm^2}$). Oxygen scavenging buffers and the 18-mer spacer show similar depletion rate constants ($(20 \pm 19) \times 10^{-6}/\mathrm{s}$, $(30 \pm 50) \times 10^{-6}/\mathrm{s}$ and $(7 \pm 4) \times 10^{-6}/\mathrm{s}$, for PO+C, PCD+PCA and 18-mer spacer, respectively), suggesting that both are similarly effective

in eliminating photo-toxic effects (Figure IV.4c,d and Table IV.2). Addition of PO+C to the 18-mer spacer did not show any further improvement for SI-FCS measurements. The given error of the close to zero depletion rates potentially underestimates the measurement uncertainty, as slow exponential decays (up to 10^6 s) are fitted only with limited accuracy based on 5-h measurements. Based on our results, we regard them indistinguishable. At the high irradiances (0.2 kW/cm^2) used for super-resolution microscopy, the 18-mer spacer is significantly less efficient in lowering the depletion (Figure IV.3). In contrast, the depletion seems to occur at a rate similar to the conventional (1) imager and does not show a significant improvement in the stability of docking sites. Adding PO+C to the 18-mer spacer (3b) eliminates the depletion of docking sites as effectively, as for the short imager (2a). We hypothesize that this difference is caused by the different irradiances intrinsic to the two applied methods. Photo-reactions from excited states are known to depend non-linearly on the excitation irradiance [Eggeling et al., 1999, Eggeling et al., 2005, Widengren et al., 2007]. Comparing the feasibility for kinetic investigations compared to localization precision, a large spacer is expected to decrease the accuracy in SMLM, due to the larger accessible space for the fluorophore upon DNA hybridization [Deschout et al., 2014]. On averaged DNA-PAINT images of several hundred origami nanostructures, the 18-mer spacer imager resolves binding sites with overall precision and accuracy (Supplementary Figure IV.8, p. 83) comparable to the imager with the fluorescent dye attached in close proximity to the docking strand. Individually localized origami nanostructures exhibit a significant loss in image quality that is additionally reduced by the lower association rate of the 18-mer spaced imager (Table IV.1). Interestingly, adding PO+C to the 18-mer spacer (3b) improves the achievable resolution, reaching results similar to the conventional imager strands (2a). We attribute the reduced blur of the 18-mer spacer with PO+C on the averages to the lower association rate and thus fewer simultaneous binding events (Supplementary Figure IV.8, p. 83). The effect is alternatively achieved in DNA-PAINT acquisitions by a lower imager concentration. A reduced association rate of the 18-mer spaced imager compared to the conventional imager can be partially attributed to a larger hydrodynamic radius, as experimentally confirmed by diffusion measurements in confocal FCS (Supplementary Figure IV.6c, p. 80). For applications based on the kinetics of binding, in particular SI-FCS [Mücksch et al., 2018] and qPAINT [Jungmann et al., 2016], adding a spacer sequence improves the photo-stability at low-irradiance conditions, while being free from chemical modifications and not requiring specialized buffers. Generally, we expect the positioning of the fluorescent dye with respect to the binding sequence to offer

unexplored optimization potential for reducing photo-toxicity in applications without the need for maximally precise localization.

In SI-FCS, a second component to the autocorrelation function can be observed at lag times larger than 10 seconds with concentrations of conventional imager strands higher than 30 to 100 nM (Supplementary Figure IV.11b, p. 87). We previously speculated that unspecific binding might be the main cause for this second component [Mücksch et al., 2018]. In the light of the results presented in this work, we now assume the photo-induced depletion of binding sites to be the primary cause (Supplementary Figure IV.11b, p. 87). While at low concentrations the applied detrending is sufficient to eliminate additional contributions in the correlation curve, with increasing concentration, the depletion and therefore the second component becomes more pronounced. The oxygen scavenging system PO+C massively reduces the depletion of docking strands even at the highest employed concentrations (300 nM, Supplementary Figure IV.11a, p. 87) and therefore removes the second contribution from the autocorrelation curves (Supplementary Figure IV.11b, p. 87). The second employed oxygen scavenging system (PCD+PCA) exhibits fluctuating intensity traces that are not fully described by a monoexponential detrending. In particular, we observe periods with increasing average fluorescence intensities that are not observed in any other experimental condition. In our hands, PCD+PCA causes less stable experimental conditions, which manifest themselves as fluctuating fluorescence intensities over time. This effect is particularly pronounced for sample life spans exceeding hours or days. The observed instabilities may potentially be attributed to a nuclease contamination of PCD [Senavirathne et al., 2015]. In case of PO+C, we did not find any hint on alterations of the sample and therefore conclude PO+C to be favorable for long lasting acquisitions. The 18-mer spacer exhibits a second component of the autocorrelation, which is becoming further pronounced by adding PO+C. We speculate that the 18-mer spacer exhibits additional dynamics on the time scale of tens of seconds, which are independent of the concentration and thus different from previously observed additional components in SI-FCS. Under all conditions, we observe at concentrations above 30 to 100 nM, depending on the condition, that the correlation curves do not decay to zero, irrespective of the addition of oxygen scavenging buffers or the extension with the 18-mer spacer. We therefore assume that a non-perfect focus stabilization, fluctuating laser intensities or temperature changes during a 5-h measurement may account for the multiple components on the time scale of min. However, those contributions separate well in time from the decay of interest of the autocorrelation function and therefore do not hinder the quantitative analysis of

autocorrelation curves.

In summary, we have shown that in DNA-PAINT super-resolution microscopy, binding sites are damaged by ROS, which are generated from excited fluorescent dyes on hybridized imager strands. Not only does this effect limit the achievable acquisition time of DNA-PAINT, but it also hinders quantitative analysis based on the kinetics of the hybridization reaction. Similarly, long acquisition series in SI-FCS show artifacts generated by the loss of binding sites even though performed at low irradiances to avoid photo-bleaching. DNA-PAINT super-resolution microscopy and SI-FCS measurements benefit from the use of oxygen scavenging buffers, of which PO+C showed best long-term stability. Further, we presented an extended imager strand with an 18-mer spacer that drastically reduces the depletion of binding sites at low irradiances without additives to the sample. In particular for applications exploiting the kinetics of DNA hybridization, not only the addition of oxygen scavenging systems, but also a design placing the dye at larger distance from the docking site, will improve quantitative analysis. We believe that these results will be of general interest for the future design of fluorescence-based, minimally invasive applications of DNA nanotechnology. To our knowledge, this is the first time that the PO+C oxygen scavenging system has been applied to enhance the performance of DNA-PAINT super-resolution microscopy and we believe this system to be of use also in the context of three-dimensional cellular imaging of fixed specimen, which requires extended acquisition times.

IV.2.4 Appendix

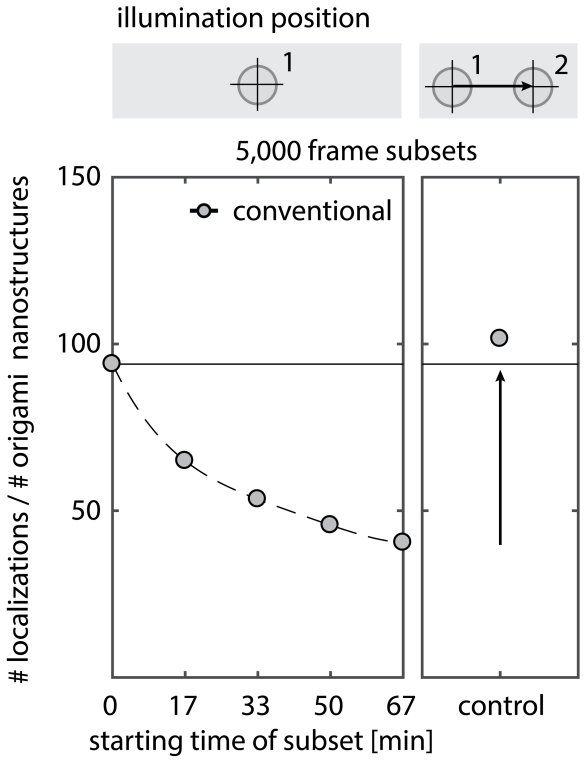

Figure IV.5: With increasing measurement time, the total number of localizations per DNA origami nanostructure decreases. One large time series of 25,000 frames (83 min) was drift corrected and subsequently divided into five subsets of 5000 frames (17 min each). Acquiring an additional 5000-frame-subset on the same sample in a previously not irradiated area recovers the initial number of localizations, indicating that bulk bleaching of fluorophores in solution is negligible compared to the locally observed decrease in the number of localizations.

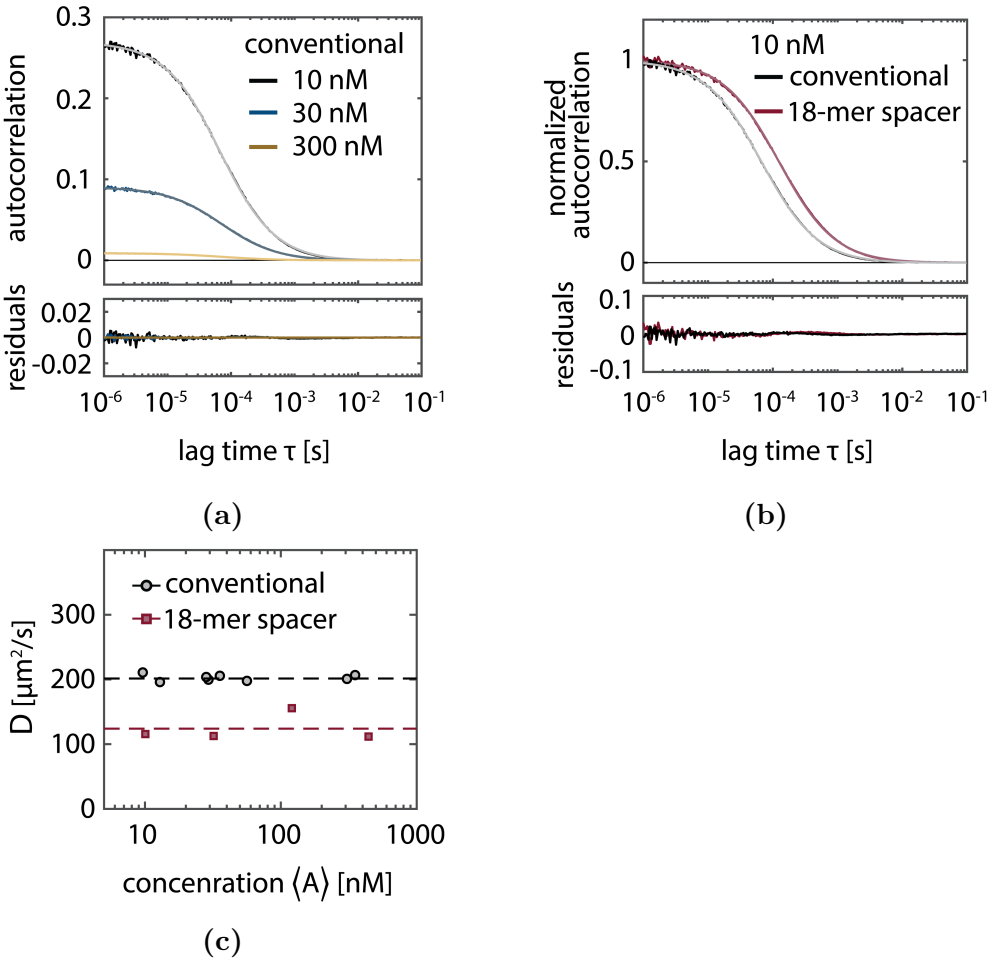

Figure IV.6: caption on next page.

Figure IV.6: Confocal FCS measurement of the imager concentration and diffusion coefficient. (a) Representative autocorrelation curves for the conventional imager with their respective fits to a simple 3D diffusion model (Equation B.1, p. 277) and residuals. The three displayed curves have the target concentrations 10 nM (black), 30 nM (blue) and 300 nM (brown) and the measured concentrations 9.8 nM, 29.7 nM and 310 nM, respectively. (b) Normalized autocorrelation curves at the target concentration 10 nM for the conventional condition (identical to (a)) and the 18-mer spacer, leading to a decrease in the diffusion time. (c) Diffusion coefficient D for the conventional and 18-mer spacer condition at different concentrations. The average diffusion coefficients (dashed lines) are determined as (mean $\pm$ std.): $(201 \pm 5)\,\mu m^2/s$ (in good agreement with previously reported results [Mücksch et al., 2018, Stellwagen et al., 2003]) and $(120 \pm 20)\,\mu m^2/s$ for the conventional and the 18-mer spacer, respectively. Based on the determined diffusion coefficients, we conclude that bleached imager within the TIRF excitation volume is predominantly recovered from solution by diffusion along the direction of the evanescent excitation. The diffusion time can be estimated as $t_D \sim d_{ev}^2/D$, with d_{ev} being the evanescent field of the TIRF illumination. Assuming the penetration depth as $d_{ev} \sim 75\,nm$ [Niederauer et al., 2018], we obtain $t_D \sim 50\,\mu s$, three orders of magnitude faster than the PAINT exposure time (200 ms) or the minimal SI-FCS correlation time (100 ms). In the high irradiance regime ($I_0 = 0.2\,kW/cm^2$), the rate of photo-bleaching within the TIRF illumination can be assumed four orders of magnitude slower than the recovery by diffusion, based on the bright times found for the conventional condition, which is shortened by photo-bleaching to $\tau_B \sim 2\,s$ (Figure IV.3b). Raw data of confocal FCS measurements is available as Supplementary Material (p. 278).

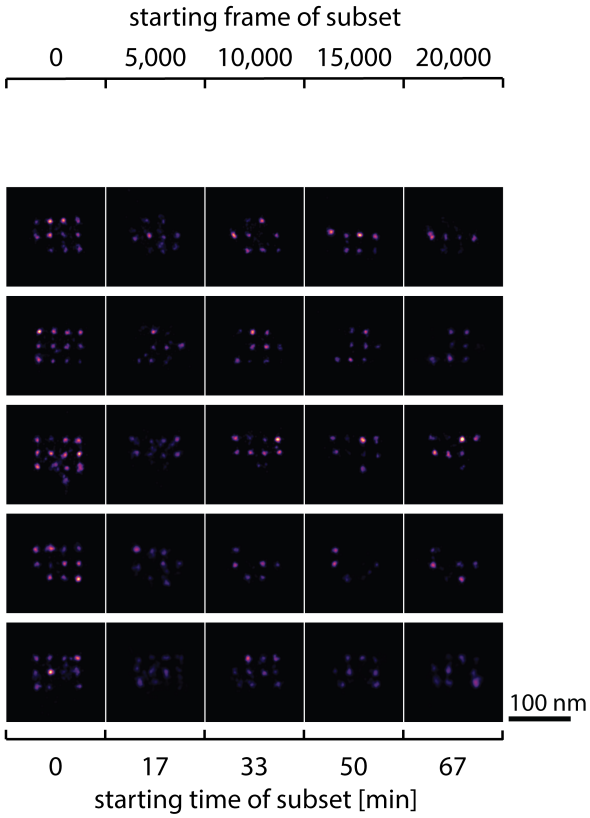

(a)

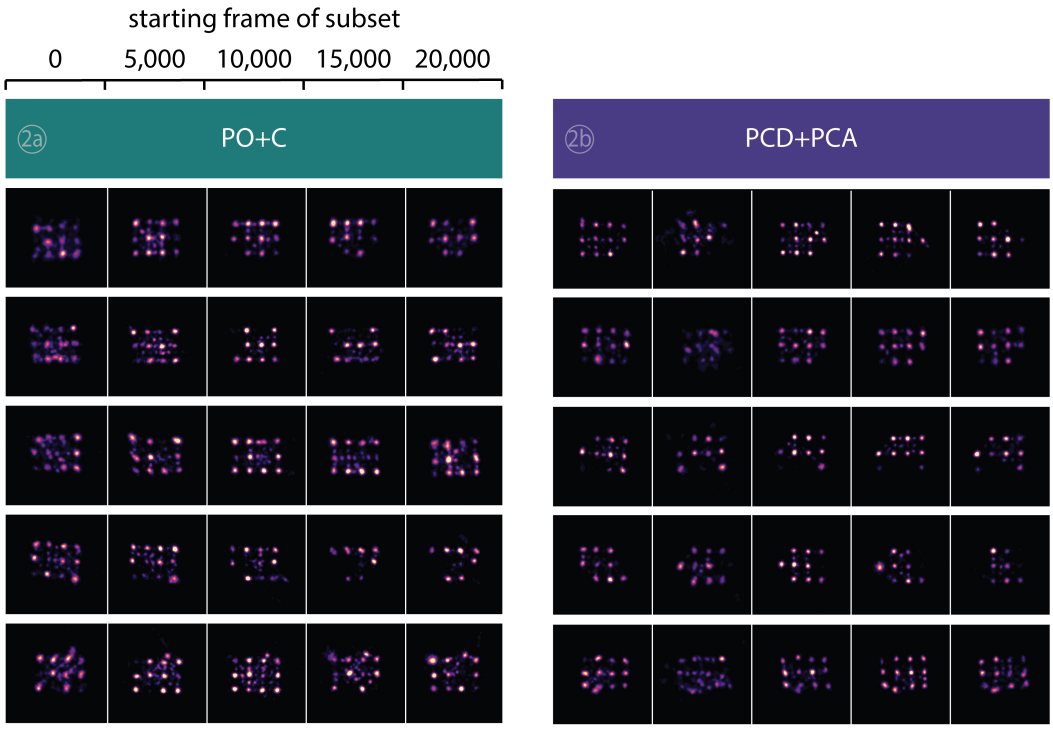

Figure IV.7: Cont.

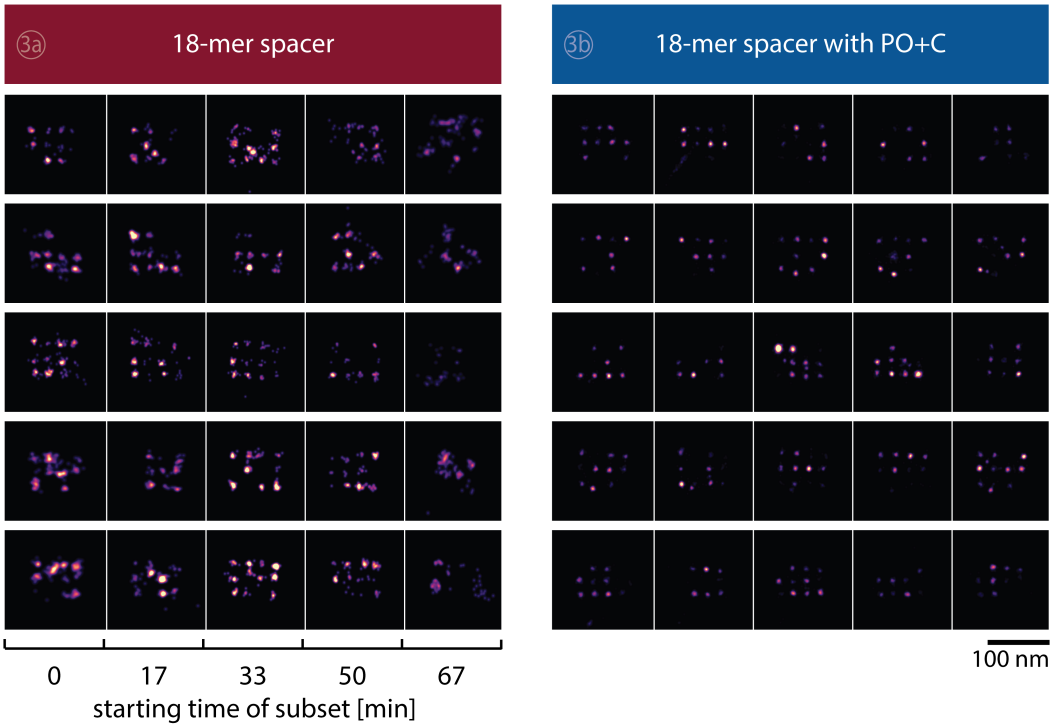

(b)

Figure IV.7: Selected DNA-PAINT super-resolved images of DNA nanostructures showing the depletion of binding sites in the five different conditions. (a) Images for the conventional imager (1). Five rows display different nanostructures that showed a high number of initially available docking sites. Images along the five columns represent the localizations within a subset of 5000 frames from a 25,000 frame long measurement. Scale bar: 100 nm. (b) Images taken with addition of the oxygen scavenging buffer PO+C (2a), PCD+PCA (2b), extension with an 18-mer spacer (3a) and the combination of 18-mer spacer and PO+C (3b).

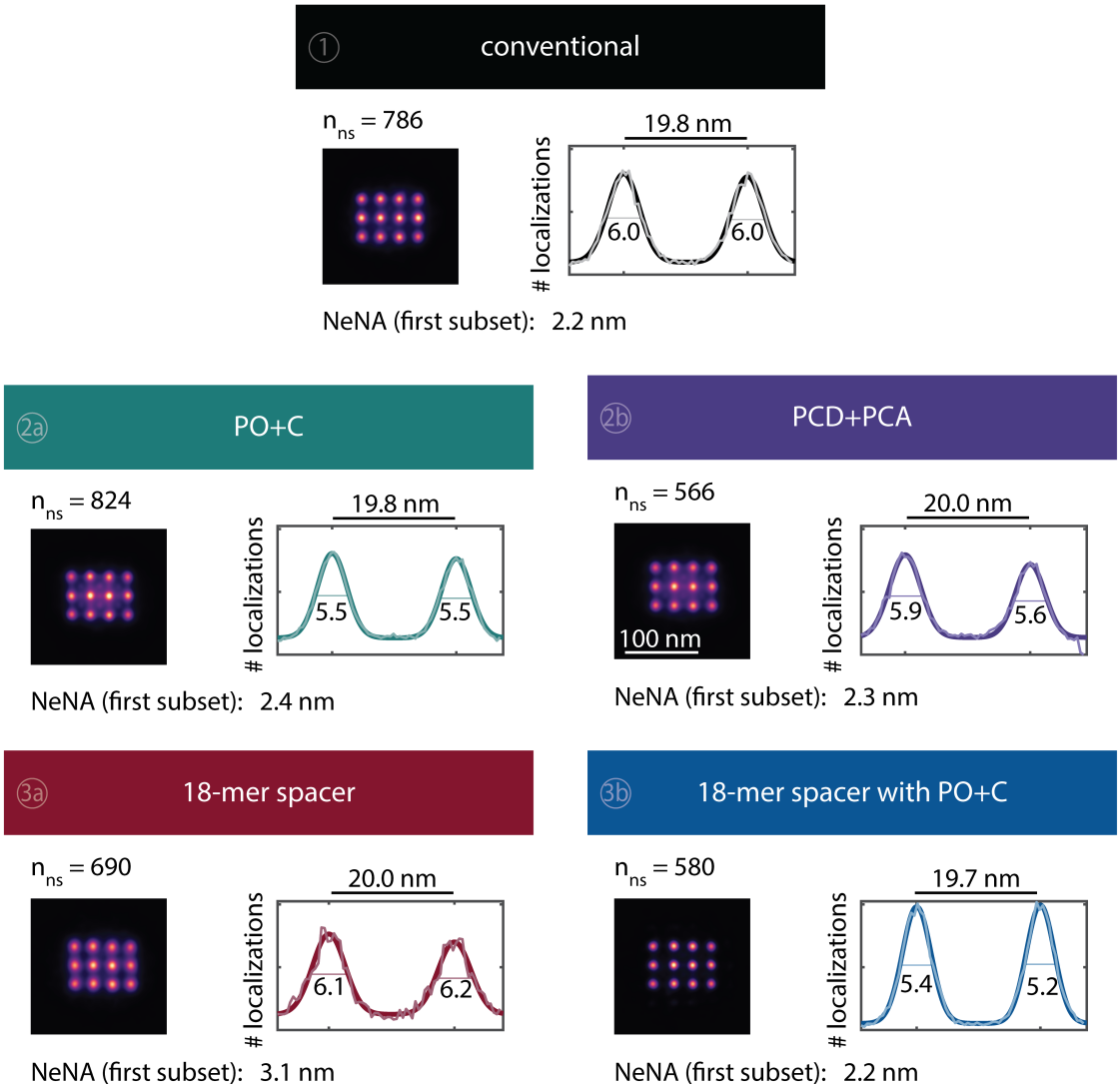

Figure IV.8: Averaged super-resolved DNA-PAINT images of DNA origami nanostructures for the whole time series of 83 min. The total numbers of identified DNA origami nanostructures n_{ns} employed for averaging are stated above the average images. Line profiles of total number of localizations through the two lower left points from each averaged image were fitted with a double Gaussian function $\left(f(x) = a_1 \exp\left[\frac{(x-b_1)^2}{2\sigma_1^2}\right] + a_2 \exp\left[\frac{(x-b_2)^2}{2\sigma_2^2}\right] + c\right)$. The number stated for each peak is the FWHM (in nm) and can be interpreted as a measure of the achievable resolution; the peak-to-peak distance is shown above the plot. Additionally, the value of the nearest neighbor analysis (NeNA) [Schnitzbauer et al., 2017, Endesfelder et al., 2014] is shown for the first subset.

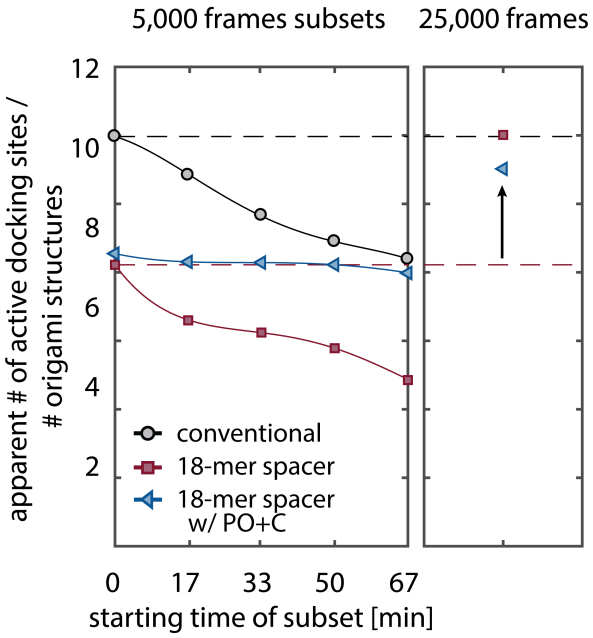

Figure IV.9: The observed lower number of active docking sites for the 18-mer spacer (conditions 3a and 3b) is caused by the lower association rate of the extended imager. Identifying active docking sites on the whole time series of 25,000 frames, recovers the number of initially active docking sites expected from the conventional imaging condition (condition 1).

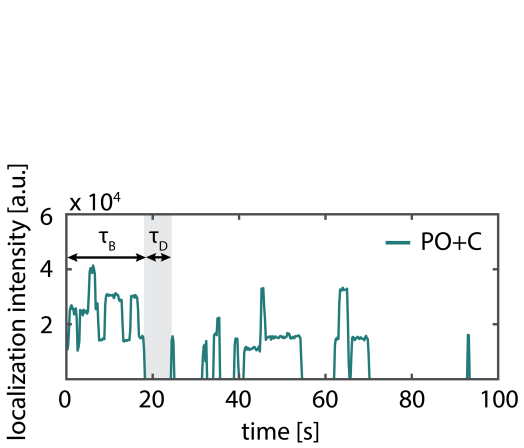

(a)

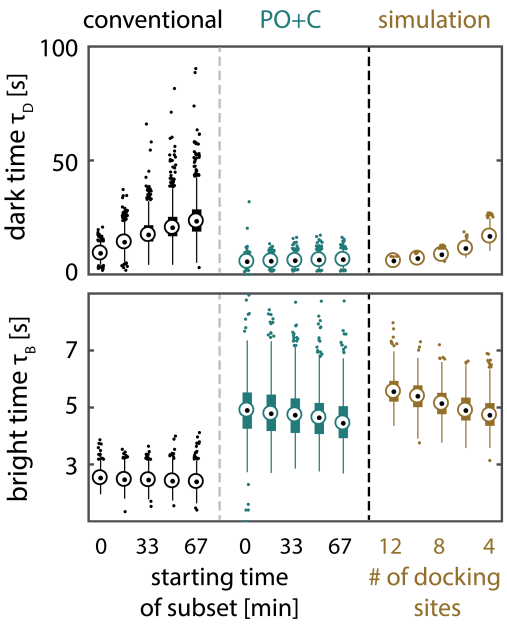

(b)

Figure IV.10: The number of available docking sites per origami structures influences the dark and bright times. (a) Intensity trace (representative section) of localizations assigned to the DNA origami presented in Figure IV.2 (PO+C) showing the effect of simultaneous binding. The step-wise increase corresponds to binding of imager strands, while the step-wise decrease indicates unbinding of an imager strand or photo-bleaching of individual fluorophores. (b) Comparison of experimentally obtained kinetics with simulations of origami nanostructures exposing a varying number of docking sites. On the one hand, a depletion of docking sites causes an increase in dark time τ_D, as individual hybridization events are as probable, but the number of possible binding partners is reduced. On the other hand, the localization algorithm counts temporally overlapping binding events within one diffraction-limited spot as one longer binding event. The probability for simultaneous binding increases with the number of binding sites in one diffraction limited spot. For the simulation, we made the following assumptions, based on the results from SI-FCS measurements (see Table IV.1): association rate $k_a = 1.5 \times 10^6\,/(\mathrm{Ms})$, $k_d = 0.3/\mathrm{s}$, $c = 10\,\mathrm{nM}$ and the number of binding sites decreasing step-wise with every subset from initially 12 to finally four binding sites. The simulated intensities from individual binding sites added up to obtain intensity traces for origami nanostructures.

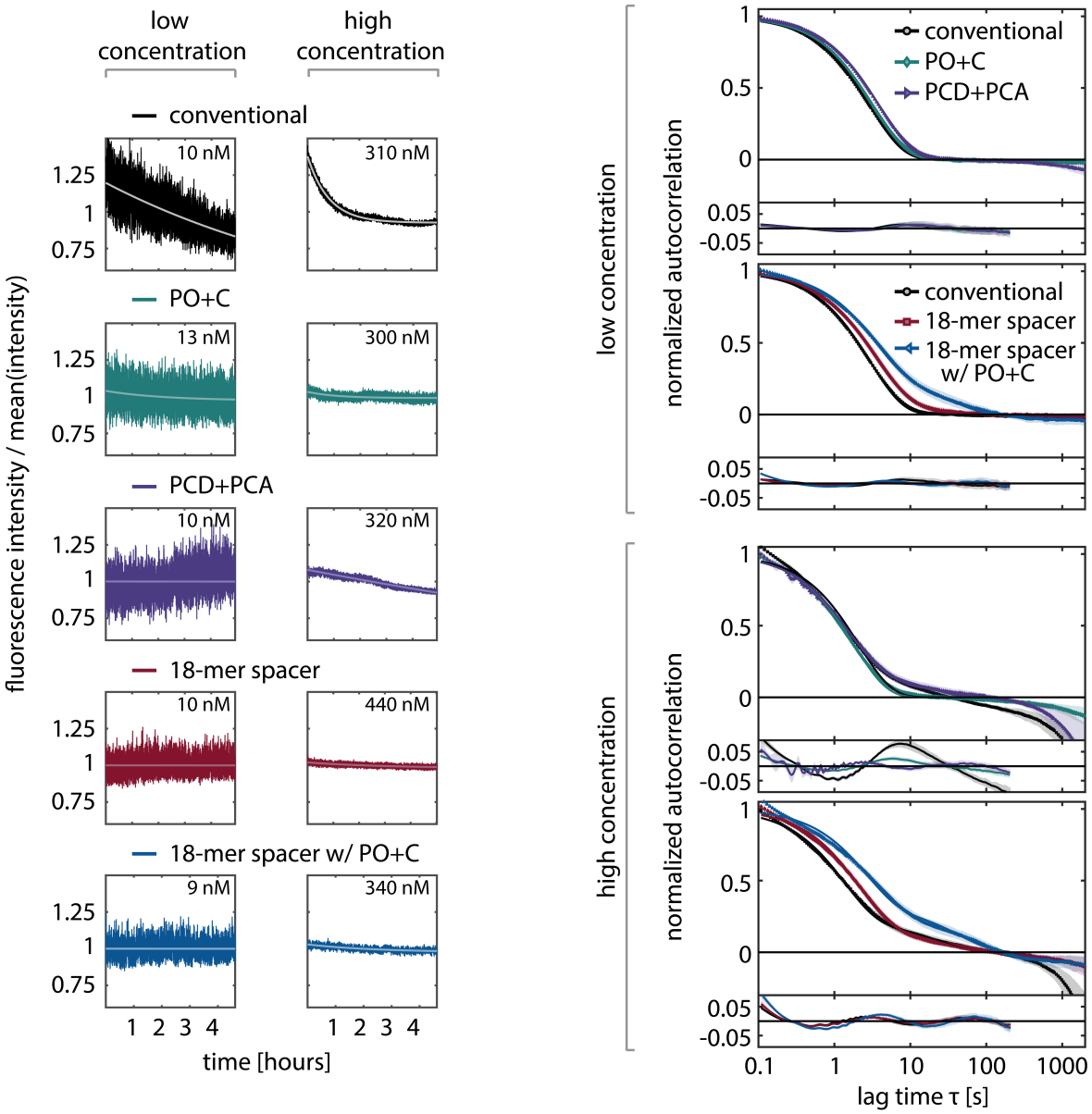

Figure IV.11: caption on next page.

Figure IV.11: Influence of the depletion of binding sites on the autocorrelation function: (a) Decays of the integrated fluorescence intensity within a representative region of interest (dark shade) and fit of the mono-exponential detrending function (Equation (IV.1), light shade). For all five conditions (conventional, addition of oxygen scavenging system (PO+C and PCD+PCA), 18-mer spacer and 18-mer spacer with PO+C) an example at low and high concentration is shown. The concentrations of individual samples were measured by confocal FCS. (b) Representative normalized autocorrelation functions and residuals with conditions as in (a) (solid lines). Shaded areas represent the standard deviation from 64 regions of interest.

The following section is not part of the contributed publication.

IV.3 Nuclease Activity of Oxygen Scavenging Systems

When using the PCD+PCA oxygen scavenging system, we found long-term intensity fluctuations on the order of tens of minutes to hours. Additionally, PCD+PCA shows a second contribution to the autocorrelation curve at high concentrations (Supplementary Figure IV.11, p. 87). Finally, we have found that the achievable long-term sample stability of DNA-PAINT samples of up to multiple days is compromised when using PCD+PCA. Senavirathne et al. found that commercially available PCD+PCA shows nuclease activity [Senavirathne et al., 2015]. To investigate nuclease activity in our samples, we compared confocal FCS measurements at different time points after the sample preparation (Figure IV.12). Imager strands without addition of oxygen scavenging system (conventional) and with the addition of PO+C show no change in the measured diffusion coefficient over multiple days. However, with addition of PCD+PCA, we observe an increase of the apparent diffusion coefficient as determined by confocal FCS. Measurements at less than 12 hours after the sample preparation lead to diffusion coefficients in agreement with the values for the conventional imager. In contrast, after three days, the apparent diffusion coefficient reaches the one of free Cy3B in solution. The observed trend is in agreement with the reported nuclease activitiy [Senavirathne et al., 2015]. In conclusion, PCD+PCA is limited in its applicability to long-term observations of DNA-based samples. PO+C did not result in apparent alterations of the sample over the time course of one week and thus appears better suited for DNA-PAINT samples.

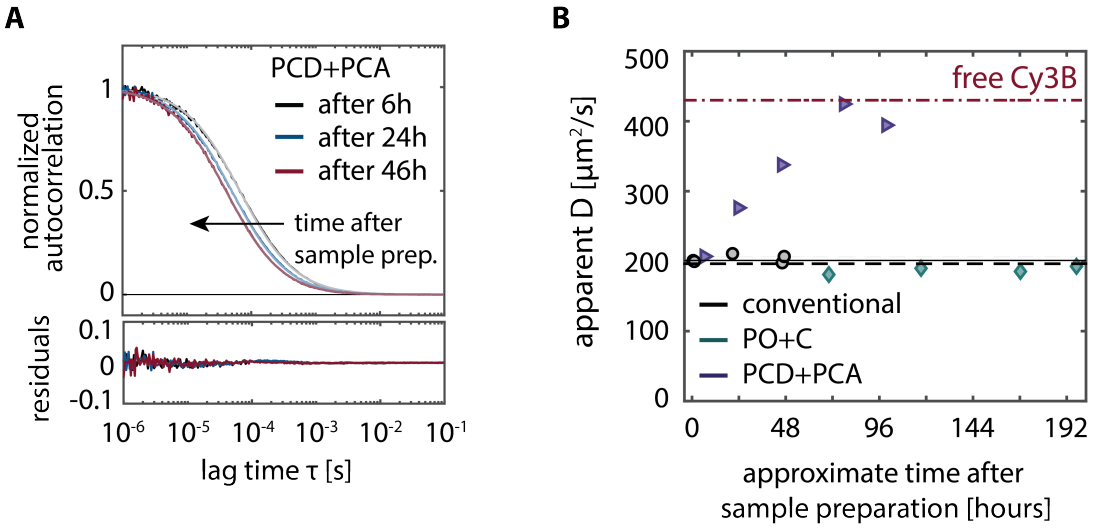

Figure IV.12: Influence of the time of sample preparation on the diffusion coefficient. (A) Confocal FCS curves for three conditions with the PCD+PCA oxygen scavenging system (2b), measured at different times after sample preparation. Autocorrelations are shown with their respective fits to a simple 3D diffusion model (Equation B.1, p. 277) and the residuals. **(B)** Resulting apparent diffusion coefficients for the conventional (1, black), PO+C (2a, turquoise) and PCD+PCA oxygen scavenging system (2b, purple). The determined average diffusion coefficient (Supplementary Figure IV.6, p. 80) is shown for comparison as solid horizontal line with the standard deviation as dashed lines. The diffusion coefficient of free Cy3B-malemide solution is shown in red (dash-dot).

V

TOWARDS THE DETERMINATION OF MILLISECOND BINDING KINETICS WITH SI-FCS: DIRECT CHARACTERIZATION OF THE TIRF EXCITATION

V.1 The Influence of Solution Diffusion on Binding Studies with SI-FCS

SI-FCS is not principally but practially limited in the accessibility of long residence times (Figure III.7, p. 47). As discussed in Chapter IV, many systems show long-term instabilities restricting individual measurements to multiple hours or up to one day and thus the accessible residence times of molecules to below 5 min. Towards short times, SI-FCS is ultimately limited by the time-resolution of the detector or the amount of photons collected from one binding event. For the employed EMCCD-based camera detection, we used 10 ms exposure times, which we estimate 10-fold higher than what is practically achievable with standard EMCCD or scientifc metal-oxide semiconductor (sCMOS) cameras [Sankaran et al., 2009, Capoulade et al., 2011, Bag et al., 2012]. Acquiring SI-FCS curves significantly below 1 ms requires either a significant reduction of the acquisition area, thus limiting multiplexing opportunities, or major adaptations to the detection scheme. The low noise of our SI-FCS acquisitions at short lag times (Figure III.2, p. 33) highlights the potential of the system under investigation to record low-noise correlation curves at lag times below 10 ms. In particular, single-point detection schemes, e.g. PMTs or APDs, can be converted into area detection by optical demagnification and allow the recording of autocorrelation curves down to microseconds. The implementation is thus similar to the initial designs by Thompson and colleagues [Thompson et al., 1981].

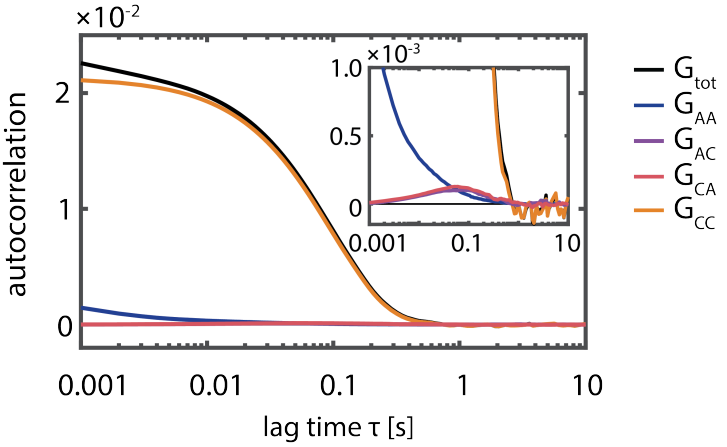

Figure V.1: Influence of solution diffusion on SI-FCS measurements as previously presented in [Mücksch, 2018]. Parameters of the simulation were: $\langle A \rangle = 10\,\mathrm{nM}$, $D_\mathrm{C} = 200\,\mu\mathrm{m}^2/\mathrm{s}$, $k_d = 10/\mathrm{s}$, $k_a = 5 \times 10^6/(\mathrm{M\,s})$, $d_\mathrm{ev} = 100\,\mathrm{nm}$, $a = 4.8\,\mu\mathrm{m}^2$.

V.1.1 Influence of the Cross-correlations of Solution Diffusion and Binding

The major challenge in this time domain, however, is not the time resolution of the detectors, but the loss of the separation of time scales of solution diffusion and binding reaction. To illustrate the contributions to the autocorrelation function we simulated the diffusion and binding ($A + B \leftrightharpoons C$) of molecules, assuming a monoexponential decay of the evanescent field, surface-immobilized binding sites and a squared integration area with side length a. The autocorrelation G_tot of the fluorescent signal from molecules in solution and bound to the surface decomposes to

$$G_\mathrm{tot}(\tau) = G_\mathrm{AA}(\tau) + G_\mathrm{AC}(\tau) + G_\mathrm{CA}(\tau) + G_\mathrm{CC}(\tau)\,. \tag{V.1}$$

Here, G_AA, G_CC, G_AC and G_CA are the autocorrelation functions of diffusing molecules, bound molecules, and the two cross-correlations, respectively. The autocorrelation curves were calculated individually from the Monte Carlo simulations, in which the number of molecules in states A and C is known for every instance in time.

As apparent in Figure V.1, the SI-FCS autocorrelation function (black) shows a clear contribution from solution diffusion (blue) at short lag times. Here the binding time is $k_d^{-1} = 0.1\,\mathrm{s}$ and thus significantly shorter than in Chapters III and IV. For lower diffusion coefficients D_A, the diffusion contribution G_AA shifts towards longer lag times. The relative

amplitude of the contributions from diffusing and bound molecules depends on the ratio of the numbers of diffusion and binding events. Thus, for higher concentrations of molecules in solution, the amplitude of the solution contribution is enhanced [Lieto et al., 2003]. Further, the solution contribution depends on both, the axial diffusion along the direction of the evanescent field and the lateral diffusion parallel to the surface through the detection volume. Larger integration ROIs and larger penetration depths therefore generally shift the solution contribution towards longer lag times [Lieto et al., 2003, Ries et al., 2008a] (Section II.1.3, p. 12).

Despite major efforts, a closed-form analytical solution for the three-dimensional autocorrelation function incorporating binding kinetics and diffusion through the evanescent field has not been found [Thompson et al., 1981, Thompson, 1982, Lagerholm and Thompson, 1998, Starr and Thompson, 2001, Lieto et al., 2003, Thompson et al., 2011, Lieto and Thompson, 2004, Ries et al., 2008a] (see also Section II.1.3, p. 12). Even more challenging is the incorporation of more complex binding models that deviate from a simple ligand-receptor binding.

As SI-FCS is aiming at the determination of binding kinetics without the need to precisely quantify diffusion coefficients, we were seeking a simple solution to remove the influence of solution diffusion on the quantification of binding dynamics. We therefore suggest that in many applications, for the determination of binding kinetics it is sufficient to use a fitting model based separately on the solution diffusion and the binding contribution. Neglecting the cross-correlations $G_{\mathrm{AC}} = G_{\mathrm{CA}} \approx 0$ (Section II.1.3) drastically simplifies the autocorrelation model

$$G(\tau) \approx G_{\mathrm{AA}}(\tau) + G_{\mathrm{CC}}(\tau)\,. \tag{V.2}$$

Most importantly, closed-form analytic solutions for the individual cases of solution diffusion (G_{AA}) and binding (G_{CC}) have been presented previously [Starr and Thompson, 2001, Ries et al., 2008a] (Section II.1.3.1). This approximation, however, will not hold generally and therefore needs to be confirmed, e.g. by simulations, for the specific case. Nonetheless, we believe this approach to be of great use in the determination of binding rates with SI-FCS as presented in Chapters III and IV, but with faster binding kinetics.

V.1.2 The Axial Autocorrelation Function in Objective-type TIR-FCS

A further difficulty arises with the use of objective-type TIR-FCS [Hassler et al., 2005a, Hassler et al., 2005b, Anhut et al., 2005]. In Section II.1.3 (p. 12) we presented the closed-form analytic solution for the autocorrelation function of diffusion in absence of binding kinetics G_{AA} [Ries et al., 2008a]. In the presented derivation and throughout the literature, the axial molecule detection function is assumed to be dominated by the evanescent field, which is characterized by a simple monoexponential decay (Equation II.18, p. 16). The importance of the axial excitation profile for accurate TIR-FCS measurements is nicely illustrated by the inverse experiment of Harlepp and colleagues, determining the penetration depth from the experimentally obtained autocorrelation function in prism-type TIR-FCS [Harlepp et al., 2004]. The accuracy of the axial autocorrelation function can be further improved by incorporating the effect of SAF [Anhut et al., 2005, Ries et al., 2008a, Ries et al., 2008b].

However, in objective-type TIRF microscopy a second, penetrating component of the TIRF excitation has been described by multiple groups [Brunstein et al., 2014b, Brunstein et al., 2014a, Mattheyses and Axelrod, 2006, Oreopoulos and Yip, 2008]. This suggested second decay, is supposedly non-evanescent and penetrates the sample at length scales significantly exceeding the penetration depth of the evanescent field. Such a second contribution would alter the axial autocorrelation function and potentially contribute to the combined autocorrelation function at time-scales relevant for the discrimination of solution diffusion and binding dynamics.

To improve the quantification of surface-binding with SI-FCS, we developed a calibration slide to precisely quantify the axial shape of the illumination profile in our objective-type TIRF microscope (Figure A.1, p. 264). As our approach is fluorescence-based, it does probe the effective detection profile as found in SI-FCS experiments, including effects from SAF [Ries et al., 2008a] and the limited objective's axial collection efficiency. The obtained TIRF profile will thus benefit not only the accurate modeling of the autocorrelation function, but quantitative assays based on the excitation profile in objective-type TIRF microscopy in general. Potential applications include the precise axial positioning of fluorescence emitters, e.g. for the calibration of three-dimensional super-resolution microscopy [Huang et al., 2008, Pavani et al., 2009] or three-dimensional resolution in TIRF microscopy by incident angle scanning [Olveczky et al., 1997, Boulanger et al., 2014].

V.2 Contributed Publication

Direct Characterization of the Evanescent Field in Objective-type Total Internal Reflection Fluorescence Microscopy

Christian Niederauer, Philipp Blumhardt, Jonas Mücksch,
Michael Heymann, Armin Lambacher, Petra Schwille

published in

Optics Express, Vol. 26, Issue 16, pp. 20492-20506
doi:10.1364/OE.26.020492

The following modifications have been made to the manuscript: citations and references to equations, tables and figures are displayed in a style consistent with this thesis; the appendix of the contributed publication is printed on pp. 280ff.

The publication contributed in this chapter is based on the outcome of the Master's thesis of Christian Niederauer [Niederauer, 2018] supervised by Jonas Mücksch and myself.

Author contributions: P.B., J.M. and P.S. conceived the study, contributed to the project design and to the writing of the manuscript. C.N. contributed to the project design and to the writing of the manuscript, conducted experiments and analyzed data. P.B. and J.M. built the TIRF microscopy setup. C.N., P.B., J.M., M.H., and A.L. contributed to the experimental design. All authors discussed and interpreted results and revised the manuscript.

V.2.1 Introduction

Total internal reflection fluorescence (TIRF) microscopy makes use of a rapidly decaying evanescent field at the interface of two media of different refractive indices to selectively excite fluorophores close to the interface, e.g. at the plasma membrane of a cell on a coverslide. The brightness of a fluorophore reflects the local excitation intensity, therefore the axial dependence of the excitation field in TIRF microscopy offers the possibility to

infer the z-position of a fluorophore. Observing the position, movement, or distribution of molecules in, or at the cell membrane provides insights into many biological processes, such as endo- and exocytosis [Merrifield et al., 2002, Midorikawa and Sakaba, 2015, Oheim et al., 1998, Saffarian and Kirchhausen, 2008, Steyer et al., 1997, Barg et al., 2010] or cellular signaling [Brodovitch et al., 2015, Poteser et al., 2016, Williamson et al., 2011, Lomakina et al., 2014, Chang et al., 2016], as well as (super-resolved) structural information [Hocdé et al., 2009, Jung et al., 2016, Boulanger et al., 2014, Olveczky et al., 1997, Cardoso Dos Santos et al., 2016, Cardoso Dos Santos et al., 2014, Fu et al., 2016]. However, a precise knowledge of the axial excitation profile is often required to accurately interpret TIRF data [Merrifield et al., 2002, Midorikawa and Sakaba, 2015, Oheim et al., 1998, Saffarian and Kirchhausen, 2008, Steyer et al., 1997, Barg et al., 2010, Brodovitch et al., 2015, Poteser et al., 2016, Williamson et al., 2011, Lomakina et al., 2014, Chang et al., 2016, Hocdé et al., 2009, Jung et al., 2016, Boulanger et al., 2014, Olveczky et al., 1997, Cardoso Dos Santos et al., 2016, Cardoso Dos Santos et al., 2014, Fu et al., 2016, Liu et al., 2009, Sarkar et al., 2004, Seol and Neuman, 2018, Tutkus et al., 2017]. Theory predicts a single-exponential decay function for the axial TIRF intensity $I_{\mathrm{exc}}(z)$ with a penetration depth d_{ev} [Gingell et al., 1987]:

$$I_{\mathrm{exc}}(z) = I_{0,\mathrm{exc}} \exp\left(-z/d_{\mathrm{ev}}\right) \tag{V.3a}$$

$$d_{\mathrm{ev}} = \frac{\lambda}{4\pi\sqrt{n_1^2 \sin^2\theta - n_2^2}} \tag{V.3b}$$

with $I_{0,\mathrm{exc}}$ the intensity directly at the interface, n_1 the refractive index of the coverslide and n_2 the refractive index of the sample. Thus, under ideal conditions, the penetration depth of the evanescent field d_{ev} depends only on the incident angle θ towards the optical axis, for given excitation wavelength λ and refractive indices $n_1 > n_2$ of the sample. Therefore, in previous studies, the penetration depth is often calculated based on measurements of the incident angle [Barg et al., 2010, Hocdé et al., 2009, Cardoso Dos Santos et al., 2014, Fish, 2009, Burghardt, 2012, Paszek et al., 2012]. However, precisely determining the incident angle may be cumbersome and complicates the optical setup. Furthermore, deviations from the theoretical single-exponential profile have been observed in objective-type TIRF microscopy, presumably caused by light scattering in the optical path or optical aberrations [Brunstein et al., 2014b, Brunstein et al., 2014a, Mattheyses and Axelrod, 2006, Oreopoulos and Yip, 2008]. Available methods for the direct characterization of the excitation profile, which are in principle sensitive to deviations from

the single-exponential profile, (i) are not applicable in typical (aqueous) refractive index environments [Olveczky et al., 1997, Mattheyses and Axelrod, 2006, Steyer and Almers, 1999], (ii) potentially alter the evanescent field by introducing a medium with a different refractive index than the sample [Boulanger et al., 2014, Steyer and Almers, 1999, Fiolka et al., 2008, Cabriel et al., 2018], (iii) require modifications of the setup [Saffarian and Kirchhausen, 2008, Liu et al., 2009, Sarkar et al., 2004, Seol and Neuman, 2018, Oreopoulos and Yip, 2008, Brutzer et al., 2012, Ramachandran et al., 2013, Graves et al., 2015] or (iv) require sophisticated sample preparation [Brutzer et al., 2012, Gell et al., 2009]. Promising attempts to fabricate a TIRF calibration slide were recently made by Unno et al. [Unno et al., 2015, Unno et al., 2017] who analyzed TIRF emission from different z-positions on a polymer substrate that matches the refractive index of water. However, their imprint lithography patterning process requires advanced cleanroom equipment and the number of available step heights was limited to three [Uchida et al., 2016].

Due to the lack of a fast and simple way to directly characterize the excitation profile particularly for biological applications, potentially valuable information encoded in the z-dependent intensity of the fluorophores is often entirely neglected or used non-quantitatively, limiting the interpretation of TIRF microscopy data [Toomre and Bewersdorf, 2010]. We here present a dip-coating based method to fabricate TIRF calibration slides with ten steps that are easy to use, applicable in a water-refractive index environment, have a long shelf-life, and are compatible with standard TIRF microscopes.

V.2.2 Methods

V.2.2.1 Dip Coating

The calibration slides were fabricated by depositing a staircase-like polymer profile onto conventional microscopy coverslides (24 mm×50 mm, thickness 170 µm±5 µm, Paul Marienfeld GmbH & Co. KG, Lauda Königshofen, Germany) (Figure V.2). The fluoropolymer material, MY-133MC (Mypolymers Ltd., Ness Ziona, Israel), was selected for its refractive index, stated to be 1.330 at a wavelength of 589 nm, closely matching that of water (Mypolymers Ltd., MY-133MC Datasheet 2018). The refractive index was confirmed using a refractometer (AR7 Automatic Refractometer, Reichert Inc., New York, USA) as $n_{\text{measured}} = 1.3292 \pm 0.0004$ (mean and standard deviation of triplicate measurements). The polymer cures upon exposure to ambient humidity, which allows for an easy manufacturing process without the need for (photo-)lithography or cleanroom equipment. Deposi-

tion of the polymer was carried out using a custom-built dip coating setup (see Appendix C.2, p. 280), which consisted of a motorized precision linear stage (LTM 45-50-HiSM with position control unit PS10-32, OWIS GmbH, Staufen, Germany) set up vertically on an optical breadboard, and a cuvette containing the dip coating solution (Makro-Küvette 6030-OG, Hellma GmbH, Müllheim, Germany). The coverslides were placed into a custom 3D-printed mount on the linear stage.

Initially, the coverslide was coated with an optical cleaning polymer (First Contact, Photonic Cleaning Technologies, Wisconsin, USA), which formed a removable layer on both sides of the coverslide. This layer was stripped off one side and the samples were then dip coated at 1 mm/s with a solution of the polymer MY-133MC, diluted in the fluorosolvent Novec 7500 (3M, Neuss, Germany), leaving a thin layer of polymer to small variations of the withdrawal speed, but highest reproducibility was achieved far from the maximum speed of the employed stage (2 mm/s) and slow speeds leading to significant evaporation during withdrawal (0.1 mm/s).

To obtain a multistep slide, dip coating of MY-133MC was repeated several times, at each iteration moving less far into the dip coating solution, thus creating a step-like pattern on the coverslide. After each iteration, the coverslide was left to cure for one hour at ambient temperature and humidity. Since the adhesion of the dip coating solution to the glass surface is different from the adhesion to the already coated surface, the initial dip coating step was performed at a concentration of 1 % (v/v), and further steps at a concentration of 3 % (v/v). In order to sample the excitation profile at a distance $h \gg d_{\mathrm{ev}}$, another step was deposited at a concentration of 10 % (v/v) (Figure V.3d). Finally, the remaining First Contact layer was removed, leaving the coverslide patterned on only one side. Final curing was achieved overnight at ambient temperature and humidity.

The cured polymer layers are chemically stable and do not show signs of deterioration over time, or due to washing with commonly used solvents (e.g. isopropyl alcohol, ethanol, purified water), as expected for polymers belonging to the fluoropolymer class [Thomas, 1999, Smith et al., 2014]. Revisiting the same slide after two months and multiple washing steps yields equivalent height distributions (see Appendix C.3, p. 281).

V.2.2.2 Characterization of the Polymer Height

The height of each polymer step relative to the coverslide surface was measured using an atomic force microscope (AFM Nano Wizard 3, JPK Instruments AG, Berlin, Germany). In order to reference to the original glass surface, the polymer coating was scratched with

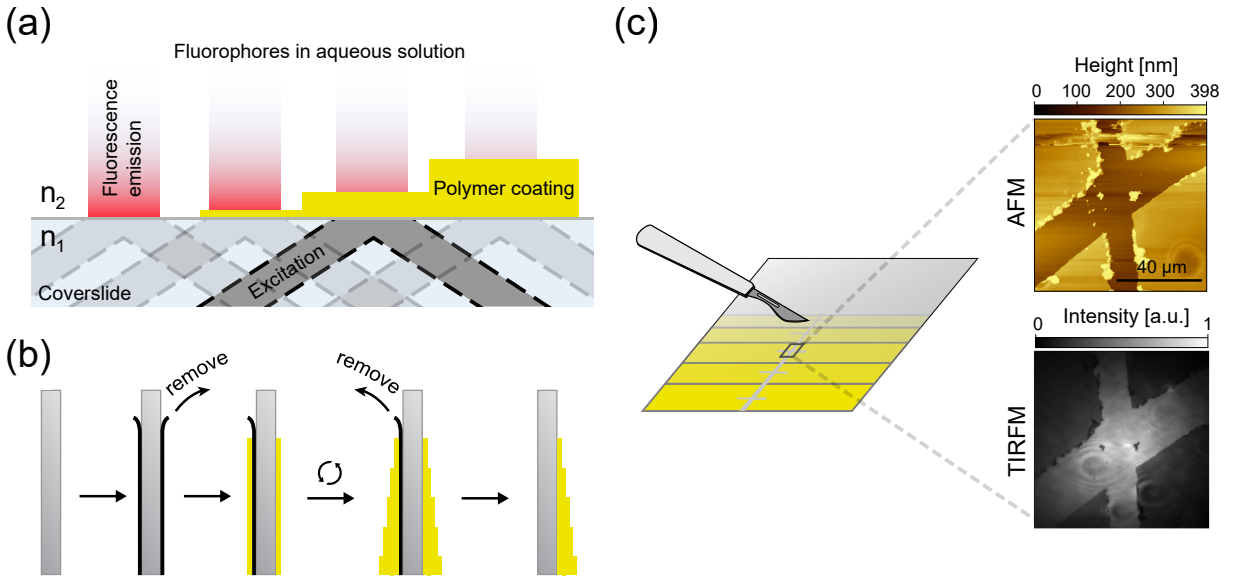

Figure V.2: (a) Calibration slide concept. The TIRF excitation profile is axially sampled by imaging the fluorescent emission of freely diffusing fluorophores in aqueous solution above water refractive index matched polymer step layers of different height on a coverslide. (b) Fabrication of the calibration slide. A coverslide is coated with a staircase-like profile of a polymer with a refractive index matching that of water (yellow) by repeatedly dip coating the coverslide in a dilute solution of the polymer. Discrete z-steps are obtained by iteratively dip coating the slide while adjusting immersion depth. A protective layer (black) enables the removal of the polymer on one side. (c) Fiducial marks for alignment and measurement of the polymer step height. Fiducials visible in both AFM and TIRF microscopy are created by scratching each polymer step layer with a blade. The scratch also enables the access to the glass surface for measuring the height of the polymer coating with the AFM (Figure V.3).

a blade (Cutfix stainless scalpel #22, Aesculap AG, Tuttlingen, Germany) along the whole length of the coating. AFM height distributions were generated using Gwyddion [Nečas and Petr, 2012] and fitted by the sum of two Gaussian functions $g(x) = a \cdot \exp(-x^2/(2\sigma_1^2)) + b \cdot \exp((-x-\mu)^2/(2\sigma_2^2))$ with free fitting parameters a and b, μ the height of the coating and σ_1 and σ_2 the respective standard deviation of the height of the glass surface and the coating. The root mean square (RMS) surface roughness of area A is calculated as $S_q = \sqrt{1/A \iint_A z^2(x,y)\,\mathrm{d}x\,\mathrm{d}y}$ with $z(x,y)$ the vertical AFM tip displacement at point (x,y).

Each step was scratched a second time, perpendicularly, creating fiducial marks to ensure AFM and TIRF imaging at the same position (Figure V.2c). Thorough removal of the coating inside the scratched trench and the absence of damage to the glass surface were confirmed by imaging the beginning of the scratch at the onset of the dip coated area (see Appendix C.3, p. 281).

V.2.2.3 TIRF Imaging

The calibration slides were imaged by a previously introduced custom-built objective-type TIRF setup with focus stabilization, which was constructed around a Nikon Ti-S microscope body (Nikon GmbH, Düsseldorf, Germany) [Mücksch et al., 2018]. Total internal reflection of the excitation laser beam was implemented by focusing the laser beam (achromatic lens, $f = 225\,\mathrm{mm}$, #47-646-INK, Edmund Optics, Karlsruhe, Germany) on the periphery of the back focal plane of the objective (Nikon SR Apo TIRF, 100x magnification, 1.49 numerical aperture). A piezo-electric stage (Q545, Physikalische Instrumente, Karlsruhe, Germany), hereafter referred to as TIR angle stage, was used for translating the excitation beam in the back focal plane in order to adjust the incident angle towards the optical axis (see Appendix C.4, p. 284). Optionally, magnification telescopes expanded the excitation laser beam three-fold or ten-fold.

Dip coated calibration slides were prepared for imaging by placing a spacer ($22\,\mathrm{mm} \times 40\,\mathrm{mm} \times 0.8\,\mathrm{mm}$ SecureSeal Hybridization Chambers, Grace Bio-Labs, Oregon, USA) on the coverslide. The calibration slides were loaded with aqueous solution of 5 µM Alexa Fluor 488 dye (Thermo Fisher Scientific Messtechnik GmbH, Munich, Germany) and imaged at an excitation wavelength of 491 nm (Cobolt Calypso 491 nm, Cobolt AB, Solna, Sweden).

Calibration data were acquired by moving the sample on the motorized xy-stage to the height-characterized areas in the vicinity of the fiducial marks and by recording the respective fluorescence intensity there. The objective was focused on the upper surface of the coverslide and was stabilized at this position throughout the measurement. TIRF

images were background corrected by imaging the respective coating steps with pure water, instead of fluorophores in solution, with otherwise unchanged conditions. The contribution of the polymer's autofluorescence to the background signal was shown to be negligible compared to the fluorescence signal level generated by the dye (see Appendix C.3, p. 281).

V.2.2.4 Data Analysis

The axial extent of the objective's detection point spread function is much larger than the penetration depth of the evanescent field, which is typically 60 nm – 200 nm. We determined the detection point spread function from the z-dependent intensity of a fluorescently labeled lipid bilayer, that can be approximated by a Lorentzian function $(s/\pi \cdot (s^2 + z^2)^{-1})$ with a full-width half maximum of $2s = 1.7\,\mu m$. Therefore, the camera detection profile can be assumed constant in the range of the evanescent field. The free fluorophores are excluded from the solid polymer step layers and an integration of the axial excitation along z from the height h of the polymer coating to infinity maintains the theoretical single-exponential excitation profile.

Fluorescence intensity data were analyzed using two different methods. For excitation laser beam diameters considerably smaller than the field of view, a z-dependent spatial separation of evanescent and non-evanescent contributions could be observed (Figure V.4a and Appendix C.5, p. 286). For each polymer step height, both contributions were fitted by a 2D Gaussian function. Penetration depths were directly obtained by single-exponential fits to the 2D Gaussian amplitudes identified with the evanescent field (Figure V.4b). Alternatively, for arbitrary excitation laser beam diameters, fluorescence intensity data were analyzed pixel by pixel after binning the data (Figure V.5a). Similar to Mattheyses and Axelrod [Mattheyses and Axelrod, 2006], the data were fit using a biexponential function, with contributions from the evanescent field (Equation V.3a), and from a non-evanescent contribution, presumably originating from scattering within the optical path and aberrations [Brunstein et al., 2014b, Mattheyses and Axelrod, 2006]. Describing the non-evanescent contribution by an exponential function with a long-range decay does not reflect on an underlying physical model, but is chosen for mathematical convenience.

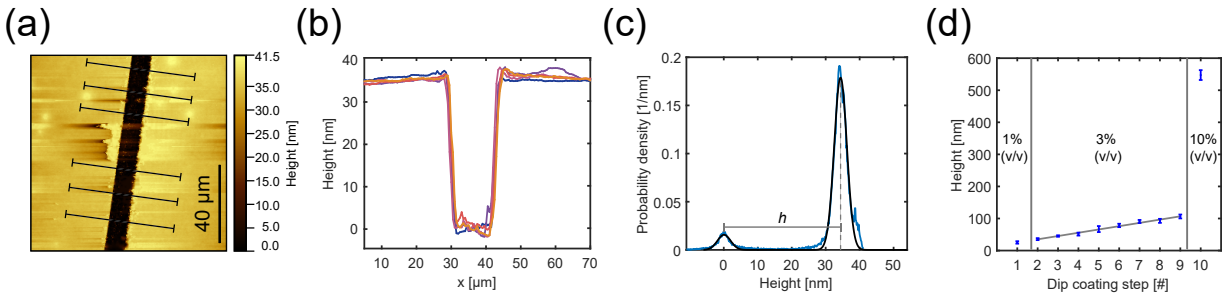

Figure V.3: (a) AFM image of a polymer coating step with a scratch exposing the coverslide surface. The image was leveled by fitting a plane through three points on the exposed coverslide surface and setting it to zero height. (b) Height profiles at positions indicated by the black lines in Figure V.3a. The height profiles show a consistent mean polymer step height of 34 nm. Each profile is averaged across a width of 6 µm. (c) Probability density compiled from the 256 × 256 height value dataset shown in Figure V.3a. Two distinct peaks are observable: the smaller peak at 0 nm corresponds to the glass surface exposed by the scratch in the polymer coating. The main peak at 34 nm corresponds to the height of the bulk coating surface. Gaussian fits to the data revealed standard deviations of the height distributions of $\sigma_{\text{glass}} = 1.8\,\text{nm}$ and $\sigma_{\text{coating}} = 1.9\,\text{nm}$. A polymer coating RMS surface roughness of 0.35 nm was calculated within a 20 µm × 20 µm area. (d) Height of the polymer coating on glass for ten dip coating iterations using three different concentrations: 1%, 3% and 10% (v/v). Data points correspond to the mean height within an area of 100 µm × 100 µm, measured on three calibration slides coated with the same dip coating procedure. Error bars correspond to the standard deviation of the triplicate measurements.

V.2.3 Results and Discussion

V.2.3.1 Polymer Step Heights

Dip coating of the coverslides with a dilute solution of the fluoropolymer reproducibly deposited homogeneous layers in the range of 25 nm to 550 nm. Figure V.3b shows absolute heights above the glass surface for a polymer step of 34 nm height. Measurements were taken across the whole field of view on several positions along a scratch uncovering the glass surface (Figure V.3a). The coating height within a 100 µm × 100 µm area shows a narrow distribution, fitted by a Gaussian function with a standard deviation of 1.8 nm (Figure V.3c). The RMS surface roughness of the polymer coating was determined as 0.35 nm within an area of interest of 20 µm × 20 µm. Correspondingly, the RMS surface roughness of the uncoated coverglass surface was determined as 0.46 nm. Therefore, height variations within the microscope's field of view (82 µm × 82 µm) as well as the local surface roughness for a given polymer step are negligible. To illustrate the excellent surface properties of the polymer coating, a high-resolution AFM image of a 2 µm × 2 µm area of interest and the corresponding height distribution are shown in Appendix C.3 (p. 281).

The deposition of a staircase-like polymer profile on a single coverslide was achieved by dip coating the coverslide repeatedly using different concentrations. Figure V.3d shows polymer layer heights ranging from 25 nm to 550 nm by employing dip coating solutions of 1%, 3% and 10% (v/v). The polymer layer height for two slides following the same dip coating protocol varied up to 15%. Therefore, the height of every step was still characterized for each slide. Further engineering for a standardization of the production process will allow to relinquish these quality controls.

V.2.3.2 Characterization of the Excitation Profile

Representative TIR images of free Alexa Fluor 488 dye in aqueous solution above polymer step layers of increasing heights are shown in Figure V.4a. As expected for a TIR excitation profile, the intensity rapidly decreases with increasing height. Accordingly, this decay can be described by an evanescent field with a purely imaginary k-vector, decaying exponentially in axial direction. In addition to the evanescent field contribution, another component is observed decaying over a much larger coating height range. 2D Gaussian fits to the 2D intensity distributions of the two components reveal one spatially fixed contribution (identified as evanescent with a penetration depth matching theoretical predictions), and one contribution spatially separating from the evanescent contribution as the polymer

layer heights increase (see Appendix C.5, p. 286). The z-dependent separation along one predominant lateral direction, and the intensity varying over a long range compared to the evanescent penetration depth, suggest a non-evanescent character for this contribution. The non-evanescent component is supposedly propagating light with real axial and lateral k-vector components.

Figure V.4b shows the amplitudes of 2D Gaussian fits to the evanescent and the non-evanescent contribution for various polymer step heights at an incident angle of 71.71° (determined by the lateral displacement of the center of fluorescence excitation upon axially translating the sample; see Appendix C.4, p. 284). An exponential fit to the amplitudes of the evanescent contribution yielded a penetration depth of $d_{\mathrm{ev}} = 67.3\,\mathrm{nm} \pm 4.3\,\mathrm{nm}$, closely matching the theoretically expected penetration depth (see section V.2.4 for a more detailed discussion). The amplitudes of 2D Gaussian fits to the non-evanescent contribution are observed to decrease much slower. Consequently, close to the surface, the evanescent excitation dominates, but for distances $h \gg d_{\mathrm{ev}}$ above the coverslide, the non-evanescent contribution prevails.

The spatial separation of both components is only observable for excitation beam diameters considerably smaller than the field of view of the microscope. In order to obtain penetration depths for arbitrary lateral illumination profiles, and to potentially resolve spatial variations of the penetration depth within the microscope's field of view, binned fluorescence intensity data of different polymer step heights were analyzed pixel by pixel (Figure V.5a). Magnification telescopes were placed into the optical path to expand the excitation laser beam diameter. Maps of the evanescent field's penetration depth for an incident angle of 71.71° (measured with the lateral displacement method) for laser beams of different diameter are presented in Figure V.5a and show similar penetration depths of $d_{\mathrm{ev,1x}} = 64.8\,\mathrm{nm} \pm 2.6\,\mathrm{nm}$, $d_{\mathrm{ev,3x}} = 66.7\,\mathrm{nm} \pm 6.9\,\mathrm{nm}$ and $d_{\mathrm{ev,10x}} = 64.9\,\mathrm{nm} \pm 6.0\,\mathrm{nm}$, equally matching the penetration depth of $67.3\,\mathrm{nm} \pm 4.3\,\mathrm{nm}$ obtained with the 2D Gaussian fit approach (Figure V.4b).

The dependence of the evanescent penetration depth on the angle of incidence of the excitation laser beam was examined by characterizing the TIRF excitation profile for a range of TIR angle stage positions. Additionally, the corresponding incident angles of the laser beam towards the optical axis were determined independently using the lateral displacement method (see Appendix C.4, p. 284). Penetration depths obtained with the calibration slide are presented in Figure V.5b, together with predicted values for the penetration depth, calculated based on incident angle data using equation V.3b. Direct

characterization with the calibration slide reproduced the theoretically expected penetration depths with errors below 10%. A systematic error towards shorter penetration depths may be explained by supercritical angle fluorescence effects, which result in an effective reduction of the evanescent field's penetration depth [Ries et al., 2008a]. Furthermore, it is important to note that the penetration depth calculated from the incident angle strongly depends on the exact values of the refractive indices n_1 and n_2. Refractive index values are often available only for few wavelengths and therefore have to be inter-/extrapolated for the wavelength used in the specific experiment [Gell et al., 2009]. Theoretically expected penetration depths in Figure V.5b were calculated using refractive indices of $n_1 = 1.5297$ (Schott AG, D263 Cover Glass Datasheet) and $n_2 = 1.333$ (Mypolymers Ltd., Study of non-cured MY-133: Refractive index vs. wavelength, 2018).

V.2.4 Conclusion

We fabricated and evaluated a calibration slide for the direct and accurate characterization of the TIRF excitation field in an aqueous refractive index environment. The calibration slides were fabricated following a simple and low-cost dip coating approach to deposit polymer step layers with a refractive index matching that of water onto a conventional coverslide. Evanescent penetration depths, obtained with the calibration slide for different incident angles were compared to penetration depths calculated based on the incident angle, measured independently with the lateral displacement method. Penetration depths obtained with both methods were in good agreement, validating our calibration slide as an adequate tool for direct evanescent field characterization in TIRF microscopy. Furthermore, deviations from the idealized single-exponential excitation profile could be observed with the calibration slide and were associated with non-evanescent light, supposedly caused by scattering in the optical path and aberrations [Brunstein et al., 2014b, Brunstein et al., 2014a, Mattheyses and Axelrod, 2006, Paige et al., 2001].

Our calibration slide may serve as a tool to routinely check the quality and reproducibility of the evanescent field generated by the multitude of commercial and custom-built TIRF setups [Deagle et al., 2017], thus simplifying interpretation and comparability of acquired data from TIRF microscopes. Furthermore, approaches where the shape of the axial excitation profile is used to infer the axial position of fluorescently labeled molecules [Merrifield et al., 2002, Midorikawa and Sakaba, 2015, Oheim et al., 1998, Saffarian and Kirchhausen, 2008, Steyer et al., 1997, Barg et al., 2010, Brodovitch et al., 2015, Poteser et al., 2016, Williamson et al., 2011, Lomakina et al., 2014, Chang et al., 2016, Hocdé et al.,

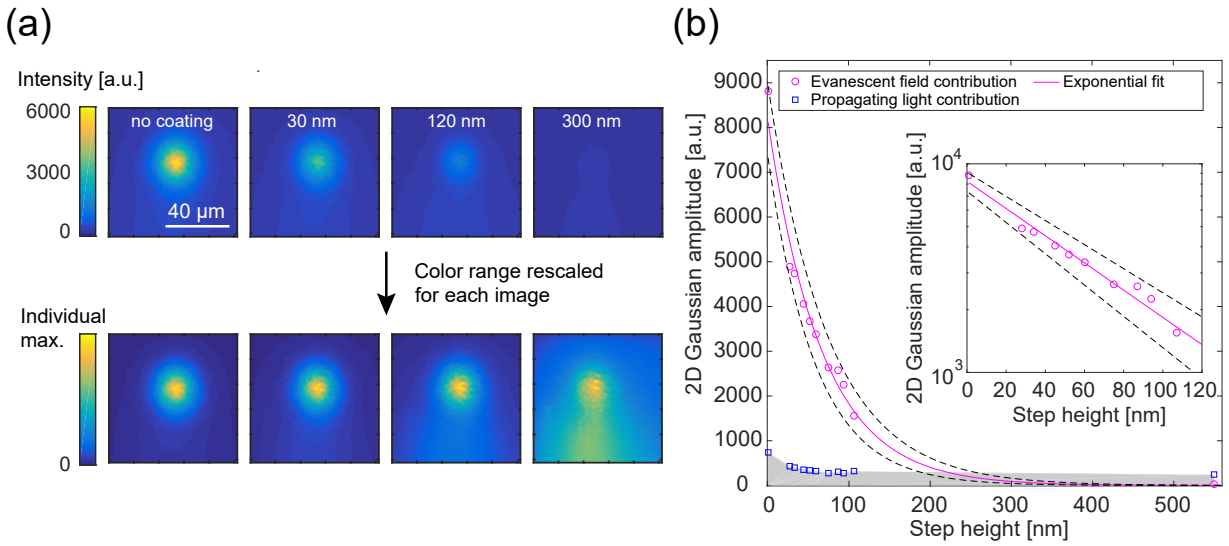

Figure V.4: (a) Representative images of free Alexa Fluor 488 dye above polymer step layers of different height. Upper row: the intensity is observed to decrease with increasing step height, as expected for an evanescent field. Lower row: corresponding images with the colormap's range rescaled to each image's individual maximum value reveals a second, putatively non-evanescent contribution. With increasing height, the relative amplitude of the evanescent and non-evanescent contributions shifts towards the non-evanescent part. Images were acquired without a beam expander. (b) Calibration data for a TIR angle stage setting of 2.8 mm (corresponding to an incident angle of the excitation laser beam of 71.71°, as measured with the lateral displacement method). The amplitudes of 2D Gaussian fits to the spatially separating contributions represent the rapidly decaying evanescent part (circles), and the rather constant non-evanescent part (squares). An exponential fit (solid line, with dotted lines representing 95% confidence intervals of the fit parameters) yields an evanescent penetration depth of $d_{\mathrm{ev}} = 67.3\,\mathrm{nm} \pm 4.3\,\mathrm{nm}$. The dataset was acquired using another calibration slide than in panel A, therefore sampling different heights. Inset: Detail of the data for step heights $h \approx d_{\mathrm{ev}}$ as a semi-log plot.

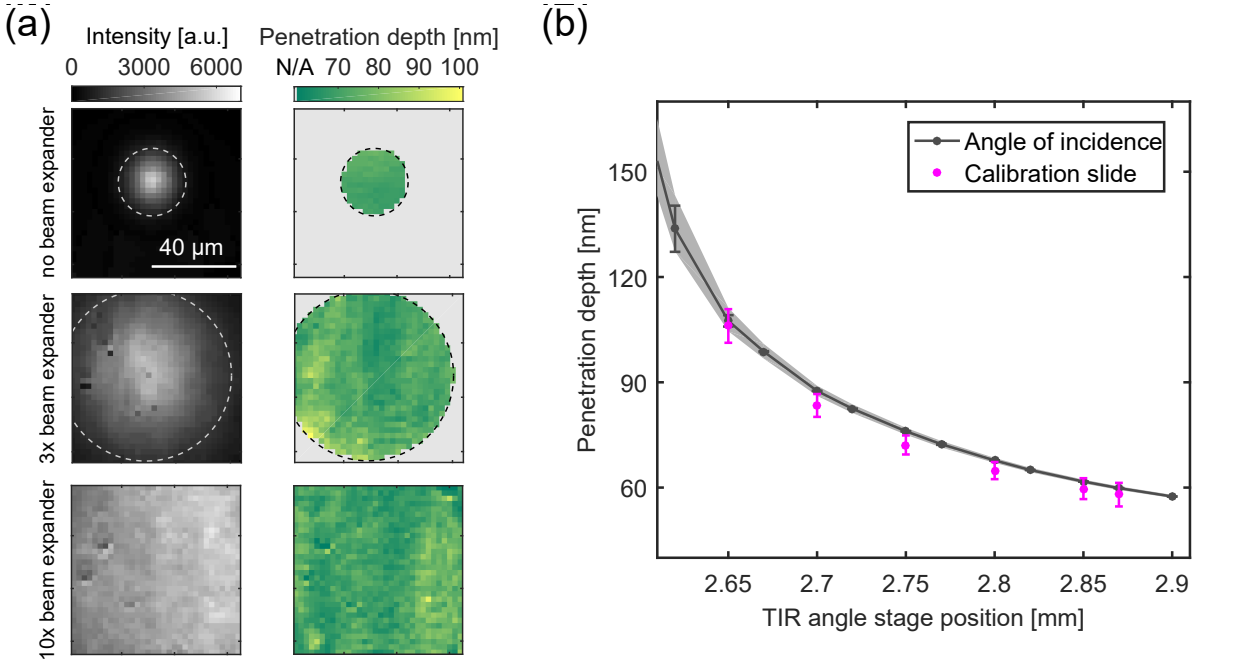

Figure V.5: (a) Illumination profile and evanescent penetration depths for different excitation beam diameters. The fluorescence intensity of free Alexa Fluor 488 for three excitation beam diameters (left column) and the corresponding evanescent penetration depths (right column) as determined with the calibration slide, are shown for a TIR angle stage position of 2.8 mm (corresponding to an incident angle of the excitation laser beam of 71.71°, as measured with the lateral displacement method). Penetration depths were evaluated in the area defined by the $1/e^2$ beam diameter (determined by a 2D Gaussian fit to the lateral illumination profile) with the exterior data assigned as not applicable (N/A) due to the low signal-to-background ratio. Upper row: no beam expander, $d_{\mathrm{ev,1x}} = 64.8\,\mathrm{nm} \pm 2.6\,\mathrm{nm}$, mid row: 3-fold beam expander $d_{\mathrm{ev,3x}} = 66.7\,\mathrm{nm} \pm 6.9\,\mathrm{nm}$, lower row: 10-fold beam expander $d_{\mathrm{ev,10x}} = 64.9\,\mathrm{nm} \pm 6.0\,\mathrm{nm}$. Binning: 32×32 pixels ($5.12\,\mu\mathrm{m} \times 5.12\,\mu\mathrm{m}$). (b) Penetration depths of the evanescent field for a range of TIR angle stage positions, corresponding to different incident angles. Data are given as the mean and standard deviation within the microscope's field of view, obtained in a single calibration run. Theoretically expected penetration depths, calculated based on incident angle data using Equation V.3b, show close agreement with directly measured values using the calibration slide. Data are given as the mean and standard deviation of three independent lateral displacement measurements (see Appendix C.4, p. 284) with the shaded area indicating an uncertainty of refractive index values of $\Delta n = 0.0015$. Both datasets were acquired without a beam expander.

2009, Jung et al., 2016, Liu et al., 2009, Sarkar et al., 2004, Seol and Neuman, 2018, Tutkus et al., 2017], in particular when combined with incident angle scanning [Boulanger et al., 2014, Olveczky et al., 1997, Cardoso Dos Santos et al., 2016, Cardoso Dos Santos et al., 2014, Fu et al., 2016], will benefit from a fast and precise single-slide calibration tool.

Moreover, the precise knowledge of the axial excitation profile offers access to the description of 3D diffusion kinetics in total internal reflection-fluorescence correlation spectroscopy (TIR-FCS) [Thompson et al., 1981].

Apart from the applications in TIRF microscopy, the calibration slide may also assist 3D single-molecule localization microscopy, where the axial localization typically relies on an initial calibration of the point spread function, using immobilized fluorescent beads [Huang et al., 2008, Pavani et al., 2009, Juette et al., 2008]. However, the point spread function of an emitter adhering to the coverslide surface is different from the point spread function of a source deeper in solution [Deng and Shaevitz, 2009, Backer and Moerner, 2014, Hell et al., 1993]. This potential error, which otherwise needs to be treated with advanced aberration corrections [Deng and Shaevitz, 2009, Izeddin et al., 2012, Bratton and Shaevitz, 2015, Shechtman et al., 2015], is circumvented by simply imaging immobilized emitters on the individual polymer step layers of the presented calibration slide. Necessary higher step sizes or a larger total height range are simply achieved by using a more concentrated polymer dip coating solution.

Taken together, we believe that the described tool will be of great help for all researchers frequently requiring simple and low-cost solutions for optical quality control and axial calibration in TIRF and single-molecule localization microscopy.

VI

QUANTIFICATION OF MEMBRANE BINDING KINETICS *VIA* SI-FCS

VI.1 The Need for A New Assay to Study Transient Membrane Binding and Partitioning

Compartmentalization is a prerequisite for the function of cells as fundamental building blocks of life. For all known life forms a membrane separates the inside from the outside of cells [Stillwell, 2016]. A plethora of fundamental processes of life are essentially membrane-related processes, including cell motility, cell signaling, endocytosis, exocytosis and in particular cytokinesis [Alberts, 2002]. Membranes are highly versatile, not only in their heterogeneous composition, but also in their interaction with the surrounding medium [Lemmon, 2008, Lingwood and Simons, 2010, Carquin et al., 2016]. The interaction with the surrounding highlights the importance to precisely quantify binding kinetics of molecules to membranes. One prominent example are Rab GTPases that are essential for membrane trafficing and mark membranes by transient attachment [Stenmark, 2009, Zerial and McBride, 2001]. Moreover, intracellular reaction diffusion mechanisms lagerly rely on transient membrane attachment, such as the bacterial MinDE model system [Loose et al., 2008, Loose et al., 2011, Halatek and Frey, 2018]. Dynamic protein filaments are based on peripheral membrane proteins that are monomeric in solution and self-organize on the membrane as a reaction matrix [Loose and Mitchison, 2013, Ramirez-Diaz et al., 2018]. The highly dynamic nature of membrane-related processes highlights that transient binding phenomena are of a great importance in this context. Thus it is highly relevant to study the rates of reversible membrane interaction in multi-component systems.

The current state-of-the-art methods to study membrane binding can be differentiated according to two fundamental key characteristics: (i) molecular specific compared to non-specific methods and (ii) bulk compared to single-molecule-based approaches.

Non-specific methods generally have the remarkable benefit of studying the system of interest without modification, e.g. without the attachment of labels. However, label-free approaches conventionally require the system to be simplified to only a few components, so that the readout can be interpreted as originating from a well-defined set of molecules.

Molecular specific methods can either be based on the intrinsic distinction of molecule species, or on specific tags to mark selected molecules. Moreover, specific labels, most importantly fluorescent tags, enable the investigation of sets of molecules in crowded and complex environments, inaccessible to most label-free approaches.

Binding and unbinding are stochastic events and as such a high number of events has to be observed for accurate characterization of the binding kinetics. Observing them in bulk has the advantage of fast readouts with intrinsic averaging over a large number of molecules. Therefore bulk experiments are usually less complex, require less expansive experience and are thus faster in execution. In contrast, single-molecule based approaches often require longer acquisition times and more sophisticated analysis of the obtained results. Importantly, single-molecule based approaches offer additional information, in particular about sub-populations frequently lost in bulk experiments. To overcome the often poor statistics in single-molecule observations, automation of high-throughput approaches employing multiplexing is a promising route to make single-molecule experiments statistically robust and easy to perform.

Although binding experiments *in vivo* are of major interest, the implementation of such experiments is challenging for several reasons. As molecules of interest need to be distinguished from the cellular background, many *in vivo* studies use fluorescent labels. However, the photophysical properties of *in vivo*-compatible fluorophores are limited, in particular restraining single-molecule experiments. The observation and distinction of membrane-bound and freely diffusing states is non-trivial and is often based on changes in diffusion properties upon binding. Finally, the reproducibility of experiments is strongly reduced with increasing complexity of the system.

As an important step towards a generally applicable method, we are therefore seeking to develop a reliable *in vitro* quantification method for membrane binding and the partitioning of biomolecules to membranes, with the prospect of it being in principle extendable to complex bio-fluids and potentially even live-cell applications.

VI.1.1 Overview of Currently Available Methods to Study Reversible Membrane Binding and Partitioning

The great importance of studying the binding of biomolecules to membranes is clearly reflected in the high number of methods developed in the past decades focusing on different aspects of this phenomenon [Kleinschmidt, 2013]. Likewise, a large number of model membrane systems has been developed to study these interactions *in vitro*, ranging from

individual lipids over micells, SLBs and vesicles (from small to giant) to lipid bilayer nanodiscs [Liu and Fletcher, 2009, Lagny and Bassereau, 2015, Kleinschmidt, 2013].

An extensive overview of the wide field of membrane binding methods would exceed the scope of this thesis. To list only a few prominent examples: (i) the structure of protein-lipid complexes has been studied by atomic force microscopy (AFM) [Engel and Gaub, 2008, Sapra, 2013], electron microscopy (EM) [Garewal et al., 2013] and neutron scattering experiments [Clifton et al., 2013]; (ii) the secondary structure of membrane-bound proteins and lipids has been examined with infrared spectroscopic methods [Shai, 2013, Tatulian, 2013] and by circular dichroism spectroscopy [Miles and Wallace, 2016, Wallace et al., 2003], even along with synchrotron radiation [Wallace and Janes, 2001]; (iii) nuclear magnetic resonance (NMR) has been vital for the determination of high resolution structures and protein dynamics [Aisenbrey et al., 2013]; (iv) structures have been determined with X-ray crystallography [Moraes et al., 2014]; and (v) the location of fluorescent amino acids has been examined by fluorescence quenching [Loura et al., 2003].

While these methodologies contribute valuable information they do usually not quantify binding kinetics of transiently binding peptides, proteins or ligands to membranes or membrane-attached binding sites. Hence, in the following section we will focus on the methods that can obtain such information and wherever possible compare them with SI-FCS highlighting similarities and complementary features.

VI.1.1.1 Label-free Techniques

Label-free techniques are frequently employed to obtain core binding parameters, like the free energy, binding enthalpy or entropy of the membrane binding reaction [Kleinschmidt, 2013].

Label-free Bulk Assays Isothermal titration calorimetry (ITC) [Velazquez-Campoy and Freire, 2006, Freyer and Lewis, 2008, Ghai et al., 2012, Swamy and Sankhala, 2013, Velazquez-Campoy et al., 2015] and differential scanning calorimetry (DSC) [McElhaney, 1982, Bunge et al., 2009, Cañadas and Casals, 2013], on the one hand, are solution-based and on the other hand, can be employed to study ligand interactions only with lipid vesicles or micells. DSC, however, is limited to the interaction of the molecules of interest with the lipids around the lipid phase transition. Both, ITC and DSC measure the enthalpy of the binding process, allowing the calculation of the equilibrium binding constant K, provided the reaction scheme is known. Furthermore, both methods are significantly limited in

their time resolution for monitoring binding kinetics, as they rely on a thermal readout of a macroscopic sample [Kleinschmidt, 2013].

SPR and QCM-D Surface plasmon resonance (SPR) [Kooyman et al., 2008, Nguyen et al., 2015, Singh, 2016], quartz crystal microbalance (QCM) [Sauerbrey, 1959, Janshoff et al., 2000, Dixon, 2008] are surface-based techniques and are therefore regularly employed to characterize the binding of peptides or proteins to surface-immobilized model membrane systems, like SLBs or surface-tethered lipid vesicles (SPR: [Beseničar et al., 2006, Hodnik and Anderluh, 2013]; QCM: [Cho et al., 2010, Speight and Cooper, 2012, Nielsen and Otzen, 2013]). Based on their ability to access binding rates, SPR and QCM with parallel monitoring of the dissipative losses (QCM-D) are most similar in the extracted information to SI-FCS among label-free methods.

SPR quantifies the change change in refractive index of the sample upon binding of biomolecules. The resonance angle for the excitation of surface plasmons is highly sensitive to the difference of the refractive index at the interface of the plasmon excitation, i.e. the surface of the SPR chip, usually made from gold. The attachment of molecules is thus monitored over time by the change of the effective refractive index and recorded as response curves with units related to the adsorbed mass (resonance units).

QCM is conceptually similar to SPR, but exploits the mass dependence of the resonance frequency of a piezo crystal to monitor the inert mass attached to the QCM chip, usually made from quartz. Adsorbed biomolecules, however, are not rigid, but maintain viscoelastic properties that can be assessed by QCM-D. Measurements are recorded as response curves of the frequency change and dissipation change.

Both, QCM-D and SPR are conventionally used for flow-based bulk measurements. The flow-based approach allows the determination of binding affinities through response curves to concentration jumps at the price of high required sample volumes, potentially exceeding hundreds of microliters [GE Healthcare Bio-Sciences, 2018]. Under certain conditions, binding rates can be extracted from the shape of the response curves. The time-resolution achievable in flow-based assays is often restricted due to the limited flow rates. Moreover, the onset of the concentration change is difficult to determine precisely. After years of engineering, the time resolution of flow-based assays is barely decreasing to the sub-second regime [GE Healthcare Bio-Sciences, 2018, Lausted et al., 2009, Campbell and Kim, 2007]. Additionally, measuring under flow is intrinsically a perturbation leading to a measurement out of equilibrium and interactions are potentially influenced by shear forces or the flow

speed at the surface.

Bio-layer interferometry (BLI) detects changes in the optical thickness of a layer of molecules adhered to a sensor surface by monitoring the shift in the wavelengths interfering constructively or destructively [Wallner et al., 2013, Frenzel and Willbold, 2014]. Thus, the principle of BLI is similar to SPR, except that the sensor is conventionally the functionalized tip of an optical fiber, which is dipped into the sample.

Bulk assays are generally less sensitive in the determination of multiple bound states and sub-populations [Walter et al., 2008]. Moreover, they react to any change made to the sample and require precisely matched buffers and control conditions. Nonetheless, the combination of label-free bulk assays often offers the fastest way for initial quantification of previously uncharacterized samples and the screening of many conditions, as no modified samples need to be produced. Moreover, the analysis of response curves usually does not require extensive post-processing. The availability of commercial instrumentation and specialized chips for membrane studies has fostered the wide spread of both techniques.

VI.1.1.2 Fluorescence-based Bulk Methods

Bulk methods using fluorescence as a readout are powerful in gaining easy access to binding affinities or parition coefficients [Loura et al., 2003, Santos et al., 2003]. In particular, fluorescence spectroscopy and photometry do not only allow the quantification of bound fractions, but also alterations in the fluorescence spectra, quantum yield or fluorescence lifetime can potentially be linked to environments and thus report on structural details [Loura et al., 2003, Matos et al., 2010, Valeur and Berberan-Santos, 2012]. Binding kinetics can be similarly extracted from time-resolved assessments.

The fluorescent amino acids tryptophan (Trp) and tryosine (Tyr) allow some spectroscopic studies to be performed label-free. If the molecule of interest does not contain Trp or Tyr, it can be artificially inserted or the molecule can be tagged by linking it to a fluorophore. The addition of labels, however, is always a modification that potentially changes the properties or even function of the investigated molecule [Szeto et al., 2004, Swulius and Jensen, 2012]. Thus, comparison with label-free results can be helpful to exclude artifacts induced by the fluorescent label. Alternatively, fluorescent membrane probes can be used to react to binding molecules. Fluorescent reporters can be combined with localized quenchers to evaluate not only the membrane binding or partitioning, but also the degree of penetration [Loura et al., 2003, Matos et al., 2010].

Spectroscopic studies employing two fluorescence dyes and observing the Förster res-

onance energy transfer (FRET) [Förster, 1949, Lakowicz, 2006], are especially powerful to access structural proximities [Roy et al., 2008]. Membrane binding can therefore be monitored by a FRET pair located at the membrane and the molceule of interest, respectively [Loura et al., 2003]. Additionally, FRET can be used to reduce the background from unbound molecules in localization-based approaches, such as single particle tracking (SPT) [Auer et al., 2017].

Binding to the membrane, which in TIRF microscopy is oriented perpendicularly to the optical axis, may orient the fluorescent dye in a preferred orientation in respect to the polarization of the excitation light. In fluorescence anisoptropy measurements, the rotational mobility of the membrane-bound molecule and the fluorescent reporter itself are extracted from the rotation of the fluorescence emission in respect to the polarized excitation [Lakowicz, 2006].

Not only fluorescence photometry and spectrometry, but also fluorescence microscopy can be used to investigate interactions with membranes. The surface selectitivity of TIRF microscopy enables the distinction of the membrane-bound fraction based on the fluorescence. However, binding studies based on the observed intensity require a correction for the fluorescent molecules in solution [Pisarchick and Thompson, 1990, Kalb et al., 1990, Hsieh et al., 1992, Thompson et al., 1997, Sheets et al., 1997]. In time-resolved assays, the fluorescence intensity is monitored after a concentration jump or a bleaching step, thus not only allowing to test for reversible binding, but also to extract binding kinetics [Müller et al., 1993, Hsieh and Thompson, 1995, Thompson et al., 1997, Sheets et al., 1997, Lagerholm et al., 2000].

Similar to fluorescence intensity measurements in TIRF, confocal microscopy can examine the equilibrium partitioning of biomolecules to membranes [Thomas et al., 2015b, Franquelim et al., 2018, Ramm et al., 2018a]. Moreover, Fluorescence recovery after photobleaching (FRAP) can be employed to extract kinetic rates in time-resolved fluorescence microscopy [Thompson et al., 1997, Sprague and McNally, 2005, Im et al., 2013].

In microscale thermophoresis (MST), an infrared laser heats a small sample volume and the change in fluorescence intensity induced by the directed movement of molecules in a temperature gradient is observed [Wienken et al., 2010, Jerabek-Willemsen et al., 2011, Jerabek-Willemsen et al., 2014, Dijkman and Watts, 2015]. MST profits from specificity of the fluorescence detection, the availability of commercial instrumentation and the small required sample volumes. However, weak reversible interactions might show altered binding kinetics depending on the temperature gradient.

VI.1.1.3 Fluorescence-based Single-molecule Methods

In contrast to bulk methods, approaches with single-molecule sensitivity offer a detailed view on the behaviour of individual molecules [Moerner and Fromm, 2003]. However, it is intrinsically difficult to observe small molecules individually at high quantities, with high temporal resolution and over long periods of time. The price to pay for the observation of individual molecules is usually a significantly extended measurement time to achieve the statistical precision of bulk measurements. For single-molecules approaches, the detection relies on bright and stable fluorophores [Ha and Tinnefeld, 2012, Gust et al., 2014]. Among fluorescence-based single-molecule methods particularly FCS [Magde et al., 1972] and SPT [Gelles et al., 1988] are frequently applied to characterize membrane binding. Both methods can be combined with (single-molecule) FRET [Ha et al., 1996, Roy et al., 2008] to increase the sensitivity for the target binding [Ferreon et al., 2009].

Fluorescence Correlation Spectroscopy FCS [Magde et al., 1972] has been used to study the partitioning of molecules to membranes [Rigler et al., 1999, Takakuwa et al., 1999, Posokhov et al., 2008], specific lipids [Rusu et al., 2004] and the binding to membrane-attached receptors [Bacia et al., 2004, Pramanik, 2004], even *in vivo* [Briddon et al., 2004, Ries et al., 2009b] (reviewed e.g. in [Ries and Schwille, 2008, Betaneli and Schwille, 2013, Melo et al., 2014]). FCS can obtain concentrations and diffusion coefficients, which both encode valuable information about the interaction with the membrane [Betaneli and Schwille, 2013].

In confocal FCS, membranes are conventionally introduced in the form of vesicles of micells that can be assumed smaller than the detection volume. The binding of molecules to membranes is thus characterized by two states: bound or unbound. For the binding to lipid versicles, the diffusion coefficient changes due to the increased hydrodynamic radius of the vesicles, compared to the molecules in solution [Rigler et al., 1999, Takakuwa et al., 1999, Ruan et al., 2004, Melo et al., 2014]. For accurate results, the brightness of the vesicles binding multiple fluorescent molecules should be carefully considered [Melo et al., 2011]. More recently, the same principle was applied for the binding to lipid bilayer nanodiscs [Nath et al., 2010, Hernández-Rocamora et al., 2012, Ly et al., 2014].

Moreover, if an extended membrane, e.g. the plasma membrane, can be considered static within the detection volume, free and bound molecules can be distinguished by the diffusion coefficient of membrane-bound molecules being drastically slower than in solution [Briddon et al., 2004]. In dual-color cross-correlation spectroscopy [Schwille et al.,

1997, Bacia and Schwille, 2007], the co-diffusion of two labeled species is apparent in the amplitude of the cross-correlation and thus allows to confirm membrane binding [Larson et al., 2005]. Emphasizing the effect on the membrane, FCS detects changes in the lipid mobility upon protein binding [Forstner et al., 2006]. Following the relaxation to equilibrium, subsequent to a perturbation, association and dissociation rates can be extracted from a series of FCS measurements [Rigler et al., 1999]. However, the individual measurement time needs to be short compared to the relaxation time to ensure a quasi-equilibrium required for FCS. Recent developments enhance the sensitivity of FCS measurements by plasmonic nanostructures [Wu et al., 2012] and calibration-free dual-color dual-focus instrumentation [Dörlich et al., 2015].

Image Correlation Spectroscopy ICS methods are based on the correlations of fluorescence intensity fluctuations and thus closely related to FCS [Petersen et al., 1993, Wiseman, 2013]. ICS operates on time-series of images and correlates intensity fluctuations not only in time, but also in space. Conceptually similar, the spatial domain can be introduced to FCS by calculating the cross-correlations for multiple positions, e.g. in TIR-FCS [Kannan et al., 2007, Sankaran et al., 2009]. An elegant adaptation of ICS correlates the fluctuations in fourier-space, resulting in simplified solutions of the involved coupled differential equations in kICS [Kolin et al., 2006b, Brandão et al., 2014]. Brandão and colleagues [Brandão et al., 2014] used kICS to quantify the binding rates of membrane-diffusing receptors to membrane protein complexes from the decrease of the diffusion coefficient. Further, they examined the reversible attachment of ligands to microtubules based on the intensity fluctuation of the ligands residing within the TIRF excitation during binding. They assumed solution diffusion of ligands within the detection volume not to contribute to the correlation function on the acquired time scale, as we did in Chapter III. For the case of ligand-receptor binding, the presented implementation of kICS is thus closely related to SI-FCS as presented above.

Single-Particle Tracking Following the first spatial detection of individual fluorescent molecules [Betzig and Chichester, 1993, Nie et al., 1994, Xie, 1996] (reviewed in [Ambrose et al., 1999, Moerner, 2007]) it became possible to follow biomolecules in space and time with SPT [Gelles et al., 1988, Funatsu et al., 1995, Schmidt et al., 1996]. Conceptually, SPT is intriguing for binding studies, as observed association and dissociation events can be directly related to the rates of the binding process. With highly sensitive EMCCD cameras and bright and stable synthetic fluorophores, individual molecules can be localized

with nanometer precision [Pertsinidis et al., 2010] and followed in space and time [Schmidt et al., 1996]. Live cell applications mostly relied on fluorescent proteins [Mashanov et al., 2004, Matsuoka et al., 2006, Vazquez et al., 2006]. As camera speeds are limited, most investigations focus on membrane diffusion that is conventionally orders of magnitude slower than solution diffusion. The extraction of the mobility of membrane molecules is reviewed elsewhere [Saxton and Jacobson, 1997, Manzo and Garcia-Parajo, 2015]. Here, we focus on SPT extracting parameters for reversible binding processes. Molecules in solution are usually fast enough to only appear as a blur on the camera so that only membrane-bound molecules are detected. Reversibly binding molecules impose an additional challenge in SPT, as in every frame a decision has to be made, if a particle appeared in a certain position from binding or diffusion. Similarly, disappearing molecules can be assigned to unbinding, diffusion or photo-bleaching events. The observation of transiently binding molecules is thus drastically simplified if bound molecules show no surface diffusion and thus need to be tracked only in time, but not in space [Funatsu et al., 1995]. Sub-resolution localization and the assignment of individual molecules to tracks can then be replaced by simple identification algorithms [Fox et al., 2009]. Most commonly, dissociation rates are extracted from fitting a binding model to experimentally obtained residence time histograms. For multiple components cumulative histograms are preferable [Walder et al., 2012].

Using SPT, the apparent association and dissociation rates of proteins or peptides containing pleckstrin homology (PH) domains have been studied binding to phosphoinositol lipids in live cells [Mashanov et al., 2004, Matsuoka et al., 2006]. Similarly, SPT helped to characterize the residence time for the binding of a tumor suppressor (PTEN) [Vazquez et al., 2006] the interfacial epsin N-terminal homology (ENTH) domain [Rozovsky et al., 2012] to phosphoinositol lipids. A combination of SPT and FRET elucidated the binding of ligands to the SNARE complex that is involved in vesicle fusion [Bowen et al., 2005,Li et al., 2007]. More complex binding kinetics of amphipathic helices were studied for the binding of the glucagon-like peptide-1 (GLP-1) to gel-phase Dipalmitoyl-phosphatidylcholine (DPPC) bilayers [Fox et al., 2009] in combination with a three-state binding model [Myers et al., 2012] (see also Section VI.3.2, p. 162). Based on sufficient observed binding events, SPT is furthermore able to identify rare events, hidden to methods employing intrinsic averaging [Knight and Falke, 2009, Walder et al., 2012]. Considerable effort is required to extend the time resolution in SPT to hours, even for surface-immobilized binding events [Elenko et al., 2010].

VI.1.2 Accessing Membrane Binding Rates with SI-FCS

VI.1.2.1 Starting from SI-FCS of Surface-immobilized Binding Sites and Single-particle Tracking

We successfully developed SI-FCS as a method to study the reversible surface-binding of fluorescently labeled molecules. Chapters III and IV describe SI-FCS as a promising tool to study the binding of ligands to surface-immobilized receptors. However, there is no principal limitation of SI-FCS to surface-immobilized binding sites. Rather, the generic concept of SI-FCS can potentially be applied to a plethora of transient surface-associations. Here, we systematically extend this concept to the binding of molecules to fluid lipid membranes.

For the quantification of surface-immobilized binding, we compared SI-FCS to the kinetic analysis capabilities of localization microscopy and in particular DNA-PAINT (Chapter III, [Mücksch et al., 2018]). SI-FCS is able to extract kinetic paramters not only in the regime where individual molecules can be localized, but also at surface concentrations and ligand concentrations orders of magnitude above the threshold for single-emitter localization (Figures III.9, III.10 and IV.10 on pp. 51, 52 and 85, respectively). Therefore, SI-FCS is able to access a broader range of conditions at the price of not accessing binding times and therefore binding rates directly. Rather, the decay time τ_c of the binding reaction depends on both, association and dissociation rate simultaneously (Equation III.1, p. 31).

Utilizing the concept of localization in microscopy [Gelles et al., 1988], SPT has been successfully applied to study membrane binding in different model membrane systems [Bowen et al., 2005, Li et al., 2007, Knight and Falke, 2009, Fox et al., 2009, Loose et al., 2011, Rozovsky et al., 2012]. Moreover, SPT has been used to characterize binding to membranes in live cells [Mashanov et al., 2004,Matsuoka et al., 2006,Mashanov and Molloy, 2007] (see also Section VI.1.1.3). The applicability of SPT to live cells highlights the potential for SI-FCS, as a related technique, to be similarly applicable to complex samples. For binding studies on membranes with SPT two principal approaches have been found:

First, binding to membrane has been studied in systems that effectively limit membrane diffusion and are thus methodologically equivalent to surface-immobilized binding sites [Fox et al., 2009, Nath et al., 2010]. In the special case of gel-phase lipid bilayers, the lateral diffusion coefficient is decreased below $0.01\,\mu m^2/s$, rendering particles effectively immobile [Benda et al., 2003, Scomparin et al., 2009, Fox et al., 2009]. As diffusion can be neglected, the quantification can be performed similar to the SI-FCS-based and

localization-based concepts described above [Fox et al., 2009, Myers et al., 2012] (Chapter III). Gel-phase membranes, however, are only one specific model-membrane system with limited applicability, as living organisms depend on fluid membranes.

Second, molecules were not only tracked in time, but additionally in space. The clear advantage is the applicability to the majority of membrane systems showing diffusion on fluid bilayers. However, lateral diffusion adds a significant motion blur to the fluorescence signal of bound particles [Liu et al., 2015]. The accurate tracking of moving molecules requires a very low density of molecules, such that localizations from adjacent frames can be assigned to one track unambigously. In practice, the analysis of SPT trajectories often requires threshold and filter settings set by the experimenter, leading to a potential bias of obtained results. Most importantly, this includes the decision to either assign a localized particles to a track of a nearby localization in previous frame or alternatively to interprete the localization event as an association event resulting in the creation of a new track. This decision is challenging in detail and leads to a bias not existing in SI-FCS. With increasing velocity of diffusing particles in SPT, the density of simultaneously bound molecules has to be further lowered to minimize errors in the track assignment. The lateral diffusion coefficient depends strongly on the employed model membrane system (reviewed in [Machán and Hof, 2010]) and can reach more than $10\,\mu m^2/s$ in lipid bilayers [Weiß et al., 2013, Ries et al., 2009a], or even up to $100\,\mu m^2/s$ in lipid monolayers [Khmelinskaia et al., 2018]. On SLBs, diffusion coefficients range, depending on temperature and lipid composition, from 0.3 to $5\,\mu m^2/s$ [Bag et al., 2014, Przybylo et al., 2006]. Cushioned lipid membranes [Spinke et al., 1992, Wagner and Tamm, 2000, Knoll et al., 2009], can be functionalized and modified to resemble the physiological conditions within the extracellular matrix [Tanaka and Sackmann, 2005]. As the thickness of the employed cushions often does not exceed the dimensions of the evanescent field in TIRF microscopy, they are principally well-suited to be combined with SPT or SI-FCS. Diffusion coefficients vary depending on the specific cushion and lipid composition but are generally in the same range as for solid-supported SLB [Deverall et al., 2008, Renner et al., 2008, Machán and Hof, 2010]. The resulting motion blur from lateral diffusion reduces the signal-to-noise ratio (SNR) of the localizations. While for surface-immobilized binding sites a simple binary information encodes the bound state of the molecule, in presence of lateral diffusion a precise localization demanding a higher SNR is conventionally required. Thus, the motion blur limits SPT on fluid membranes to fast acquisition rates accompanied by high excitation irradiances.

In practice, SPT suffers from limitations due to the photophysical properties of the

fluorescent dyes. Long residence times and fast diffusion dynamics are best observed at different ends of the achievable time resolutions of the camera acquisition. Fast tracking on the millisecond time-scale is often incompatible with the long-term observation covering the entire residence of particles on the time-scale of multiple minutes. The motion blur of laterally diffusing, bound molecules further increases the necessary time resolution, usually coinciding with higher irradiances. If molecules need to be localized more frequently, a sufficient localization precision is conventionally reached by an increase in irradiance, leading to a maintained number of detected photons per frame.

Significant progress was made recently in lowering the minimal photon budget required for precise SPT in live cells with a super-resolution technique termed MINFLUX, which, however, is only able to observe one particle at a time [Balzarotti et al., 2017]. This limitation and the high technical demands render routine measurements of binding dynamics with MINFLUX currently unfeasible. Nonetheless, remarkable efforts are being made in the development of more stable fluorophores and non-bleaching fluorescent particles [Jin et al., 2018, van der Velde et al., 2016, Zheng et al., 2014b, Altman et al., 2011]. In contrast to methodological improvements in SPT, improvements in fluorescent tags potentially benefit SI-FCS alike. Long-term acquisition, observation of a large number of molecules and high time resolution so far remain difficult to achieve in SPT.

In comparison to SPT, FCS does not require the identification of individual particles to explore the single-molecule based binding kinetics. The intensity fluctuation originating from the movement or the fluorescent state of molecules is sufficient to calculate the autocorrelation curve, without the need to infer particle positions within the detection volume. The irradiances required for FCS are therefore by orders of magnitude lower compared to irradiances required to track particles in SPT. Even more importantly, the density of similarly bound molecules can be orders of magnitude higher in SI-FCS compared to SPT (Figures III.9 and III.10, pp. 51ff.).

In summary, there has been a vast interest to quantify transient binding dynamics, paired with the mobility in the membrane upon binding. SPT has proven to be a valuable tool, but so far could not keep up with this demanding challenge. Thus, in this chapter an alternative approach based on SI-FCS is pursued to quantify binding to fluid membranes.

VI.1.2.2 Distinction of Binding to Sparse Membrane-associated Binding Sites and Direct Partitioning of Biomolecules to Membranes

As lateral diffusion is a common feature of membrane-bound molecules, we explored the influence of membrane diffusion on the SI-FCS autocorrelation and developed strategies on how to account for the lateral mobility of bound molecules in SI-FCS experiments. Furthermore, we distinguish between specific binding of molecules to lipid head groups or membrane-bound proteins and the partitioning of molecules to the lipid bilayer as such.

For the stoichiometric binding of ligands to permanently membrane-bound receptors, only lateral diffusion is added as additional complexity to the systems in Chapter III. This binding reaction is sometimes termed membrane binding, but maintains the concept of a set of surface-bound binding sites (Figure VI.1A and B) and follows the reaction scheme

$$A + B \underset{k_d}{\overset{k_a}{\rightleftharpoons}} C \tag{VI.1}$$

Here, we use the terminology of conversion to a bound state C, as frequently found in the FCS literature [Thompson et al., 1981, Starr and Thompson, 2001, Ries et al., 2008a], whereas the notation $A + B \rightleftharpoons AB$ is more common in other fields. When diffusion is treated or eliminated properly, the reaction fully resembles the case discussed in Chapter III. Accordingly, the determination of binding rates can be performed by titrating the ligand concentration, as in the case of surface-immobilized binding sites (Chapter III, Equation III.1; for experimental realization see Section VI.2.3). Although the state B is non-fluorescent and therefore invisible in the individual images, it significantly influences the binding kinetics of A and C [Thompson, 1982, Lieto and Thompson, 2004].

Conceptually different, however, is the determination of binding rates in the case of partitioning of biomolecules to membranes independent of specific receptors or sparse lipid head groups. Amphipatic helices are an abundant example of protein sequences mediating membrane binding due to electrostatic and hydrophobic interaction (Figure VI.1C). This case is less well approximated by a bimolecular binding reaction and is therefore often investigated as a partitioning phenomenon, where the molecules partition into a hydrophilic phase, the solution, and a hydrophobic phase, the bilayer. More precisely, the partitioning into the complex interphase layer of the membrane differs additionally from partitioning in bulk, leading to the development of the interfacial hydrophobicity scale [Wimley and White, 1996, Wimley et al., 1996, White and Wimley, 1998]. While the concepts of the equilibrium binding constant and partition coefficient are interconvertable in some cases [Thomas

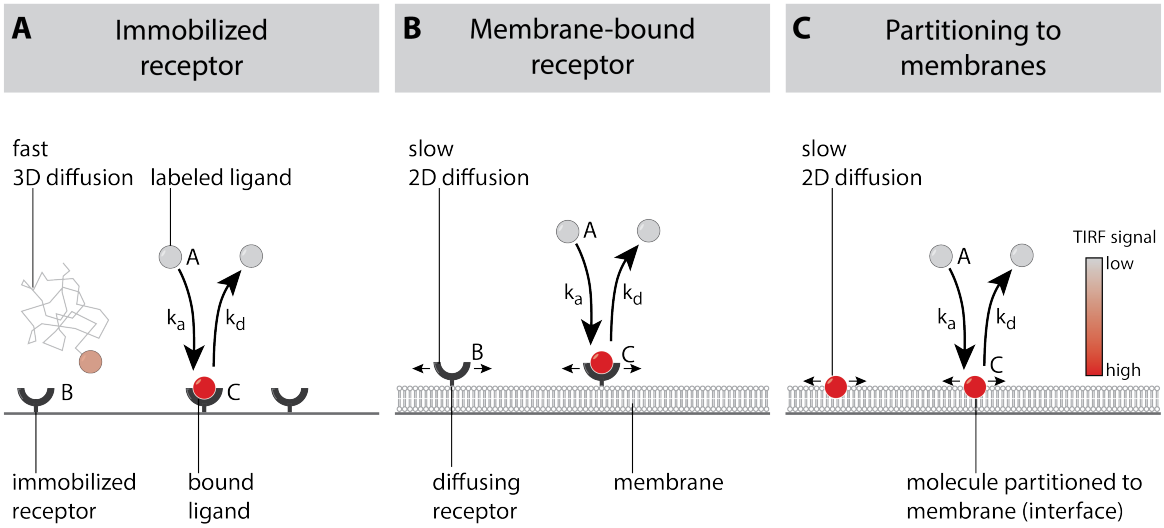

Figure VI.1: Extending the SI-FCS concept from surface-immobilized receptors to membrane binding. In the case of binding of ligands to surface-immobilized receptors **(A)** (see Chapter III), the separation of bound and unbound states is achieved by a separation of time scales on which these dynamics cause fluorescence fluctuations. Fast 3D diffusing ligands in solution and binding occur on different time scales. **(B)** Membrane-bound receptors additionally diffuse laterally, adding additional complexity to the system, but maintaining the reaction scheme $A + B \rightleftharpoons C$. **(C)** For the partitioning of biomolecules to membranes independent of specific receptors or sparse lipid head groups, no distinct binding sites are present, requiring a reaction model of the type $A \rightleftharpoons C$.

et al., 2015a], their compatability is limited in general [Cevc, 2015]. In contrast to bulk partitioning, the reversible association of biomolecules to the interface layer of membrane and solution is generally a surface-association with the molecule in constant contact with both phases and thus a straightforward definition of association and dissociation rate.

Therefore, this reaction can be described formally as a transition of the molecule from a unbound (solution) state A to a surface-attached state C

$$A \underset{k_d}{\overset{k_a}{\rightleftharpoons}} C\,, \tag{VI.2}$$

without the unoccupied state of surface binding sites B. Equation VI.2 assumes that the rates for association are constant and therefore neglects any saturation of the state C on the membrane. A surface saturation lowers the probability of conversion from state A to C, thus inducing a concentration dependence of k_a in this model. Far from saturation, one can either regard the membrane as one extended binding site that can bind multiple molecules or regard the membrane as a dense array of practically unlimited binding sites. Consequently, the binding does in this case not depend on the concentrations of A or C. Practically, this eliminates the influence of the average solution concentration $\langle A \rangle$ on the decay time τ_c of the autocorrelation function, as long as saturation is not reached. In return, at membrane-bound concentrations close to saturation, lateral interactions of the bound molecules have to be considered and the always assumed independence of binding sites has to be re-evaluated. Interactions of the bound molecules with the bilayer were shown to alter the bilayer at high concentrations [Hsieh et al., 2010, Shih et al., 2011, Melo et al., 2009, Brogden, 2005, Cornell and Taneva, 2006, Khandelia et al., 2008], enhancing the complexity of membrane-binding in this concentration regime. Above all, the question has to be considered carefully, if the behavior of the molecule of interest close to saturation is of physiological relevance. In conclusion, we explore an alternative approach to obtain association and dissociation kinetics without the need to saturate the membrane (Section VI.3, pp. 155ff.). First, however, we address the binding to specific binding sites on the membrane, similar to membrane-bound receptors or the specific binding of protein binding domains to sparse lipid head groups.

VI.1.2.3 Effect of Lateral Membrane Diffusion on the SI-FCS Autocorrelation Function

Lateral diffusion is common to both cases, the binding to membrane-bound receptors or specific lipid head groups and the partitioning of molecules directly to the membrane. Hence, we first focus on the appropriate treatment of the effects of lateral diffusion on the autocorrelation curves. SI-FCS distinguishes bound and unbound particles based on the intensity fluctuation resulting from the signal increase upon binding. Particles diffusing in solution into the detection volume correlate similarly, but on different time-scales and can therefore often be neglected in practice (Chapter III). For slowly diffusing molecules in solution or fast binding kinetics, resulting in strongly overlapping contributions to the autocorrelation function, the separation of times-scales has to be re-evaluated as discussed above (Section V.1).

Observing molecules diffusing laterally on the membrane adds an additional contribution to the autocorrelation function. Molcules diffusing in or out of the detection volume induce intensity fluctuations indistinguishable in the intensity trace from binding and unbinding events (Figure VI.2). Membrane diffusion on SLBs is by orders of magnitude slower than solution diffusion of small molecules [Weidemann et al., 2014,Bag et al., 2012,Przybylo et al., 2006]. Depending on the particular system and especially the dimension of the detection volume, membrane diffusion can principally add contributions to the autocorrelation function on the time scale of solution diffusion or the binding kinetics, respectively [Ries et al., 2008a]. In SI-FCS, the lateral detection size is large compared to the recording of FCS traces with diffraction limited confocal pinholes. Thus, we focus on the differentiation of binding dynamics and lateral membrane diffusion. For simplicity, we continue to assume the contribution from solution to be fully equilibrated on the time scale of the binding reaction.

The characteristic time for two-dimensional diffusion τ_{2D} through a rectangular integrated surface area with the side length a, can be estimated as [Bag et al., 2012, Wawrezinieck et al., 2005]:

$$\tau_{2D} = \frac{a^2}{D_C}\,, \tag{VI.3}$$

with D_C denoting the lateral diffusion coefficient of membrane bound molecules C.

Binding events can only be sampled in high numbers if the diffusion time is at least on the order of the binding time ($\tau_{2D} \gtrsim \tau_c$). Otherwise diffusion in and out of the surface-integrated area suppress any contributions from binding kinetics to the autocorrelation

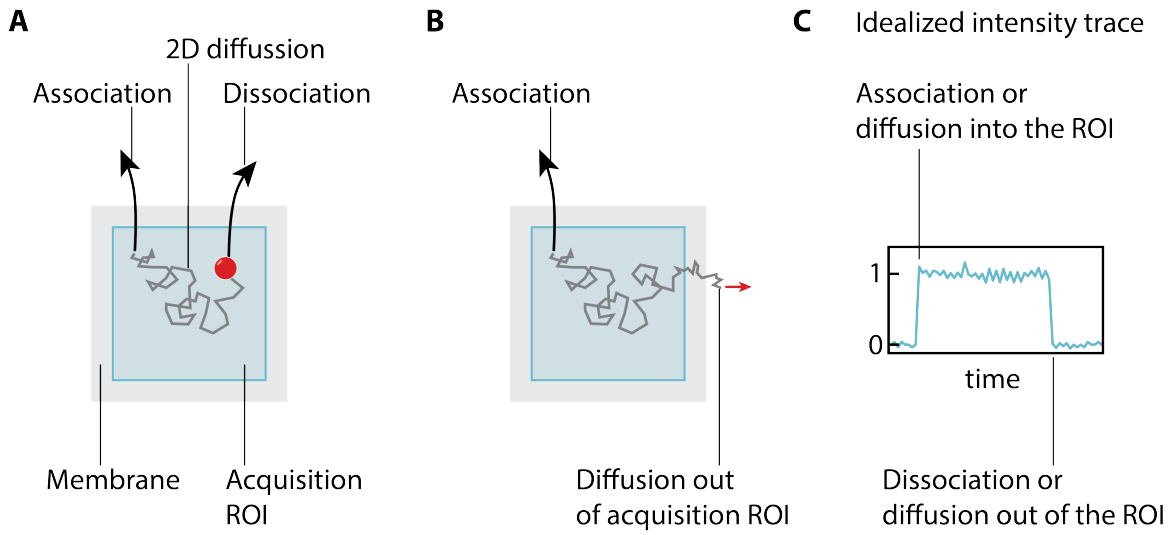

Figure VI.2: Membrane diffusion adds an additional component to the SI-FCS autocorrelation. **(A)** In SI-FCS, the autocorrelation is blind to diffusion of bound molecules on the membrane within the acquisition ROI. Therefore, binding kinetics can be obtained from binding events of molecules that associate, diffuse and dissociate within the integrated region. **(B)** Particles entering or exiting the integrated ROI laterally by diffusion on the membrane add an additional decay to the autocorrelation function. **(C)** Events originating from binding or diffusion appear similarly in the intensity trace and therefore both contribute to the autocorrelation.

function.

VI.1.2.4 Extracting Parameters on Binding to Fluid Lipid Bilayers with SI-FCS

We developed three separate strategies to treat 2D lateral diffusion on the membrane in combination with SI-FCS: (A) the diffusion can be included into the model for the autocorrelation function [Ries et al., 2008a] and different integration areas can be used for calibration-free determination of diffusion coefficients [Bag et al., 2012] (Figure VI.3A); (B) a separation of time scales can be ensured by large integration areas or similarly a small lateral diffusion coefficient (Figure VI.3B); or (C) the diffusion can be confined to an area smaller than the observation area, eliminating intensity fluctuations from diffusion after surface integration (Figure VI.3C).

Ries and colleagues [Ries et al., 2008a] presented a semiempirical three-dimensional solution for the full autocorrelation including binding dynamics, largely based on the pioneering works of Thompson, Starr and colleagues [Thompson et al., 1981,Starr and Thompson, 2001]. The solution is described in detail in Section II.1.3 (p. 12) and therefore only repeated here briefly in essential points.

The autocorrelation has principally contributions from solution diffusion $g_{\mathrm{AA}}(\tau)$, from surface-bound molecules $g_{\mathrm{CC}}(\tau)$ and the cross-terms $g_{\mathrm{AC}}(\tau)$ (Equation II.28, p. 18)

$$G(\tau)\langle F\rangle^2 = \langle A\rangle(g_{\mathrm{AA}}(\tau) + 2g_{\mathrm{AC}}(\tau) + g_{\mathrm{CC}}(\tau))\,, \tag{VI.4}$$

further defined by Equations II.28b-d for the individual correlation contributions. In axial direction, the contributions ultimately depend on the reaction rate R_{r}, the transport rate in solution R_{t} and the transport rate through the evanescent field R_{e} (Equations II.33 to II.35) in a rather complex way (Equations II.36a-c).

The full autocorrelation model depends on at least four independent fitting parameters: (i) the autocorrelation amplitude, (ii) a parameter describing solution diffusion, (iii) a parameter describing membrane diffusion, and (iv) the reaction rate. Depending on the amount of prior knowledge, (v) the axial and lateral bulk diffusion need to be treated separately as the relation of evanescent field penetration depth to the lateral bulk diffusion is commonly not known. The lateral diffusion additionally depends on (vi) the extension of the detection PSF σ (Equation II.21, p. 16).

The number of free fitting parameters has to be further extended in the case of surface

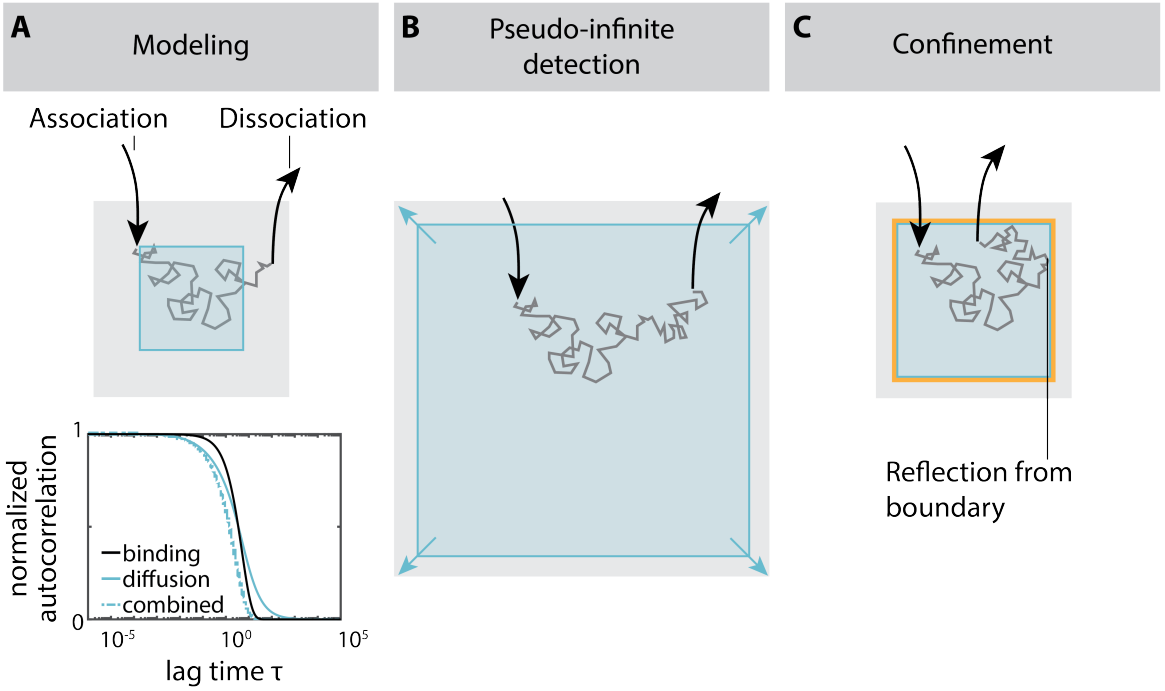

Figure VI.3: Obtaining binding kinetics from the SI-FCS autocorrelation function in presence of lateral membrane diffusion. We found three principal ways of obtaining binding kinetics from the SI-FCS autocorrelation function in presence of lateral diffusion of bound molecules on the membrane. **(A)** Theoretical modeling enables the description of the autocorrelation function consisting of two components describing (i) the binding of molecules to the membrane or membrane-bound receptors and (ii) the diffusion in and out of the acquisition ROI. In particular the diffusion contribution depends on the ROI size and in combination with camera acquisition can be varied in the analysis. **(B)** A separation of time scales can be achieved by increasing the ROI size, so that the diffusion time becomes much larger than the binding time of molecules. **(C)** Confinement of the diffusing molecules allows for arbitrary ROI sizes without the need for theoretical modeling.

binding reactions going beyond the simple monoexponentially distributed residence times or if multiple species are present in the sample. The amplitude of the experimentally obtained autocorrelation function is furthermore lowered by background noise. If the amplitudes of the autocorrelation function are of relevance in addition to the decay times, a background correction will be necessary on most samples to extract accurate parameters from the fit amplitude. Samples with reduced background contribution can potentially be based on a FRET pair consisting of ligand and receptor [Auer et al., 2017]. The high number of free fitting parameters is intrinsically difficult to be extracted simultaneously and robustly from one correlation curve. In the specific case of camera detection, the fitting of faster contributions becomes even more unreliable as the number of data points at short lag times is limited by the frame rate of the camera acquisition. We therefore pursue a significantly simplified initial approach.

Following the concept of Chapter III, we neglect the solution diffusion so that the terms for $g_{\mathrm{AA}}(\tau)$ and the cross-term $g_{\mathrm{AC}}(\tau)$ vanish in the approximation and Equation VI.4 simplifies to

$$G(\tau)\langle F\rangle^2 = \langle A\rangle g_{\mathrm{CC}}(\tau)\,, \tag{VI.5a}$$

$$g_{\mathrm{CC}}(\tau) = g_{\mathrm{CC,z}}(\tau) g_{\mathrm{xy}}(\tau, D_{\mathrm{C}})\,. \tag{VI.5b}$$

Furthermore, we assume that the axial term $g_{\mathrm{CC,z}}(\tau)$ is described by the reaction limited regime, i.e. the reaction rate R_{r} is much smaller than the diffusion rates R_{t} and R_{e} [Starr and Thompson, 2001]. In other words, the solution diffusion is equilibrated on the time scale of the binding reaction, as assumed above (Chapter III). We arrive at a considerably simplified autocorrelation (Equation II.39, p. 21)

$$G(\tau) = \frac{\langle C\rangle \beta^*}{\langle F\rangle^2} \exp\left(-R_{\mathrm{r}}\tau\right) g_{\mathrm{xy}}(\tau, D_{\mathrm{C}})\,. \tag{VI.6}$$

The autocorrelation function g_{xy} for lateral diffusion and square-shaped detection areas was proposed by Ries and colleagues [Ries et al., 2008a], and was experimentally confirmed with camera-based detection [Sankaran et al., 2009, Bag et al., 2012]. The squared integration area in SI-FCS is mathematically identical to a squared pinhole of side length a

(Equation II.26)

$$g_{\mathrm{xy}}(\tau) = \frac{1}{a^2}\left(\frac{1}{\sqrt{\pi}\mu}\left(e^{-\mu^2}-1\right)+\mathrm{erf}(\mu)\right)^2, \tag{VI.7a}$$

$$\mu = \frac{a}{2\sqrt{\sigma^2 + D_{\mathrm{C}}\tau}}. \tag{VI.7b}$$

with the PSF extension σ from Equation II.21 (p. 16)

$$\sigma = \sigma_0 \frac{\lambda}{\mathrm{NA}}, \tag{VI.8}$$

the emission wavelength λ, and the numerical aperture NA [Zhang et al., 2007]. A theoretically derived pre-factor of 0.21 [Zhang et al., 2007] was assumed in the solution of Ries and colleagues [Ries et al., 2008a]. In experiments studying lateral diffusion on SLBs, σ was found to deviate from the theoretically expected value and to be better described by $\sigma_0 = 0.4$ [Bag et al., 2012]. The increase can be partially attributed to the noise levels in EMCCD detection [Michalet et al., 2007]. In best case, σ_0 should therefore be determined from the experimental data in the specific setup [Sankaran et al., 2009, Bag et al., 2012]. For large integration areas, the dependence of the autocorrelation function on σ is decreasing, and autocorrelation curves are well approximated by $\sigma = 0$ ($a \gg \sigma$) [Guo et al., 2008, Sankaran et al., 2009].

As evident from equation VI.7a, the decay time of the autocorrelation function depends not only on the lateral diffusion coefficient D_{C}, but similarly on the side length a of the integrated area. This dependence can be exploited to achieve a calibration-free determination of lateral diffusion coefficients on SLBs [Bag et al., 2012]. For large ROI sizes a considered here, the shape of the PSF resulting in a blur of the pinhole edges becomes negligible and the precise determination of σ is less critical ($a \gg \sigma$). For diffusion studies on membranes, a is conventionally chosen on the order of few camera pixels, in our case 160 nm. As we are interested in sampling binding dynamics, our ROI sizes are on the order of multiple micrometers.

The amplitude of the experimentally obtained autocorrelation depends not only on the signal from membrane diffusion and binding, essentially determined by the number of bound and diffusing molecules, but additionally depends on the average noise contribution

$\langle B_\mathrm{g}\rangle$ and the solution diffusion $\langle F_\mathrm{A}\rangle$ (Equation II.42) [Thompson, 1999]

$$G(\tau) = G_\mathrm{meas}(\tau)\frac{\left(\langle F_\mathrm{A}\rangle + \langle F_\mathrm{C}\rangle + \langle B_\mathrm{g}\rangle\right)^2}{\langle F_\mathrm{C}\rangle^2}\,. \tag{VI.9}$$

For simplicity, we summarize all amplitude contributions to an experimentally observed amplitude G_0 and write the fitting function to the autocorrelation curves as

$$G(\tau) = G_0' \underbrace{\exp\left(-\frac{\tau}{\tau_\mathrm{c}}\right)}_{\text{binding}} \underbrace{\frac{1}{a^2}\left(\frac{1}{\sqrt{\pi}\mu}\left(e^{-\mu^2}-1\right)+\mathrm{erf}(\mu)\right)^2}_{\text{lateral diffusion}} + G_\infty\,, \tag{VI.10a}$$

$$\text{with}\quad \mu = \frac{a}{2\sqrt{\sigma^2 + D_\mathrm{C}\tau}} \tag{VI.10b}$$

Alternatively, Equations VI.10 can be expressed with an amplitude $G_0 = G_0' g_\mathrm{xy}(\tau = 0)$ multiplied with otherwise normalized contributions from binding and lateral diffusion (Equation VI.7):

$$G(\tau) = G_0 \underbrace{\exp\left(-\frac{\tau}{\tau_\mathrm{c}}\right)}_{\text{binding}} \underbrace{\frac{g_\mathrm{xy}(\tau, D_\mathrm{C})}{g_\mathrm{xy}(\tau = 0)}}_{\text{lateral diffusion}} + G_\infty\,. \tag{VI.11}$$

In Equations VI.11 and VI.10, we added the offset G_∞ and used the characteristic decay time τ_c, depending on the association rate k_a and the dissociation rate k_d as

$$\tau_\mathrm{c} = (k_a\langle A\rangle + k_d)^{-1}\,. \tag{VI.12}$$

Further, as our integration sizes are large compared to the PSF, the obtained autocorrelation curves only depend very weakly on σ (Equation VI.8) [Guo et al., 2008, Sankaran et al., 2009] and for convenience, we assume $\sigma_0 = 0.4$ as found in [Bag et al., 2012].

VI.1.2.5 Consequences of the Selected Autocorrelation Model for the Experimental Design

Based on the developed model for the autocorrelation function (Equation VI.11), we are able to address some fundamental consequences and limitations of the approaches introduced above to treat membrane diffusion in SI-FCS (Section VI.1.2.4). As the amplitude of the autocorrelation function scales with the integrated area (Equation VI.7a), changes in the decay time of the combined autocorrelation are best observed for the normalized

autocorrelation function

$$G_N(\tau) = \exp\left(-\frac{\tau}{\tau_\mathrm{c}}\right)\frac{g_\mathrm{xy}(\tau, D_\mathrm{C})}{g_\mathrm{xy}(\tau = 0)}\,, \tag{VI.13}$$

with $g_\mathrm{xy}(\tau)$ from Equation VI.7.

Figure VI.4 illustrates the effect of the ROI side length a on the decay of the autocorrelation function in presence of surface binding. With increasing size of the integrated area, the contribution to the autocorrelation function from lateral diffusion is shifting towards larger lag times (Figure VI.4B, blue to red, Equation VI.7a). The contribution from binding to the normalized autocorrelation function (black solid line) is independent of the integrated area. The combined autocorrelation function describing binding and diffusion kinetics is therefore dominated by diffusion for small integration areas ($\tau_\mathrm{2D} \ll \tau_c$) with no possibility to extract binding dynamics (Figure VI.4C, blue dashed line). For large integration areas ($\tau_\mathrm{2D} \gg \tau_c$), the combined autocorrelation function is dominated by binding and shows practically no observable modulation originating from diffusion (red dashed line). In an intermediate range, the autocorrelation function is affected by both diffusion and binding similarly ($\tau_\mathrm{2D} \approx \tau_c$, purple line). Thus, a model for the autocorrelation incorporating binding and lateral diffusion on the membrane (Figure VI.2A) can only extract reliable binding kinetics when the diffusion time is approaching or exceeding the average binding time ($\tau_\mathrm{2D} \gtrsim \tau_c$). Notably, the tail of the diffusion contribution of the autocorrelation function is decaying over a longer time scale than the monoexponential decay of the binding contribution, if both contributions show equal half-times (Figures VI.3 and III.7, p. 47).

Based on the autocorrelation model (Equation VI.13), it can be estimated which integration area is sufficient to result in an acceptable error, when applying the approach of pseudo-infinite detection (Figure VI.2B). A detailed analysis of the error follows in Section VI.2.2 (Figure VI.7). Practically, the maximally achievable ROI size will be limited by the instrumentation and a decreasing SNR of the autocorrelation curves with increasing ROI size. Thus, the approach to integrate the signal over a pseudo-infinite area (Figure VI.2B) requires prior knowledge of diffusion dynamics and binding kinetics to validate its feasibility in the specific case. The field of view of high numerical aperture (NA) objectives, allowing objective-type TIRF microscopy, limits integration areas on the order of $(250\,\mu\mathrm{m})^2$. Even for such large integration areas, the autocorrelation function shows contributions from membrane diffusion, as the diffusion term decays slower for equal half-times.

Moreover, amplitude of the autocorrelation function is decreasing with increasing inte-

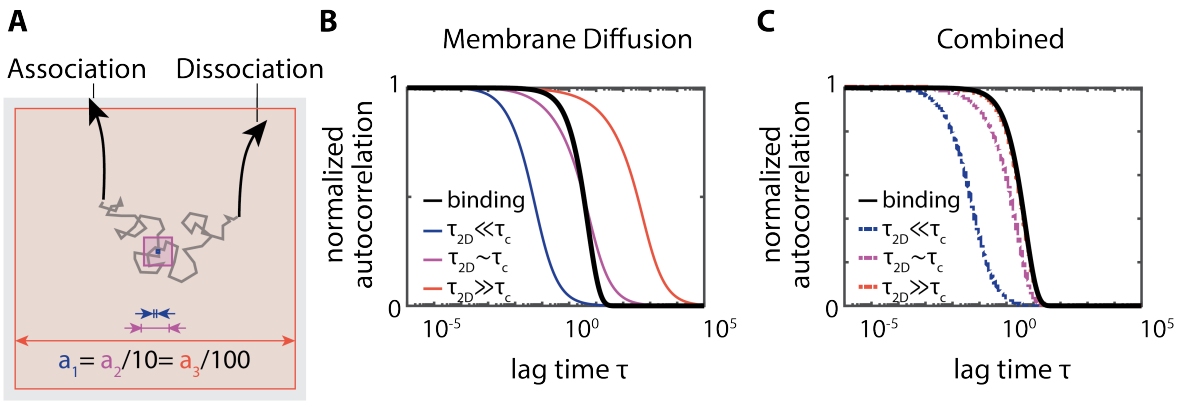

Figure VI.4: Accessibility of the binding kinetics depends on the diffusion decay. (A) The diffusion time τ_{2D} depends on the size a of the acquisition ROI. The larger the ROI, the longer the average time to traverse the ROI by diffusion. **(B)** While the decay of the diffusion contribution to the autocorrelation function shifts in time with the ROI size (blue to red), the decay of the binding term τ_c is independent of the ROI size (black). **(C)** The experimentally obtained autocorrelation depends on the diffusion decay and the binding decay time (Equation VI.11). For small ROIs ($\tau_{2D} \ll \tau_c$), the autocorrelation is dominated by the diffusion decay (blue). If $\tau_{2D} \sim \tau_c$, the shape of the autocorrelation function depends on both, diffusion and binding (purple). For large ROIs ($\tau_{2D} \gg \tau_c$), the binding contribution dominates the autocorrelation function (red). The displayed autocorrelation functions are calculated based on Equation VI.13 (C), with the binding term set to 1 ($\tau_c \to \infty$) for (B). Parameters of the displayed curves are: $\tau_c = 5\,\mathrm{s}$, $D_C = 2\,\mu\mathrm{m}^2/\mathrm{s}$, $a_1 = 1\,\mu\mathrm{m}$, $a_2 = 10\,\mu\mathrm{m}$, $a_3 = 100\,\mu\mathrm{m}$, resulting in $\tau_{2D} = (0.1\tau_c, 10\tau_c, 1000\tau_c)$, respectively and $\sigma = 70\,\mathrm{nm}$.

grated surface area. Therefore, the low amplitude marks an upper limit to practically achievable integration areas and surface concentrations. For smaller integrated areas, molecules entering or exiting the observation volume dominate the autocorrelation function. For larger integrated areas, however, the background signal $\langle B_g \rangle$ is increasing, while the amplitude of the autocorrelation function decreases. Therefore, fluorescent ligands in solution additionally decrease the amplitude of the autocorrelation function, even if their contribution can be treated as uncorrelated background $\langle F_A \rangle$ [Thompson, 1999, Mücksch et al., 2018]. Further, minimal fluctuations in the setup, in particular fluctuations of the excitation laser, any kind of drift or mechanical instabilities can easily induce fluctuations not only in the signal of the fluorescent molecules of interest, but also in the background signal. The smaller the ratio of signal fluctuations to background fluorescence, the more severe is the influence of unwanted fluctuations on the autocorrelation curve. This is different from confocal FCS where the background is usually not larger than the signal of interest. Thus, large integration areas are intrinsically prone to be more sensitive towards instabilities. Decreasing the density of bound molecules to increase the amplitude of the autocorrelation function, similarly changes the ratio of the desired signal to the background signal in an unfavorable way. In practice, the background signal therefore imposes a limitation to the approach of pseudo-infinite detection. If applicable, however, a pseudo-infinite detection offers an otherwise unmatched level of simplicity. Background-reduced samples, based on FRET pairs [Auer et al., 2017] have the potential to significantly improve the SNR of large area SI-FCS autocorrelation curves.

The third approach, the confinement of diffusing molecules within the integration area (Figure VI.2C), combines reasonable correlation amplitudes with the benefit of a simple fitting model, essentially defined only by the binding reaction. The simplicity of the fitting model allows for a robust quantification. However, the obtained binding kinetics are potentially influenced by interactions of bound molecules with the confinement. Prominent examples of confined bilayer structures compatible with TIRF microscopy include (i) bilayers micropatterned with polymers [Spinke et al., 1992, Hovis and Boxer, 2000, Orth et al., 2003, Tanaka and Sackmann, 2005] or biomolecules [Kung et al., 2000, Tanaka et al., 2004], (ii) anorganic structures preventing the formation of bilayers or limiting membrane diffusion [Groves et al., 1997], (iii) surface-immobilized lipid bilayer nanodiscs [Nath et al., 2010], or (iv) patches of membranes [Danelon et al., 2006, Perez et al., 2006, Chiaruttini et al., 2015].

Applying all three approaches in combination, (A) the autocorrelation model function

incorporating lateral diffusion, (B) pseudo-infinite integration areas and (C) confinement of membrane diffusion, offers the potential for validating the obtained results based on different assumptions. We will experimentally verify the three approaches A, B and C in Sections VI.2.1, VI.2.2 and VI.2.3, respectively.

VI.2 Quantifying the Binding to Individual Membrane-attached Binding Sites with SI-FCS

The transient binding of ligands to membrane-bound receptors is of exceptional relevance for cell biology as well as pharmacology [Alberts, 2002, Yıldırım et al., 2007]. As discussed above (Section VI.1.2), lateral diffusion on the membrane significantly increases the complexity of the system. Based on our investigations of DNA hybridization on surface-immobilized origami nanostructures (Chapter III), we established a simple proof-of-concept system with well-characterized binding kinetics, mimicking the situation found for the binding to sparse membrane binding sites (Section VI.1.2.2 and Figure VI.1B).

With this implementation, we increase the complexity stepwise by introducing lateral diffusion of membrane-bound receptors (Figure VI.1A and B), but not yet to the level of the direct partitioning of biomolecules to membranes (Figure VI.1C). Experimentally, we realized this by employing the same hybridizing DNA sequences (9 nt) as in Chapter III and IV, but with the docking strands bound to cholesterol at the 5'-end (chol-DNA), instead of immobilizing them on DNA origami nanostructures. Cholesterol is a lipophilic molecule and constituent of many natural membranes and partitions into lipid bilayers with a free energy of approximately $23 k_B T$ [Kessel et al., 2001]. DNA oligonucleotides, modified with a tetraethylene glycol (TEG)-linked cholesterol serve as mobile DNA handles on membranes, as described and intensively characterzied previously [Pfeiffer and Höök, 2004, Czogalla et al., 2016]. Chol-DNA molecules were found to bind to membranes without altering the membrane structure [Bunge et al., 2009], to diffuse on the lipid bilayer and to hybridize with complementary strands from solution [Bunge et al., 2007, Banchelli et al., 2008, Banchelli et al., 2010]. At low surface concentrations, chol-DNA was found to be monomeric and is thus likely to show similar hybridization kinetics as free DNA [Banchelli et al., 2008, Banchelli et al., 2010, Gambinossi et al., 2010]. Moreover, such mobile DNA handles have been applied in DNA nanotechnology to obtain DNA nanostructures capable of interacting with lipid membranes [Czogalla et al., 2013, Langecker et al., 2014, Khmelinskaia et al., 2016, Franquelim et al., 2018]. Hence, an improved quantification of DNA hybridization will also support the engineering of complex reversible binding mechanisms.

Membrane-bound receptors are frequently found in cells in the form of integral membrane proteins. However, incorporated into SLBs on solid supports, they have been found to show altered behavior compared to their native state, in particular immobilization based upon interactions with the support [Merkel et al., 1989, Przybylo et al., 2006, Scomparin

et al., 2009]. In contrast, chol-DNA sticks out of the membrane only from the upper leaflet and is thus not hindered by the glass support.

We characterized the hybridization to membrane-bound chol-DNA staples using three different approaches and critically evaluated their performance: (A) modeling the membrane diffusion, (B) pseudo-infite detection, and (C) confinement of membrane diffusion (Figure VI.3 and Section VI.1.2.4). The acquisition of autocorrelation curves was performed as described above (Chapters III and IV) with only small modifications noted in the respective sections. For surface-immobilized binding sites we showed that the decay time τ_c of the autocorrelation function is independent of the size of the integrated ROI (Figure III.12, p. 55). Here, we expect a dependence of the autocorrelation function on the ROI size and exploit it to extract binding kinetics independent of diffusion dynamics. Essentially, we combine camera-based TIR-FCS [Kannan et al., 2007, Sankaran et al., 2009], including its capability to study membrane diffusion without prior calibration [Bag et al., 2012] with the binding contribution as studied in SI-FCS (Chapter III).

VI.2.1 Evaluation of the Approximated Autocorrelation Model Incorporating Binding and Membrane Diffusion

First, we set out to validate the dependence of the autocorrelation decay on the size of the integrated ROI in presence of membrane diffusion. We prepared an SLB from 1,2-dioleoyl-*sn*-glycero-3-phosphocholine (DOPC) and incubated it with chol-DNA staples at a concentration as low as 0.1 nM for 2 min. Low concentrations of hybridized duplexes on the surface do not only enable the integration over large surface areas, while maintaining detectable fluctuations from individual molecules (compare Section VI.1.2.5), but also avoid artifacts based on higher order structures of bound cholesterol observed for micromolar concentrations [Czogalla et al., 2016]. After washing to remove unbound chol-DNA docking strands from solution, we added 10 nM of imager strands, similar to the conditions used in Chapters III and IV. We used buffers as above, but unlike before, without the addition of Tween-20. Tween-20 is conventionally added to the immobilization (buffer A+) and imaging buffer (buffer B+) of DNA-PAINT samples to reduce non-specific binding to glass. However, being a detergent, Tween-20 can impair membrane integrity. Compared to Chapter III, we further expanded the illuminated area so that the extension of the illumination (estimated as $\omega_{\mathrm{FWHM}} \approx 150\,\mu\mathrm{m}$ from the magnification optics of the excitation beam and confirmed by Figure VI.15, p. 175) exceeds the field of view of the full-frame camera acquisition (82 µm) and can thus be assumed homogeneous within the field of

view. We increased the average excitation power accordingly to maintain the irradiances determined previously as bleaching-free regime (Figure III.4, p. 45). As a compromise between high camera frame rates (85 Hz) and spatial resolution, we maintained 4×4 pixels hardware binning on the camera. Further, we extracted autocorrelation curves by integrating the fluorescence signal within squared ROI of different size. Binning an increasing number of image pixels results in integrated areas ranging from 1.3 to 82 µm (Figure VI.5A). Detailed Materials and Methods are listed in Section D.1 of the appendix.

The obtained autocorrelation curves from the different integrated surface areas support the trend suggested by theory (Section VI.1.2.4 and II.1.3). With increasing ROI size, the autocorrelation amplitude decreases and the decay shifts towards longer lag times, as evident from the normalized autocorrelation curves (Figure VI.5B and C).

We initally attempted to fit the obtained average autocorrelation curves for each ROI size individually to the autocorrelation model accounting for diffusion and binding dynamics (Equation VI.11). However, the individual fits did not show consistent results for the different probed ROI sizes, as the binding contribution becomes negligible for small ROI, while the contribution from membrane diffusion becomes negligible for large ROI. We therefore fitted all obtained autocorrelation curves in one global fit procedure to obtain one set of parameters matching all curves simultaneously (Equation VI.11, p. 130). Conceptually, this is similar to the determination of membrane diffusion coefficients *via* TIR-FCS [Sankaran et al., 2009, Bag et al., 2012] with additional binding contributions and small modifications in the implementation. The amplitude G_0 and the offset G_∞ were free fit parameters, individual to every integrated ROI size. The decay time τ_c of the binding contribution and the diffusion coefficient D_C were optimized globally to match all displayed autocorrelation curves. The detection PSF was assumed constant and determined by Equation VI.8 with $\sigma_0 = 0.4$, $\lambda = 572$ nm, the emission maximum of Cy3B [Cooper et al., 2004], and NA = 1.49, as specified by the objective's manufacturer. Similarly, the ROI size a was assumed to match $a =$ [native camera pixel] $\times$ 0.16 µm, as expected from the camera specifications and the microscope's theoretical magnification. As the different autocorrelation curves vary in amplitude by three orders of magnitude ($G_0(1.3\,\mu m) = 8 \times 10^{-2}$, $G_0(82\,\mu m) = 4 \times 10^{-5}$, as determined by the fit), it is essential to normalize the data prior to fitting, in order to find the result matching small and large ROIs in equal measure.

The global fit does not only resemble the shape of the individual autocorrelation curves, but similarly accounts for the change in the decay of the autocorrelation with increasing ROI size. Systematic residuals indicate a mismatch of the autocorrelation model (Equation

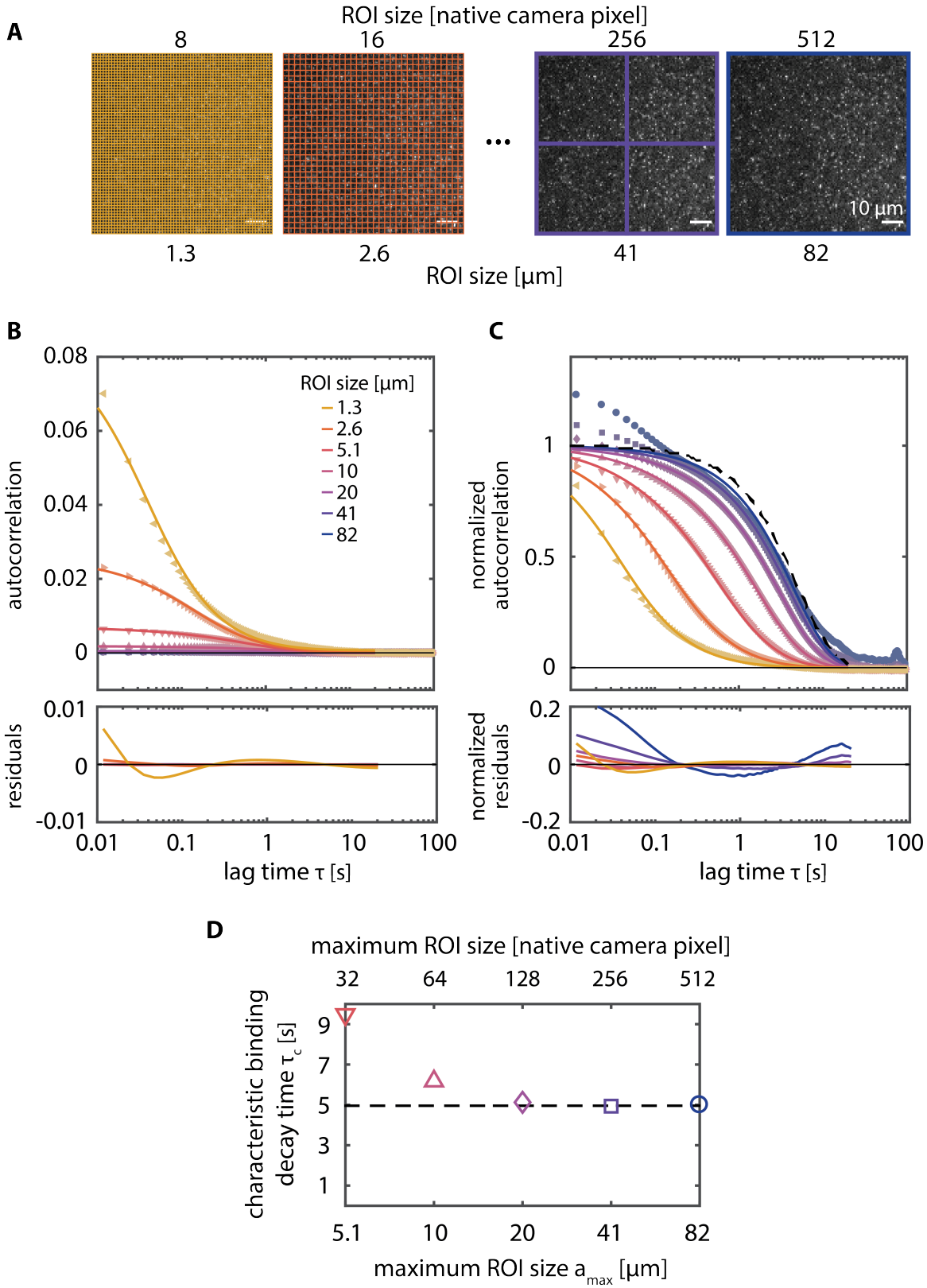

Figure VI.5: caption on next page.

Figure VI.5: Autocorrelation curves showing contributions from membrane diffusion and binding. DNA hybridization (9 nt) on chol-DNA docking strands diffusing laterally on a DOPC SLB. **(A)** Representative frame of the acquired image series overlaid with increasing ROI sizes (orange to blue), here depicted for a = (1.3, 2.6, 41, 82)µm. **(B)** Data points represent the average of autocorrelation curves obtained from binning an increasing number of pixels as integration ROIs. With increasing ROI size, the amplitude decreases (orange to blue). Solid lines represent the global fit to all shown autocorrelation functions with the membrane diffusion coefficient D_C and the decay time of the binding term τ_c common to all curves. Amplitude and offset were fitted for each curve individually (Equation VI.11). The residuals to the fit are shown in the lower panel. **(C)** Normalized autocorrelation curves are dominated by membrane diffusion for small ROI (orange) and by binding for large ROI (blue). Curves are displayed as in (B). The monoexponential binding contribution obtained from the fit with $\tau_c = 5.0\,\mathrm{s}$ is shown as black dashed line and the diffusion coefficient was found as $D_C = 4.9\,\mu\mathrm{m}^2/\mathrm{s}$. The implementation of the fitting routine in its current form does not allow for an estimation of the uncertainty of the fit or the extracted parameters. **(D)** The characteristic decay time τ_c of the binding contribution depends on the maximum ROI size used for the global fit. For every displayed ROI size, the global fit was repeated, but with $a \leq a_{\max}$. SLB composition: DOPC with 0.05 mol % Atto-488-DOPE, imager concentration: 10 nM P1 in buffer B, 0.1 nM chol-DNA.

VI.11) and the experimental data for the smallest and largest ROI sizes. In particular the two largest ROI (a = 41 and 82 µm) show strong deviations at short times ($\tau < 0.1\,\mathrm{s}$), highlighting the role of the ROI size for the magnitude of the residuals. We suggest that the major contribution is originating from lateral solution diffusion of imager strands, shifting to longer times with increasing ROI size. The contribution to the autocorrelation curve accounting for lateral diffusion in solution follows the same functional shape as in the case of membrane diffusion (Equation II.26, p. 17 and Section II.1.3). The obtained diffusion coefficient is $D_C = 4.9\,\mu\mathrm{m}^2/\mathrm{s}$, and thus faster than previously reported values [Machán and Hof, 2010]. Generally, the mobility of SLB on glass strongly depends on the employed preparation [Scomparin et al., 2009]. Here, the preparation protocol was optimized for highly mobile bilayers [Ramm et al., 2018b], in line with the increased diffusion coefficient. The characteristic binding time was determined as $\tau_c = 5.0\,\mathrm{s}$, in agreement with our previously determined characteristic decay time (Figure III.2, p. 33).

Even for the largest probed ROI, the obtained autocorrelation curve differs significantly from the isolated binding contribution (Figure VI.5C, black dashed line), hinting at a remaining contribution from membrane diffusion. Notably, the binding decay is described by a monoexponential term that decays significantly faster than a diffusion contribution

with similar half times (Figure VI.4C). This does not only have implications for the required measurement time in order to acquire an unbiased autocorrelation curve (Figure III.7, p. 47), but also indicates that even for diffusion times τ_{2D} exceeding the binding contribution τ_c, the autocorrelation function is still influenced by the contribution from membrane diffusion. Notably, for large ROI, the autocorrelation curves exhibit a significant noise contribution for large lag times. Further increasing the total measurement time beyond 5 h is experimentally challenging. The increased noise level is in agreement with previous observations on surface-immobilized DNA origami samples, namely that large ROI are generally more sensitive to noise and are also in line with the small amplitudes of the recorded autocorrelation curves.

In order to investigate the influence of the acquired ROI sizes a on the accuracy of the obtained decay time τ_c of the binding contribution, we reapplied the global fit procedure to a subset of ROIs below a maximum ROI size ($a \leq a_{\max}$, Figure VI.5D). For large maximum ROI sizes ($a_{\max} \geq 20\,\mu M$), τ_c converges to 5.0 s. For smaller maximum ROI sizes, however, the binding contribution has only negligible influence on the fitted autocorrelation functions. Therefore, the penalty in the fit of an arbitrarily large τ_c vanishes and the determined τ_c becomes inaccurate. Accordingly, the global fit procedure only extracts reliable binding information as long as the diffusion time of the largest investigated ROI size τ_{2D} is on the order of the binding decay time τ_c.

In order to further validate the analysis based on our simplified autocorrelation model (Equation VI.11), we propose a list of additional experiments. First, quantification of different imager sequences will show if the approach is able to resolve differences in membrane binding rates. The 7 nt, 8 nt and 10 nt imager employed in Chapter III (Figure III.2, p. 33) will show for which range of binding times the global fit procedure is able to extract reliable binding times. Supposedly, longer binding times will be more challenging to quantify by modeling of the autocorrelation function, as the modulation of the autocorrelation function only sets in for even larger ROI sizes. Moreover, when performing titration experiments, the amplitude will decrease even further as the imager concentration increases, below the already low amplitudes for large ROI sizes. It is not evident from our data if a full titration can be performed and which range of binding rates can be quantified. As large ROI sizes additionally shift the contribution from solution diffusion towards longer lag times, the initially assumed separation of time scales of solution diffusion, on the one hand, and binding and membrane diffusion, on the other hand, needs to be carefully re-validated. Potentially, the autocorrelation function can be extended by a term approximating the lateral diffusion

in solution. In particular, the origin of the observed residuals can be tested with a blank sample including imager, but no docking strands. As the lipid bilayer serves as a high quality surface passivation, solution diffusion can presumably be quantified separately and later on better corrected for in binding studies.

Finally, SI-FCS has the potential to quantify not only simple binding kinetics originating from a monoexponential decay, but also recover more complex binding phenomena, as shown above for the biexponential decay originating from two independent species (Figure III.2, p. 33). However, with increasing complexity of the fitting function and multiple components overlapping in the autocorrelation function, it will become increasingly challenging to investigate complex binding reactions. We therefore seek for an approach, allowing for a more direct determination of the binding kinetics with an autocorrelation model function, consisting of as few and simple contributions as possible.

VI.2.2 Pseudo-infinite Detection Neglecting Contributions from Diffusion

Our second approach, i.e. extending the integrated area to suppress the contribution to the autocorrelation function from membrane diffusion (Figure VI.3B), can be validated by reanalyzing the data obtained in the previous section (Figure VI.5). Following the concept of pseudo-infinite detection, we apply the monoexponential fit model:

$$G(\tau) = G_0 \exp\left(-\frac{\tau}{\tau_c}\right) + G_\infty \,. \tag{VI.14}$$

While we previously applied this fit model successfully to the hybridization reaction of surface-immobilized binding sites (Section A.1, p. 265), membrane diffusion causes significant deviations for small ROI sizes. For large ROI sizes, however, the combined autocorrelation (Equation VI.11) simplifies to the monoexponential decay determined by the binding contribution (Equation VI.14).

The rigorously simplified fit model describes the decay of the autocorrelation function for large lag times ($\tau > 0.5\,\mathrm{s}$) and large ROI ($a > 20\,\mu\mathrm{m}$) with satisfactory precision and residuals on the order of 1 % (Figure VI.6A). For shorter lag times or smaller ROI, however, the fits show systematic deviations from the data. For small ROI the fit model does not describe the experimentally obtained correlations properly, as diffusion on the membrane out of the integrated area decreases the apparent decay time, but is not properly accounted for in the fitting model. The residuals to the fit are accordingly large and systematic (up

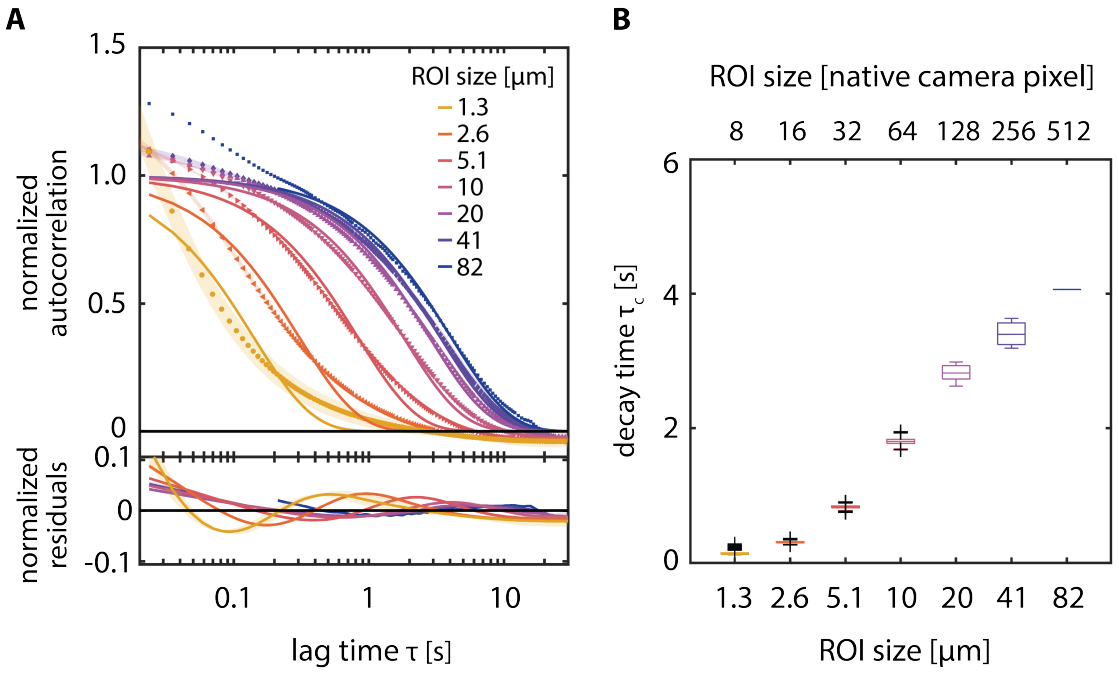

Figure VI.6: Pseudo-infinite detection: Analyzing large ROI with a rigorously simplified fit model. Experimental autocorrelation curves (symbols) are identical to Figure VI.5. **(A)** Normalized autocorrelation curves for ROI sizes increasing from 1.3 µm to 82 µm (orange to blue). The standard deviation of the acquired autocorrelation curves is shown as shaded area. Fit to a single exponential fit model (Equation VI.14) (upper panel) and residuals of data points to the fit (lower panel) are shown as solid lines. **(B)** Box plot of the obtained decay times τ_c depending on the ROI size. The center lines mark the median. The box edges correspond to upper and lower quartile, and are extended by the whiskers marking 1.5 times the inter-quartile range. Data points outside the whiskers are marked by black crosses. For faster acquisition, images were recorded with 4×4 hardware binning. For better comparability, pixels are given in native camera pixels, not binned image pixels. SLB composition: DOPC with 0.05 mol % Atto-488-DOPE, imager concentration: 10 nM P1 in buffer B, 0.1 nM chol-DNA.

to 10 %).

As the contribution from membrane diffusion shifts to longer lag times with increasing ROI size, also the apparent decay time is increasing with increasing ROI size (Figure VI.6B). For large ROI sizes and diffusion times τ_{2D} exceeding the characteristic binding time τ_c by orders of magnitude, the apparent τ_c is expected to saturate at the characteristic decay time of the binding in absence of membrane diffusion. For the maximum investigated ROI size of $a = 82\,\mu m$, a saturation of τ_c could not be obtained. However, the course of change in τ_c with increasing ROI size suggest a saturation around $(5 \pm 1)\,s$, on the order of the value obtained from the global fit of a autocorrelation model function incorporating membrane diffusion (Section VI.2.1). The maximum measured decay time is $\tau_c = 4.1\,s$ for the integration of the whole field of view ($a = 82\,\mu m$).

With the combination of our setup and the exemplified binding reaction, we were unable to reach a saturation of the obtained decay time τ_c. This highlights the most severe limitation of the presented approach, its limited applicability. A simplified estimate of the applicability of the approach of pseudo-infinite detection can be made from the comparison of the autocorrelation model function in presence and in absence of membrane diffusion (Equations VI.11 and VI.14). To estimate the expected error in the determined binding decay time τ_c, we fitted the autocorrelation function for the simplified model incorporating membrane diffusion (Equation VI.11) with the non-matching monoexponential model (Equation VI.14) (Figure VI.7). Further, we determined the threshold ROI size for a range of decay times and diffusion coefficients, resulting in an error in the obtained $\tau_{c,\,fit}$ of less than 10 % compared to the true decay time $\tau_{c,\,input}$ (Figure VI.7E). Following this estimation and further assuming the obtained numbers from the global fit (Figure VI.5, $\tau_c = 5.0\,s$, $D_C = 4.9\,\mu m^2/s$), we expect the required ROI size for a measurement accuracy of 10 % with the pseudo-infinite detection to be approximately 175 µm, significantly exceeding the possibilities of our instrumentation. For smaller diffusion coefficients, however, a much larger range of binding decay times should become accessible with the approach of pseudo-infinite detection. Obtained membrane diffusion coefficients are sensitive to a number of parameters, among others: membrane composition [Bag et al., 2014], membrane structure [Simons and Vaz, 2004, Carquin et al., 2016], crowding [Guigas and Weiss, 2016, Metzler et al., 2016], bilayer preparation [Machán and Hof, 2010, Scomparin et al., 2009] and the diffusing molecule species [Vaz et al., 1984, Jacobson et al., 1987, Gambin et al., 2006]. Based on our estimations, for diffusion coefficients of $D_C \leq 0.1\,\mu m^2/s$, residence times of up to 100 s can be analyzed by SI-FCS with pseudo-infinite detection with

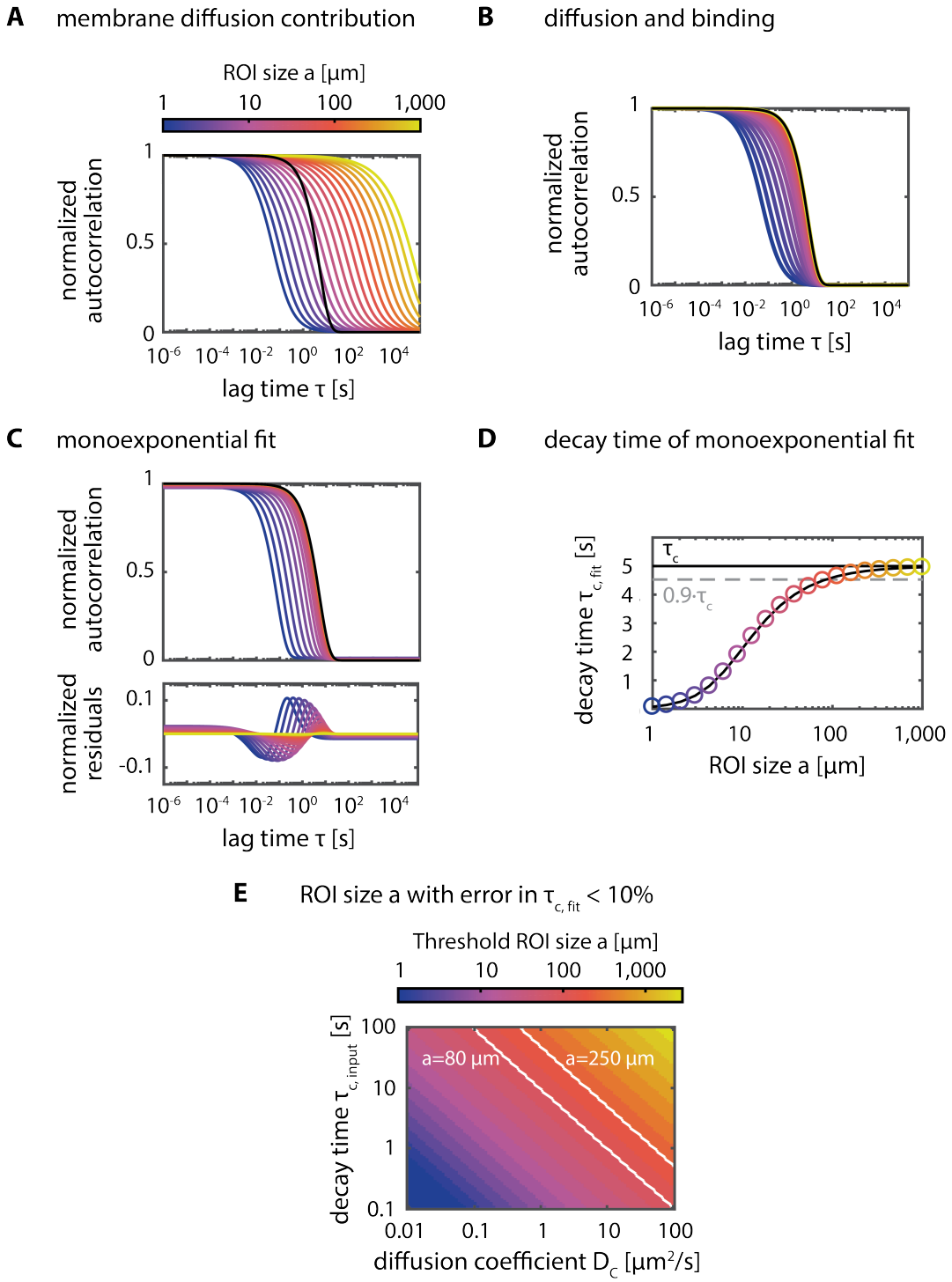

Figure VI.7: caption on next page.

Figure VI.7: Performance of the pseudo-infinite detection depending on the membrane diffusion coefficient and the binding decay time. **(A)** Normalized contribution of the membrane diffusion for increasing ROI sizes (1 µm to 1000 µm shown in blue to yellow, respectively). The contribution of binding is independent of the ROI size ($\tau_{\mathrm{c,\,input}} = 5\,\mathrm{s}$, black). **(B)** Normalized autocorrelation function resulting from the multiplication of membrane diffusion and binding contribution for ROI sizes as in (A, blue to yellow) and the binding contribution shown for reference (black). **(C)** Monoexponential fit (Equation VI.14) describing the binding contribution fitted to the autocorrelation curves from (B). For small ROI sizes the fit does not accurately describe the autocorrelation function (upper panel) and results in systematic residuals (lower panel). **(D)** The decay time $\tau_{\mathrm{c,\,fit}}$ of the monoexponential fit for ROI sizes (blue to yellow circles) approaches the true value $\tau_{\mathrm{c,\,input}} = 5\,\mathrm{s}$ (black solid line). For ROI sizes larger than 100 µm the error in $\tau_{c,\,fit}$ as determined from the fit is lower than 10 % in this example (gray dashed line). **(E)** Dependence of the necessary ROI size to achieve an error of less than 10 % on ideal data, depending on the diffusion coefficient D_{C} and the decay time $\tau_{\mathrm{c,\,input}}$. The experimentally accessible range of ROI sizes is marked by white contour lines: $a = 80\,\mu\mathrm{m}$ as currently available on our instrumentation, and $a = 250\,\mu\mathrm{m}$ with 63× TIRF objective and demagnified detection. Here, noise contributions, solution diffusion and the practical limitation originating from the required measurement times (Figure III.7, p. 47) are neglected.

a bias of less than 10 % in τ_c for a field of view exceeding 80 µm (Figure VI.7E).

VI.2.3 Lateral Confinement of Membrane Diffusion

The two approaches presented above, namely modeling the diffusion (A) and pseudo-infinite detection (B), are both limited in their sensitivity and accuracy of detecting changes in the decay time τ_c of the binding contribution. For typical ROI sizes as previously employed in SI-FCS (up to 20 µm, Figure III.12, p. 55) or camera-based TIR-FCS (up to 2 µm [Krieger et al., 2015, Bag et al., 2012]) the autocorrelation curves are influenced by membrane diffusion (Figure VI.7). Even larger ROI sizes reduce the influence of diffusion, but simultaneously increase the sensitivity to instabilities in the sample and the setup. We developed the strategy of confining the diffusion (Figure VI.3C) to combine the advantages of a simple and robust fitting function while decoupling the accessible binding kinetics from the employed ROI sizes. In this way, diffusion may still be present in the system, but is rendered invisible to the autocorrelation function, as bound molecules are prevented from diffusing in and out of the detection volume.

One elegant way of achieving confinement in a reproducible and well-defined way, are photolithograpically patterened diffusion barriers isolating individual membrane cor-

rals [Groves et al., 1997, Groves, 2002, Lin et al., 2010, Nair et al., 2011]. Different materials have previously been tested concerning their influence on the membrane formation and fluidity [Groves et al., 1998]. Aluminium oxide inhibits the formation of lipid bilayers in coated areas, while chromium and indium tin oxide (ITO) allow vesicle fusion and thus the formation of SLBs. Bilayers on chromium and ITO, however, are immobile and thus form diffusion barriers. Ligand-receptor binding has previously been studied to membrane receptors incorporated into membrane microarrays by observing changes in bulk fluorescence [Fang et al., 2002] or the effect of the binding on molecular mobility [Yamazaki et al., 2005].

For SI-FCS, we designed grid shaped diffusion barriers, exposing the cover glass in patches of 10 µm side length, enclosed by 1-2 µm wide chromium lines (Figure VI.8). In brief, a positive photo resist is patterned on standard microscopy coverslips, prior to sputtering of a few nanometer thick chromium layer. Lift-off of the photo resist frees coated areas from chromium, exposing the cover glass. The employed photolithography allows to form arbitrary lateral shapes on the scale of few micrometers and larger. While in areas exposing the cover glass standard SLB can be formed by fusion of small unilamellar vesicles (SUVs) [Ramm et al., 2018b], areas coated with chromium serve as a barrier to lateral diffusion. Detailed Materials and Methods are listed in Section D.1.3 of the Appendix (p. 292). In TIRF microscopy barriers preventing the formation of SLB and barriers hindering the diffusion will both appear as dark areas, as excitation light is back-reflected from the chromium patterns. The usability of the cover slides is considerably enhanced by their ability to be reused. Lipid bilayers on chromium coated coverslips can be removed by washing with ethanol and water prior to plasma cleaning. Reused slides were without observable deterioration of the chromium pattern or compromises in membrane quality.

FRAP experiments confirm that the membrane is fluid within one membrane corral (Figure VI.8C), while no exchange of lipids of neighboring corrals is observed (Figure VI.8D). The designed grid structures therefore serve as the desired diffusion barrier without apparent alterations of the lateral diffusion within the membrane corrals.

To investigate membrane binding, we incubated the SLB with chol-DNA staples for 2 min, before removal of unbound chol-DNA (Figure VI.9). Further, we increased concentration of chol-DNA (10 nM) compared to standard SLB (0.1 nM, Figure VI.5 and VI.6) to ensure chol-DNA incorporation in all membrane corrals. Examining individual bound imager strands by eye, it appears that chol-DNA experiences the chromium grid as a reflective boundary. We did visually neither observe trapping of chol-DNA nor an increase

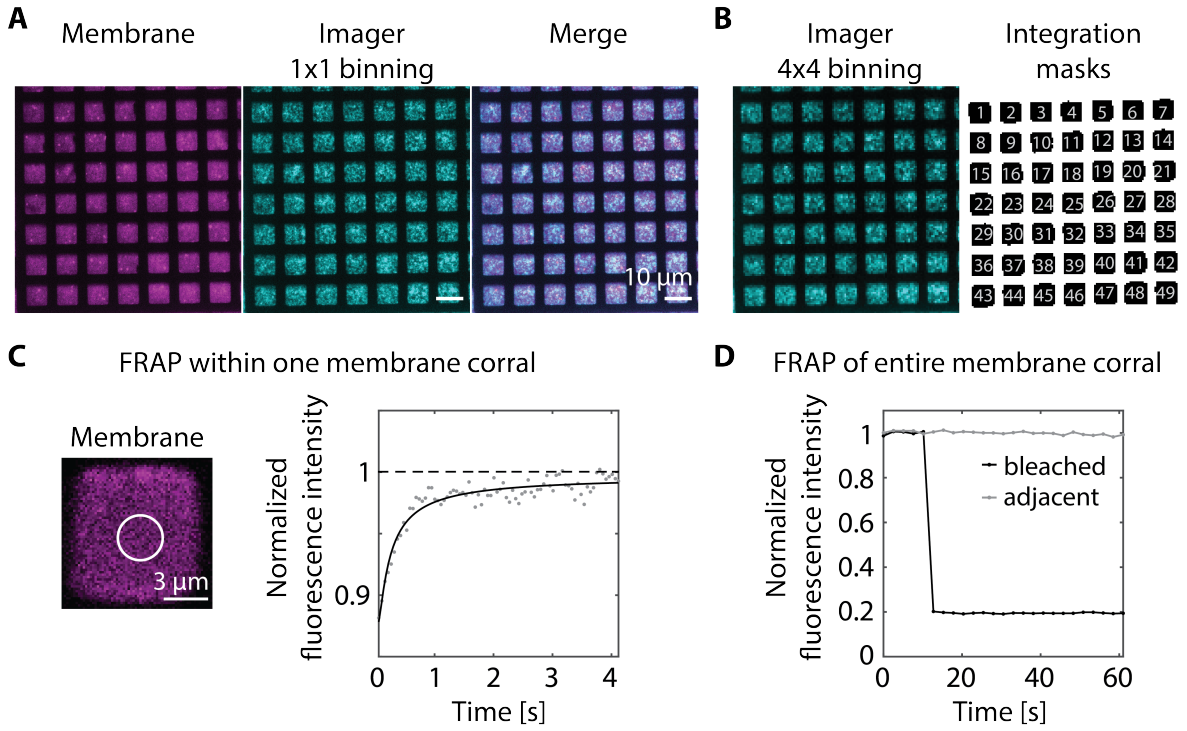

Figure VI.8: Deposition of patterned SLB on chromium microstructures. A grid microstructure is deposited on a coverslip by photolithography and metal evaporation (courtesy of Beatrice Ramm, Hiro Eto and Philipp Altpeter, for details see Appendix D.1.3, p. 292). **(A)** A DOPC SLB is deposited on the microstructures, resulting in an array of membrane corrals separated by the chromium structures (magenta). Chol-DNA staples bind to the SLB exposing the docking sequence. Fluorescent imager strands hybridize transiently to the docking strands (cyan). Scale bar: 10 µm. **(B)** For SI-FCS acquisition, the signal from the imager strands is recorded with 4×4 binning (left). ROIs for integration are obtained from thresholding on the imager signal after averaging the measurement in time, resulting in 49 independent ROIs. **(C)** FRAP measurement of the lipid mobility within one membrane corral after bleaching a circular spot with 3 µm diameter (gray data points). Fitting a FRAP model (Equation D.1, p. 293, solid black line) reveals a diffusion coefficient of $D = (7 \pm 2)\,\mu m^2/s$, consistent with the high mobility found for cholesterol staples with TIR-FCS (Figure VI.5). Scale bar: 3 µm. **(D)** No recovery in fluorescence intensity is observed when an entire membrane corral is bleached (black solid line). Neighboring membrane corrals are unaffected (gray solid line). SLB composition: DOPC with 0.05 mol % Atto-488-DOPE in A and B, imager concentration: 10 nM P1 in buffer B, 0.1 nM chol-DNA, DOPC with 0.05 mol % Atto-655-DOPE without imager strands and chol-DNA in C and D.

in unbinding when diffusing molecules encountered the boundaries of the chromium grid. To extract intensity traces from the image series, we generated binary masks by thresholding of the time-averaged image series. Fluorescence intensity traces for SI-FCS analysis were then obtained by integration of the fluorescence signal within the areas described by the binary masks (Figure VI.8B). This implementation ensures the independence of the analysis on the rotation of the grid compared to the axes of the camera.

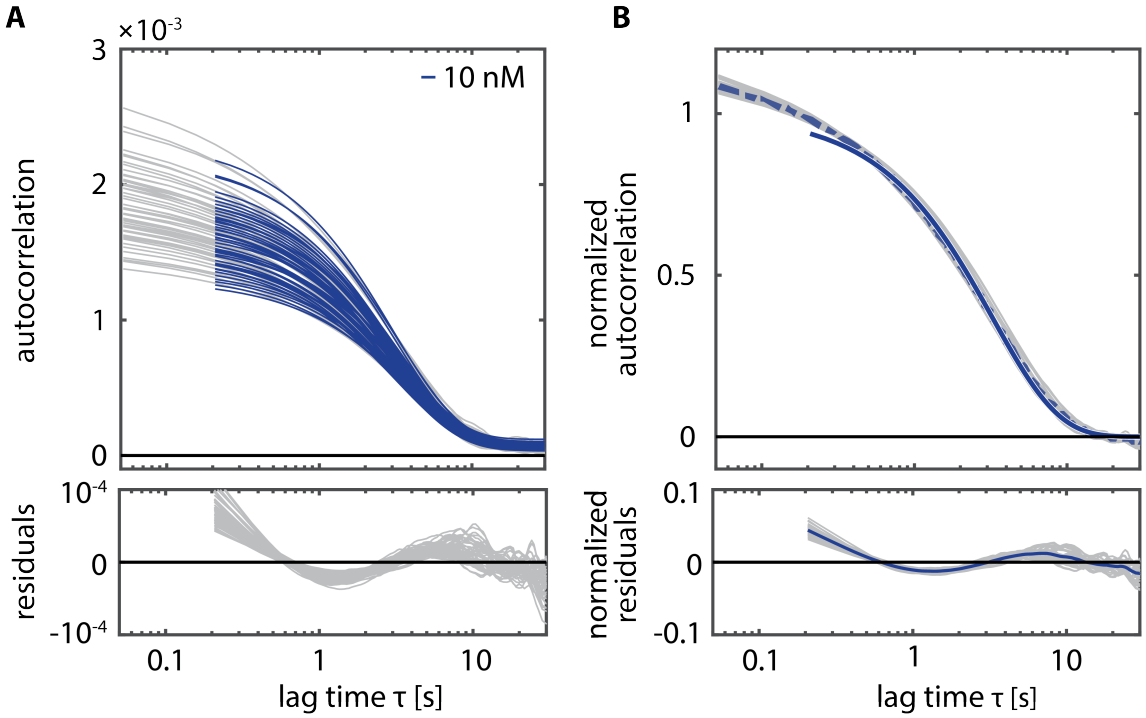

Figure VI.9: SI-FCS autocorrelation curves acquired from micropatterned membrane corrals on chromium grids. **(A)** SI-FCS autocorrelation curves (gray, upper panel) obtained from integration of confined SLB patches on chromium grids (Figure VI.8). Fits to the individual autocorrelation curves are shown as solid lines (Equation VI.14, upper panel). Respective residuals are shown in the lower panel. **(B)** Normalized autocorrelation curves, displayed as in (A), but with the average of the normalized autocorrelation curves (blue dash-dot line) and the fit to the average autocorrelation curved (blue solid line). Lower panel: Fits for the individual normalized autocorrelation curves (gray) and the average autocorrelation curve (blue). SLB composition: DOPC with 0.05 mol % Atto-488-DOPE, imager concentration: 10 nM P1 in buffer B, 5 nM chol-DNA.

We obtained 49 independent autocorrelation curves from one field of view (Figure VI.9) with an imager concentration of $\langle A \rangle = 10\,\text{nM}$, as above (Figures VI.5 and VI.6). To extract binding times, we fitted the autocorrelation curves with the model function for

binding in absence of any diffusion (Equation VI.14). Further, we averaged the normalized autocorrelation curves and fitted the average autocorrelation curve. The fits describe the data with an overall accuracy at the same level as for our investigations of DNA hybridization to surface-immobilized docking strands (Figure III.2, p. 33) and yield an average characteristic decay time of $\tau_c = (3.01 \pm 0.13)\,\mathrm{s}$ (mean ± std.).

Based on the high quality of the obtained results, we recorded a titration curve to extract not only the characteristic binding time, but the association and dissociation rate, k_a and k_d, respectively. To limit the number of bound imager strands within one membrane corral, we lowered concentration of chol-DNA from 5 nM to 1 nM with increasing imager concentration from 10 nM to 2 µM, respectively. By varying the concentration of chol-DNA, high concentrations of imager strands in solution result in fluctuations that are still sufficient to extract autocorrelation curves from the image series. Table D.1 (p. 293) in the appendix lists the pairs of concentrations of imager strands and chol-DNA.

With increasing concentration of imager strands in solution, the autocorrelation curves show a decreasing characteristic decay time τ_c (Figure VI.10). As for the titrations of the imager concentration in Chapters III and IV, we fitted the obtained decay times with Equation III.1 (Figure VI.10B, black solid line). One point of the titration series ($\langle A \rangle = 300\,\mathrm{nM}$) does not follow the general trend for unknown reasons. Concentrations were assumed to match the taret concentration and were thus not confirmed by confocal FCS, different from previous experiments (Figure A.1, p. 269). Excluding the data point at $\langle A \rangle = 300\,\mathrm{nM}$, we obtain as association and dissociation rate, $k_a = (0.9 \pm 0.6) \times 10^6/(\mathrm{M\,s})$ and $k_d = (0.33 \pm 0.04)/\mathrm{s}$, respectively (Figure VI.10B, red solid line). The rates are in agreement with the values obtained for surface-immobilized binding sites (Chapter IV, Table IV.1, p. 68), yet lower than in Chapter III (Table III.1, p. 35). Table VI.1 lists the obtained binding parameters including and excluding the outlier at $\langle A \rangle = 300\,\mathrm{nM}$, as well as the binding kinetics for surface-immobilized DNA-origami nanostructures (Chapters III and IV) [Mücksch et al., 2018, Blumhardt et al., 2018].

While the presented results are preliminary and require further validation, they do highlight the potential of SI-FCS to quantify reaction rates of ligands to membrane-bound receptors in presence of diffusion. Not only does the recording of SI-FCS autocorrelation curves on micropatterned SLBs render the effects of membrane diffusion negligible, it also allows for the multiplexing of multiple autocorrelation curves within one field of view. The obtained data are within the range observed in previous experiments, suggesting that the diffusion barriers do not have a strong effect on the binding kinetics. The design of

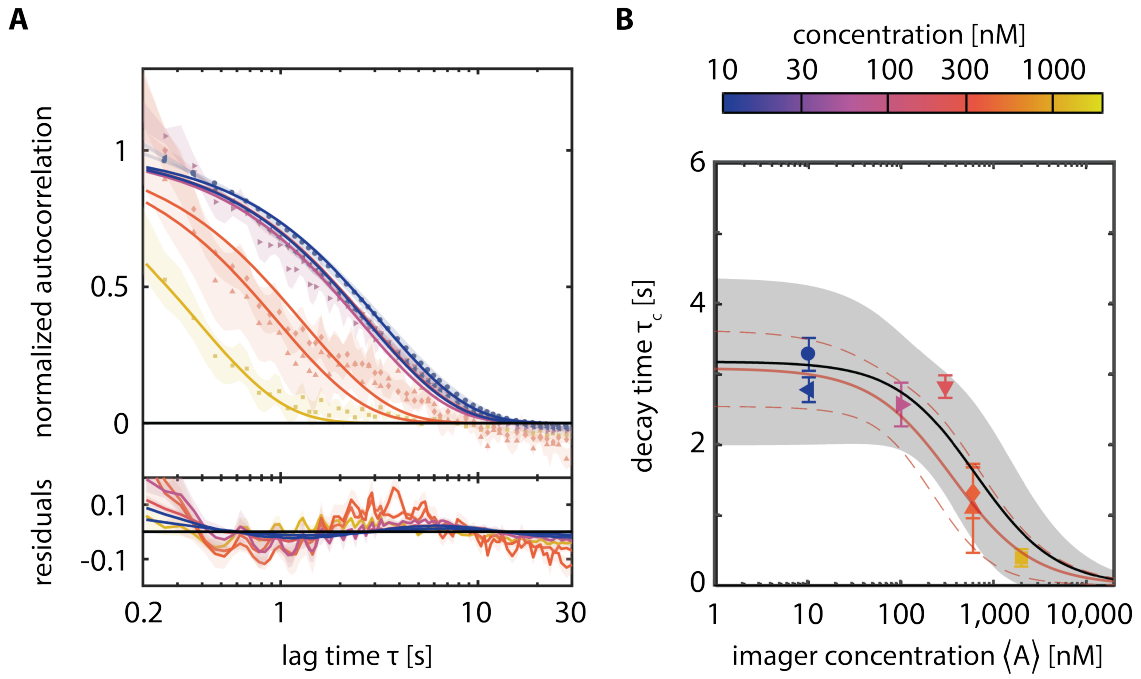

Figure VI.10: Determination of binding rates to diffusing membrane-bound receptors. **(A)** Normalized SI-FCS autocorrelation curves as in Figure VI.9, but for increasing concentrations of imager strands (10 nM to 20 µM, blue to yellow). Data points represent the average of the autocorrelation curves from at least 36 membrane corrals with the standard deviation as shaded area. The fits (Equation VI.14, upper panel) and residuals (lower panel) are shown as solid lines. **(B)** The characteristic decay time τ_c decreases with increasing concentration of imager strands in solution. The fit to the titration model (Equation III.1, p. 31) is shown as solid black line with the 95 % confidence bounds as shaded area. The fit and confidence bounds obtained by excluding the measurement at 300 nM are shown as red solid and dashed lines, respectively. SLB composition: DOPC with 0.05 mol % Atto-488-DOPE, imager concentration: 10 nM to 2 µM P1 in buffer B, 1 nM to 5 nM chol-DNA.

Table VI.1: Hybridization kinetics with 9 nt overlap on chol-DNA and surface-immobilized DNA origami nanostructures. Association rate k_a, dissociation rate k_d and the dissociation constant $K_d = k_d/k_a$ for the hybridization on chol-DNA diffusing on fluid SLBs (first row). One data point did not follow the general trend and was excluded (second row) for better comparison of the obtained results in Chapter IV (third row, from Table IV.1) and III (bottom row, from Table III.1).

docking strand condition	$\mathbf{k_a}$ [$\mathbf{10^6/(M\,s)}$]	$\mathbf{k_d}$ [1/s]	$\mathbf{K_d}$ [nM]
chol-9nt	0.5 ± 0.5	0.31 ± 0.09	600 ± 800
chol-9nt (w/o $\langle A \rangle = 300\,\mathrm{nM}$)	0.9 ± 0.6	0.33 ± 0.04	400 ± 300
9nt immobilized, DNA origami, [Blumhardt et al., 2018]	1.49 ± 0.17	0.303 ± 0.001	200 ± 30
9nt immobilized, DNA origami, [Mücksch et al., 2018]	2.5 ± 0.5	0.180 ± 0.012	72 ± 16

structures with varying confinement geometries and dimensions will allow to control for possible interactions with the chromium barrier in the future.

VI.2.4 Combined Discussion of the Quantification of Ligand Binding to Membrane-bound Receptors

We have successfully implemented the quantification of our model system for the binding to membrane-bound receptors with SI-FCS. All three proposed approaches are principally able to measure binding kinetics on highly fluid SLBs.

For the first two tested approaches (A and B), the decay time of the binding contribution τ_c at an imager concentration of 10 nM was estimated with 5 s (Figures VI.5 and VI.6), and thus higher than the (3.01 ± 0.13) s for the confined diffusion (C, Figure VI.9). The concentration of imager strands of 10 nM is low enough to assume the decay time τ_c to be the inverse of the dissociation rate ($\tau_c \approx 1/k_d$) for the approaches (A) and (B). The resulting dissociation rates of the three approaches agree within a factor of 1.7 (Table VI.2). However, taking into account the estimated error margins, the values differ significantly for the three applied approaches. This difference demands further controls, as the employed SLB composition, DNA handles, buffers and excitation irradiance were identical for all three approaches. Samples can thus be regarded as replicates, except for the chromium microstructures, the performed analysis and the concentration of chol-DNA docking strands. In approach C the concentration was increased, as the low concentration of 0.1 nM employed on the conventional SLB left some fields on the chromium grid

apparently unoccupied.

Notably, the difference of the three approaches is of the same magnitude as in between the two measurements of Chapters III and IV (Table VI.1). Excluding the outlier at $\langle A \rangle = 300\,\mathrm{nM}$, obtained association rates differ maximally by a factor of 2.8 and dissociation rates by maximally a factor of 1.8 in between approach C and Chapters III and IV.

We previously accounted differences of the observed magnitude to slight mismatches in buffer conditions, in particular the pH, and the temperature of the sample. The temperature is intrinsically a sensitive parameter for transient binding reactions with binding energies on the order of $k_B T$, and thus in particular for the DNA hybridization with 9 nt overlap [Jungmann et al., 2010]. Furthermore, the recorded titrations in Chapter III and IV were obtained from the same batch of materials within the respective chapters, but fresh stocks of material (DNA-origami, imager and buffers) for each chapter.

On the one hand, the difference is significant, requiring careful control of the accuracy of the experiments. On the other hand, it highlights the achievable precision of the SI-FCS quantification with a factor of two in the binding rates being clearly resolvable.

All three approaches have revealed specific advantages and pitfalls that make them promising candidates for complementary measurements and for cross-checking the obtained results. As the chromium grids are not extended over the whole coverslip, areas covering multiple fields of view with unpatterned SLB can be found. We therefore propose to exploit the ability of the three presented approaches to directly compare measurements from one identical sample. Subsequently sampling an unpatterned and a patterned membrane region, allows to rule out buffer mismatches, temperature or sample variation as possible cause.

Modeling the diffusion in the autocorrelation function (A) is the only way to extract the diffusion coefficient D_C of the binding sites on the membrane simultaneously to the binding kinetics. Principally, the diffusion coefficient D_C can similarly be obtained within confined membrane corrals (C) for ROI sizes smaller than the extension of the corrals. The limited size of the membrane corrals is however expected to influence the autocorrelation function of the membrane diffusion, as well known from simulations with limited box sizes and reflective boundary conditions.

The global fit extracts the characteristic binding decay time τ_c reliably, as long as the ROI size is large enough, such that the autocorrelation function is modulated by the binding contribution (Figure VI.5D). Noise at large lag times is increasing with large ROI sizes, limiting both the fitting of the diffusion contribution (A) and the pseudo-infinite integration

(B). Pseudo-infinite detection (B) is most simple in its analysis and the employed fitting model. Unfortunately, it is systematically biased towards shortened decay times due to a ROI size not sufficient to reach a saturation of τ_c. Effectively, the first two approaches (A and B) can only be performed for short binding decay times or small diffusion coefficients (Figure VI.7). Thus, they are currently incompatible with residence times on the order of 100 s, as observed for the hybridization of a 10 nt duplex (Figure III.1, p. 31), as long as the diffusion coefficient $D_C \gg 0.1\,\mu m^2\,s$.

Confinement of diffusing molecules in membrane corrals (C) combines the advantages of a simple one component fitting model with the multiplexed acquisition of multiple autocorrelation curves from one field of view. In particular, confinement is the only identified approach that combines (i) fluid lipid bilayers, (ii) small ROI sizes resulting in large SI-FCS autocorrelation amplitudes, coinciding with superior SNR, and finally (iii) principally unlimited residence times. The major challenge of the approach is to avoid an alteration of the binding kinetics upon encounters with the diffusion barrier. As we were unable to rule them out entirely, further experiments will be necessary to finally decide on the applicability of the approach. Furthermore, the more complex sample preparation of the membrane corrals impairs the simplicity and availability of the method. On the other hand, modified and specialized structures can be created as controls or for specific applications. Compared to SPR and QCM-D, requiring specialized chips, the sample preparation is simple and cost-efficient. As chromium structures effectively block fluorescence light in covered areas, they can potentially serve as physical pinholes in the sample plane to be combined with fast detection schemes like large-area PMTs or APDs (Chapter IV) and reduce sample bleaching outside of the desired ROI. Additional data points below the currently achievable camera acquisition cycle times will benefit the fitting of the solution contribution and thus the accuracy of the obtained results.

Spatially resolved acquisition, on the other hand, offers the fundamental advantage over point or area detection that the acquisition region of interest can be adapted in post-processing and does not need to be experimentally defined on the setup. Moreover, spatial detection has the potential to generate binding maps, identifying local changes in binding kinetics. For the specific case of membrane binding, the assessment of membrane quality in a separate fluorescent channel benefits the quality of the experimental data. In particular, camera acquisition is therefore favorable over APD- or PMT-based detection, as long as the time resolution of the camera is sufficient.

For applications beyond our chol-DNA-based proof-of-concept system, the reversible

Table VI.2: Obtained binding kinetics for the three approaches to determine binding rates in the presence of membrane diffusion. The approaches are presented in Section VI.1.2.4 and illustrated in Figure (VI.3). The quantification is based on the autocorrelation curves presented in Figures VI.5, VI.6 and VI.8, respectively.

analysis scheme	τ_c **(10 nM)** [s]	D_{2D} [$\mu m^2/s$]	k_a [$10^6/(M\,s)$]	k_d [1/s]	**chol-DNA** [nM]
global fitting	5.0	4.9	-	0.20	0.1
pseudo-infinite ROI	4.1[1]	-	-	0.24	0.1
chromium grid	3.02 ± 0.14	-	0.9 ± 0.6	0.33 ± 0.04	1, 2 or 5

binding of ligands to integral membrane receptors is of high relevance for not only biology, but also pharmacology. Studies of integral membrane receptors in combination with SLB have been hindered by the interaction of transmembrane proteins with the solid support. The spacing of the lipid bilayer to the cover glass has been increased by various methods to combine solid-supported membranes with laterally mobile integral membrane proteins [Tanaka and Sackmann, 2005]. As the distances are well below the penetration depth of the TIRF excitation, they are readily suitable for SI-FCS measurements. Prominent examples include cushions made from polymer [Spinke et al., 1992], DNA-tethered multilayers [Chung et al., 2009] or surface-tethered vesicles [Yoon et al., 2006] (reviewed in [Tanaka and Sackmann, 2005, Chan and Boxer, 2007]). Moreover, such cushions have been micropatterned, allowing their potential application as confinement strategies with SI-FCS.

Taken together, once proper controls are in place to rule out significant interactions with the chromium structures, membrane corrals offer the most versatile and most promising route for quantification of membrane binding rates with SI-FCS. The three tested approaches highlight that SI-FCS is principally able to precisely quantify ligand-receptor interactions, even on highly fluid lipid bilayers with high specificity and single-molecule sensitivity – a combination so far widely unavailable to the scientific community.

VI.3 Quantifying Complex Membrane Partitioning of Biomolecules with SI-FCS

Taking SI-FCS even further, we explored the potential for quantifying the kinetic rates of the partitioning of biomolecules to membranes. The binding of proteins to membranes can be quite complex in detail. Specific binding to membrane-incorporated receptors (Section VI.2) or partitioning to the hydrophobic phase of the lipid bilayer represent two concepts of protein-lipid interaction. Moreover, electrostatic attraction or repulsion [Murray et al., 1997], the interaction of binding domains of proteins with specific lipids [Lemmon, 2008] and membrane curvature recognition induce different levels of specificity [Cornell and Taneva, 2006]. The transient binding of peripheral membrane proteins can futher be triggered by posttranslational modifications such as lipidation (e.g. palmitoylation or prenylation) [Resh, 2006,Linder and Deschenes, 2007]. In addition, a large set of peripheral membrane proteins bind membranes via amphipathic helical segments, a motif recurrently found in protein structures mediating reversible membrane binding [Cornell and Taneva, 2006]. Amphipathic helices have polar residues that aid water solubility and hydrophobic residues that intercalate the glycerol backbone of the lipid bilayer [Drin and Antonny, 2010]. The challenge of investigating amphipathic helices is mutlifaceted: The partitioning in between solution and membrane typically induces a transition from a non-helical to helical confirmation. Based on this confirmational transition, the binding of the amphipathic peptide GLP-1 has been reported to not follow a monoexponential distribution of residence times. Rather, it has been shown to follow a more complex binding mechanism [Fox et al., 2009,Myers et al., 2012,Constantinescu and Lafleur, 2004,Gerlach et al., 2009]. Overall, the binding of amphipathic helices does not occur on well-defined receptors that can be easily saturated in a titration experiment. Thus, the binding of amphipathic proteins or peptides can only within certain limits be characterized in the framework of molecular binding and the respective assignment of binding affinities. Remaining specificity for curvature, lipid domains or lipid head groups might not be accurately described in a partitioning picture either. Further, binding to the bilayer, amphipathic molecules localize within the complex interfacial region formed by the aqueous solution, the lipid head groups and the gylcerol backbone region. The pioneering work of Wimley and White highlights the importance of this interface in contrast to the classic bulk partitioning picture [Wimley and White, 1996, Wimley et al., 1996, White and Wimley, 1998]. The quantification of the membrane interaction of peripheral membrane proteins is thus in great need for a precise and accurate

assays.

The aforementioned points highlight the need for appropriate theoretical models not only describing the binding process in general, but also the SI-FCS autocorrelation functions of the system in particular. Considerable effort has been invested towards a closed-form analytic description of the autocorrelation function for binding to membranes, however, with a focus on ligand-receptor interactions [Thompson et al., 1981, Thompson, 1982,Lagerholm and Thompson, 1998,Starr and Thompson, 2001,Lieto et al., 2003,Thompson et al., 2011,Lieto and Thompson, 2004,Ries et al., 2008a] (see also Sections II.1.3, p. 12 and V.1, p. 91). Eliminating lateral diffusion of membrane-bound molecules is key to obtain models that rely on a limited number of experimentally accessible fitting parameters. Here, we contribute to an all-embracing description, primarily by systematic assessments through Monte Carlo simulations (Sections VI.3.1 and VI.3.2). Despite the progress presented here, additional work is required to obtain the full set of physical quantities from the autocorrelation function. In Section VI.3.3, we list identified membrane binding peptides potentially suited to test the performance of SI-FCS. Section VI.3.4 to VI.3.6 explore the experimental possibilities for obtaining autocorrelation curves of peptide binding to three different model membrane systems that confine the membrane diffusion.

VI.3.1 Autocorrelation Function for Membrane Partitioning Below the Saturation Regime

Quantifying the binding rates to the membranes in absence of specific binding sites imposes an additional experimental challenge, compared to a model describing ligand-recptor binding. If membrane binding sites are sparse and independent, an increase in the solution concentration ultimately leads to a saturation of surface binding sites (Section VI.1.2.2). However, the situation is more complex if the membrane can be regarded as one extended binding site or as a dense array of binding sites. While at low surface concentrations binding sites can be regarded as independent and binding kinetics are well-defined, for densities close to surface saturation, binding kinetics potentially change. In particular, changes in membrane integrity and lateral interactions of bound molecules have to be carefully considered at high surface concentrations [Hsieh et al., 2010, Shih et al., 2011, Melo et al., 2009, Brogden, 2005, Cornell and Taneva, 2006, Khandelia et al., 2008].

Here, we present a quantification of membrane binding kinetics at low surface occupations that satisfy the independence of individual binding events even for direct binding to membrane. In Section III.2.1 (p. 39), we derived the autocorrelation function for a binding

to surface-immobilized binding sites of the type

$$\mathrm{A} + \mathrm{B} \underset{\mathrm{k}_d}{\overset{\mathrm{k}_a}{\rightleftharpoons}} \mathrm{C}\,, \tag{VI.15}$$

with A being the molecules in solution, B the unoccupied binding sites and C the formed duplex of ligand and surface-binding sites.

Without specific binding sites on the surface, the reaction is better described by the conversion of the molecules from a solution state A to a bound state C

$$\mathrm{A} \underset{\mathrm{k}_d}{\overset{\mathrm{k}_a}{\rightleftharpoons}} \mathrm{C}\,. \tag{VI.16}$$

Here, we assume (i) as before, that diffusion of A in solution is fully equilibrated on the time scale of binding (Chapter III and VI.1.2.4) and (ii) that the lateral diffusion of bound molecules C on the membrane is eliminated by adequate measures, as have been developed before (Section VI.1.2.4).

The autocorrelation function thus depends only on the fluctuations in the number of bound molecules. The change in the concentration C is described by the differential equation

$$\frac{\mathrm{d}C(\vec{r},t)}{\mathrm{d}t} = k_a A(\vec{r},t)\lambda^{-1} - k_d C(\vec{r},t)\,, \tag{VI.17a}$$

consisting of an association and a dissociation term. Note that in difference to Equation III.8 (p. 40), the association term $k_a A\lambda^{-1}$ is independent of the availability of binding sites B and therefore has the unit 1/s. Here, we introduced the characteristic length λ to account for $A(\vec{r},t)$ being a volume concentration and $C(\vec{r},t)$ being a surface concentration, similar to Myers and colleagues [Myers et al., 2012]. In Chapter III, we neglected the difference in dimensionality and treated B and C as effective volume concentrations.

We can express the concentrations as a variation around the mean, $A(\vec{r},t) = \langle A\rangle + \delta A(\vec{r},t)$ and $C(\vec{r},t) = \langle C\rangle + \delta C(\vec{r},t)$, respectively. In equilibrium, the average concentrations are constant and the rates of binding and unbinding are equal, $k_\mathrm{d}\langle C\rangle = k_\mathrm{a}\langle A\rangle\lambda^{-1}$.

As differential equation of the fluctuations of bound molecules $\delta C(\vec{r},t)$, we obtain

$$\underbrace{\frac{\mathrm{d}\langle C\rangle}{\mathrm{d}t}}_{=0}+\frac{\mathrm{d}\delta C(\vec{r},t)}{\mathrm{d}t}=\underbrace{k_a\langle A\rangle\lambda^{-1}-k_d\langle C\rangle}_{=0}+k_a\delta A(\vec{r},t)\lambda^{-1}-k_d\delta C(\vec{r},t) \tag{VI.17b}$$

$$\frac{\mathrm{d}\delta C(\vec{r},t)}{\mathrm{d}t}=k_a\delta A(\vec{r},t)\lambda^{-1}-k_d\delta C(\vec{r},t) \tag{VI.17c}$$

The equilibrium binding constant

$$K_0=\frac{k_d}{k_a}=\frac{\langle A\rangle}{\langle C\rangle} \tag{VI.18}$$

is the ratio of a volume concentration and a surface concentration and therefore has the unit of a length [Myers et al., 2012]. As in Chapter III, we assume a large reservoir of molecules in solution, compared to the fraction bound to the membrane. The fluctuations in the solution concentration are therefore negligible ($\delta A=0$).

As above, the autocorrelation function $G(\tau)$ is determined by the concentration correlation $\Phi_{\mathrm{CC}}(\tau)=\langle\delta C(0)\delta C(\tau)\rangle$:

$$G(\tau)=\frac{\int\mathrm{d}^3r\int\mathrm{d}^3r'\,\Phi_{\mathrm{CC}}(\tau)\delta(\vec{r}-\vec{r}\,')}{\langle C\rangle^2(\int\mathrm{d}^3r)^2}\,. \tag{VI.19}$$

The differential equation for the concentration correlation writes as (compare Equation III.10, p. 41)

$$\frac{\mathrm{d}\Phi_{\mathrm{CC}}(\tau)}{\mathrm{d}\tau}=-k_d\,\Phi_{\mathrm{CC}}(\tau) \tag{VI.20}$$

with the same solution as above (Equation III.11, p. 41),

$$\Phi_{\mathrm{CC}}(\tau)=\Phi_0e^{-\tau/\tau_d}\,, \tag{VI.21}$$

but with the characteristic decay time being equal to the dissociation time $\tau_c=\tau_d=k_d^{-1}$.

In equilibrium the average rates of binding and unbinding are constant $k_{\mathrm{d}}\langle C\rangle=k_{\mathrm{A}}\langle A\rangle\lambda^{-1}$ and the fluctuations δC thus follow Poisson statistics. The amplitude of the concentration correlation function is thus given by the variance of C, equal to the average $\langle C\rangle$

$$\Phi_0=\mathrm{Var}(C)=\langle C\rangle\,. \tag{VI.22}$$

The average number of bound molecules is given by $N_C = \langle C \rangle V$, where we use the detection volume $V = \int \mathrm{d}^3 r$. Inserting the obtained expressions for Φ_0 and $\Phi_{\mathrm{CC}}(\tau)$ in Equation (VI.19), we obtain the analytic expression for the autocorrelation function for unspecific binding far from surface saturation as

$$G(\tau) = \frac{\Phi_0}{\langle C \rangle^2 V} e^{-k_d \tau} \tag{VI.23a}$$

$$= \frac{1}{N_C} e^{-k_d \tau} = \frac{k_d}{k_a \langle A \rangle \lambda^{-1} V} e^{-k_d \tau} . \tag{VI.23b}$$

Equation VI.23 is valid in the absence of lateral diffusion into or out of the detection volume and in the reaction limit with equilibrated diffusion dynamics in solution, well separated in time from the binding kinetics.

To verify and illustrate these results, we performed Monte Carlo simulations of the binding reaction. Molecules were switching between states A and C with the effective association and the dissociation rate, $k_{\mathrm{AC}} = k_{\mathrm{a}} \langle A \rangle \lambda^{-1}$ and $k_{\mathrm{CA}} = k_d$, respectively. While the influx of molecules far from saturation is independent of the surface occupation and thus randomly distributed to satisfy the average binding rate, bound molecules are dissociating with the probability

$$P_d = 1 - \exp(-k_d \Delta t) , \tag{VI.24}$$

with Δt being the time step of the simulation. Molecules in state C contributed as 1 to the fluorescent signal and the generated intensity trace was correlated to obtain $G(\tau)$. We explored the dependence of the autocorrelation function by changing the effective association rate k_{AC}, which is experimentally equivalent to a concentration titration of $\langle A \rangle$, while keeping k_d constant (Figure VI.11A and B). Similarly, we varied the dissociation rate k_d with constant k_{AC} (Figure VI.11C and D). Detailed materials and methods for the Monte Carlo simulation are listed in the Appendix D.2.1 (p. 295).

The results of the simulation resemble the theoretical predictions (Equation VI.23) within the precision of the simulation (Figure VI.11). For increasing concentration of molecules in solution $\langle A \rangle$ and thus an increased effective association rate, the amplitude of the autocorrelation drops and is given by the ratio of effective association and dissociation rate, $G_0 = k_d (k_a \langle A \rangle)^{-1} \lambda$. In contrast to the binding to distinct binding sites, the decay time of the autocorrelation function does not depend on the effective association rate (Figure VI.11B, left panel), but only on the dissociation dynamics $\tau_c = \tau_d = k_d^{-1}$ (Figure VI.11D,

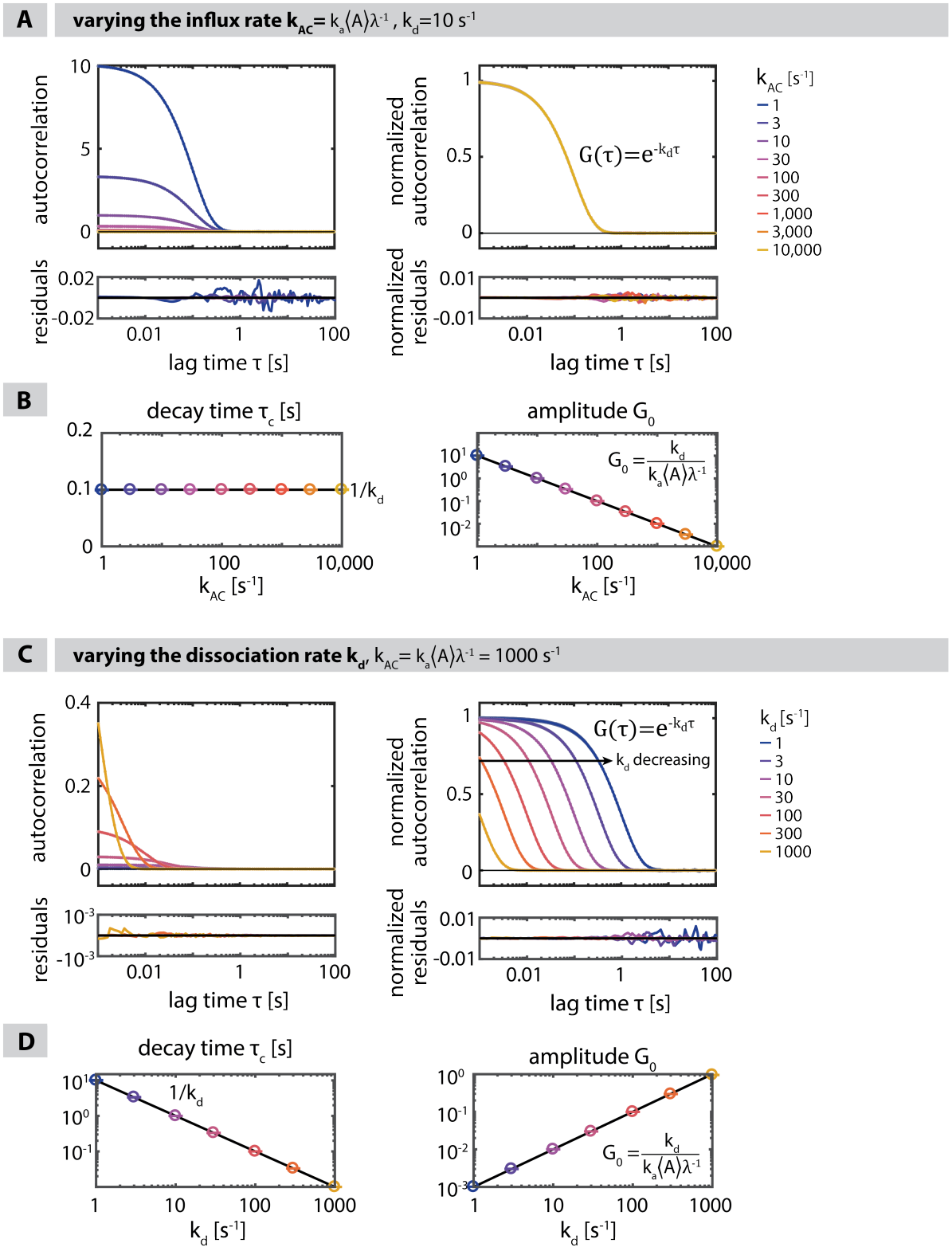

Figure VI.11: caption on next page.

Figure VI.11: Monte Carlo simulation of the autocorrelation function of unspecific surface binding in a two-state system far from surface saturation. **(A)** Simulated autocorrelation curves (upper panel) for the system following the reaction scheme $A \leftrightharpoons C$. The reaction is characterized by the association and dissociation rates k_a and k_d, respectively. We varied the effective association rate $k_{\mathrm{AC}} = k_a \langle A \rangle \lambda^{-1}$ from 1/s (blue) to 10.000/s (yellow). The dissociation rate was fixed to $k_d = 10/\mathrm{s}$. The average of five repetitions, the standard deviation (shaded area) and the fits to the average (solid lines) match the simulated data within the displayed line width. The residuals to the fit are shown in the lower panels. The normalized autocorrelation curve, fit and residuals to the fit (right panel) are independent of the effective association rate k_{AC} and all normalized autocorrelation curves are indistinguishable from $G(\tau) = e^{-k_d \tau}$ within the precision of the simulation. **(B)** Decay time τ_c and amplitude G_0 of the simulated autocorrelation curves overlap with the values predicted by Equation (VI.23) within the precision of the simulation. Error bars represent the standard deviation of the five repetitions and are below the marker size. **(C)** As in (A) but for a fixed effective association rate $k_{\mathrm{AC}} = 1000/\mathrm{s}$ and increasing dissociation rates k_d from 1/s to 1000/s (blue to yellow). **(D)** Decay time τ_c and amplitude G_0 of the autocorrelation curves from (C), displayed as in (B).

left panel).

Importantly, our simulations suggest that taking into account the amplitude information, the effective association rate and dissociation rate can be determined independently from the fit without a saturation of the surface. The accuracy of the amplitude information is improved if the appropriate background correction is performed (Equation II.42, p. 22).

We believe this finding to be of high relevance for the quantification of membrane binding, when no surface saturation can be reached. In particular, the binding rates of the partitioning of amphipathic peptides to membrane are one potential application. Well-characterized membrane binding reactions exhibiting a single-exponential binding behavior are, however, difficult to identify. We therefore propose to first examine the experimental realization with the model system of DNA hybridization on chol-DNA docking strands diffusing laterally in membrane corrals formed from chromium microstructures (Section VI.2). Increasing the concentration of chol-DNA docking strands, but maintaining imager concentrations far from surface saturation, potentially mimics the situation for membrane binding without further specificity. Identical samples without chol-DNA docking strands allow for precise background quantification from imager strands in solution. In the following section, we investigate the effect of more complex binding mechanism on the autocorrelation function.

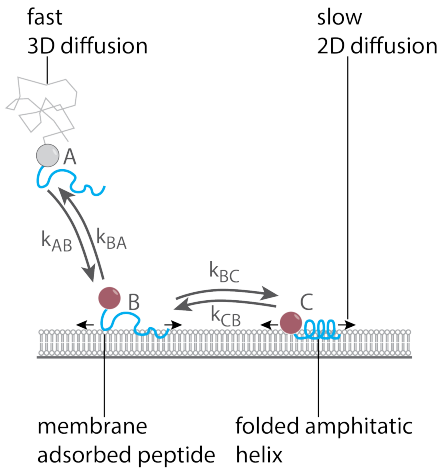

Figure VI.12: Three state model for binding of amphipathic helices following Myers and colleagues [Myers et al., 2012]. The molecule in solution (state A) diffuses fast and the membrane adhesion to state B is characterized by the association rate k_{AB} and the dissociation rate k_{BA}. The adhered molecule can subsequently convert from the unstructured, adhered form B to the folded helical form C with the rates k_{BC} and k_{CB} for forward and back reaction, respectively. The fluorescence signal of the molecule depends on its axial position within the TIRF illumination. Molecules bound to the membrane contribute fluorescence signal (red), while molecules outside the TIRF illumination are not detected (gray). The unbound state A freely diffusing in solution is invisible in the SI-FCS autocorrelation if a separation of time scales between 3D diffusion and binding can be assumed.

VI.3.2 Three-State-Model for Membrane Binding of Amphipathic Helices

For the binding of amphipathic helices to membrane, complex binding kinetics have been observed that go beyond a simple transient binding with monoexponentially distributed residence times [Constantinescu and Lafleur, 2004, Fox et al., 2009, Gerlach et al., 2009]. Myers and colleagues used a three-state model to explain the biexponential cumulative distribution of decay times they observed for the binding of GLP-1 to gel-phase DPPC SLB *via* SPT [Myers et al., 2012]. In this model, the amphipathic helix is unstructured in solution (state A), adheres in a fast reaction with the rate k_{AB} to the membrane (state B) and folds into the helical structure while it is bound to the membrane (Figure VI.12). The folded state C can only be reached from the adhered state and can only decay back into the adhered state with the rates k_{BC} and k_{CB}, respectively. From the adhered state B the molecule can dissociate from the membrane with the rate k_{BA}.

To explore the shape of the autocorrelation function expected from such a three-state model, we performed Monte Carlo simulations resembling the peptide binding. We extended the simulations of the previous section (Section VI.3.1) by introducing a third state B as intermediate state of the strongly bound state C and the solution state A,

$$\mathrm{A} \underset{\mathrm{k_{BA}}}{\overset{\mathrm{k_{AB}}}{\rightleftharpoons}} \mathrm{B} \underset{\mathrm{k_{CB}}}{\overset{\mathrm{k_{BC}}}{\rightleftharpoons}} \mathrm{C}\,. \tag{VI.25}$$

We assume the brightness to be homogeneous and identical for peptides adhered in state B or inserted in state C to the membrane. For the fluorescence detection, the states are therefore indistinguishable. Only the different residence times can be used to infer information about states B or C. In practice, fluorescent properties can change upon interaction with the membrane, but changes can be minimized by flexible linkers keeping the fluorophore in solution. As before, molecules diffusing in solution were simulated by a constant influx on the membrane k_{AB}. We assumed no observable lateral diffusion, as expected for a pseudo-infinite detection or a confinement with reflective boundaries. Furthermore, fluorescent molecules are invisible prior to binding, equivalent to a fully equilibrated solution diffusion on the time scale of the binding reaction. For very fast exchange of molecules between solution and membrane or very large lateral integration areas, the solution diffusion has to be taken into account, as discussed before (Sections V.1 and VI.2). In all cases, we assume no lateral interaction of bound molecules and no saturation of the surface. Notably, we simulated five fluorescence intensity traces per condition, in absence of noise for a measurement time of $t_{\mathrm{tot}} = 6\,\mathrm{h}$ each.

We systematically varied the reaction rates in our simulation to test the effect on the obtained autocorrelation curves (Figure VI.13). We found that generally the autocorrelation curves are well described by a bi-exponential decay of the form

$$G(\tau) = G_1 e^{-r_1\tau} + G_2 e^{-r_2\tau}\,, \tag{VI.26}$$

with the decay rates r_1 and r_2 and the amplitudes G_1 and G_2. The residuals to the fit show no systematic deviation, suggesting that the model matches the autocorrelation function within the precision of the simulation. Strikingly, the two reactions appear as two distinct contributions of the autocorrelation function, even if they are indistinguishable in their fluorescent signal. The decay rates depend on the reaction rates k_{BA}, k_{BC} and k_{CB} (Figure VI.13D, F and H). Notably, we do not find a dependence of the decay rates on the adsorption rate k_{AB} to the membrane (Figure VI.13A and B). This finding is in agreement

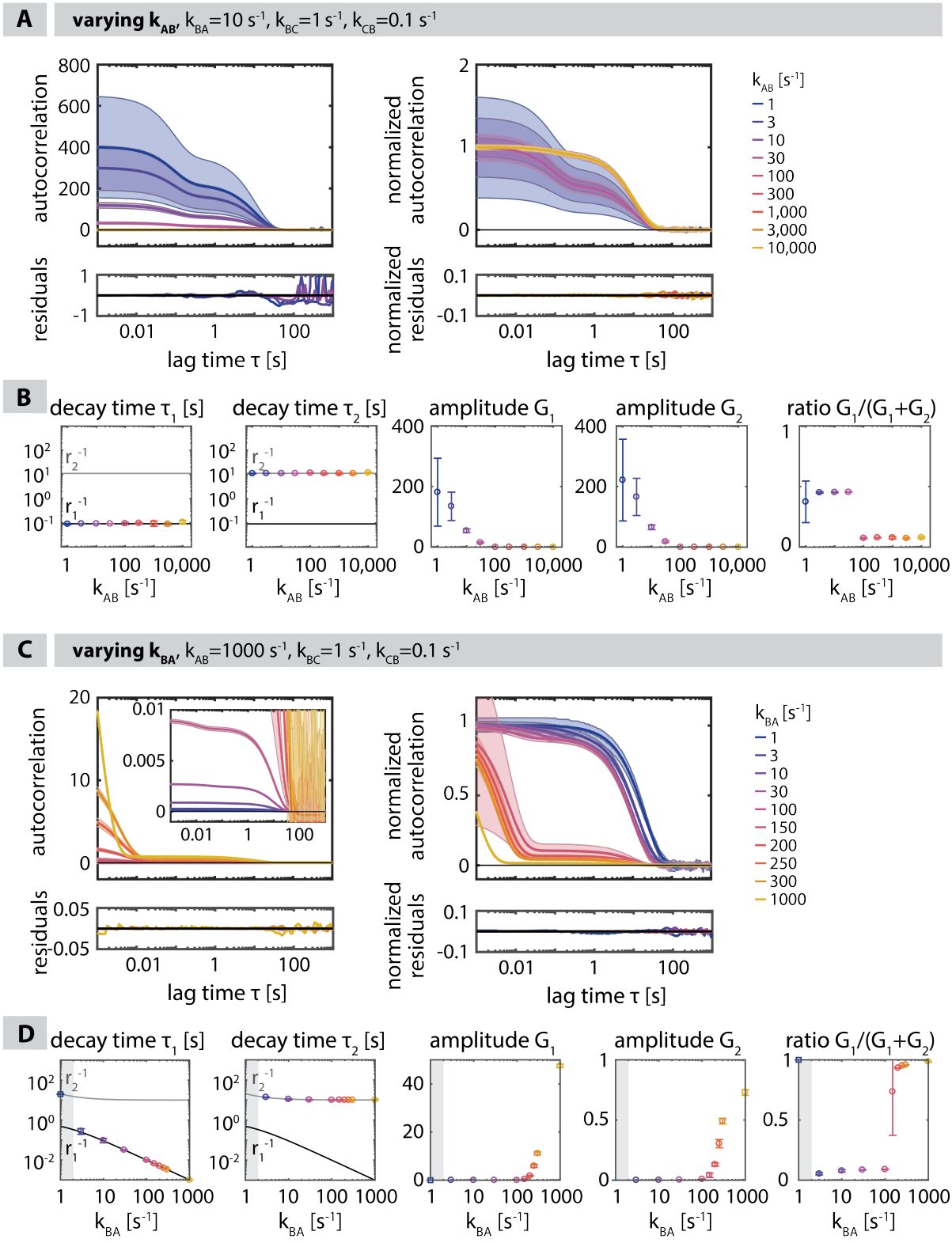

Figure VI.13: continues on next page.

Figure VI.13: cont.

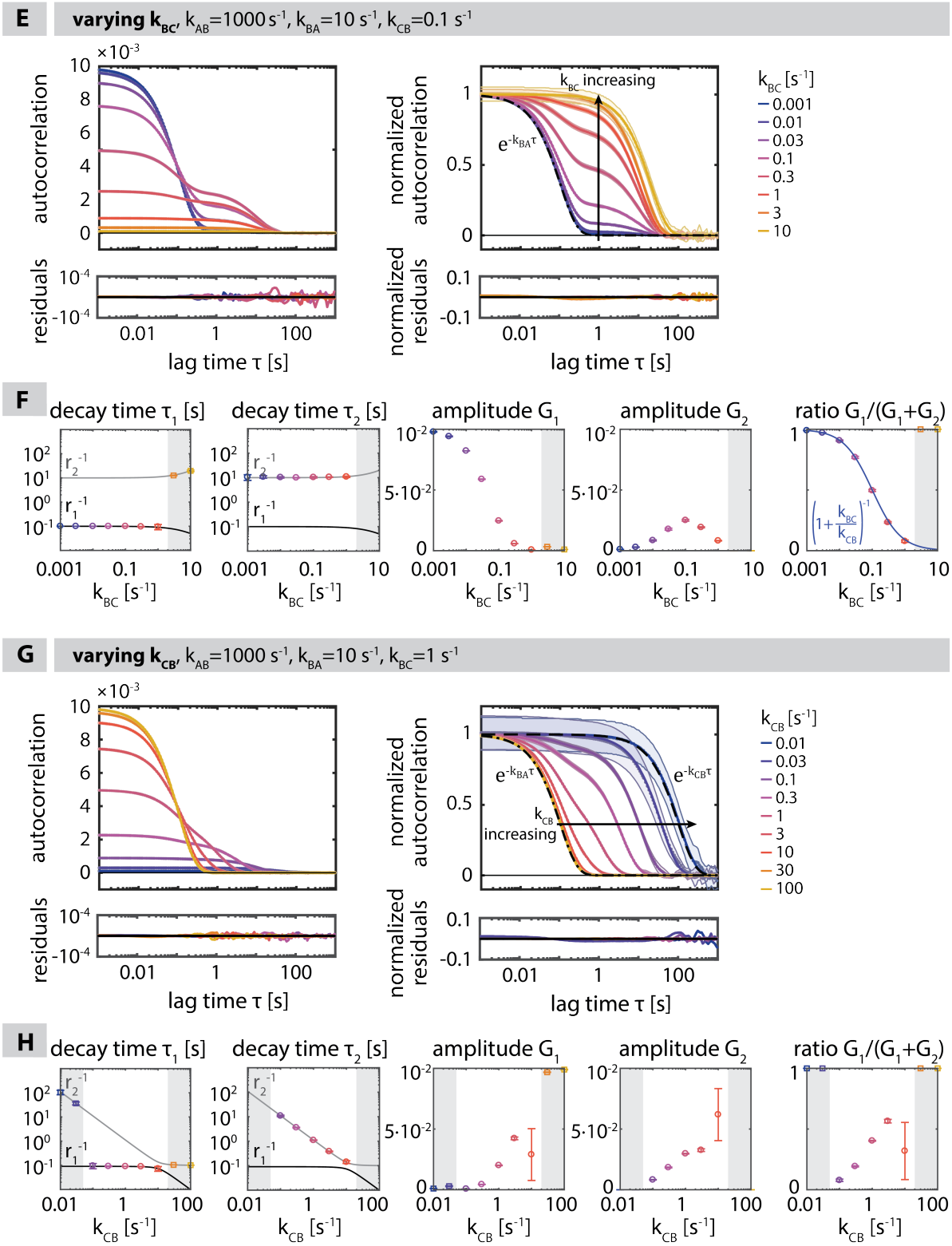

Figure VI.13: caption on next page.

Figure VI.13: Monte Carlo simulation of the autocorrelation function of a three-state system. (A) Effect of the variation of k_{AB} from 1/s (blue) to 10 000/s (orange) on the autocorrelation curves (left upper panel) and the normalized autocorrelation (right upper panel). Data points of the autocorrelation curves are overlaid with the respective fits (Equation VI.26, solid lines). Residuals to the fits are shown in the respective lower panels. Errors are given by the standard derivation of five repetitions. **(B)** Panels for the fit parameters from (A) (left to right): (i) decay time $\tau_1 = r_1^{-1}$ and (ii) decay time $\tau_2 = r_2^{-1}$, with the expected decay times from Equation (VI.28a, black solid line) and (VI.28b, gray solid line); (iii) amplitude G_1, (iv) amplitude G_2 and (v) the ratio of the amplitudes $G_1/(G_1+G_2)$. **(C)** Variation of k_{BA} from 1/s (blue) to 1000/s (orange), displayed as in (A). For large k_{BA} ($k_{BA} \geq 300$/s), the amplitude G_1 increases strongly and is fully displayed in the inset. **(D)** Fit parameters from (C), displayed as in (B). For $k_{BA} \leq 1$/s, the decay was better described by a monoexponential decay (Equation VI.27) and is thus marked by squares (gray shaded area). **(E)** Variation of k_{BC} from 0.001/s (blue) to 10/s (orange), displayed as in (A). In the limiting case of small k_{BC}, the decay time of the autocorrelation is determined by k_{BA} (black dot-dashed line). **(F)** Fit parameters from (E), displayed as in (B) and (D), but with the monoexponential fit applied for $k_{BC} \geq 3$/s (squares and gray shaded areas). Empirically we found the amplitude ratio $G_1/(G_1+G_2)$ to follow $(1+k_{BC}/k_{CB})^{-1}$ (blue line). **(G)** Variation of k_{CB} from 0.01/s (blue) to 100/s (orange), displayed as in (A). The monoexponential limiting cases for small and large k_{CB} were found as $G(\tau) \sim \exp(-k_{CB}\tau)$ (black dashed line) and $G(\tau) \sim \exp(-k_{BA}\tau)$ (black dot-dashed line), respectively. **(H)** Fit parameters from (C), displayed as in (B) and (D). The monoexponential fit was applied for $0.03\text{/s} \leq k_{CB} \leq 30$/s (squares and gray shaded areas).

with the membrane binding of a two-state model system (Section VI.3.1), where in absence of surface saturation the decay time is only determined by the dissociation rate (Figure VI.11). If the amplitude of one contribution to the autocorrelation curves is vanishing or the decay times converged to common value, the autocorrelation curves are more accurately described by a monoexponential model (Figure VI.13)

$$G(\tau) = G_1 e^{-r_1 \tau} \,. \tag{VI.27}$$

Analyzing the decay rates $r_1 = \tau_1^{-1}$ and $r_2 = \tau_2^{-1}$ of the autocorrelation curves, we found the rates extracted from our simulations to be in good agreement with the decay rates previously derived for the three-state system by Myers and colleagues [Myers et al., 2012] for the special case of residence time histograms (Figure VI.13, Panels τ_1 and τ_2). The rates of the autocorrelation function and the residence time histograms r_1 and r_2

depend on the reaction rates k_{BA}, k_{BC} and k_{CB} as:

$$r_1 = \frac{1}{2}\left(k_{\mathrm{BA}} + k_{\mathrm{BC}} + k_{\mathrm{CB}} + \sqrt{(k_{\mathrm{BA}} + k_{\mathrm{BC}} + k_{\mathrm{CB}})^2 - 4k_{\mathrm{BA}}k_{\mathrm{CB}}}\right) , \tag{VI.28a}$$

$$r_2 = \frac{1}{2}\left(k_{\mathrm{BA}} + k_{\mathrm{BC}} + k_{\mathrm{CB}} - \sqrt{(k_{\mathrm{BA}} + k_{\mathrm{BC}} + k_{\mathrm{CB}})^2 - 4k_{\mathrm{BA}}k_{\mathrm{CB}}}\right) . \tag{VI.28b}$$

We displayed the dependence of r_1 and r_2 as black and gray solid lines in Figure VI.13 (Panels τ_1 and τ_2), respectively. Varying the reaction rates over multiple orders of magnitude throughout our simulation, we did not find significant deviations of our simulations from Equation VI.28. We therefore conclude that Equation VI.28 accurately describes the decay rates of the autocorrelation function of the investigated three-state system. However, for similar decay rates r_1 and r_2, the rates and amplitudes of the autocorrelation curves are only extracted with limited accuracy from the biexponential fit ($k_{\mathrm{CB}} = (10, 30)$/s, Figure VI.13H). This effect is a problem of the fitting routine and the noise of the simulation, but does not indicate a mismatch of theory (Equation VI.28) and simulated data.

Of special interest are limiting cases of the decay rates r_1 and r_2 depending on the ratio of the determining reaction rates. For some ratios, the dependence of the measured decay rates on the molecular reaction rates simplifies drastically, allowing for a direct experimental extraction of the reaction rates. Importantly, if the reaction rate k_{BC} to state C is much smaller than the back reaction k_{CB}, i.e. state C has a long lifetime, the decay rates r_1 and r_2 are determined directly by the two reaction rates k_{BA} and k_{CB}, respectively:

$$\text{for } k_{\mathrm{BC}} \ll k_{\mathrm{CB}}, k_{\mathrm{BA}}: \quad r_1 \approx k_{\mathrm{BA}} , \tag{VI.29}$$

$$r_2 \approx k_{\mathrm{CB}} . \tag{VI.30}$$

Our simulations suggest that in the limit of very small k_{BC} the autocorrelation function will be dominated by G_1 and thus only r_1 is experimentally accessible (Figure VI.13E and F). In return, in this limit the autocorrelation directly encodes the decay rate from B to A, k_{BA} and state C becomes negligible.

For small k_{CB}, i.e. a long lived state C, the contribution to the autocorrelation function at larger lag times is mainly determined by k_{CB} (Figure VI.13G and H). Assuming $k_{\mathrm{BC}} \gg k_{\mathrm{CB}}$, for $k_{\mathrm{CB}}/k_{\mathrm{BA}} < 100$, we find a monoexponential decay determined by k_{CB}. In the intermediate range $100 < k_{\mathrm{CB}}/k_{\mathrm{BA}} < 1$, we find a biexponential decay, with the two decay times directly related to the lifetime of the states B and C, $r_1 \approx k_{\mathrm{BA}}$ and $r_2 \approx k_{\mathrm{CB}}$.

In some cases, Equation VI.28 may aid in extracting the underlying molecular reaction

rates from the decay rates of the autocorrelation function. To determine the reaction rates independently, the amplitudes or the ratio of the amplitudes need to be considered.

The amplitude shows a strong dependence on the underlying reaction rates. Up to now, we are unable to provide a consistent theory describing the amplitudes G_1 and G_2 of the autocorrelation function in dependence of the reaction rates. For the variation of k_{BC} we found empirically that the ratio of the the amplitudes is described by (Figure VI.13F)

$$\frac{G_1}{G_1 + G_2} = \frac{1}{1 + \frac{k_{\mathrm{BC}}}{k_{\mathrm{CB}}}} \quad (k_{\mathrm{AB}}\,, k_{\mathrm{BA}}\,, k_{\mathrm{CB}} = \mathrm{const.})\,, \tag{VI.31}$$

highlighting that the amplitudes encode valuable information about the reaction rates, similar to the two-state case (Section VI.3.1). The biexponential autocorrelation function, exhibiting two decay times and two amplitudes will potentially contain a similar set of information compared to the single-particle residence time histograms, previously used to determine the complete set of binding rates by Myers and colleagues [Myers et al., 2012]. While Myers and colleagues required immobilized binding events to gel-phase lipid bilayers for the determination of residence times, taking into account the advantages of SI-FCS over SPT, investigations on fluid lipid bilayers become possible. Especially the lower irradiances required for quantification allow SI-FCS to extract binding kinetics in systems exhibiting lateral diffusion, when quantification with SPT fails due to the increased motion blur. We therefore highlight the importance of finding the correct dependence of the amplitudes G_1 and G_2 on the reaction rates.

VI.3.3 Examples of Reversibly Membrane-partitioning Peptides

The underlying principles of the partitioning of biologically relevant proteins towards lipid membranes can be quite complex and are thus best studied utilizing synthesized peptides instead of full purified proteins [White and Wimley, 1998]. In the following, we identified multiple candidates for the initial study of the membrane partitioning of amphipathic helical peptides with SI-FCS.

In the context of the *in vitro* reconstitution of bacterial cytokinesis, we investigated the membrane binding of in total eight different bacterial peptides acting as membrane targeting sequences (MTSs) [Ramm et al., 2018a]. In a simplified approach, we estimated the partitioning in solution and bound to the membrane by confocal fluorescence microscopy (Figure D.3, p. 306). Prokaryotic membranes usually contain charged lipid head groups and the binding of bacterial MTS depends on electrostatic attraction. Systematically in-

vestigating the binding rates of the MTS would facilitate a first quantitative glimpse at the binding modalities of an entire class of proteins long known to organize bacterial cells at many levels [Surovtsev and Jacobs-Wagner, 2018, Stewart, 2005, Pichoff and Lutkenhaus, 2005, Carballido-López, 2006, Kretschmer and Schwille, 2016].

Fox, Myers and colleagues investigated binding of the human peptide hormone GLP-1 to DPPC bilayers [Fox et al., 2009, Myers et al., 2012]. GLP-1 is involved in the glucose metabolism and is thus of special interest as therapeutic target against diabetes type 2 and obesity [Kieffer and Francis Habener, 1999, Choi et al., 2004, Nielsen et al., 2004, Meier and Nauck, 2005]. Myers and colleagues found a biexponential distribution of residence times with $\tau_1 = (1.19 \pm 0.05)\,\mathrm{s}$ and $\tau_2 = (19 \pm 2)\,\mathrm{s}$ and therefore both in a time range accessible to SI-FCS. However, DPPC forms gel-phase membranes at room temperature. While gel-phase bilayers simplify their SPT routine, DPPC bilayers are of limited physiological relevance and are expected to significantly alter membrane partitioning. For binding to fluid membrane compositions, the binding is potentially stronger as the bilayer is easier to penetrate.

For investigating the anchoring of DNA origami structures to free standing model membranes and subsequent induction of membrane curvature, Macrini, Franquelim and colleagues characterized the membrane binding of multiple eukaryotic amphipathic peptides (unpublished data, in parts found in [Macrini, 2015]), such as the N-terminal amphipathic helix of the COPII small G-protein Sar1p [Lee et al., 2005], the amphipathic lipid packing sensor (ALPS) of the COPI protein ArfGAP1 [Vanni et al., 2013], the N-terminal domain of the N-BAR protein Endophilin [Gallop et al., 2006], the N-terminal amphipathic helix of the ESCRT-III Snf7 protein (Snf7) and finally the MPER domain of the HIV-1 viral envelope protein (gp41) [Veiga and Castanho, 2007, Sun et al., 2008, Montero et al., 2008, Apellaniz et al., 2010, Franquelim et al., 2010].

Of the aforementioned amphipathic helices, we identified fluorescently labeled MPER (sequence: ELDKWASLWNWF, Section D.2.2, p. 297) as the most promising candidate for an initial study with SI-FCS. MPER is a segment of the transmembrane domain of the gp41 protein of the HIV-1 virus and has been identified as target for broadly neutralizing antibodies [Nelson et al., 2007, Frey et al., 2008, Sun et al., 2008]. Moreover, MPER serves as MTS for the anti-HIV drug Enfuvirtide [LaBonte et al., 2003, Lalezari et al., 2003] increasing its potency [Champagne et al., 2009, Wexler-Cohen and Shai, 2007, Peisajovich et al., 2003] (reviewed in e.g. [Liu et al., 2014]).

Given the large relevance of MPER, its membrane interaction has been characterized

intensively [Veiga and Castanho, 2007,Sun et al., 2008]. Structurally, the full-length MPER consists of two helical segments connected by a hinge. Here, we study the N-terminal helix utilized for Enfuvirtde, which binds to bilayers irrespective of membrane curvature and is thus highly suited for studies on SLB [Franquelim et al., 2011]. Other amphipathic peptides like ALPS and Snf7 only bind to curved membranes, i.e. lipid vesicles. Further, MPER has a net negative charge of -1 and binds to membranes widely independent of electrostatics. MPER has been described to exhibit a cholsterol-binding motif [Vincent et al., 2002]. Further, cholesterol plays an important role in HIV infection [Montero et al., 2008] and the viral membrane has a high cholesterol to phospholipid ratio [Raulin, 2002]. Thus, it is of high relevance to determine MPER binding rates in dependence on the cholesterol content of the membrane.

VI.3.4 Confinement of Lateral Diffusion on SLB Patches

Confinement of the lateral membrane diffusion allows to apply remarkably simplified fitting models (Section VI.1.2, p. 118 and Section VI.2.3, p. 145). Furthermore, some amphipathic helices show a complex binding behavior [Fox et al., 2009, Myers et al., 2012, Constantinescu and Lafleur, 2004, Gerlach et al., 2009] (see also Monte Carlo simulations in Section VI.3.2, p. 162). Eliminating the influence of diffusion on the autocorrelation function enables a direct assessment of the binding contribution to the autocorrelation function and thus appears as a promising approach for quantifying the membrane binding of amphipathic helices and MPER.

We initially tested a minimal modification of the well-established SLBs, by preparing patches of SLB formed from bursted giant unilamellar vesicles (GUVs) on a microscopy coverslip [Hamai et al., 2007, Chiaruttini et al., 2015]. Advantages of SLBs are the high mobility of the upper leaflet and thus also the adaptation to inserted molecules [Tamm and McConnell, 1985]. Patches of SLB have been previously used to study the reversible membrane attachment of the MinDE system with high speed AFM [Miyagi et al., 2017]. In brief, we electroformated GUVs from DOPC doped with 0.05 % Atto655-1,2-dioleoyl-*sn*-glycero-3-phosphoethanolamine (DOPE) in sucrose solution to let them sink in an SLB chamber down to the coverslip. Mixing of the buffer solution lets the GUVs burst on the coverslip, creating patches of SLB with diameters ranging from 1 to 100 µm (for detailed Materials and Methods see Appendix D.2.3, p. 297). The density of the SLB patches can easily be tuned by dilution of the initial GUV solution prior to incubation on the coverslip.

We further incubated the SLB patches with MPER to investigate the peptide-membrane

binding. Before measuring SI-FCS autocorrelation curves, we encountered problems arising from unspecific binding and long-term sample instabilities of Atto488-MPER, both interfering with the SI-FCS measurements. Large area TIRF microscopy tile scans revealed not only unspecific binding of MPER to the coverslip area not covered by SLB, but also areas covered by a largely homogeneous layer of MPER (Figure VI.14A and C). Passivation of the glass surface with 5 mg/ml β-caseine prior to the addition of MPER reduced the non-specific binding of MPER and prevented the formation of islands of MPER on the coverslip (Figure VI.14B). With passivation binding is primarily observed to areas covered with SLB patches. However, even in presence of β-caseine we were unable to rule out residual unspecific binding to the coverslip.

During the long acquisition series required for accurate SI-FCS quantification, we observed an increase of the fluorescence signal over time in the observation region (Figure VI.15A). Acquiring TIRF microscopy tile scans covering the previously illuminated region, we found the increase in fluorescence intensity to be localized within the area illuminated during the times series (Figure VI.15C). Apparently, excitation of Atto488-MPER is generating an imprint of the illumination pattern in the sample. Remarkably, imperfections of the illumination pattern are transferred to the immobilized peptide layer. We speculate, that a potential cause might be the photo-induced cross-linking of the irradiated peptide with the glass coverslip or the β-caseine coating. The increasing fluorescence intensity indicates that, in our hands, the rate of photo-induced immobilization of MPER on the passivated coverslip is higher than the rate of photo-bleaching of the Atto488 fluorescent label. The imprinted pattern shows a remarkable linearity with the excitation pattern and could potentially be exploited for peptide-based photo-lithography applications. To test if the photo-induced immobilization of MPER is a direct process or if it is mediated indirectly via ROS, we recorded a time series in presence of the oxygen scavenger PO+C (see chapter IV for details on PO+C). In the presence of PO+C, we observe a drastically reduced increase in the fluorescence intensity around the recorded SLB patch (Figure VI.15B). Accordingly, the illumination pattern is imprinted in a strongly decreased intensity, highlighting the involvement of ROS in the photo-induced immobilization of MPER. As photo-bleaching of Atto488 is reduced in the presence of PO+C, we conclude from the lower fluorescence intensities that ROS are the main contributor to the photo-immobilization. We observe a residual increase over time in fluorescence intensity on the SLB patch and on the surrounding coverslip even in the presence of PO+C. As the extent of photo-immobilization of MPER-Atto488 is reduced below the bleaching rate of Atto488 in presence of PO+C, it

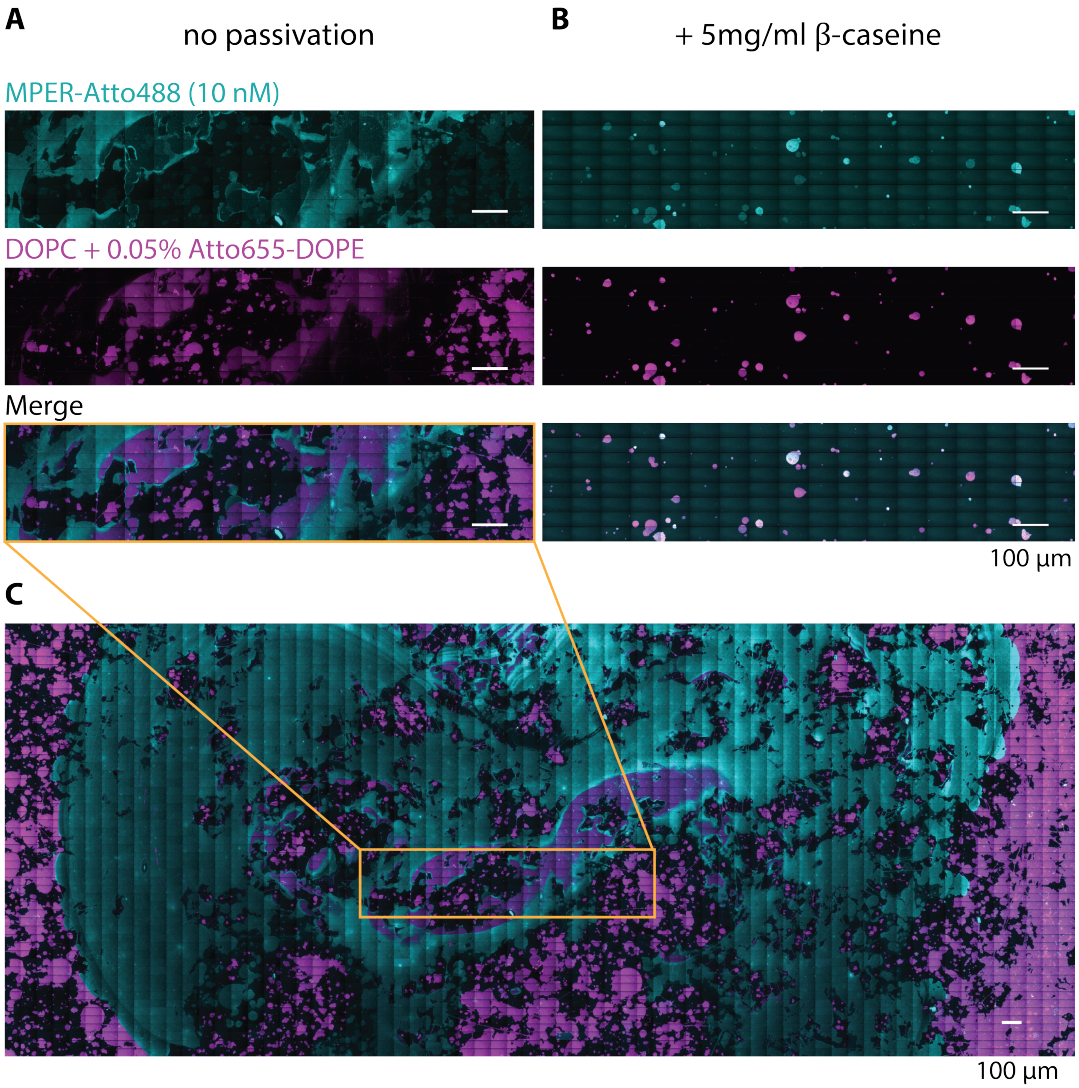

Figure VI.14: MPER binds unspecifically to glass and forms islands of peptide. Representative TIRF microscopy tile scans (A, B: 18 × 8 tiles, C: 67 × 53 tiles, each 81 × 41 µm^2) to investigate the binding of MPER to SLB patches and glass. **(A)** MPER (cyan) binds to the exposed glass surface of the coverslip in absence of passivation, preferentially to areas not covered by SLB patches (magenta). **(B)** Passivating the cover glass with 5 mg/mL β-caseine reduces MPER binding to glass. MPER is binding preferentially to SLB patches.**(C)** Overview image highlighting the large scale distribution of MPER and SLB patches in the sample in (A). The displayed brightness was adjusted individually in (A) and (B). SLB patch composition DOPC with 0.05 mol % Atto655-DOPE, 10 nM Atto488-MPER in SLB buffer.

can be neglected. The residual long-term trend of the intensity is corrected by de-trending of the intensity [Macháň et al., 2016] (Section VI.3.4.2 and D.1.4). The photo-induced immobilization of MPER highlights once more the importance of oxygen scavenging systems to avoid photo-induced artifacts in long fluorescence microscopy acquisition series (Chapter IV).

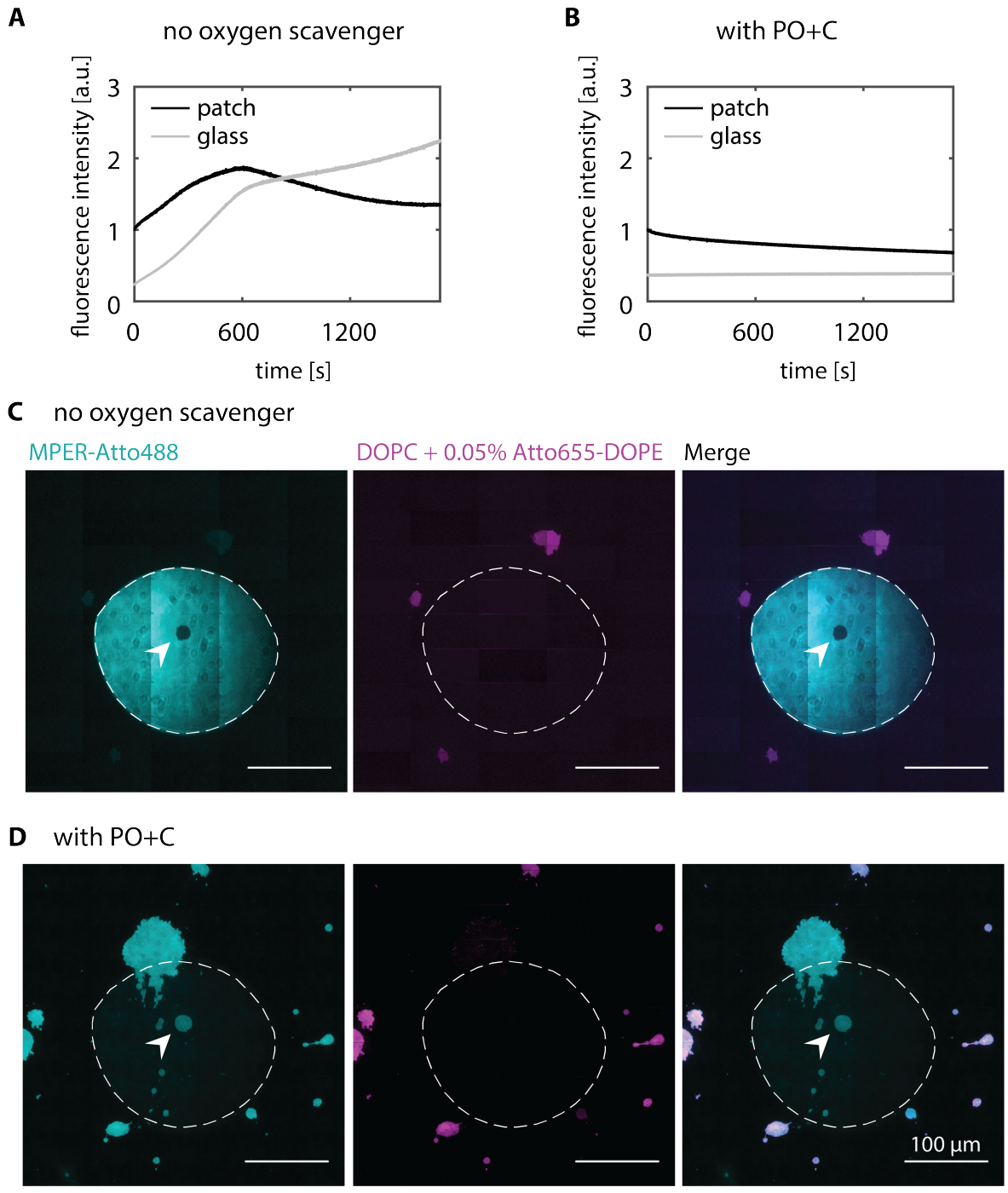

Figure VI.15: caption on next page.

Figure VI.15: MPER irreversibly attaches to glass upon irradiation with excitation light. Excitation at a wavelength of 488 nm imprints the excitation pattern as surface-attached peptide on the passivated cover-glass. **(A)** Change in fluorescence intensity on the SLB patch (black) and the surrounding cover glass (gray). The cover glass was passivated with 5 mg/mL β-caseine prior to addition of MPER. **(B)** In the presence of oxygen scavenger (PO+C), the increase in fluorescence intensity on the patch (black) and the surrounding passivated coverslip (gray) is significantly reduced. **(C)** TIRF microscopy tile scan of the irradiated area after the acquisition shown in (A). The excitation pattern, including fringes from non-perfect optics, is imprinted as bright fluorescent signal on the sample (left panel, cyan, white dashed outline). The observed SLB patch is dark, as it increased less in fluorescence intensity than the surrounding coverslip (white arrow). The lipid-anchored dye in the SLB patch is photo-bleached at the end of the acquisition, while SLB patches outside the illuminated area are unaffected (center panel, magenta). Overlay of MPER and membrane signal (right panel). **(D)** In presence of oxygen scavenger, after irradiation during the time series shown in (B), the SLB patch (white arrow) is bright compared to the surrounding cover glass. A low intensity imprint of the excitation is barely visible after 1.2 h of irradiation (white outline, left panel). The membrane staining of the investigated SLB patch is photo-bleached over the acquisition in (B) (center panel). Overlay of MPER and membrane signal (right panel). The displayed brightness was adjusted individually in (C) and (D). SLB patch composition DOPC with 0.05 mol % Atto655-DOPE, 10 nM Atto488-MPER in SLB buffer with 5 mg/ml β-caseine.

VI.3.4.1 Determining the Saturation Regime of MPER Binding to SLBs

A saturation of surface binding sites can be exploited in titration series to extract the binding rates from the change in the characteristic decay time τ_c of SI-FCS autocorrelation curves (Chapter III). However, for binding of peptides to SLBs and thus in the absence of individual sparse binding sites, a change in the characteristic decay time potentially coincides with a fully covered SLB (Sections VI.1.2 and VI.3.2). In this case, high concentrations of membrane-attached peptide result in small fluorescence fluctuations arising from individual molecules reversibly binding to the the lipid bilayer. Thus, autocorrelation curves are difficult to extract in the saturation regime, while additionally the assumption of independent binding sites is potentially violated. Peptide-peptide interactions and compromised membrane integrity further complicate the interpretation of obtained results [Hsieh et al., 2010,Shih et al., 2011,Melo et al., 2009,Brogden, 2005,Cornell and Taneva, 2006,Khandelia et al., 2008]. Consequently, for our exploration of the capabilities of SI-FCS to quantify binding kinetics, it is important to determine the saturation regime of peptide binding to the membrane.

In brief, we recorded TIRF microscopy images of increasing concentrations of fluorescently labeled MPER (Atto488-MPER) binding to DOPC SLBs (Figure VI.16). For detailed Materials and Methods see Appendix D.2.4 (p. 299). The fluorescence intensity approaches a saturation for MPER concentrations above 1 µM of MPER in solution. In principle, from the titration of the binding peptide and by fitting with an appropriate binding model the partition coefficient K_p or the association constant K_d can be extracted [Pisarchick and Thompson, 1990, Kalb et al., 1990, Hsieh et al., 1992, Thompson et al., 1997, Sheets et al., 1997, Wieprecht and Seelig, 2002]. The measured fluorescence intensity is determined by the concentration of MPER bound to the SLB and the concentration of MPER in solution [Kalb et al., 1990, Thompson et al., 1997]. Precise quantification of the saturation curve thus requires separate determination of the solution fluorescence contribution. Unspecific binding of MPER (Figure VI.14) hindered the determination of the solution contribution. We added a Langmuir isotherm as a guide to the eye in Figure VI.16, but refrained from extracting K_d. Assuming that MPER does not alter the photophysical properties of Atto488, a dye solution can potentially be used to calibrate the solution concentration in future experiments.

The solution concentration of MPER leading to membrane saturation is higher than 1 µM. However, at such high solution concentrations, the solution contribution starts to dominate the autocorrelation function and binding fluctuations become negligible, as dis-

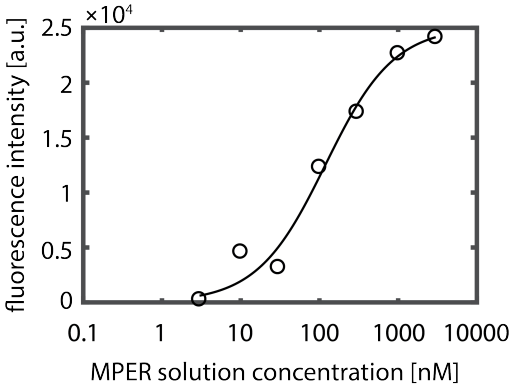

Figure VI.16: Determination of saturation regime of MPER binding to SLBs. Average fluorescence intensities of TIRF microscopy images of Atto488-MPER binding to a DOPC SLB (circles). Data points were fit to a Langmuir isotherm (Equation D.6, p. 299) as a guide to the eye. SLB composition DOPC with 0.05 mol % Atto655-DOPE, Atto488-MPER in SLB buffer.

cussed above (Section VI.1.2.5 and Figure VI.10). Therefore, it is challenging to extract reliable parameters from SI-FCS curves. This limits in particular the accessibility of binding rates in titration experiments. For MPER concentrations below 100 nM, however, saturation effects can be neglected.

VI.3.4.2 Membrane Diffusion of MPER is Confined to SLB Patches and the Binding Contribution Shows Multiple Components

After reducing unspecific binding and photo-induced immobilization of Atto488-MPER, we recorded SI-FCS autocorrelation curves on individual SLB patches. Most importantly, we set out to verify that SLB patches confine the lateral membrane diffusion.

We recorded time series of the reversible binding of fluorescently labeled MPER to SLB patches as described previously (Section VI.2). In an initial test, we integrated the fluorescence signal in rectangular areas centered on the SLB patch to obtain intensity traces (Figure VI.17A). For the binding of MPER to SLB patches, a monoexponential detrending (Chapter III) did not properly account for the long-term drift of the fluorescence intensity trace. We therefore corrected the traces with a polynomial detrending (see Materials and Methods, Section D.1.4 in the Appendix, p. 295), as it offers more flexibility in correcting arbitrary fluctuations in the intensity trace [Macháň et al., 2016]. Importantly, corrected autocorrelation curves decay close to zero, while uncorrected traces decay over a wide range

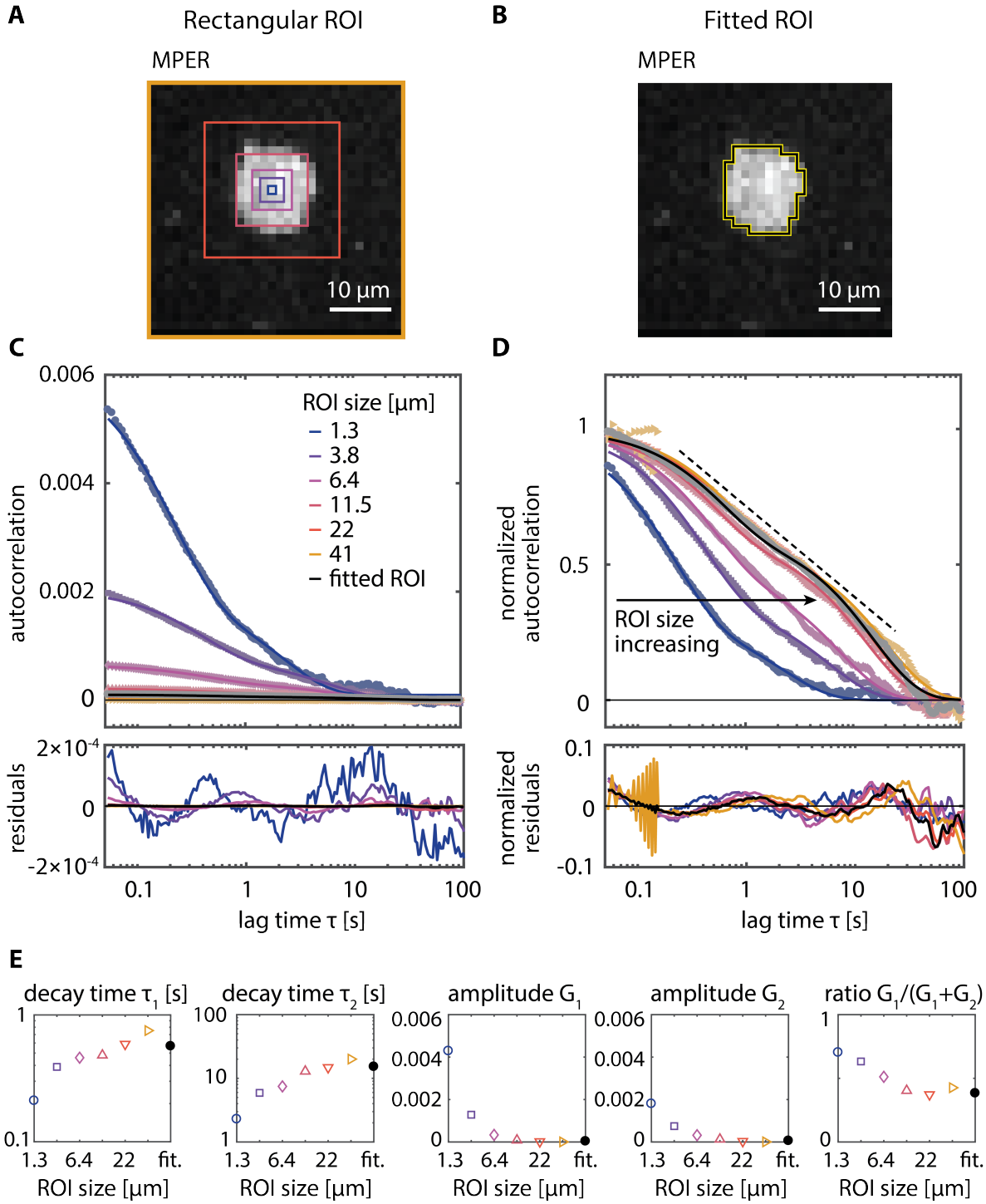

Figure VI.17: caption on next page.

Figure VI.17: Influence of the integrated area on the autocorrelation function on SLB patches. (A) Individual frame of the time series showing one SLB patch covered with MPER (white). Rectangular ROI over which the signal was integrated are indicated. The size of the ROI was increasing from 1.3 µm (blue) to 41 µm (orange). Scale bar: 10 µm. **(B)** Fitted ROI enclosing the the patch (black-yellow outline). **(C)** Autocorrelation curves (left panel) calculated from intensity traces generated by integration over the ROI shown in (A, colored) and (B, experimental data gray, fit black). Data points were fitted with a biexponential fit model (Equation VI.32) (solid lines). An imaginary convergence boundary is shown as guide to the eye with an arrow indicating the change in the decay time of the autocorrelation function with increasing ROI size. **(D)** Normalized autocorrelation curves otherwise displayed as in (C). **(E)** Extracted parameters of the biexponential fit for the different ROI sizes. From left to right: the decay time τ_1 of the faster component, the decay time τ_2 of the slower component, amplitudes G_1 and G_2 of the two components and the ratio $G_1/(G_1 + G_2)$. Rectangular ROI are indicated by open colored symbols, the fitted ROI (fit.) as black filled circle. SLB patch composition DOPC with 0.05 mol % Atto655-DOPE, 20 nM Atto488-MPER in SLB buffer with 5 mg/ml β-caseine.

of time scales.

Increasing the side length a of the integrated region, we observe a decrease in the amplitude of the autocorrelation curves and a shift of the decay towards longer times (Figure VI.17C and D, blue to orange). Strikingly, these results are in line with our observations for laterally diffusing chol-DNA handles hybridizing with fluorescent imager strands from solution (Figure VI.6, p. 142). Both shifts are supposedly caused by diffusion dynamics of MPER on the membrane, creating intensity fluctuations when crossing the integrated ROI. For large acquisition regions, fully enclosing the SLB patch, we observe a saturation of the decay of the autocorrelation curves (Figure VI.17D). The saturation of the decay times is a direct consequence of the confinement, which eliminates fluctuations originating from diffusion.

To reduce the influence of unspecific binding events on the obtained autocorrelation curves, we integrated the fluorescence signal over a binary pixel mask covering the SLB patch (Figure VI.17B and Materials and Methods Section D.2.7 in the Appendix, p. 301). Multiplexing of the acquisition of SLB patches is achieved by multiple patches and non-overlapping ROIs in one field of view. The autocorrelation curve obtained from the fitted ROI is displayed in gray (Figure VI.17C and D).

Based on our previous results (Section VI.2), we assume that the autocorrelation curves for ROIs enclosing the SLB patch are dominated by binding dynamics, while smaller ROIs are additionaly influenced by lateral membrane diffusion. However, the autocorrelation

curves show clear deviations from a monoexponential binding model (Equation VI.14, p. VI.14). Following our Monte Carlo simulations for the three-state model binding of amphipathic helices (Section VI.3.2, p. 162), we fitted the autocorrelation curves with a biexponential binding model:

$$G(\tau) = G_1 \exp\left(-\frac{\tau}{\tau_1}\right) + G_2 \exp\left(-\frac{\tau}{\tau_2}\right) + G_\infty \,. \tag{VI.32}$$

Here, G_1 and G_2 denote the amplitudes of the two components and τ_1 and τ_2 the respective decay times. To account for autocorrelation curves decaying to values slightly different from zero for large lag times, we introduce the offset G_∞.

Applying the fit model (Equation VI.32) we found the fits to be in agreement with the experimentally obtained autocorrelation curves. However, we observe systematic residuals, but to an extent comparable with our observations in DNA hybridization experiments (Figure VI.17D and Figure VI.9B, p. 148). The extracted fit parameters support the qualitative observations: The decay times τ_1 and τ_2 saturate for increasing rectangular ROI sizes, while the amplitude is decreasing. The decrease in the ratio of the amplitudes $G_1/(G_1 + G_2)$ highlights the decreasing contribution from lateral diffusion for increasing ROI sizes that is primarily accounted for by the faster decay $G_1 \exp(\tau/\tau_1)$. For large ROIs ($a > 22\,\mu\text{m}$) the ratio $G_1/(G_1 + G_2)$ saturates. The fit parameters for the fitted ROI are in agreement with the fit parameters for the large rectangular ROIs. For short lag times τ, we observe that the experimental autocorrelation curves are systematically higher than the fitting function. As above, we attribute this effect to a residual contribution from surface diffusion (Chapter III and Section VI.2). For long lag times, the autocorrelation curves exhibit a significant noise contribution. Larger ROI are generally more sensitive to noise. Accordingly, we observe additional modulations of the autocorrelation function for the largest rectangular ROI (41 µm) at short lag times that are most likely caused by a setup instability, invisible to all other ROI sizes. Further, we attribute the increased decay times for $a = 41\,\mu\text{m}$ ($\tau_1 = 0.75\,\text{s}$, $\tau_2 = 20\,\text{s}$) compared to the values for already saturated ROIs (22 µm: $\tau_1 = 0.59\,\text{s}$, $\tau_2 = 15\,\text{s}$; fitted ROI: $\tau_1 = 0.57\,\text{s}$, $\tau_2 = 15\,\text{s}$) to contributions from noise or unspecific binding.

VI.3.4.3 Size of SLB Patches Does not Influence Decay Times

If binding kinetics are altered by interaction with the boundary of the SLB patches, smaller patches should result in different binding kinetics compared to larger SLB patches. En-

counters with the perimeter potentially alter the binding probability, leading to faster unbinding events or increased residence times. For a reflective boundary condition, however, the patch size is expected not to influence the decay times of the MPER binding.

Principally, it is possible to extract the perimeter from the recorded images. However, our recordings do not offer a sufficient resolution to the resolve the edges of the SLB patches on a nanometer scale. We thus explored the dependence of the obtained autocorrelation curves on the approximate diameter d of the patch

$$d \approx \sqrt{\frac{4A_{\text{patch}}}{\pi}}\,, \tag{VI.33}$$

with the patch area A_{patch} defined by the area of the fitted integration mask (Figure VI.18).

Analyzing the autocorrelation curves from 14 SLB patches, we observed a clear trend for the amplitudes of the biexponential fit (Equation VI.32) to decrease with increasing ROI size (Figure VI.18C). A quadratic dependence $G_i \sim 1/d^2$ was added in Figure VI.18C for G_1 and G_2 as a guide to the eye. Remarkably, the amplitude ratio $G_1/(G_1+G_2)$ appears constant within the precision of the measurement. In our Monte Carlo simulations of the three-state binding (Section VI.3.2, p. 162), we found the amplitude ratio $G_1/(G_1 + G_2)$ to be a valuable parameter determined by the reaction rates, rather than the total number of events.

Further, we do not observe a trend of the measured decay times τ_1 and τ_2 with the size of the patch. The observed decay times rather seem to scatter randomly around their mean values $\tau_1 = (1.6 \pm 0.5)\,\text{s}$ and $\tau_2 = (50 \pm 20)\,\text{s}$ (mean $\pm$ standard deviation of the individual fit parameters). We therefore conclude that a trend with the SLB patch area is, if present, smaller than our measurement precision and further assume the SLB patch perimeter to act as a reflective boundary.

VI.3.4.4 Dependence of the Autocorrelation Function on the Peptide Concentration

Finally, we set out to investigate if we are able to observe a dependence of our SI-FCS autocorrelation curves on the peptide concentration in solution. Our Monte Carlo simulations suggest that far from surface saturation, only the amplitude of the autocorrelation function depends on the peptide concentration (Figure VI.13A and B, p. 166). Investigating the saturation of the fluorescence intensity of MPER binding to SLBs, we found that a surface saturation sets in around $\langle A \rangle_{\text{MPER}} = 1\,\mu\text{M}$ (Figure VI.16). We recorded

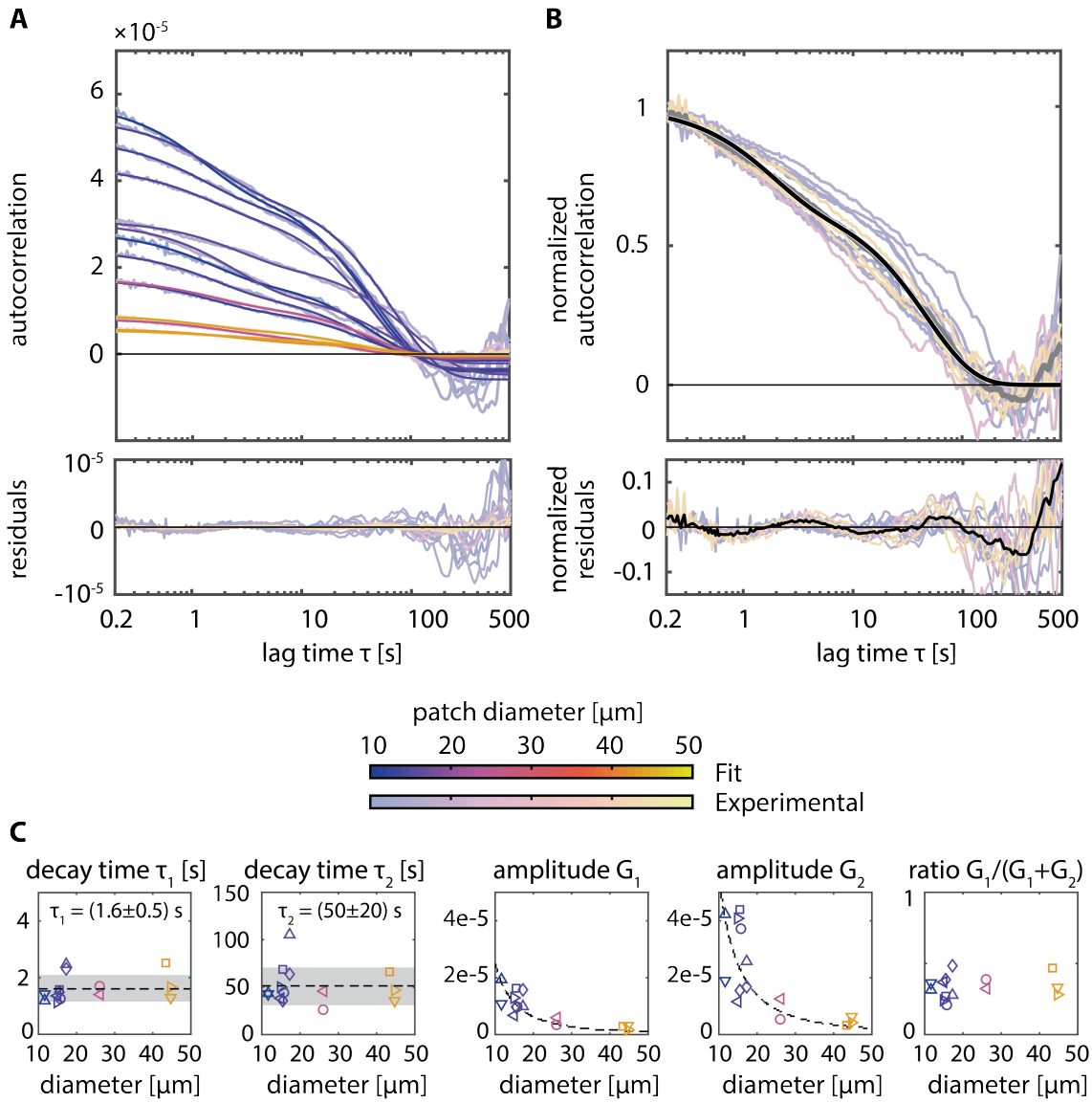

Figure VI.18: Dependence of the autocorrelation function on the size of the SLB patch. (A) Autocorrelation curves (light shade) and respective fits (dark shade) for different patch sizes. Patches with the approximate diameters ($d \approx \sqrt{4A_{\mathrm{patch}}/\pi}$) from 10 µm to 45 µm are indicated in blue to orange, respectively. Residuals to the fits are shown in the lower panel. **(B)** Normalized autocorrelation curves, displayed as in (A). The average of all displayed autocorrelation curves is displayed in gray with the fit to the average displayed in black. **(C)** Extracted parameters from the biexponential fits in (A) for different approximate patch diameters, displayed as in Figure VI.17. The mean and standard deviation of the decay times τ_1 and τ_2 is displayed as black dashed line and as gray shaded area, respectively. For G_1 and G_2 we added a quadratic fit $G_i = p_{1,i}/d^2$ as guide to the eye, with $p_{1,i}$ being a proportionality factor. SLB patch composition DOPC with 0.05 mol % Atto655-DOPE, 20 nM Atto488-MPER in SLB buffer with 5 mg/ml β-caseine.

SI-FCS autocorrelation curves at varying concentrations from 15 nM to 600 nM (Figure VI.19A and B). To improve the quality of the curves, we increased the measurement time to 6 h per patch, such that the titration series is based on 18 measurements and a total measurement time of 108 h. Unfortunately, fluorescence intensity traces showed long-term drifts that were not properly accounted for by the polynomial detrending and only stable segments of intensity traces were analyzed. Effective measurement times therefore varied from 5.8 h down to 0.8 h in the case of 600 nM. As it proved difficult to obtain reliable SI-FCS autocorrelation curves for 600 nM we did not proceed to higher concentrations.

Within the precision of our measurements, we did not find a clear dependence on the MPER concentration for the decay times τ_1 and τ_2, the amplitudes G_1 and G_2 or the ratio $G_1/(G_1 + G_2)$ (Figure VI.19C). We did, however, confirm a dependence of the amplitudes on the patch size (Figure VI.19D). In this new data set, we also find a slight dependence of the amplitude ratio $G_1/(G_1 + G_2)$ on the approximate patch diameter (Figure VI.19D, right panel). Future experiments will need to confirm if this dependence is reflecting on an influence of the patch size on the binding kinetics. In Section VI.3.6, we therefore use microstructures that allow to control the confinement geometry.

Generally, the scatter of the fit parameters to the autocorrelation curves is large compared to the change with the MPER concentration. Only the influence of the patch diameter on the amplitude of the autocorrelation function is significantly larger than the scatter of the fit values. Strikingly, the effect of the patch diameter on the amplitudes is much more pronounced than a potential effect of the concentration. If the MPER binding does not depend on the concentration in solution, this would hint towards partitioning model and indicate that a ligand-receptor binding model would not describe the MPER attachment accurately. We therefore conclude that a more precise control over the patch size is necessary in order to characterize the peptide binding by the autocorrelation amplitude. In the following sections we are thus exploring options to confine the lateral diffusion of MPER in well-defined geometries.

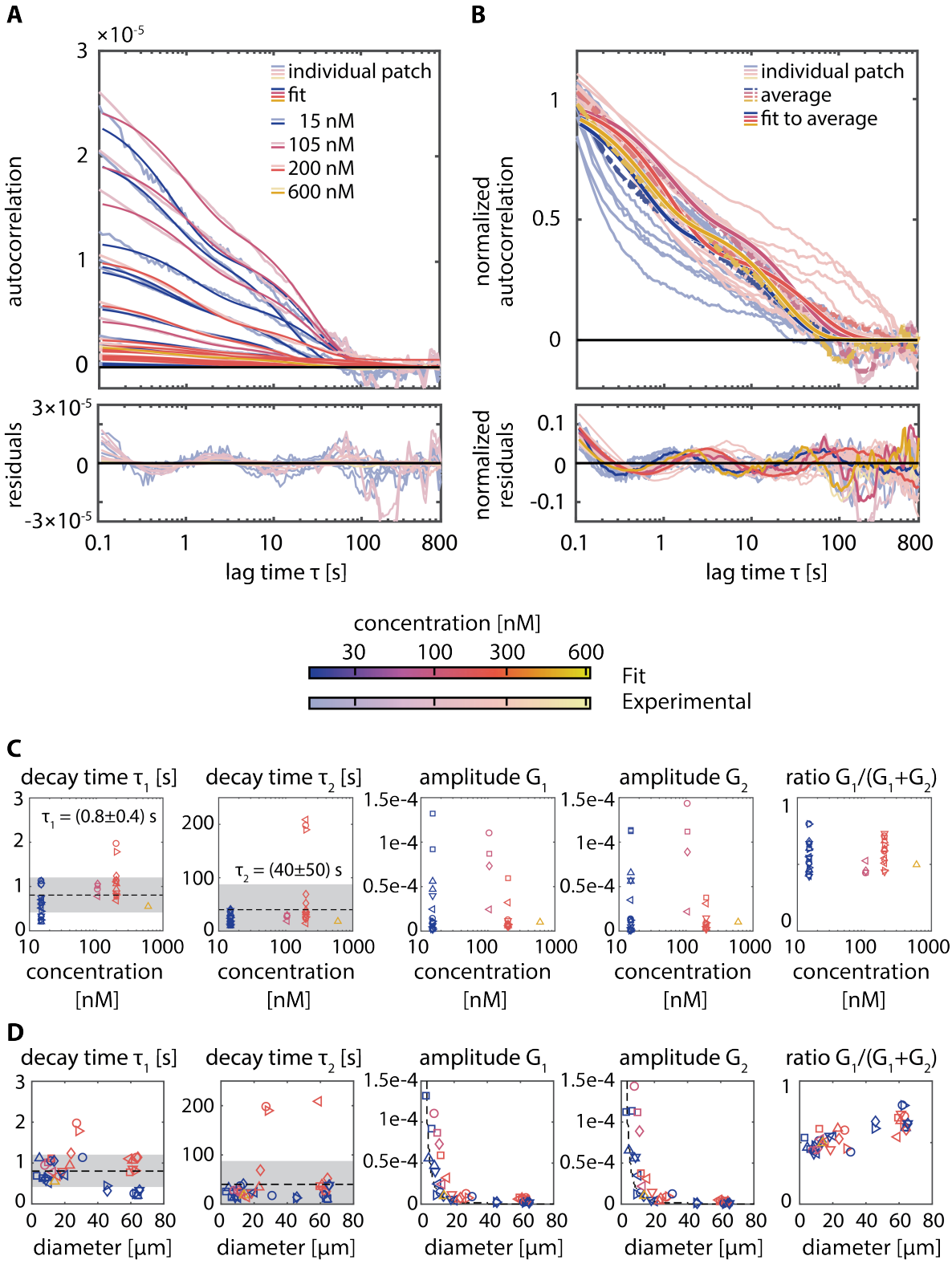

Figure VI.19: caption on next page.

Figure VI.19: Concentration dependence of the MPER binding kinetics. (A) Measured autocorrelation curves (light shade) and respective fits (Equation VI.32, dark shade) for different concentrations of MPER in solution. Residuals to the fits are shown in the lower panel. The measurement time per recorded autocorrelation curve was 6 h. Due to long-term intensity fluctuations of the system under investigation, the analyzed traces were limited to stable sections of the intensity traces. **(B)** Normalized autocorrelation curves displayed as in (A), but for better visibility without fits for the individual autocorrelation curves. Average autocorrelation curves for each recorded concentration are displayed as dashed-lines, fits to the averages as solid lines. Residuals are shown for the averages, as well as, the fits to the individual autocorrelation curves. **(C)** Extracted fit parameters, displayed as in Figure VI.17 for different concentration of MPER in solution. For the decay times τ_1 and τ_2, mean and standard deviation are indicated by black dashed lines and gray shaded areas, respectively. **(D)** Extracted fit parameters as in (C) but displayed over the respective patch diameter; otherwise displayed as in Figure VI.18. SLB patch composition DOPC with 0.05 mol % Atto655-DOPE, Atto488-MPER in SLB buffer with 5 mg/ml β-caseine.

VI.3.5 Confinement of Lateral Diffusion in Lipid Bilayer Nanodiscs

Looking for means of confining lateral membrane diffusion in SI-FCS, we identified surface-immobilized lipid bilayer nanodiscs as a promising approach [Nath et al., 2008,Zalisko et al., 2017]. In lipid bilayer nanodiscs, a membrane scaffold protein (MSP) wraps around a lipid bilayer with its hydrophobic alkyl chains forming a disc-shaped membrane that is dissolvable in aqueous solution [Bayburt et al., 2002,Bayburt and Sligar, 2010,Denisov and Sligar, 2016]. The size and thus the number of contained lipids depends on the scaffold protein of choice [Denisov et al., 2004]. We employ the scaffold protein MSP1E3 forming nanodiscs with a diameter of approximately 12 nm [Denisov et al., 2004, Bayburt et al., 2006], containing approximately 295 lipd molecules [Bayburt et al., 2006]. One major advantage of nanodiscs over SLB is their capability to incorporate integral membrane proteins [Bayburt et al., 2006, Leitz et al., 2006, Boldog et al., 2006] and bind peripheral membrane proteins [Shaw et al., 2007, Morrissey et al., 2008]. Studies characterizing protein-lipid interactions with nanodiscs by confocal FCS in solution [Nath et al., 2010, Hernández-Rocamora et al., 2012, Ly et al., 2014] or single-molecule TIRF microscopy imaging of surface-immobilized nanodiscs [Nath et al., 2008, Nath et al., 2010, Zalisko et al., 2017] are of particular interest in the context of this work. However, none of the studies above exploits the potential of investigating the binding to surface-immobilized nanodiscs with

FCS.

Here, we combine FCS with surface-immobilization and explore the capabilities of nanodiscs to serve as template for SI-FCS quantification of membrane binding. One advantage of nanodiscs over SLB patches is the potential to incorporate charged lipids in reproducible fractions [Nath et al., 2010, Roos et al., 2014]. The electroformation of GUVs hinders the the production of SLB patches with charged lipid head groups. For nanodisc preparation we used a mixture of 70 mol % DOPC and 30 mol % 1,2-dioleoyl-*sn*-glycero-3-phospho-(1'-*rac*-glycerol) (DOPG) to allow binding studies of MTS, relying on electrostatic interaction (Appendix D.3.3, p. 305). We further doped the nanodiscs with 1 % fluorescently labeled DOPE to monitor nanodisc binding (Atto488-DOPE or Atto655-DOPE, for details see Materials and Methods in Section D.2.5, p. 299 of the Appendix).

To acquire SI-FCS autocorrelation curves, we immobilized MSP1E3 nanodiscs on microscopy coverslips. We found that the nanodiscs attach reproducibly and homogeneously to coverslips cleaned with piranha solution, following protocols for treatment of the coverslips as in SLB preparations. Nanodiscs appeared to saturate on the surface at solution concentrations above 1 µM (Figure VI.20). For all concentrations we observe a homogeneous distribution of nanodiscs on the coverslips over millimeters.

Adding MPER to the surface-immobilized nanodiscs, we observe binding of the peptide to the surface (Figure VI.21). At low concentrations the transient binding of MPER can be observed by visible intensity fluctuations. Increasing the concentration of MPER above 30 nM, we observe a further increase of MPER bound to the surface (Atto488), but simultaneously a decrease of the fluorescence signal of the labeled nanodiscs (Atto655). We speculate that the nanodiscs detach from the surface and potentially even rupture due to multiple MPER molecules inserting simultaneously into one nanodisc. Based on these observations, we suspect that nanodiscs can only be employed for binding studies at low concentrations of amphipathic helices inserting into the bilayer.

VI.3.5.1 Binding to Nanodiscs Results in Low-Noise SI-FCS Curves at Low Concentrations

We further acquired SI-FCS autocorrelation curves as described above in the case of surface-immobilized binding sites. Lateral diffusion of membrane-bound molecules is limited to the area of the nanodiscs ($\sim 110\,\mathrm{nm}^2$) and thus localized below the resolution limit. As nanodiscs are randomly and homogeneously distributed on length scales much smaller than the integration area ($5.1 \times 5.1\,\mu\mathrm{m}^2$), they can be treated as surface-immobilized binding

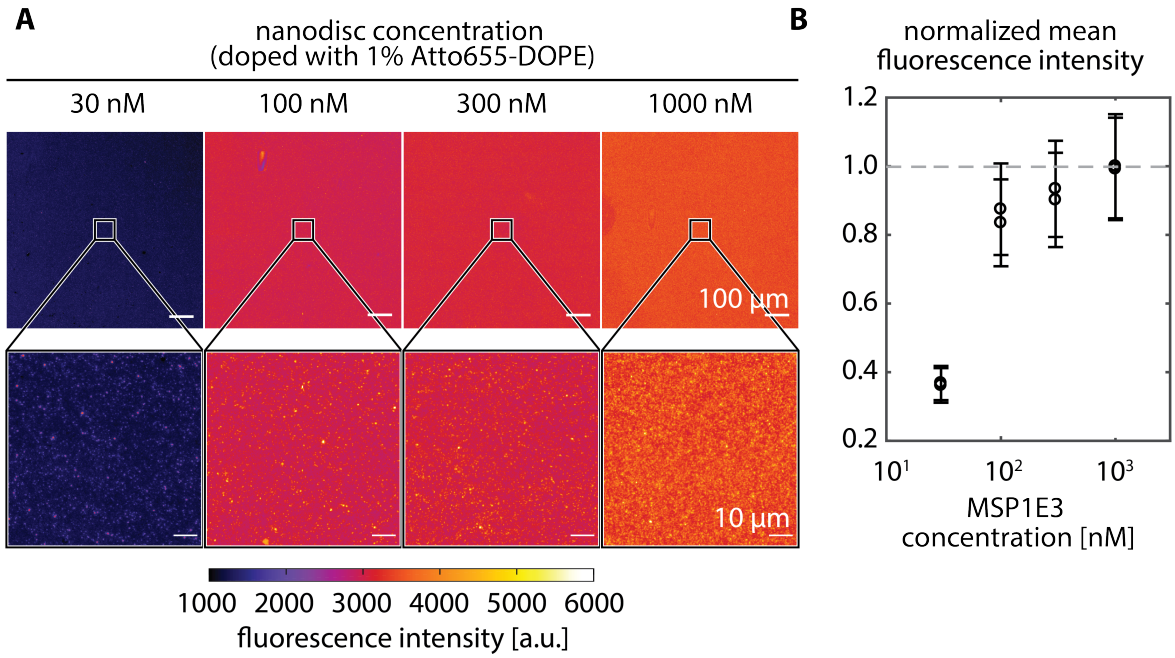

Figure VI.20: Nanodiscs (MSP1E3) immobilized on piranha cleaned glass. (A) Immobilization of MSP1E3 was measured by TIRF imaging of the fluorescently labeled lipid Atto655-DOPE added with an average molar concentration of 1 % to the lipid mixture. Nanodiscs bind homogeneously on large (upper panels) and small spatial scales (lower panels). Tile scans were recorded in fields of 10×10 tiles, each $82 \times 82\,\mu m^2$ in size. As the images were close to homogeneous, we performed a correction for impurities in the illumination profile by dividing each tile by the average of all tiles with the mean normalized to one. **(B)** For increasing concentration of nanodiscs, a saturation of the mean fluorescence intensity is approached. Circles and error bars indicate the mean and standard deviation of the $(820 \times 820)\mu m^2$ full tile scan (A, upper panel).

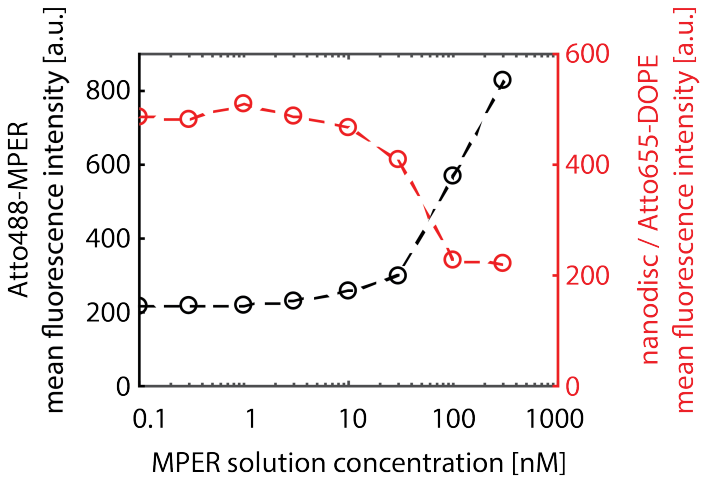

Figure VI.21: Nanodisc integrity is compromised at high MPER concentrations. Mean fluorescence intensity of Atto488-MPER (black) and the labeled lipid Atto655-DOPE incorporated in the nanodiscs (red) for increasing MPER concentrations. Dashed lines are a guide to the eye. Nanodisc composition 7:3 DOPC:DOPG with 1 mol % Atto655-DOPE, Atto488-MPER in SLB buffer.

sites (Chapter III). We thus recorded autocorrelation curves by integration of squared ROIs ($5.1 \times 5.1\,\mu m^2$).

As in the case of surface-immobilized binding sites, the decay times of the obtained autocorrelation curves are independent of the selected ROI size (Figure D.1, p. 302). The obtained autocorrelation curves resemble shape and time scales of the autocorrelation curves obtained for the MPER binding to SLB patches (Figure VI.22). The noise level of the autocorrelation curves, however, is significantly lower compared to SLB patches (Figure VI.18, p. 182). Averaging over 49 ROIs additionally improves the SNR of the autocorrelation curves. The changed lipid composition (DOPC only for SLB patches, 7:3 DOPC:DOPG for nanodiscs) potentially influences the binding of MPER. However, we find that, assuming a biexponential autocorrelation function, the obtained decay times $\tau_1 = (1.5 \pm 0.7)\,s$ and $\tau_2 = (53 \pm 18)\,s$ (mean $\pm$ standard deviation of the fit to the individual ROI) are in agreement with the results obtained on SLB patches, namely $\tau_1 = (1.6 \pm 0.5)\,s$ and $\tau_2 = (50 \pm 20)\,s$ (Figure VI.18). As nanodiscs appear incompatible with high concentrations of peptide (Figure VI.21), we did not attempt to perform a titration of MPER binding to nanodiscs.

The peptide sequence of our MPER construct incorporates one cysteine at the N-terminus (Section D.2.2, p. 297) and is therefore prone to dimerize by cysteine-cysteine

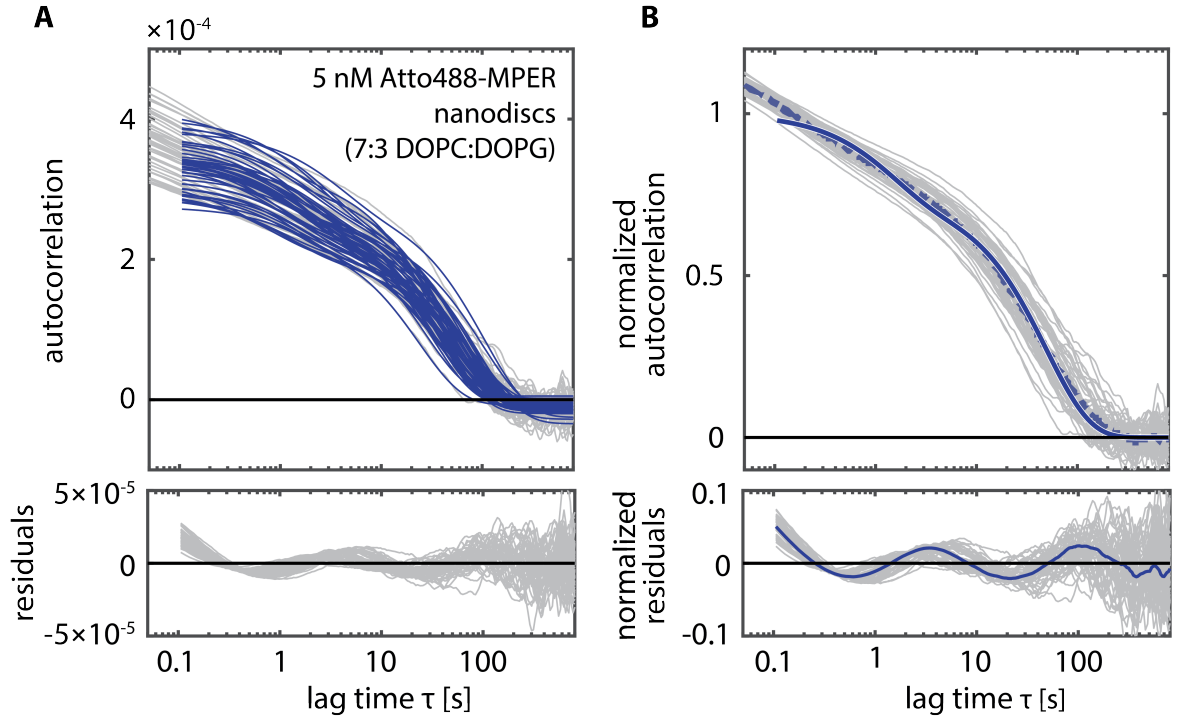

Figure VI.22: SI-FCS autocorrelation curves for MPER binding to surface-immobilized nanodiscs (MSP1E3). (A) SI-FCS autocorrelation curves (gray, upper panel) obtained from integration of 49 ROIs and the fits (Equation VI.32) to the individual autocorrelation curves (blue, upper panel). Respective residuals are shown in the lower panel. **(B)** Normalized autocorrelation curves, displayed as in (A), but with the average of the normalized autocorrelation curves (blue dash-dot line) and the fit to the average autocorrelation curved (blue solid line). Lower panel: Fits for the individual normalized autocorrelation curves (gray) and the average autocorrelation curve (blue). Nanodisc composition 7:3 DOPC:DOPG with 1 mol % Atto655-DOPE, 5 nM Atto488-MPER in SLB buffer.

interactions. In our experiments, however, we find no change in binding kinetics when adding 0.25 mM Tris(2-carboxyethyl)phosphin (TCEP) to ensure monomeric MPER (Supplementary Figure D.2, p. 304).

Moreover, the experiments indicate that for immobilized nanodiscs it is intrinsically difficult to distinguish unspecific surface binding from binding to the nanodiscs. We therefore suggest for future experiments to examine if the obtained autocorrelation curves depend on the surface density of immobilized nanodiscs.

Within the experiments presented here, we find no difference in the binding kinetics of MPER to SLB patches and nanodiscs. Interestingly, we do not find a dependence of the binding of MPER on the membrane composition including charge lipid head groups (30 % DOPG) in case of nanodiscs. A change in binding kinetics is, however, expected for stronger charged amphipathic peptides that rely on electrostatic attraction, e.g. bacterial MTS (Section D.3.3, p. 305).

In summary, the results highlight that high quality SI-FCS autocorrelation curves can be obtained for the binding to lipid bilayer nanodiscs.

VI.3.6 Confinement in Micropatterned Membrane Corrals

The quality of autocorrelation curves obtained for the binding of MPER to nanodiscs (Figure VI.22) clearly exceeds the quality for binding to SLB patches (Figure VI.18). In particular, the averaging over multiple ROIs within one field of view offers not only a higher statistical power of individual experiments, but simultaneously intrinsic quality controls. However, nanodiscs are limited to low peptide concentrations and are thus not suited for titration series to determine molecular binding rates. Moreover, unspecific binding may occur in between immobilized nanodiscs. To overcome the aforementioned limitations, we investigated the binding of MPER to membrane corrals formed by micropatterned chromium lattices (Section VI.2.3). One key advantage for the study of peptide binding is coverage of the surface by a complete SLB and thus no remaining exposed glass surface, requiring passivation. To reduce unspecific binding to potential defects in the SLB we maintained the concentration of 5 mg/mL of β-caseine for the following experiment. Furthermore, standard protocols for SLB formation are compatible with the chromium microstructures, allowing an easy modification of membrane composition. Finally, the shape of the chromium microstructures can be tailored to the specific application.

We formed DOPC membrane corrals with a side length of 10 µm, as described above (Section VI.2.3 and Appendix D.1.3). As we frequently encountered problems in the sta-

bility of intensity traces in combination with the laser diode excitation at a wavelength of 491 nm, we switched to the diode-pumped solid state (DPSS) laser excitation with a wavelength of 561 nm. As this required replacing the fluorescent dye, we resynthetized MPER with the fluorescent dye Cy3B [Cooper et al., 2004], intensively characterized in combination with SI-FCS in Chapters III and IV.

Incubating the bilayer with 10 nM Cy3B-MPER and PO+C oxygen scavenging system, we acquired SI-FCS autocorrelation curves. After longer measurement times, we observe spikes of fluorescence that apparently originate from clusters of fluorescently labeled molecules binding to the bilayer. Notably, the respective membrane corrals can easily be excluded from further analysis without discarding the entire measurement. In Section VI.3.4, when only one to four SLB patches are recorded within one field of view, rare binding events of clusters require truncating or discarding of measurements. Averaging over 34 remaining membrane corrals, we obtain autocorrelation curves of comparable quality as in the case of lipid bilayer nanodiscs (Figure VI.23). The obtained decay times $\tau_1 = (3.1 \pm 1.4)$ s and $\tau_2 = (90 \pm 60)$ s are slightly longer than for the binding on nanodiscs or SLB patches, however within the standard deviation.

Table VI.3 gives an overview of the obtained MPER binding kinetics of the individual experiments. For all measurements, we obtain consistent decay times τ_1 and τ_2 and consistent amplitude ratios $G_1/(G_1+G_2)$. Thus, we conclude that SI-FCS can reliably extract these parameters of the membrane binding of peptides to different model membrane systems. In the following section, we will discuss the obtained results for all three model membrane systems.

Table VI.3: Comparison of the fit parameters for MPER binding to SLB patches, nanodiscs and microstructured membrane corrals. ROIs refers to the number of analyzed patches in the case of SLB patches, the number of ROIs in the case of nanodiscs and the number of analyzed membrane corrals. For τ_1, τ_2 and $G_1/(G_1+G_2)$ values represent the mean and standard deviation over the analyzed ROIs. The last column refers to the figure with the data analyzed.

Confinement	**TCEP**	**ROIs**	**DOPC: DOPG**	τ_1 [s]	τ_2 [s]	$\frac{G_1}{G_1+G_2}$	**Figure**
SLB patches	-	14	1:0	1.6 ± 0.5	50 ± 20	0.34 ± 0.08	VI.18
Nanodiscs	-	49	7:3	1.5 ± 0.7	53 ± 18	0.26 ± 0.03	VI.22
Nanodiscs	-	98	7:3	3 ± 4	90 ± 70	0.23 ± 0.09	D.2
Nanodiscs	0.25 mM	98	7:3	2 ± 4	80 ± 50	0.25 ± 0.05	D.2
Chromium lattice	-	34	1:0	3.1 ± 1.4	90 ± 60	0.36 ± 0.05	VI.23

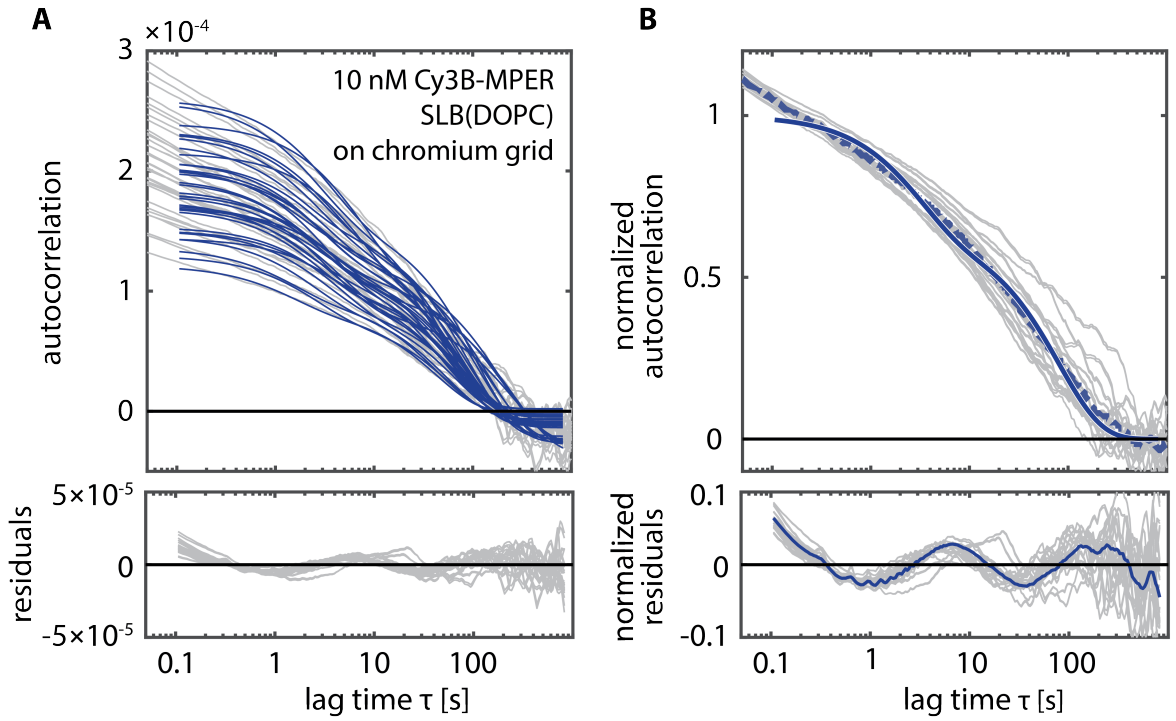

Figure VI.23: SI-FCS autocorrelation curves for MPER binding to membrane corrals formed on a micropatterned chromium lattice. **(A)** and **(B)** displayed as in Figure VI.22. Gray lines show experimental curves of 34 ROI, blue solid lines show fits to Equation VI.32. In (B) the dashed-dot line is the average of the normalized experimental autocorrelation curves together with the fit to the average as solid line. SLB composition DOPC with 0.05 mol % Atto655-DOPE, 10 nM Cy3B-MPER in SLB buffer with 5 mg/ml β-caseine.

VI.4 Conclusion

In this chapter, we introduced SI-FCS as a novel technique to measure binding rates in reversible membrane associations. We assessed this quantification approach using three different strategies: (i) we presented the hybridization of fluorescently labeled ssDNA to chol-DNA handles as a robust model system to step-wise increase the complexity from surface-immobilized binding sites (Section VI.2); (ii) we simulated the effect of a three-state model consisting of a weakly-bound (adhered) state and a strongly-bound (inserted or folded) state on the SI-FCS autocorrelation function (Section VI.3.2); and (iii) we measured SI-FCS autocorrelation curves of the peptide-membrane interaction of the amphipathic helix MPER.

One major challenge when switching from surface-immobilized binding sites to membrane binding is the handling of lateral diffusion present in most physiologically relevant membrane systems. We thoroughly tested three general approaches to describe or eliminate the effect of diffusion on the autocorrelation function in our model system of laterally diffusing docking strands (Figure VI.2).

First, we presented a simplified fitting function incorporating membrane diffusion that describes the effect of varying the ROI size. This approach extracted the binding time of the DNA duplex reliably, but is limited in the accessible binding times (Figure VI.5). Complex binding models, as the three-state model for the binding of amphipathic helix (Figure VI.13) or complex diffusive modes [Veerapathiran and Wohland, 2018] impose an additional challenge, as only a limited number of parameters can be reliably extracted from the autocorrelation function simultaneously.

Second, we explored the limiting case of large integration ROIs that ultimately render lateral diffusion negligible compared to the binding kinetics (Figure VI.6). While this approach offers a simple fitting function, it is limited in the accessible diffusion coefficients, binding times, and density of binding events (Figure VI.7).

Last, we confined the membrane diffusion within the detection ROI, rendering membrane diffusion invisible to the autocorrelation function. Micrometer-sized membrane corrals formed by diffusion barriers of chromium microstructures were identified as a promising route in routinely acquiring SI-FCS autocorrelation curves that highlight primarily the binding contribution. Potential interactions with the confinement, however, require stringent controls to ensure accurate quantification. In the specific case of DNA hybridization with 9 nt overlap, we successfully reproduced association and dissociation rates from

previous experiments (Table VI.1).

Two types of membrane binding have to be distinguished: the binding of ligands to membrane bound receptors and the partitioning of amphipathic peptides or proteins to the hydrophobic bilayer itself without specific binding sites. In particular the binding to specific head groups is referred to as membrane binding, while in the conceptual image of SI-FCS it can be treated as ligand-receptor binding. In the case of membrane binding without further specificity, the extraction of the association rate from a titration series of the concentration of the binding molecule is intrinsically difficult. A dense packing of bound molecules does not only coincide with a range of potential problems from lateral interactions over bilayer integrity to a violation of the dependence of binding sites, but also leads to experimentally challenging small autocorrelation amplitudes. We therefore developed the theoretical framework to determine the association rate based on its contribution to the amplitude of the autocorrelation function far from surface saturation (Section VI.3.1).

Going beyond binding models with monoexponentially distributed residence times, the shape of the autocorrelation function becomes increasingly complex, as expected for the binding of some amphipathic helices. We showed that assuming the three-state model employed by Myers and colleagues [Myers et al., 2012], the autocorrelation function is well described by a biexponential with a known relation of characteristic decay rates and the molecular transition rates. The autocorrelation amplitude presumably contains further information that may facilitate the determination of molecular transition rates in future studies.

For the partitioning of the amphipathic peptide MPER to membranes, we not only confirmed experimentally the biexponential shape of the autocorrelation function, but also presented three means of confining the lateral diffusion (Figure VI.24). First, SLB patches effectively confine the diffusion and are a minimal modification to homogeneous SLBs, but produce autocorrelation curves with comparably high levels of noise and a strong dependence of the autocorrelation amplitude on the patch diameter (Figure VI.18). Second, lipid bilayer nanodiscs confine the diffusion on a nanometer scale, allowing SI-FCS acquisitions as in the case of surface-immobilized binding sites. Obtained autocorrelation curves show superior noise characterstics, but measurements are limited to low concentrations of binding peptide to ensure nanodisc integrity (Figure VI.21). Finally, the most promising are diffusion barriers based on chromium microstructures, as they combine multiplexing, reproducibility, flexible sample design and standard SLB preparations. Based on chromium microstructures, we obtained low-noise average autocorrelation curves, eliminating the

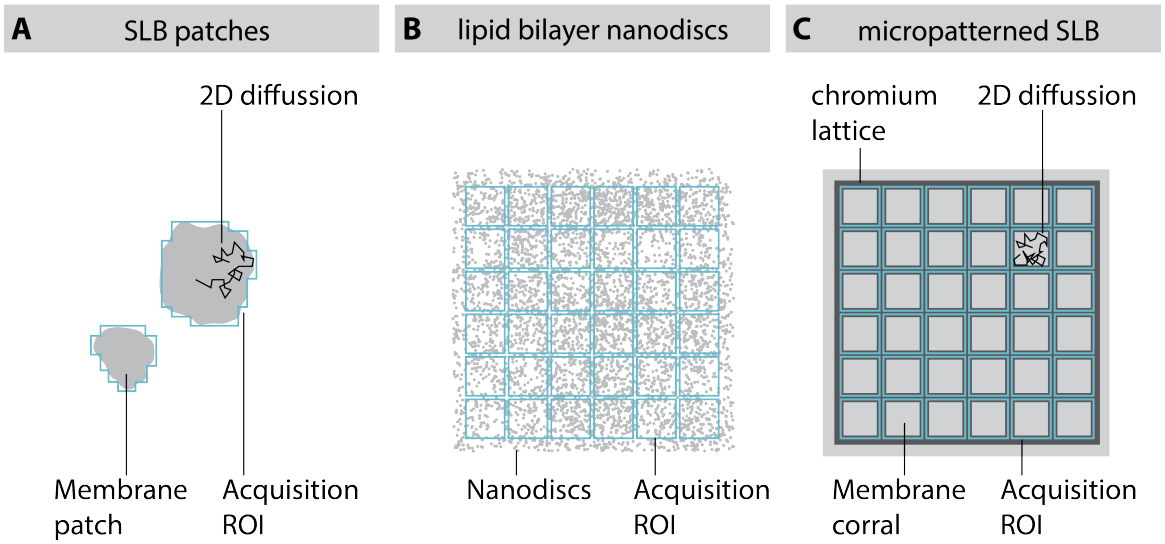

Figure VI.24: Schematic of the investigated approaches to confine membrane diffusion. (A) SLB patches (gray) formed from bursted GUV with ROIs (blue) enclosing the patches. For details see Section VI.3.4. **(B)** Lipid bilayer nanodiscs (gray) that are randomly and homoegenously surface-immobilized on length scales below the resolution limit of the microscope. Acquisition ROIs (blue) can therefore be chosen arbitrary, as in the case of suface-immobilized binding sites (Chapter III). For details see Section VI.3.5. **(C)** Membrane corrals (light gray) formed by a chromium microstructure (dark gray). Acquisition ROIs enclose the individual membrane corrals (blue). For details see Section VI.2.3 and VI.3.6.

need for thorough surface passivation to avoid unspecific binding (Figure VI.23). The decay times of all three approaches are in agreement within the precision of the measurements (Table VI.3).

In summary, we believe that the tools developed within this thesis will significantly advance the quantification of membrane binding with SI-FCS. In contrast to many available methods to quantify membrane binding, SI-FCS has the potential to not only determine affinities or partition coefficients, but the underlying molecular binding rates. Fluorescent labels contribute the specificity required to work not only in well-defined *in vitro* systems, but similarly in complex bio-fluids or even live cells. SI-FCS improves upon SPT in the lower required photon-budget, as molecules do not need to be localized. Irradiances are therefore orders of magnitude lower, allowing the combination of high frame rates and long acquisition series, as necessary to accurately characterize binding processes showing both relatively short and long residence times on the order of milliseconds and minutes, respectively.

VII

CURRENT STATE OF SI-FCS AND FUTURE PERSPECTIVES

Within this work, we developed SI-FCS as a novel, precise method to quantify surface binding reactions. We did not only apply SI-FCS to surface-immobilized binding sites, but similarly to the binding of ligands to membrane-bound receptors and the partitioning of amphipathic proteins and peptides to membranes.

Based on the spatial integration of the fluorescence signal from surface-attached molecules, SI-FCS in its current implementation uses TIRF microscopy to achieve surface selectivity and EMCCD camera detection for multiplexing multiple acquisition regions in one field of view (**Chapter III**, Figure III.1). Following the concept and mathematical description by Thompson and colleagues [Thompson et al., 1981] (Section III.2.1), the autocorrelation function encodes not only surface densities, but also association and dissociation rates of the surface binding. We quantified the hybridization of complementary DNA strands with varying nucleotide (nt) overlaps and one ssDNA strand immobilized on a DNA origami nanostructure (Figures III.1). The same DNA origami constructs have been commonly used in pioneering work on DNA-PAINT super resolution microscopy [Jungmann et al., 2010, Jungmann et al., 2016, Schnitzbauer et al., 2017, Auer et al., 2017, Strauss et al., 2018] (Figure III.11). Within the limit of low concentrations ($k_d \gg k_a\langle A\rangle$), the decay of the monoexponential SI-FCS autocorrelation function reports predominantly dissociation dynamics. For 7 nt to 10 nt DNA hybridizations, we thus obtained dissociation times of (0.44 ± 0.01) s to (90 ± 7) s, respectively (Figure III.2A). The obtained autocorrelation curves are highly reproducible, highlighting the achievable precision in SI-FCS acquisitions (Figure III.5). Mixed species, comprising pairs of 7 nt with 8 nt or 9 nt hybridization length, respectively, showed clearly biexponential autocorrelation curves allowing the extraction of the individual kinetics with a bias of less than 20 % (Figure III.2B). Further, we determined association and dissociation rates from titration series (Figure III.3), which were in good agreement with several previous studies [Jungmann et al., 2010, Dupuis et al., 2013, Peterson et al., 2016]. We performed extensive series of Monte Carlo simulations and SI-FCS experiments to evaluate the relation between the SI-FCS measurement duration and its inherent bias on the autocorrelation function. Our results establish that SI-FCS

measurements should be at least 300 times longer than the characteristic decay time to achieve a bias below 10 % (Figure III.7). Compared to SPT, SI-FCS determines binding kinetics for orders of magnitude higher surface densities (Figures III.9 and III.10).

During SI-FCS acquisitions on the order of multiple hours, we encountered a loss in fluorescence signal (**Chapter IV**, Figure IV.11) that originates from a photo-induced depletion of binding sites in SI-FCS (Figure IV.4) and even more pronounced in DNA-PAINT microscopy (Figures IV.2 and IV.3). In SI-FCS the depletion of docking sites manifests itself as an additional contribution to the autocorrelation function (Figure IV.11). The depletion can be prevented to a large extent by the use of oxygen scavenging buffers (Figures IV.3 and IV.4). With PO+C and PCD+PCA, we tested two different oxygen scavenging buffers, of which PO+C was found better suited for DNA-based samples, as PCD+PCA apparently is prone to nuclease contamination [Senavirathne et al., 2015] (Figure IV.12). Further, we introduced an extended imager handle, placing the fluorescent dye at a greater distance from the docking site and thus similarly reducing the depletion of binding sites in low-irradiance SI-FCS acquisitions (Figures IV.3 and IV.4). Comparing the capabilities to extract binding kinetics from SPT traces and SI-FCS measurements, we encountered a bias towards shortened dark times and extended bright times if multiple imager strands hybridize simultaneously on one DNA origami nanostructure (Figure IV.10). Accordingly, to ensure accurate binding kinetics in DNA-PAINT, binding events need to be individually resolvable. Avoiding the bias from double binding events severely limits either the achievable surface-density of immobilized docking sites or the maximum solution concentration of imager strands. The SI-FCS autocorrelation takes into account the increase in brightness of two simultaneous binding events and is thus free from this bias.

Aiming at the quantification of fast surface-binding reactions with residence times significantly below 0.5 s, the contributions of solution diffusion and binding start to overlap in the autocorrelation function. As both contributions modulate the autocorrelation function on similar time scales, an autocorrelation model incorporating both effects is required (**Chapter V**, Figure V.1). While the axial molecule detection function in TIR-FCS is conventionally assumed to be limited by the supposedly monoexponential shape of the evanescent field [Thompson et al., 1981, Lieto et al., 2003, Ries et al., 2008a], a biexponential decay was previously reported for objective-type TIRF microscopy [Mattheyses and Axelrod, 2006, Oreopoulos and Yip, 2008, Brunstein et al., 2014b]. TIR is an interface effect, which strongly depends on the change in refractive index. Consequently, a sampling of the evanescent field ought to be close to the refractive index of biological samples. Un-

fortunately, previously presented methods to directly characterize the TIR excitation do not maintain the refractive index expected for aqueous samples [Mattheyses and Axelrod, 2006], require specialized instrumentation [Oreopoulos and Yip, 2008] or sophisticated sample preparation (see Section V.2.1). To directly characterize the axial molecule detection function, we developed a calibration slide based on a fluoropolymer with the refractive index of water (Figure V.2). The excitation profile is integrated over axial sections by recording the fluorescence intensity above non-fluorescent polymer steps of defined heights (Figure V.2), which makes the sampling very straightforward. This direct characterization revealed a second, penetrating contribution (Figures V.4 and V.5). The precise knowledge of the excitation profile will be helpful to improve quantitative TIRF imaging including SAF and three-dimensional TIRF-based super-resolution microscopy in the axial direction. Moreover, an implementation of a biexponential molecule detection function will contribute to the a more accurate model of the TIR-FCS autocorrelation function at sub-second lag times.

Quantifying the binding of biomolecules to membrane-attached binding sites and the partitioning of amphipathic proteins or peptides from solution to membranes with SI-FCS (**Chapter VI**) imposes multiple additional challenges compared to the study of surface-immobilized binding sites (Chapter III).

First, physiologically relevant membrane compositions form fluid membranes and thereby lead to diffusion of bound molecules on the lipid bilayer. We combined in a proof-of-concept system membrane-attached chol-DNA handles with the previously characterized DNA hybridization reaction (Chapter III) to test three approaches to account for membrane diffusion or eliminate its influence on the autocorrelation function (Figure VI.2): (i) an autocorrelation model describing both membrane diffusion and binding (Figure VI.5), (ii) a pseudo-infinite detection emphasizing the binding contribution relative to the diffusion contribution (Figure VI.6 and VI.7), and (iii) the confinement of membrane diffusion (Figure VI.8 and VI.9). For the last approach, we successfully extracted binding rates in agreement with the results obtained on surface-immobilized docking sites (Table VI.1).

Second, when molecules bind or partition directly to the lipid bilayer without mediation by membrane-attached receptors or specific spare lipid head groups, it becomes challenging to saturate binding sites in a titration experiment and further extract association and dissociation rates independently. Lateral interactions of bound molecules, compromised membrane integrity and small autocorrelation amplitudes hinder the accurate quantification at high membrane-bound concentrations. We therefore present an autocorrelation

model extracting association and dissociation rates for a two-state binding reaction far from membrane saturation (Section VI.3.1). Moreover, we verified the obtained relations with Monte Carlo simulations (Figure VI.11). For a more complex three-state binding model, we systematically investigated the dependence of the autocorrelation function on the transition rates. We find the autocorrelation function to be in excellent agreement with a biexponential decay with rates as previously derived for SPT residence time histograms [Myers et al., 2012] (Figure VI.13).

Finally, we acquired SI-FCS autocorrelation curves for the partitioning of the amphipathic peptide MPER to three different model membrane systems that provide a confinement of the membrane diffusion (Figure VI.24). The autocorrelation curves of MPER partitioning are best described by a biexponential model with characteristic decay times consistent for all confinement strategies (Table VI.3). While SLB patches are a small modification to homogeneous SLBs, the autocorrelation amplitude depends strongly on the approximate patch diameter (Figure VI.18). The uncontrolled scattering of patch shapes translates into a large scatter of amplitude values, thus reducing the reproducibility. Lipid bilayer nanodiscs and membrane corrals confined by chromium microstructures profit from reproducible shapes and thus more reproducible autocorrelation amplitudes (Figures VI.22 and VI.23). However, nanodiscs are limited to small concentrations of the partitioning peptide (Figure VI.21) and it is intrinsically difficult to distinguish specific from unspecific binding. In contrast, chromium microstructures allow the straightforward adaptation of membrane composition according to standard preparation protocols. The surface is fully covered with lipid bilayer, thus limiting unspecific binding to a minimum. In conclusion, microstructured membrane corrals are the most promising route for the routine quantification of membrane binding or partitioning with SI-FCS. Future work will need to carefully confirm the independence of the SI-FCS quantification from the confinement perimeter. Besides chromium microstructures, a variety of micropatterned bilayers are available to be tested with SI-FCS [Spinke et al., 1992, Wagner and Tamm, 2000, Deng et al., 2008, Knoll et al., 2009, Roder et al., 2011, Oliver and Parikh, 2010].

The simplicity of the current implementation of SI-FCS on standard wide-field microscopes, including the largely overlapping instrumentation requirements with TIRF-based localization microscopy setups, will benefit the rapid implementation of SI-FCS in the scientific community. Building upon the versatile concept of FCS and ICS, further developments will include faster detection, potentially in combination with sCMOS, PMT or APD detection to extract shorter time-scales. Dual-color cross-correlation spectroscopy

potentially benefits the examination of complex multi-component systems. To reduce the solution contribution to the autocorrelation function, the surface-selectivity can be increased by using FRET pairs for ligands and receptors. Moreover, metal induced engery transfer (MIET) [Karedla et al., 2014] and SAF [Ruckstuhl et al., 2003, Ruckstuhl and Verdes, 2004, Ries et al., 2008b] are two emerging means of enhancing surface-selectivity that appear compatible with SI-FCS. Following the works of Thompson and Lieto [Thompson, 1982, Lieto et al., 2003, Lieto and Thompson, 2004], non-fluorescent competitors may circumvent issues with high solution concentrations or allow the indirect quantification of non-fluorescent species. A label-free implementation of SI-FCS could potentially be based on the correlation of surface and membrane binding events as monitored by interferometric scattering (iSCAT) [Kukura et al., 2009, Djaker et al., 2016, Cole et al., 2017, Spindler et al., 2018].

Importantly, SI-FCS does not only have the potential to extract kinetic rates, but also surface-densities. This includes explicitly the counting of binding sites in DNA-PAINT super-resolution microscopy, when double binding events hinder a quantification with a simple binary extraction of timing information from the intensity traces. A future study will highlight the information content of the autocorrelation amplitude to count surface-bound molecules.

The field of DNA nanotechnology impressively illustrates the versatility of the DNA hybridization reaction. SI-FCS is ideally suited to study more complex binding reactions involving multiple binding steps, competitive binding or the cooperative binding of connected DNA sequences. Precise quantification of the hybridization reaction might not only deepen our understanding, but also benefit the emerging field of DNA computing [Dirks and Pierce, 2004, Chatterjee et al., 2017].

Based on the results of this work, SI-FCS is now at the point to systematically investigate membrane binding and partitioning. The list of potential systems to study with SI-FCS is extensive and includes not only variants of MPER and a large set of membrane binding peptides (Section VI.3.3). Rather, a plethora of of relevant questions centers around transiently membrane-binding proteins, ligand-receptor interactions, binding to specific lipid head groups, binding to membrane domains and the dependence of partitioning on the membrane composition. Moreover, cushioned SLBs may extend SI-FCS to the study of integral membrane receptors. The rich concepts of surface-immobilization employed for SPR and QCM-D can potentially be transferred to work similarly with SI-FCS, thus allowing the study of reversible binding in quasi-equilibrium and at fast time-scales

inaccessible to flow-based assays. Surface-immobilized vesicles will enable the investigation of membrane-curvature dependencies. Furthermore, we are only beginning to envision the potential of SI-FCS to quantify relevant binding kinetics for immunology, pharmacology and surface chemistry.

Bibliography

[Abramowitz and Stegun, 1965] Abramowitz, M. and Stegun, I. A. (1965). *Handbook of mathematical functions: with formulas, graphs, and mathematical tables*, volume 55. Courier Corporation.

[Adam and Delbrück, 1968] Adam, G. and Delbrück, M. (1968). Reduction of dimensionality in biological diffusion processes. *Structural chemistry and molecular biology*, 198:198–215.

[Aisenbrey et al., 2013] Aisenbrey, C., Michalek, M., Salnikov, E. S., and Bechinger, B. (2013). Solid-State NMR Approaches to Study Protein Structure and Protein–Lipid Interactions. In Kleinschmidt, J. H., editor, *Lipid-Protein Interactions: Methods and Protocols*, pages 357–387. Humana Press, Totowa, NJ.

[Aitken et al., 2008] Aitken, C. E., Marshall, R. A., and Puglisi, J. D. (2008). An Oxygen Scavenging System for Improvement of Dye Stability in Single-Molecule Fluorescence Experiments. *Biophysical Journal*, 94(5):1826–1835.

[Akira and Takeda, 2004] Akira, S. and Takeda, K. (2004). Toll-like receptor signalling. *Nature Reviews Immunology*, 4:499.

[Alberts, 2002] Alberts, B. (2002). *Molecular Biology of the cell*. Garland Science, 4 edition.

[Altman et al., 2011] Altman, R. B., Terry, D. S., Zhou, Z., Zheng, Q., Geggier, P., Kolster, R. A., Zhao, Y., Javitch, J. A., Warren, J. D., and Blanchard, S. C. (2011). Cyanine fluorophore derivatives with enhanced photostability. *Nature Methods*, 9:68.

[Ambrose et al., 1999] Ambrose, W. P., Goodwin, P. M., Jett, J. H., Van Orden, A., Werner, J. H., and Keller, R. A. (1999). Single Molecule Fluorescence Spectroscopy at Ambient Temperature. *Chemical Reviews*, 99(10):2929–2956.

[Anhut et al., 2005] Anhut, T., Hassler, K., Lasser, T., Koenig, K., and Rigler, R. (2005). Fluorescence correlation spectroscopy on dielectric surfaces in total internal reflection geometries.

[Apellaniz et al., 2010] Apellaniz, B., García-Sáez, A. J., Huarte, N., Kunert, R., Vorauer-Uhl, K., Katinger, H., Schwille, P., and Nieva, J. L. (2010). Confocal microscopy of giant vesicles supports the absence of HIV-1 neutralizing 2F5 antibody reactivity to plasma membrane phospholipids. *FEBS Letters*, 584(8):1591–1596.

[Aragón and Pecora, 1976] Aragón, S. R. and Pecora, R. (1976). Fluorescence correlation spectroscopy as a probe of molecular dynamics. *The Journal of Chemical Physics*, 64(4):1791–1803.

[Arecchi et al., 1971] Arecchi, F. T., Corti, M., Degiorgio, V., and Donati, S. (1971). Measurements of light intensity correlations in the subnanosecond region by photomultipliers. *Optics Communications*, 3(4):284–288.

[Auer et al., 2017] Auer, A., Strauss, M. T., Schlichthaerle, T., and Jungmann, R. (2017). Fast, Background-Free DNA-PAINT Imaging Using FRET-Based Probes. *Nano Letters*, 17(10):6428–6434.

[Axelrod, 1981] Axelrod, D. (1981). Cell-substrate contacts illuminated by total internal reflection fluorescence. *The Journal of Cell Biology*, 89(1):141–145.

[Bacia et al., 2006] Bacia, K., Kim, S. A., and Schwille, P. (2006). Fluorescence cross-correlation spectroscopy in living cells. *Nature Methods*, 3:83.

[Bacia et al., 2004] Bacia, K., Schuette, C. G., Kahya, N., Jahn, R., and Schwille, P. (2004). SNAREs Prefer Liquid-disordered over "Raft" (Liquid-ordered) Domains When Reconstituted into Giant Unilamellar Vesicles. *Journal of Biological Chemistry*, 279(36):37951–37955.

[Bacia and Schwille, 2007] Bacia, K. and Schwille, P. (2007). Practical guidelines for dual-color fluorescence cross-correlation spectroscopy. *Nature Protocols*, 2(11):2842–2856.

[Backer and Moerner, 2014] Backer, A. S. and Moerner, W. E. (2014). Extending Single-Molecule Microscopy Using Optical Fourier Processing. *The Journal of Physical Chemistry B*, 118(28):8313–8329.

[Baddeley and Bewersdorf, 2018] Baddeley, D. and Bewersdorf, J. (2018). Biological Insight from Super-Resolution Microscopy: What We Can Learn from Localization-Based Images. *Annual Review of Biochemistry*, 87(1):965–989.

[Bag et al., 2016] Bag, N., Ng, X. W., Sankaran, J., and Wohland, T. (2016). Spatiotemporal mapping of diffusion dynamics and organization in plasma membranes. *Methods and Applications in Fluorescence*, 4(3):34003.

[Bag et al., 2012] Bag, N., Sankaran, J., Paul, A., Kraut, R. S., and Wohland, T. (2012). Calibration and Limits of Camera-Based Fluorescence Correlation Spectroscopy: A Supported Lipid Bilayer Study. *ChemPhysChem*, 13(11):2784–2794.

[Bag and Wohland, 2014] Bag, N. and Wohland, T. (2014). Imaging Fluorescence Fluctuation Spectroscopy: New Tools for Quantitative Bioimaging. *Annual Review of Physical Chemistry*, 65(1):225–248.

[Bag et al., 2014] Bag, N., Yap, D. H. X., and Wohland, T. (2014). Temperature dependence of diffusion in model and live cell membranes characterized by imaging fluorescence correlation spectroscopy. *Biochimica et Biophysica Acta (BBA) - Biomembranes*, 1838(3):802–813.

[Balzarotti et al., 2017] Balzarotti, F., Eilers, Y., Gwosch, K. C., Gynnå, A. H., Westphal, V., Stefani, F. D., Elf, J., and Hell, S. W. (2017). Nanometer resolution imaging and tracking of fluorescent molecules with minimal photon fluxes. *Science*, 355(6325):606 LP – 612.

[Banchelli et al., 2008] Banchelli, M., Betti, F., Berti, D., Caminati, G., Bombelli, F. B., Brown, T., Wilhelmsson, L. M., Nordén, B., and Baglioni, P. (2008). Phospholipid Membranes Decorated by Cholesterol-Based Oligonucleotides as Soft Hybrid Nanostructures. *The Journal of Physical Chemistry B*, 112(35):10942–10952.

[Banchelli et al., 2010] Banchelli, M., Gambinossi, F., Durand, A., Caminati, G., Brown, T., Berti, D., and Baglioni, P. (2010). Modulation of Density and Orientation of Amphiphilic DNA on Phospholipid Membranes. II. Vesicles. *The Journal of Physical Chemistry B*, 114(21):7348–7358.

[Barg et al., 2010] Barg, S., Knowles, M. K., Chen, X., Midorikawa, M., and Almers, W. (2010). Syntaxin clusters assemble reversibly at sites of secretory granules in live cells. *Proceedings of the National Academy of Sciences*, 107(48):20804 LP – 20809.

[Bayburt et al., 2002] Bayburt, T. H., Grinkova, Y. V., and Sligar, S. G. (2002). Self-Assembly of Discoidal Phospholipid Bilayer Nanoparticles with Membrane Scaffold Proteins. *Nano Letters*, 2(8):853–856.

[Bayburt et al., 2006] Bayburt, T. H., Grinkova, Y. V., and Sligar, S. G. (2006). Assembly of single bacteriorhodopsin trimers in bilayer nanodiscs. *Archives of Biochemistry and Biophysics*, 450(2):215–222.

[Bayburt and Sligar, 2010] Bayburt, T. H. and Sligar, S. G. (2010). Membrane protein assembly into Nanodiscs. *FEBS Letters*, 584(9):1721–1727.

[Benda et al., 2003] Benda, A., Beneš, M., Mareček, V., Lhotský, A., Hermens, W. T., and Hof, M. (2003). How To Determine Diffusion Coefficients in Planar Phospholipid Systems by Confocal Fluorescence Correlation Spectroscopy. *Langmuir*, 19(10):4120–4126.

[Benesch and Benesch, 1953] Benesch, R. E. and Benesch, R. (1953). Enzymatic Removal of Oxygen for Polarography and Related Methods. *Science*, 118(3068):447 LP – 448.

[Berland et al., 1996] Berland, K. M., So, P. T., Chen, Y., Mantulin, W. W., and Gratton, E. (1996). Scanning two-photon fluctuation correlation spectroscopy: particle counting measurements for detection of molecular aggregation. *Biophysical Journal*, 71(1):410–420.

[Beseničar et al., 2006] Beseničar, M., Maček, P., Lakey, J. H., and Anderluh, G. (2006). Surface plasmon resonance in protein-membrane interactions. *Chemistry and Physics of Lipids*, 141(1-2):169–178.

[Betaneli and Schwille, 2013] Betaneli, V. and Schwille, P. (2013). Fluorescence Correlation Spectroscopy to Examine Protein-Lipid Interactions in Membranes. In Kleinschmidt, J. H., editor, *Lipid-Protein Interactions: Methods and Protocols*, pages 253–278. Humana Press, Totowa, NJ.

[Betzig and Chichester, 1993] Betzig, E. and Chichester, R. J. (1993). Single Molecules Observed by Near-Field Scanning Optical Microscopy. *Science*, 262(5138):1422 LP – 1425.

[Betzig et al., 2006] Betzig, E., Patterson, G. H., Sougrat, R., Lindwasser, O. W., Olenych, S., Bonifacino, J. S., Davidson, M. W., Lippincott-Schwartz, J., and Hess, H. F. (2006). Imaging Intracellular Fluorescent Proteins at Nanometer Resolution. *Science*, 313(5793):1642 LP – 1645.

[Bierbaum and Bastiaens, 2013] Bierbaum, M. and Bastiaens, P. I. (2013). Cell Cycle-Dependent Binding Modes of the Ran Exchange Factor RCC1 to Chromatin. *Biophysical Journal*, 104(8):1642–1651.

[Blom et al., 2009] Blom, H., Chmyrov, A., Hassler, K., Davis, L. M., and Widengren, J. (2009). Triplet-State Investigations of Fluorescent Dyes at Dielectric Interfaces Using Total Internal Reflection Fluorescence Correlation Spectroscopy. *The Journal of Physical Chemistry A*, 113(19):5554–5566.

[Blumhardt et al., 2018] Blumhardt, P., Stein, J., Mücksch, J., Stehr, F., Bauer, J., Jungmann, R., and Schwille, P. (2018). Photo-Induced Depletion of Binding Sites in DNA-PAINT Microscopy.

[Boldog et al., 2006] Boldog, T., Grimme, S., Li, M., Sligar, S. G., and Hazelbauer, G. L. (2006). Nanodiscs separate chemoreceptor oligomeric states and reveal their signaling properties. *Proceedings of the National Academy of Sciences*, 103(31):11509 LP – 11514.

[Bonnett and Martinez, 2001] Bonnett, R. and Martinez, G. (2001). Photobleaching of sensitisers used in photodynamic therapy. *Tetrahedron*, 57(47):9513–9547.

[Boulanger et al., 2014] Boulanger, J., Gueudry, C., Münch, D., Cinquin, B., Paul-Gilloteaux, P., Bardin, S., Guérin, C., Senger, F., Blanchoin, L., and Salamero, J. (2014). Fast high-resolution 3D total internal reflection fluorescence microscopy by incidence angle scanning and azimuthal averaging. *Proceedings of the National Academy of Sciences*, 111(48):17164–17169.

[Bowen et al., 2005] Bowen, M. E., Weninger, K., Ernst, J., Chu, S., and Brunger, A. T. (2005). Single-Molecule Studies of Synaptotagmin and Complexin Binding to the SNARE Complex. *Biophysical Journal*, 89(1):690–702.

[Brandão et al., 2014] Brandão, H. B., Sangji, H., Pandžić, E., Bechstedt, S., Brouhard, G. J., and Wiseman, P. W. (2014). Measuring ligand-receptor binding kinetics and dynamics using k-space image correlation spectroscopy. *Methods*, 66(2):273–282.

[Bratton and Shaevitz, 2015] Bratton, B. P. and Shaevitz, J. W. (2015). Simple Experimental Methods for Determining the Apparent Focal Shift in a Microscope System. *PLOS ONE*, 10(8):e0134616.

[Briddon et al., 2004] Briddon, S. J., Middleton, R. J., Cordeaux, Y., Flavin, F. M., Weinstein, J. A., George, M. W., Kellam, B., and Hill, S. J. (2004). Quantitative analysis of the formation and diffusion of A_1-adenosine receptor-antagonist complexes in single living cells. *Proceedings of the National Academy of Sciences of the United States of America*, 101(13):4673 LP – 4678.

[Brinkmeier et al., 1999] Brinkmeier, M., Dörre, K., Stephan, J., and Eigen, M. (1999). Two-Beam Cross-Correlation: A Method To Characterize Transport Phenomena in Micrometer-Sized Structures. *Analytical Chemistry*, 71(3):609–616.

[Brodovitch et al., 2015] Brodovitch, A., Limozin, L., Bongrand, P., and Pierres, A. (2015). Use of TIRF to Monitor T-Lymphocyte Membrane Dynamics with Submicrometer and Subsecond Resolution. *Cellular and Molecular Bioengineering*, 8(1):178–186.

[Brogden, 2005] Brogden, K. A. (2005). Antimicrobial peptides: pore formers or metabolic inhibitors in bacteria? *Nature Reviews Microbiology*, 3:238.

[Brunstein et al., 2014a] Brunstein, M., Hérault, K., and Oheim, M. (2014a). Eliminating Unwanted Far-Field Excitation in Objective-Type TIRF. Part II. Combined Evanescent-Wave Excitation and Supercritical-Angle Fluorescence Detection Improves Optical Sectioning. *Biophysical Journal*, 106(5):1044–1056.

[Brunstein et al., 2014b] Brunstein, M., Teremetz, M., Hérault, K., Tourain, C., and Oheim, M. (2014b). Eliminating unwanted far-field excitation in objective-type TIRF. Part I. Identifying sources of nonevanescent excitation light. *Biophysical Journal*, 106(5):1020–1032.

[Brutzer et al., 2012] Brutzer, H., Schwarz, F. W., and Seidel, R. (2012). Scanning Evanescent Fields Using a pointlike Light Source and a Nanomechanical DNA Gear. *Nano Letters*, 12(1):473–478.

[Bunge et al., 2007] Bunge, A., Kurz, A., Windeck, A.-K., Korte, T., Flasche, W., Liebscher, J., Herrmann, A., and Huster, D. (2007). Lipophilic Oligonucleotides Spontaneously Insert into Lipid Membranes, Bind Complementary DNA Strands, and Sequester into Lipid-Disordered Domains. *Langmuir*, 23(8):4455–4464.

[Bunge et al., 2009] Bunge, A., Loew, M., Pescador, P., Arbuzova, A., Brodersen, N., Kang, J., Dähne, L., Liebscher, J., Herrmann, A., Stengel, G., and Hus-

ter, D. (2009). Lipid Membranes Carrying Lipophilic Cholesterol-Based Oligonucleotides—Characterization and Application on Layer-by-Layer Coated Particles. *The Journal of Physical Chemistry B*, 113(51):16425–16434.

[Burghardt, 2012] Burghardt, T. P. (2012). Measuring incidence angle for through-the-objective total internal reflection fluorescence microscopy. *Journal of Biomedical Optics*, 17(12):126007.

[Burghardt and Axelrod, 1981] Burghardt, T. P. and Axelrod, D. (1981). Total internal reflection/fluorescence photobleaching recovery study of serum albumin adsorption dynamics. *Biophysical Journal*, 33(3):455–467.

[Burkhardt and Schwille, 2006] Burkhardt, M. and Schwille, P. (2006). Electron multiplying CCD based detection for spatially resolved fluorescence correlation spectroscopy. *Optics Express*, 14(12):5013–5020.

[Burstyn and Sengers, 1983] Burstyn, H. C. and Sengers, J. V. (1983). Time dependence of critical concentration fluctuations in a binary liquid. *Physical Review A*, 27(2):1071–1085.

[Cabriel et al., 2018] Cabriel, C., Bourg, N., Dupuis, G., and Lévêque-Fort, S. (2018). Aberration-accounting calibration for 3D single-molecule localization microscopy. *Optics Letters*, 43(2):174–177.

[Cadet and Teoule, 1978] Cadet, J. and Teoule, R. (1978). Comparative Study of Oxidation of Nucleic Acid Components by Hydroxyl Radicas, Singlet Oxygen and Superoxide Anion Radicals. *Photochemistry and Photobiology*, 28(4-5):661–665.

[Campbell and Kim, 2007] Campbell, C. T. and Kim, G. (2007). SPR microscopy and its applications to high-throughput analyses of biomolecular binding events and their kinetics. *Biomaterials*, 28(15):2380–2392.

[Cañadas and Casals, 2013] Cañadas, O. and Casals, C. (2013). Differential Scanning Calorimetry of Protein–Lipid Interactions. In Kleinschmidt, J. H., editor, *Lipid-Protein Interactions: Methods and Protocols*, pages 55–71. Humana Press, Totowa, NJ.

[Capoulade et al., 2011] Capoulade, J., Wachsmuth, M., Hufnagel, L., and Knop, M. (2011). Quantitative fluorescence imaging of protein diffusion and interaction in living cells. *Nature Biotechnology*, 29:835.

[Carballido-López, 2006] Carballido-López, R. (2006). The Bacterial Actin-Like Cytoskeleton. *Microbiology and Molecular Biology Reviews*, 70(4):888 LP – 909.

[Cardoso Dos Santos et al., 2014] Cardoso Dos Santos, M., Déturche, R., Vézy, C., and Jaffiol, R. (2014). Axial nanoscale localization by normalized total internal reflection fluorescence microscopy. *Optics Letters*, 39(4):869–872.

[Cardoso Dos Santos et al., 2016] Cardoso Dos Santos, M., Déturche, R., Vézy, C., and Jaffiol, R. (2016). Topography of Cells Revealed by Variable-Angle Total Internal Reflection Fluorescence Microscopy. *Biophysical Journal*, 111(6):1316–1327.

[Carquin et al., 2016] Carquin, M., D'Auria, L., Pollet, H., Bongarzone, E. R., and Tyteca, D. (2016). Recent progress on lipid lateral heterogeneity in plasma membranes: From rafts to submicrometric domains. *Progress in Lipid Research*, 62:1–24.

[Cevc, 2015] Cevc, G. (2015). Partition coefficient vs. binding constant: How best to assess molecular lipophilicity. *European Journal of Pharmaceutics and Biopharmaceutics*, 92:204–215.

[Champagne et al., 2009] Champagne, K., Shishido, A., and Root, M. J. (2009). Interactions of HIV-1 Inhibitory Peptide T20 with the gp41 N-HR Coiled Coil. *Journal of Biological Chemistry*, 284(6):3619–3627.

[Chan and Boxer, 2007] Chan, Y.-H. M. and Boxer, S. G. (2007). Model membrane systems and their applications. *Current Opinion in Chemical Biology*, 11(6):581–587.

[Chang et al., 2016] Chang, V. T., Fernandes, R. A., Ganzinger, K. A., Lee, S. F., Siebold, C., McColl, J., Jönsson, P., Palayret, M., Harlos, K., Coles, C. H., Jones, E. Y., Lui, Y., Huang, E., Gilbert, R. J. C., Klenerman, D., Aricescu, A. R., and Davis, S. J. (2016). Initiation of T cell signaling by CD45 segregation at 'close contacts'. *Nature Immunology*, 17:574.

[Chatterjee et al., 2017] Chatterjee, G., Dalchau, N., Muscat, R. A., Phillips, A., and Seelig, G. (2017). A spatially localized architecture for fast and modular DNA computing. *Nat Nano*, 12(9):920–927.

[Chiaruttini et al., 2015] Chiaruttini, N., Redondo-Morata, L., Colom, A., Humbert, F., Lenz, M., Scheuring, S., and Roux, A. (2015). Relaxation of Loaded ESCRT-III Spiral Springs Drives Membrane Deformation. *Cell*, 163(4):866–879.

[Cho et al., 2010] Cho, N.-J., Frank, C. W., Kasemo, B., and Höök, F. (2010). Quartz crystal microbalance with dissipation monitoring of supported lipid bilayers on various substrates. *Nature Protocols*, 5:1096.

[Choi et al., 2004] Choi, S., Baudys, M., and Kim, S. W. (2004). Control of Blood Glucose by Novel GLP-1 Delivery Using Biodegradable Triblock Copolymer of PLGA-PEG-PLGA in Type 2 Diabetic Rats. *Pharmaceutical Research*, 21(5):827–831.

[Chung et al., 2009] Chung, M., Lowe, R. D., Chan, Y.-H. M., Ganesan, P. V., and Boxer, S. G. (2009). DNA-tethered membranes formed by giant vesicle rupture. *Journal of Structural Biology*, 168(1):190–199.

[Clifton et al., 2013] Clifton, L. A., Neylon, C., and Lakey, J. H. (2013). Examining Protein–Lipid Complexes Using Neutron Scattering. In Kleinschmidt, J. H., editor, *Lipid-Protein Interactions: Methods and Protocols*, pages 119–150. Humana Press, Totowa, NJ.

[Cole et al., 2017] Cole, D., Young, G., Weigel, A., Sebesta, A., and Kukura, P. (2017). Label-Free Single-Molecule Imaging with Numerical-Aperture-Shaped Interferometric Scattering Microscopy. *ACS Photonics*, 4(2):211–216.

[Colson et al., 1992] Colson, A. O., Besler, B., Close, D. M., and Sevilla, M. D. (1992). Ab initio molecular orbital calculations of DNA bases and their radical ions in various protonation states: Evidence for proton transfer in GC base pair radical anions. *The Journal of Physical Chemistry*.

[Constantinescu and Lafleur, 2004] Constantinescu, I. and Lafleur, M. (2004). Influence of the lipid composition on the kinetics of concerted insertion and folding of melittin in bilayers. *Biochimica et Biophysica Acta (BBA) - Biomembranes*, 1667(1):26–37.

[Cooper et al., 2004] Cooper, M., Ebner, A., Briggs, M., Burrows, M., Gardner, N., Richardson, R., and West, R. (2004). Cy3B™: Improving the Performance of Cyanine Dyes. *Journal of Fluorescence*, 14(2):145–150.

[Cornell and Taneva, 2006] Cornell, R. B. and Taneva, S. G. (2006). Amphipathic Helices as Mediators of the Membrane Interaction of Amphitropic Proteins, and as Modulators of Bilayer Physical Properties.

[Czogalla et al., 2016] Czogalla, A., Franquelim, H. G., and Schwille, P. (2016). DNA Nanostructures on Membranes as Tools for Synthetic Biology. *Biophysical Journal*, 110(8):1698–1707.

[Czogalla et al., 2013] Czogalla, A., Petrov, E. P., Kauert, D. J., Uzunova, V., Zhang, Y., Seidel, R., and Schwille, P. (2013). Switchable domain partitioning and diffusion of DNA origami rods on membranes. *Faraday discussions*, 161:31–43.

[Danelon et al., 2006] Danelon, C., Perez, J.-B., Santschi, C., Brugger, J., and Vogel, H. (2006). Cell Membranes Suspended Across Nanoaperture Arrays. *Langmuir*, 22(1):22–25.

[Dave et al., 2009] Dave, R., Terry, D. S., Munro, J. B., and Blanchard, S. C. (2009). Mitigating Unwanted Photophysical Processes for Improved Single-Molecule Fluorescence Imaging. *Biophysical Journal*, 96(6):2371–2381.

[Davidson, 1979] Davidson, R. S. (1979). Mechanisms of photo-oxidation reactions. *Pesticide Science*, 10(2):158–170.

[Deagle et al., 2017] Deagle, R. C., Wee, T.-L. E., and Brown, C. M. (2017). Reproducibility in light microscopy: Maintenance, standards and SOPs. *The International Journal of Biochemistry & Cell Biology*, 89:120–124.

[Deng and Shaevitz, 2009] Deng, Y. and Shaevitz, J. W. (2009). Effect of aberration on height calibration in three-dimensional localization-based microscopy and particle tracking. *Applied Optics*, 48(10):1886–1890.

[Deng et al., 2008] Deng, Y., Wang, Y., Holtz, B., Li, J., Traaseth, N., Veglia, G., Stottrup, B. J., Elde, R., Pei, D., Guo, A., and Zhu, X.-Y. (2008). Fluidic and Air-Stable Supported Lipid Bilayer and Cell-Mimicking Microarrays. *Journal of the American Chemical Society*, 130(19):6267–6271.

[Denisov et al., 2004] Denisov, I. G., Grinkova, Y. V., Lazarides, A. A., and Sligar, S. G. (2004). Directed Self-Assembly of Monodisperse Phospholipid Bilayer Nanodiscs with Controlled Size. *Journal of the American Chemical Society*, 126(11):3477–3487.

[Denisov and Sligar, 2016] Denisov, I. G. and Sligar, S. G. (2016). Nanodiscs for structural and functional studies of membrane proteins. *Nature Structural &Amp; Molecular Biology*, 23:481.

[Deschout et al., 2014] Deschout, H., Zanacchi, F. C., Mlodzianoski, M., Diaspro, A., Bewersdorf, J., Hess, S. T., and Braeckmans, K. (2014). Precisely and accurately localizing single emitters in fluorescence microscopy. *Nature Methods*, 11:253.

[Deverall et al., 2008] Deverall, M. A., Garg, S., Lüdtke, K., Jordan, R., Rühe, J., and Naumann, C. A. (2008). Transbilayer coupling of obstructed lipid diffusion in polymer-tethered phospholipid bilayers. *Soft Matter*, 4(9):1899–1908.

[Di Paolo and De Camilli, 2006] Di Paolo, G. and De Camilli, P. (2006). Phosphoinositides in cell regulation and membrane dynamics. *Nature*, 443(7112):651–657.

[Diaspro et al., 2006] Diaspro, A., Chirico, G., Usai, C., Ramoino, P., and Dobrucki, J. (2006). Photobleaching. In Pawley, J. B., editor, *Handbook Of Biological Confocal Microscopy*, pages 690–702. Springer US, Boston, MA.

[Digman et al., 2005a] Digman, M. A., Brown, C. M., Sengupta, P., Wiseman, P. W., Horwitz, A. R., and Gratton, E. (2005a). Measuring Fast Dynamics in Solutions and Cells with a Laser Scanning Microscope. *Biophysical Journal*, 89(2):1317–1327.

[Digman et al., 2005b] Digman, M. A., Sengupta, P., Wiseman, P. W., Brown, C. M., Horwitz, A. R., and Gratton, E. (2005b). Fluctuation Correlation Spectroscopy with a Laser-Scanning Microscope: Exploiting the Hidden Time Structure. *Biophysical Journal*, 88(5):L33–L36.

[Dijkman and Watts, 2015] Dijkman, P. M. and Watts, A. (2015). Lipid modulation of early G protein-coupled receptor signalling events. *Biochimica et Biophysica Acta (BBA) - Biomembranes*, 1848(11, Part A):2889–2897.

[Dirks and Pierce, 2004] Dirks, R. M. and Pierce, N. A. (2004). An algorithm for computing nucleic acid base-pairing probabilities including pseudoknots. *Journal of Computational Chemistry*, 25(10):1295–1304.

[Dittrich and Schwille, 2002] Dittrich, P. S. and Schwille, P. (2002). Spatial Two-Photon Fluorescence Cross-Correlation Spectroscopy for Controlling Molecular Transport in Microfluidic Structures. *Analytical Chemistry*, 74(17):4472–4479.

[Dixit and Cyr, 2003] Dixit, R. and Cyr, R. (2003). Cell damage and reactive oxygen species production induced by fluorescence microscopy: effect on mitosis and guidelines for non-invasive fluorescence microscopy. *The Plant Journal*, 36(2):280–290.

[Dixon, 2008] Dixon, M. C. (2008). Quartz Crystal Microbalance with Dissipation Monitoring: Enabling Real-Time Characterization of Biological Materials and Their Interactions. *Journal of Biomolecular Techniques*, 19(3):151–158.

[Djaker et al., 2016] Djaker, N., Sultana, S., Issaad, D., Boca, S., Moustaoui, H., Spadavecchia, J., Medjahed, A., Bouafia, M., Astilean, S., and de la Chapelle, M. L. (2016). Spherical and Flower-Shaped Gold Nanoparticles Characterization by Scattering Correlation Spectroscopy. *The Journal of Physical Chemistry C*, 120(21):11700–11708.

[Dörlich et al., 2015] Dörlich, R. M., Chen, Q., Niklas Hedde, P., Schuster, V., Hippler, M., Wesslowski, J., Davidson, G., and Nienhaus, G. U. (2015). Dual-color dual-focus line-scanning FCS for quantitative analysis of receptor-ligand interactions in living specimens. *Scientific Reports*, 5:10149.

[Dorn et al., 1998] Dorn, I. T., Neumaier, K. R., and Tampé, R. (1998). Molecular Recognition of Histidine-Tagged Molecules by Metal-Chelating Lipids Monitored by Fluorescence Energy Transfer and Correlation Spectroscopy. *Journal of the American Chemical Society*, 120(12):2753–2763.

[Drin and Antonny, 2010] Drin, G. and Antonny, B. (2010). Amphipathic helices and membrane curvature. *FEBS Letters*, 584(9):1840–1847.

[Dupuis et al., 2013] Dupuis, N. F., Holmstrom, E. D., and Nesbitt, D. J. (2013). Single-Molecule Kinetics Reveal Cation-Promoted DNA Duplex Formation Through Ordering of Single-Stranded Helices. *Biophysical Journal*, 105(3):756–766.

[Dustin and Groves, 2012] Dustin, M. L. and Groves, J. T. (2012). Receptor Signaling Clusters in the Immune Synapse. *Annual Review of Biophysics*, 41(1):543–556.

[Edelstein et al., 2010] Edelstein, A., Amodaj, N., Hoover, K., Vale, R., and Stuurman, N. (2010). Computer Control of Microscopes Using μManager. *Current Protocols in Molecular Biology*, 92(1):14.20.1–14.20.17.

[Eggeling et al., 2005] Eggeling, C., Volkmer, A., and Seidel, C. A. M. (2005). Molecular Photobleaching Kinetics of Rhodamine 6G by One- and Two-Photon Induced Confocal Fluorescence Microscopy. *ChemPhysChem*, 6(5):791–804.

[Eggeling et al., 2006] Eggeling, C., Widengren, J., Brand, L., Schaffer, J., Felekyan, S., and Seidel, C. A. M. (2006). Analysis of Photobleaching in Single-Molecule Multicolor

Excitation and Förster Resonance Energy Transfer Measurements. *The Journal of Physical Chemistry A*, 110(9):2979–2995.

[Eggeling et al., 1998] Eggeling, C., Widengren, J., Rigler, R., and Seidel, C. A. M. (1998). Photobleaching of Fluorescent Dyes under Conditions Used for Single-Molecule Detection: Evidence of Two-Step Photolysis. *Analytical Chemistry*, 70(13):2651–2659.

[Eggeling et al., 1999] Eggeling, C., Widengren, J., Rigler, R., and Seidel, C. A. M. (1999). Photostability of Fluorescent Dyes for Single-Molecule Spectroscopy: Mechanisms and Experimental Methods for Estimating Photobleaching in Aqueous Solution BT - Applied Fluorescence in Chemistry, Biology and Medicine. In Rettig, W., Strehmel, B., Schrader, S., and Seifert, H., editors, *Applied Fluorescence in Chemistry, Biology and Medicine*, pages 193–240. Springer Berlin Heidelberg, Berlin, Heidelberg.

[Eigen and Rigler, 1994] Eigen, M. and Rigler, R. (1994). Sorting single molecules: application to diagnostics and evolutionary biotechnology. *Proceedings of the National Academy of Sciences*, 91(13):5740–5747.

[Einstein, 1905] Einstein, A. (1905). Über die von der molekularkinetischen Theorie der Wärme geforderte Bewegung von in ruhenden Flüssigkeiten suspendierten Teilchen. *Annalen der Physik*, 322(8):549–560.

[Elenko et al., 2010] Elenko, M. P., Szostak, J. W., and van Oijen, A. M. (2010). Single-molecule binding experiments on long time scales. *Review of Scientific Instruments*, 81(8):83705.

[Elf et al., 2007] Elf, J., Li, G.-W., and Xie, X. S. (2007). Probing Transcription Factor Dynamics at the Single-Molecule Level in a Living Cell. *Science*, 316(5828):1191–1194.

[Elson, 2011] Elson, E. L. (2011). Fluorescence Correlation Spectroscopy: Past, Present, Future. *Biophysical Journal*, 101(12):2855–2870.

[Elson and Magde, 1974] Elson, E. L. and Magde, D. (1974). Fluorescence correlation spectroscopy. I. Conceptual basis and theory. *Biopolymers*, 13(1):1–27.

[Enderlein, 1999] Enderlein, J. (1999). Fluorescence detection of single molecules near a solution/glass interface – an electrodynamic analysis. *Chemical Physics Letters*, 308(3):263–266.

[Endesfelder et al., 2014] Endesfelder, U., Malkusch, S., Fricke, F., and Heilemann, M. (2014). A simple method to estimate the average localization precision of a single-molecule localization microscopy experiment. *Histochemistry and Cell Biology*, 141(6):629–638.

[Engel and Gaub, 2008] Engel, A. and Gaub, H. E. (2008). Structure and Mechanics of Membrane Proteins. *Annual Review of Biochemistry*, 77(1):127–148.

[Englander et al., 1987] Englander, S., Calhoun, D. B., and Englander, J. J. (1987). Biochemistry without oxygen. *Analytical Biochemistry*, 161(2):300–306.

[Fahey et al., 1977] Fahey, P. F., Koppel, D. E., Barak, L. S., Wolf, D. E., Elson, E. L., and Webb, W. W. (1977). Lateral diffusion in planar lipid bilayers. *Science*, 195(4275):305 LP – 306.

[Fang et al., 2002] Fang, Y., Frutos, A. G., and Lahiri, J. (2002). Membrane Protein Microarrays. *Journal of the American Chemical Society*, 124(11):2394–2395.

[Feinerman et al., 2008] Feinerman, O., Germain, R. N., and Altan-Bonnet, G. (2008). Quantitative challenges in understanding ligand discrimination by $\alpha\beta$ T cells. *Molecular Immunology*, 45(3):619–631.

[Ferreon et al., 2009] Ferreon, A. C. M., Gambin, Y., Lemke, E. A., and Deniz, A. A. (2009). Interplay of α-synuclein binding and conformational switching probed by single-molecule fluorescence. *Proceedings of the National Academy of Sciences*, 106(14):5645 LP – 5650.

[Fiolka et al., 2008] Fiolka, R., Belyaev, Y., Ewers, H., and Stemmer, A. (2008). Even illumination in total internal reflection fluorescence microscopy using laser light. *Microscopy Research and Technique*, 71(1):45–50.

[Fish, 2009] Fish, K. N. (2009). Total Internal Reflection Fluorescence (TIRF) Microscopy. *Current Protocols in Cytometry*, 50(1):12.18.1–12.18.13.

[Förster, 1949] Förster, T. (1949). Experimentelle und theoretische Untersuchung des zwischenmolekularen Übergangs von Elektronenanregungsenergie.

[Forstner et al., 2006] Forstner, M. B., Yee, C. K., Parikh, A. N., and Groves, J. T. (2006). Lipid Lateral Mobility and Membrane Phase Structure Modulation by Protein Binding. *Journal of the American Chemical Society*, 128(47):15221–15227.

[Fox et al., 2009] Fox, C. B., Wayment, J. R., Myers, G. A., Endicott, S. K., and Harris, J. M. (2009). Single-Molecule Fluorescence Imaging of Peptide Binding to Supported Lipid Bilayers. *Analytical Chemistry*, 81(13):5130–5138.

[Franquelim et al., 2011] Franquelim, H. G., Chiantia, S., Veiga, A. S., Santos, N. C., Schwille, P., and Castanho, M. A. R. B. (2011). Anti-HIV-1 antibodies 2F5 and 4E10 interact differently with lipids to bind their epitopes. *AIDS*, 25(4).

[Franquelim et al., 2018] Franquelim, H. G., Khmelinskaia, A., Sobczak, J.-P., Dietz, H., and Schwille, P. (2018). Membrane sculpting by curved DNA origami scaffolds. *Nature Communications*, 9(1):811.

[Franquelim et al., 2010] Franquelim, H. G., Veiga, A. S., Weissmüller, G., Santos, N. C., and Castanho, M. A. R. B. (2010). Unravelling the molecular basis of the selectivity of the HIV-1 fusion inhibitor sifuvirtide towards phosphatidylcholine-rich rigid membranes. *Biochimica et Biophysica Acta (BBA) - Biomembranes*, 1798(6):1234–1243.

[Frenzel and Willbold, 2014] Frenzel, D. and Willbold, D. (2014). Kinetic Titration Series with Biolayer Interferometry. *PLOS ONE*, 9(9):e106882.

[Frey et al., 2008] Frey, G., Peng, H., Rits-Volloch, S., Morelli, M., Cheng, Y., and Chen, B. (2008). A fusion-intermediate state of HIV-1 gp41 targeted by broadly neutralizing antibodies. *Proceedings of the National Academy of Sciences*, 105(10):3739 LP – 3744.

[Freyer and Lewis, 2008] Freyer, M. W. and Lewis, E. A. (2008). Isothermal Titration Calorimetry: Experimental Design, Data Analysis, and Probing Macromolecule/Ligand Binding and Kinetic Interactions. In *Biophysical Tools for Biologists, Volume One: In Vitro Techniques*, volume 84 of *Methods in Cell Biology*, pages 79–113. Academic Press.

[Fu et al., 2016] Fu, Y., Winter, P. W., Rojas, R., Wang, V., McAuliffe, M., and Patterson, G. H. (2016). Axial superresolution via multiangle TIRF microscopy with sequential imaging and photobleaching. *Proceedings of the National Academy of Sciences*, 113(16):4368 LP – 4373.

[Funatsu et al., 1995] Funatsu, T., Harada, Y., Tokunaga, M., Saito, K., and Yanagida, T. (1995). Imaging of single fluorescent molecules and individual ATP turnovers by single myosin molecules in aqueous solution. *Nature*, 374(6522):555–559.

[Gallop et al., 2006] Gallop, J. L., Jao, C. C., Kent, H. M., Butler, P. J. G., Evans, P. R., Langen, R., and McMahon, H. T. (2006). Mechanism of endophilin N-BAR domain-mediated membrane curvature. *The EMBO Journal*, 25(12):2898 LP – 2910.

[Gambin et al., 2006] Gambin, Y., Lopez-Esparza, R., Reffay, M., Sierecki, E., Gov, N. S., Genest, M., Hodges, R. S., and Urbach, W. (2006). Lateral mobility of proteins in liquid membranes revisited. *Proceedings of the National Academy of Sciences of the United States of America*, 103(7):2098–2102.

[Gambinossi et al., 2010] Gambinossi, F., Banchelli, M., Durand, A., Berti, D., Brown, T., Caminati, G., and Baglioni, P. (2010). Modulation of Density and Orientation of Amphiphilic DNA Anchored to Phospholipid Membranes. I. Supported Lipid Bilayers. *The Journal of Physical Chemistry B*, 114(21):7338–7347.

[García-Sáez et al., 2010] García-Sáez, A. J., Carrer, D. C., and Schwille, P. (2010). Fluorescence Correlation Spectroscopy for the Study of Membrane Dynamics and Organization in Giant Unilamellar Vesicles. In Weissig, V., editor, *Liposomes: Methods and Protocols, Volume 2: Biological Membrane Models*, pages 493–508. Humana Press, Totowa, NJ.

[García-Sáez and Schwille, 2008] García-Sáez, A. J. and Schwille, P. (2008). Fluorescence correlation spectroscopy for the study of membrane dynamics and protein/lipid interactions. *Methods*, 46(2):116–122.

[Garewal et al., 2013] Garewal, M., Zhang, L., and Ren, G. (2013). Optimized Negative-Staining Protocol for Examining Lipid-Protein Interactions by Electron Microscopy. In Kleinschmidt, J. H., editor, *Lipid-Protein Interactions: Methods and Protocols*, pages 111–118. Humana Press, Totowa, NJ.

[GE Healthcare Bio-Sciences, 2018] GE Healthcare Bio-Sciences (2018). Selection guide Biacore™ systems.

[Gebhardt et al., 2013] Gebhardt, J. C. M., Suter, D. M., Roy, R., Zhao, Z. W., Chapman, A. R., Basu, S., Maniatis, T., and Xie, X. S. (2013). Single-molecule imaging of transcription factor binding to DNA in live mammalian cells. *Nature Methods*, 10:421.

[Gell et al., 2009] Gell, C., Berndt, M., Enderlein, J., and Diez, S. (2009). TIRF microscopy evanescent field calibration using tilted fluorescent microtubules. *Journal of Microscopy*, 234(1):38–46.

[Gelles et al., 1988] Gelles, J., Schnapp, B. J., and Sheetz, M. P. (1988). Tracking kinesin-driven movements with nanometre-scale precision. *Nature*, 331(6155):450–453.

[Gerlach et al., 2009] Gerlach, H., Laumann, V., Martens, S., Becker, C. F. W., Goody, R. S., and Geyer, M. (2009). HIV-1 Nef membrane association depends on charge, curvature, composition and sequence. *Nature Chemical Biology*, 6:46.

[Ghai et al., 2012] Ghai, R., Falconer, R. J., and Collins, B. M. (2012). Applications of isothermal titration calorimetry in pure and applied research - survey of the literature from 2010. *Journal of Molecular Recognition*, 25(1):32–52.

[Gingell et al., 1987] Gingell, D., Heavens, O. S., and Mellor, J. S. (1987). General electromagnetic theory of total internal reflection fluorescence: the quantitative basis for mapping cell-substratum topography. *Journal of Cell Science*, 87(5):677 LP – 693.

[Gösch et al., 2004] Gösch, M., Serov, A., Rochas, A., Blom, H., Anhut, T., Besse, P.-A., Popovic, R., Lasser, T., and Rigler, R. (2004). Parallel single molecule detection with a fully integrated single-photon 2×2 CMOS detector array. *Journal of Biomedical Optics*, 9(5):913–921.

[Govern et al., 2010] Govern, C. C., Paczosa, M. K., Chakraborty, A. K., and Huseby, E. S. (2010). Fast on-rates allow short dwell time ligands to activate T cells. *Proceedings of the National Academy of Sciences*, 107(19):8724 LP – 8729.

[Graves et al., 2015] Graves, E. T., Duboc, C., Fan, J., Stransky, F., Leroux-Coyau, M., and Strick, T. R. (2015). A dynamic DNA-repair complex observed by correlative single-molecule nanomanipulation and fluorescence. *Nature Structural & Molecular Biology*, 22:452.

[Greenberg, 2004] Greenberg, M. M. (2004). In vitro and in vivo effects of oxidative damage to deoxyguanosine. *Biochemical Society Transactions*, 32(1):46 LP – 50.

[Groves, 2002] Groves, J. T. (2002). Membrane array technology for drug discovery. *Current Opinion in Drug Discovery and Development*, 5(4):606–612.

[Groves and Kuriyan, 2010] Groves, J. T. and Kuriyan, J. (2010). Molecular mechanisms in signal transduction at the membrane. *Nature Structural &Amp; Molecular Biology*, 17:659.

[Groves et al., 1997] Groves, J. T., Ulman, N., and Boxer, S. G. (1997). Micropatterning Fluid Lipid Bilayers on Solid Supports. *Science*, 275(5300):651 LP – 653.

[Groves et al., 1998] Groves, J. T., Ulman, N., Cremer, P. S., and Boxer, S. G. (1998). Substrate-Membrane Interactions: Mechanisms for Imposing Patterns on a Fluid Bilayer Membrane. *Langmuir*, 14(12):3347–3350.

[Guigas and Weiss, 2016] Guigas, G. and Weiss, M. (2016). Effects of protein crowding on membrane systems. *Biochimica et Biophysica Acta (BBA) - Biomembranes*, 1858(10):2441–2450.

[Guo et al., 2008] Guo, L., Har, J. Y., Sankaran, J., Hong, Y., Kannan, B., and Wohland, T. (2008). Molecular Diffusion Measurement in Lipid Bilayers over Wide Concentration Ranges: A Comparative Study. *ChemPhysChem*, 9(5):721–728.

[Gust et al., 2014] Gust, A., Zander, A., Gietl, A., Holzmeister, P., Schulz, S., Lalkens, B., Tinnefeld, P., and Grohmann, D. (2014). A Starting Point for Fluorescence-Based Single-Molecule Measurements in Biomolecular Research. *Molecules*, 19(10):15824–15865.

[Ha et al., 1996] Ha, T., Enderle, T., Ogletree, D. F., Chemla, D. S., Selvin, P. R., and Weiss, S. (1996). Probing the interaction between two single molecules: fluorescence resonance energy transfer between a single donor and a single acceptor. *Proceedings of the National Academy of Sciences*, 93(13):6264 LP – 6268.

[Ha and Tinnefeld, 2012] Ha, T. and Tinnefeld, P. (2012). Photophysics of Fluorescent Probes for Single-Molecule Biophysics and Super-Resolution Imaging. *Annual Review of Physical Chemistry*, 63(1):595–617.

[Halatek and Frey, 2018] Halatek, J. and Frey, E. (2018). Rethinking pattern formation in reaction–diffusion systems. *Nature Physics*, 14(5):507–514.

[Hamai et al., 2007] Hamai, C., Cremer, P. S., and Musser, S. M. (2007). Single Giant Vesicle Rupture Events Reveal Multiple Mechanisms of Glass-Supported Bilayer Formation. *Biophysical Journal*, 92(6):1988–1999.

[Hansen and Harris, 1998a] Hansen, R. L. and Harris, J. M. (1998a). Measuring Reversible Adsorption Kinetics of Small Molecules at Solid/Liquid Interfaces by Total Internal Reflection Fluorescence Correlation Spectroscopy. *Analytical Chemistry*, 70(20):4247–4256.

[Hansen and Harris, 1998b] Hansen, R. L. and Harris, J. M. (1998b). Total Internal Reflection Fluorescence Correlation Spectroscopy for Counting Molecules at Solid/Liquid Interfaces. *Analytical Chemistry*, 70(13):2565–2575.

[Harada et al., 1990] Harada, Y., Sakurada, K., Aoki, T., Thomas, D. D., and Yanagida, T. (1990). Mechanochemical coupling in actomyosin energy transduction studied by in vitro movement assay. *Journal of Molecular Biology*, 216(1):49–68.

[Harlepp et al., 2004] Harlepp, S., Robert, J., Darnton, N. C., and Chatenay, D. (2004). Subnanometric measurements of evanescent wave penetration depth using total internal reflection microscopy combined with fluorescent correlation spectroscopy. *Applied Physics Letters*, 85(17):3917–3919.

[Hassler et al., 2005a] Hassler, K., Anhut, T., Rigler, R., Gösch, M., and Lasser, T. (2005a). High Count Rates with Total Internal Reflection Fluorescence Correlation Spectroscopy. *Biophysical Journal*, 88(1):L01 – L03.

[Hassler et al., 2005b] Hassler, K., Leutenegger, M., Rigler, P., Rao, R., Rigler, R., Gösch, M., and Lasser, T. (2005b). Total internal reflection fluorescence correlation spectroscopy (TIR-FCS) with low background and high count-rate per molecule. *Opt. Express*, 13(19):7415–7423.

[Hassler et al., 2007] Hassler, K., Rigler, P., Blom, H., Rigler, R., Widengren, J., and Lasser, T. (2007). Dynamic disorder in horseradish peroxidase observed with total internal reflection fluorescence correlation spectroscopy. *Opt. Express*, 15(9):5366–5375.

[Haupts et al., 1998] Haupts, U., Maiti, S., Schwille, P., and Webb, W. W. (1998). Dynamics of fluorescence fluctuations in green fluorescent protein observed by fluorescence correlation spectroscopy. *Proceedings of the National Academy of Sciences*, 95(23):13573–13578.

[Hebert et al., 2005] Hebert, B., Costantino, S., and Wiseman, P. W. (2005). Spatiotemporal Image Correlation Spectroscopy (STICS) Theory, Verification, and Application to Protein Velocity Mapping in Living CHO Cells. *Biophysical Journal*, 88(5):3601–3614.

[Heilemann et al., 2008] Heilemann, M., van de Linde, S., Schüttpelz, M., Kasper, R., Seefeldt, B., Mukherjee, A., Tinnefeld, P., and Sauer, M. (2008). Subdiffraction-Resolution Fluorescence Imaging with Conventional Fluorescent Probes. *Angewandte Chemie International Edition*, 47(33):6172–6176.

[Heinze et al., 2009] Heinze, K. G., Costantino, S., De Koninck, P., and Wiseman, P. W. (2009). Beyond Photobleaching, Laser Illumination Unbinds Fluorescent Proteins. *The Journal of Physical Chemistry B*, 113(15):5225–5233.

[Helenius et al., 2006] Helenius, J., Brouhard, G., Kalaidzidis, Y., Diez, S., and Howard, J. (2006). The depolymerizing kinesin MCAK uses lattice diffusion to rapidly target microtubule ends. *Nature*, 441(7089):115–119.

[Hell et al., 1993] Hell, S., Reiner, G., Cremer, C., and Stelzer, E. H. K. (1993). Aberrations in confocal fluorescence microscopy induced by mismatches in refractive index. *Journal of Microscopy*, 169(3):391–405.

[Hernández-Rocamora et al., 2012] Hernández-Rocamora, V. M., Reija, B., García, C., Natale, P., Alfonso, C., Minton, A. P., Zorrilla, S., Rivas, G., and Vicente, M. (2012). Dynamic Interaction of the Escherichia coli Cell Division ZipA and FtsZ Proteins Evidenced in Nanodiscs. *Journal of Biological Chemistry*, 287(36):30097–30104.

[Hess et al., 2006] Hess, S. T., Girirajan, T. P., and Mason, M. D. (2006). Ultra-High Resolution Imaging by Fluorescence Photoactivation Localization Microscopy. *Biophysical Journal*, 91(11):4258–4272.

[Hirakawa et al., 2003] Hirakawa, K., Suzuki, H., Oikawa, S., and Kawanishi, S. (2003). Sequence-specific DNA damage induced by ultraviolet A-irradiated folic acid via its photolysis product. *Archives of Biochemistry and Biophysics*, 410(2):261–268.

[Hocdé et al., 2009] Hocdé, S. A., Hyrien, O., and Waugh, R. E. (2009). Molecular Accessibility in Relation to Cell Surface Topography and Compression Against a Flat Substrate. *Biophysical Journal*, 97(1):369–378.

[Hodnik and Anderluh, 2013] Hodnik, V. and Anderluh, G. (2013). Surface Plasmon Resonance for Measuring Interactions of Proteins with Lipid Membranes. In Kleinschmidt, J. H., editor, *Lipid-Protein Interactions: Methods and Protocols*, pages 23–36. Humana Press, Totowa, NJ.

[Hoogenboom et al., 2005] Hoogenboom, J. P., van Dijk, E. M. H. P., Hernando, J., van Hulst, N. F., and García-Parajó, M. F. (2005). Power-Law-Distributed Dark States are the Main Pathway for Photobleaching of Single Organic Molecules. *Physical Review Letters*, 95(9):97401.

[Hoops et al., 2006] Hoops, S., Sahle, S., Gauges, R., Lee, C., Pahle, J., Simus, N., Singhal, M., Xu, L., Mendes, P., and Kummer, U. (2006). COPASI—a COmplex PAthway SImulator. *Bioinformatics*, 22(24):3067–3074.

[Hovis and Boxer, 2000] Hovis, J. S. and Boxer, S. G. (2000). Patterning Barriers to Lateral Diffusion in Supported Lipid Bilayer Membranes by Blotting and Stamping. *Langmuir*, 16(3):894–897.

[Hsieh et al., 2010] Hsieh, C.-W., Lin, T.-Y., Lai, H.-M., Lin, C.-C., Hsieh, T.-S., and Shih, Y.-L. (2010). Direct MinE–membrane interaction contributes to the proper localization of MinDE in E. coli. *Molecular Microbiology*, 75(2):499–512.

[Hsieh and Thompson, 1995] Hsieh, H. V. and Thompson, N. L. (1995). Dissociation Kinetics between a Mouse Fc Receptor (Fc.gamma.RII) and IgG: Measurement by Total Internal Reflection with Fluorescence Photobleaching Recovery. *Biochemistry*, 34(38):12481–12488.

[Hsieh et al., 1992] Hsieh, H. V., Thompson, N. L., and Poglitsch, C. L. (1992). Direct Measurement of the Weak Interactions between a Mouse Fc Receptor (FcγRII) and IgGl in the Absence and Presence of Hapten: A Total Internal Reflection Fluorescence Microscopy Study. *Biochemistry*, 31(46):11562–11566.

[Huang et al., 2009] Huang, B., Bates, M., and Zhuang, X. (2009). Super-Resolution Fluorescence Microscopy. *Annual Review of Biochemistry*, 78(1):993–1016.

[Huang et al., 2008] Huang, B., Wang, W., Bates, M., and Zhuang, X. (2008). Three-Dimensional Super-Resolution Imaging by Stochastic Optical Reconstruction Microscopy. *Science*, 319(5864):810–813.

[Huang and Pralle, 2011] Huang, H. and Pralle, A. (2011). Continuous monitoring of membrane protein micro-domain association during cell signaling. *arXiv preprint arXiv:1101.5087*.

[Huang et al., 2015] Huang, H., Simsek, M. F., Jin, W., Pralle, A., Ishibashi, M., and Miwa, Y. (2015). Effect of Receptor Dimerization on Membrane Lipid Raft Structure Continuously Quantified on Single Cells by Camera Based Fluorescence Correlation Spectroscopy. *PLOS ONE*, 10(3):e0121777.

[Huang and Thompson, 1996] Huang, Z. and Thompson, N. L. (1996). Imaging fluorescence correlation spectroscopy: nonuniform IgE distributions on planar membranes. *Biophysical Journal*, 70(4):2001–2007.

[Im et al., 2013] Im, K.-B., Schmidt, U., Kang, M.-S., Lee, J.-Y., Bestvater, F., and Wachsmuth, M. (2013). Diffusion and binding analyzed with combined point FRAP and FCS. *Cytometry Part A*, 83(9):876–889.

[Izeddin et al., 2012] Izeddin, I., El Beheiry, M., Andilla, J., Ciepielewski, D., Darzacq, X., and Dahan, M. (2012). PSF shaping using adaptive optics for three-dimensional single-molecule super-resolution imaging and tracking. *Optics Express*, 20(5):4957–4967.

[Jacobson et al., 1987] Jacobson, K., Ishihara, A., and Inman, R. (1987). Lateral diffusion of proteins in membranes. *Annual review of physiology*, 49(1):163–175.

[Janshoff et al., 2000] Janshoff, A., Galla, H.-J., and Steinem, C. (2000). Piezoelectric Mass-Sensing Devices as Biosensors—An Alternative to Optical Biosensors? *Angewandte Chemie International Edition*, 39(22):4004–4032.

[Jerabek-Willemsen et al., 2014] Jerabek-Willemsen, M., André, T., Wanner, R., Roth, H. M., Duhr, S., Baaske, P., and Breitsprecher, D. (2014). MicroScale Thermophoresis: Interaction analysis and beyond. *Journal of Molecular Structure*, 1077:101–113.

[Jerabek-Willemsen et al., 2011] Jerabek-Willemsen, M., Wienken, C. J., Braun, D., Baaske, P., and Duhr, S. (2011). Molecular Interaction Studies Using Microscale Thermophoresis. *ASSAY and Drug Development Technologies*, 9(4):342–353.

[Jin et al., 2018] Jin, D., Xi, P., Wang, B., Zhang, L., Enderlein, J., and van Oijen, A. M. (2018). Nanoparticles for super-resolution microscopy and single-molecule tracking. *Nature Methods*, 15(6):415–423.

[Juette et al., 2008] Juette, M. F., Gould, T. J., Lessard, M. D., Mlodzianoski, M. J., Nagpure, B. S., Bennett, B. T., Hess, S. T., and Bewersdorf, J. (2008). Three-dimensional sub–100 nm resolution fluorescence microscopy of thick samples. *Nature Methods*, 5:527.

[Jung et al., 2009] Jung, H., Robison, A. D., and Cremer, P. S. (2009). Multivalent ligand–receptor binding on supported lipid bilayers. *Journal of Structural Biology*, 168(1):90–94.

[Jung et al., 2016] Jung, Y., Riven, I., Feigelson, S. W., Kartvelishvily, E., Tohya, K., Miyasaka, M., Alon, R., and Haran, G. (2016). Three-dimensional localization of T-cell receptors in relation to microvilli using a combination of superresolution microscopies. *Proceedings of the National Academy of Sciences*, 113(40):E5916 LP – E5924.

[Jungmann et al., 2016] Jungmann, R., Avendano, M. S., Dai, M., Woehrstein, J. B., Agasti, S. S., Feiger, Z., Rodal, A., and Yin, P. (2016). Quantitative super-resolution imaging with qPAINT. *Nat Meth*, 13(5):439–442.

[Jungmann et al., 2014] Jungmann, R., Avendaño, M. S., Woehrstein, J. B., Dai, M., Shih, W. M., and Yin, P. (2014). Multiplexed 3D cellular super-resolution imaging with DNA-PAINT and Exchange-PAINT. *Nature Methods*, 11:313.

[Jungmann et al., 2010] Jungmann, R., Steinhauer, C., Scheible, M., Kuzyk, A., Tinnefeld, P., and Simmel, F. C. (2010). Single-Molecule Kinetics and Super-Resolution Microscopy by Fluorescence Imaging of Transient Binding on DNA Origami. *Nano Letters*, 10(11):4756–4761.

[Kahya and Schwille, 2006] Kahya, N. and Schwille, P. (2006). Fluorescence correlation studies of lipid domains in model membranes (Review). *Molecular Membrane Biology*, 23(1):29–39.

[Kalb et al., 1990] Kalb, E., Engel, J., and Tamm, L. K. (1990). Binding of proteins to specific target sites in membranes measured by total internal reflection fluorescence microscopy. *Biochemistry*, 29(6):1607–1613.

[Kannan et al., 2007] Kannan, B., Guo, L., Sudhaharan, T., Ahmed, S., Maruyama, I., and Wohland, T. (2007). Spatially Resolved Total Internal Reflection Fluorescence Correlation Microscopy Using an Electron Multiplying Charge-Coupled Device Camera. *Analytical Chemistry*, 79(12):4463–4470.

[Kannan et al., 2006] Kannan, B., Har, J. Y., Liu, P., Maruyama, I., Ding, J. L., and Wohland, T. (2006). Electron Multiplying Charge-Coupled Device Camera Based Fluorescence Correlation Spectroscopy. *Analytical Chemistry*, 78(10):3444–3451.

[Karedla et al., 2014] Karedla, N., Chizhik, A. I., Gregor, I., Chizhik, A. M., Schulz, O., and Enderlein, J. (2014). Single-Molecule Metal-Induced Energy Transfer (smMIET): Resolving Nanometer Distances at the Single-Molecule Level. *ChemPhysChem*, 15(4):705–711.

[Kessel et al., 2001] Kessel, A., Ben-Tal, N., and May, S. (2001). Interactions of Cholesterol with Lipid Bilayers: The Preferred Configuration and Fluctuations. *Biophysical Journal*, 81(2):643–658.

[Kestin et al., 1978] Kestin, J., Sokolov, M., and Wakeham, W. A. (1978). Viscosity of liquid water in the range -8 C to 150 C. *Journal of Physical and Chemical Reference Data*, 7(3):941–948.

[Khandelia et al., 2008] Khandelia, H., Ipsen, J. H., and Mouritsen, O. G. (2008). The impact of peptides on lipid membranes. *Biochimica et Biophysica Acta (BBA) - Biomembranes*, 1778(7):1528–1536.

[Khmelinskaia et al., 2016] Khmelinskaia, A., Franquelim, H. G., Petrov, E. P., and Schwille, P. (2016). Effect of anchor positioning on binding and diffusion of elongated 3D DNA nanostructures on lipid membranes. *Journal of Physics D: Applied Physics*, 49(19):194001.

[Khmelinskaia et al., 2018] Khmelinskaia, A., Mücksch, J., Conci, F., Chwastek, G., and Schwille, P. (2018). FCS Analysis of Protein Mobility on Lipid Monolayers. *Biophysical Journal*, 114(10):2444–2454.

[Kholodenko et al., 2000] Kholodenko, B. N., Hoek, J. B., and Westerhoff, H. V. (2000). Why cytoplasmic signalling proteins should be recruited to cell membranes. *Trends in Cell Biology*, 10(5):173–178.

[Kieffer and Francis Habener, 1999] Kieffer, T. J. and Francis Habener, J. (1999). The Glucagon-Like Peptides. *Endocrine Reviews*, 20(6):876–913.

[Kim and Yethiraj, 2010] Kim, J. S. and Yethiraj, A. (2010). Crowding Effects on Association Reactions at Membranes. *Biophysical Journal*, 98(6):951–958.

[Kim et al., 2007] Kim, S. A., Heinze, K. G., and Schwille, P. (2007). Fluorescence correlation spectroscopy in living cells. *Nature Methods*, 4:963.

[Kim et al., 2012] Kim, S.-E., Lee, I.-B., and Hong, S.-C. (2012). The effect of the oxygen scavenging system on the pH of buffered sample solutions: in the context of single-molecule fluorescence measurements. *Bulletin of the Korean Chemical Society*, 33(3):958–962.

[Kinjo and Rigler, 1995] Kinjo, M. and Rigler, R. (1995). Ultrasensitive hybridization analysis using fluorescence correlation spectroscopy. *Nucleic Acids Research*, 23(10):1795–1799.

[Kleinschmidt, 2013] Kleinschmidt, J. H. (2013). *Lipid-protein interactions : methods and protocols*. Humana Press.

[Knight and Falke, 2009] Knight, J. D. and Falke, J. J. (2009). Single-molecule fluorescence studies of a PH domain: New insights into the membrane docking reaction. *Biophysical Journal*, 96(2):566–582.

[Knoll et al., 2009] Knoll, W., Bender, K., Förch, R., Frank, C., Götz, H., Heibel, C., Jenkins, T., Jonas, U., Kibrom, A., Kügler, R., Naumann, C., Naumann, R., Reisinger, A., Rühe, J., Schiller, S., and Sinner, E.-K. (2009). Polymer-Tethered Bimolecular Lipid Membranes. In Meier, W. P. and Knoll, W., editors, *Polymer Membranes/Biomembranes*, pages 197–233. Springer Berlin Heidelberg, Berlin, Heidelberg.

[Kolin et al., 2006a] Kolin, D. L., Costantino, S., and Wiseman, P. W. (2006a). Sampling Effects, Noise, and Photobleaching in Temporal Image Correlation Spectroscopy. *Biophysical Journal*, 90(2):628–639.

[Kolin et al., 2006b] Kolin, D. L., Ronis, D., and Wiseman, P. W. (2006b). k-Space Image Correlation Spectroscopy: A Method for Accurate Transport Measurements Independent of Fluorophore Photophysics. *Biophysical Journal*, 91(8):3061–3075.

[Kooyman et al., 2008] Kooyman, R. P. H., Corn, R. M., Wark, A., Lee, H. J., Gedig, E., Engbers, G., Walstrom, L., de Mol, N. J., Hall, D. R., Yager, P., Chinowsky, T., Fu, E., Nelson, K., McWhirter, A., Fischer, M. J. E., Lokate, A. M. C., Beusink, J. B., Pruijn, G. J. M., Knoll, W., Kasry, A., Liu, J., Neumann, T., Niu, L., Park, H., Paulsen, H., Robelek, R., Yu, F., Schuck, P., Schasfoort, R. B. M., and Tudos, A. J. (2008). *Handbook of Surface Plasmon Resonance*. The Royal Society of Chemistry.

[Koppel et al., 1976] Koppel, D. E., Axelrod, D., Schlessinger, J., Elson, E. L., and Webb, W. W. (1976). Dynamics of fluorescence marker concentration as a probe of mobility. *Biophysical Journal*, 16(11):1315–1329.

[Kretschmer and Schwille, 2016] Kretschmer, S. and Schwille, P. (2016). Pattern formation on membranes and its role in bacterial cell division. *Current Opinion in Cell Biology*, 38(Supplement C):52–59.

[Krichevsky and Bonnet, 2002] Krichevsky, O. and Bonnet, G. (2002). Fluorescence correlation spectroscopy: the technique and its applications. *Reports on Progress in Physics*, 65(2):251.

[Krieger et al., 2015] Krieger, J. W., Singh, A. P., Bag, N., Garbe, C. S., Saunders, T. E., Langowski, J., and Wohland, T. (2015). Imaging fluorescence (cross-) correlation spectroscopy in live cells and organisms. *Nature Protocols*, 10:1948.

[Kukura et al., 2009] Kukura, P., Ewers, H., Müller, C., Renn, A., Helenius, A., and Sandoghdar, V. (2009). High-speed nanoscopic tracking of the position and orientation of a single virus. *Nature Methods*, 6:923.

[Kung et al., 2000] Kung, L. A., Kam, L., Hovis, J. S., and Boxer, S. G. (2000). Patterning Hybrid Surfaces of Proteins and Supported Lipid Bilayers. *Langmuir*, 16(17):6773–6776.

[Kyoung and Sheets, 2006] Kyoung, M. and Sheets, E. D. (2006). Manipulating and probing the spatio-temporal dynamics of nanoparticles near surfaces.

[Kyoung and Sheets, 2008] Kyoung, M. and Sheets, E. D. (2008). Vesicle Diffusion Close to a Membrane: Intermembrane Interactions Measured with Fluorescence Correlation Spectroscopy. *Biophysical Journal*, 95(12):5789–5797.

[LaBonte et al., 2003] LaBonte, J., Lebbos, J., and Kirkpatrick, P. (2003). Enfuvirtide. *Nature Reviews Drug Discovery*, 2:345.

[Lagerholm et al., 2000] Lagerholm, B. C., Starr, T. E., Volovyk, Z. N., and Thompson, N. L. (2000). Rebinding of IgE Fabs at Haptenated Planar Membranes: Measurement by Total Internal Reflection with Fluorescence Photobleaching Recovery. *Biochemistry*, 39(8):2042–2051.

[Lagerholm and Thompson, 1998] Lagerholm, B. C. and Thompson, N. L. (1998). Theory for Ligand Rebinding at Cell Membrane Surfaces. *Biophysical Journal*, 74(3):1215–1228.

[Lagerholm and Thompson, 2000] Lagerholm, B. C. and Thompson, N. L. (2000). Temporal Dependence of Ligand Dissociation and Rebinding at Planar Surfaces. *The Journal of Physical Chemistry B*, 104(4):863–868.

[Lagny and Bassereau, 2015] Lagny, T. J. and Bassereau, P. (2015). Bioinspired membrane-based systems for a physical approach of cell organization and dynamics: usefulness and limitations. *Interface Focus*, 5(4):20150038.

[Lakowicz, 2006] Lakowicz, J. R. (2006). *Principles of Fluorescence Spectroscopy*. Springer, Boston, MA, 3rd edition.

[Lalezari et al., 2003] Lalezari, J. P., Henry, K., O'Hearn, M., Montaner, J. S. G., Piliero, P. J., Trottier, B., Walmsley, S., Cohen, C., Kuritzkes, D. R., Eron, J. J., Chung, J., DeMasi, R., Donatacci, L., Drobnes, C., Delehanty, J., and Salgo, M. (2003). Enfuvirtide, an HIV-1 Fusion Inhibitor, for Drug-Resistant HIV Infection in North and South America. *New England Journal of Medicine*, 348(22):2175–2185.

[Landau and Lifshitz, 1980] Landau, L. D. and Lifshitz, E. M. (1980). Statistical physics, part 1: Volume 5 (course of theoretical physics, volume 5). *Publisher: Butterworth-Heinemann*, 3.

[Lang and Schwarz, 2007] Lang, B. E. and Schwarz, F. P. (2007). Thermodynamic dependence of DNA/DNA and DNA/RNA hybridization reactions on temperature and ionic strength. *Biophysical Chemistry*, 131(1):96–104.

[Langecker et al., 2014] Langecker, M., Arnaut, V., List, J., and Simmel, F. C. (2014). DNA Nanostructures Interacting with Lipid Bilayer Membranes. *Accounts of Chemical Research*, 47(6):1807–1815.

[Larson et al., 2005] Larson, D. R., Gosse, J. A., Holowka, D. A., Baird, B. A., and Webb, W. W. (2005). Temporally resolved interactions between antigen-stimulated IgE receptors and Lyn kinase on living cells. *The Journal of Cell Biology*, 171(3):527 LP – 536.

[Laurence and Weiss, 2003] Laurence, T. A. and Weiss, S. (2003). How to Detect Weak Pairs. *Science*, 299(5607):667 LP – 668.

[Lausted et al., 2009] Lausted, C., Hu, Z., Hood, L., and Campbell, C. T. (2009). SPR imaging for high throughput, label-free interaction analysis. *Combinatorial chemistry & high throughput screening*, 12(8):741–751.

[Lee et al., 2005] Lee, M. C. S., Orci, L., Hamamoto, S., Futai, E., Ravazzola, M., and Schekman, R. (2005). Sar1p N-Terminal Helix Initiates Membrane Curvature and Completes the Fission of a COPII Vesicle. *Cell*, 122(4):605–617.

[Leitz et al., 2006] Leitz, A. J., Bayburt, T. H., Barnakov, A. N., Springer, B. A., and Sligar, S. G. (2006). Functional reconstitution of β2-adrenergic receptors utilizing self-assembling Nanodisc technology. *BioTechniques*, 40(5):601–612.

[Lemmon, 2008] Lemmon, M. A. (2008). Membrane recognition by phospholipid-binding domains. *Nature Reviews Molecular Cell Biology*, 9(2):99–111.

[Leutenegger et al., 2006] Leutenegger, M., Blom, H., Widengren, J., Eggeling, C., Gösch, M., Leitgeb, R. A., and Lasser, T. (2006). Dual-color total internal reflection fluorescence cross-correlation spectroscopy. *Journal of Biomedical Optics*, 11(4):40502–40503.

[Leutenegger et al., 2012] Leutenegger, M., Ringemann, C., Lasser, T., Hell, S. W., and Eggeling, C. (2012). Fluorescence correlation spectroscopy with a total internal reflection fluorescence STED microscope (TIRF-STED-FCS). *Opt. Express*, 20(5):5243–5263.

[Li and Yang, 2018] Li, H. and Yang, H. (2018). A versatile optical microscope for time-dependent single-molecule and single-particle spectroscopy. *The Journal of Chemical Physics*, 148(12):123316.

[Li et al., 2007] Li, Y., Augustine, G. J., and Weninger, K. (2007). Kinetics of Complexin Binding to the SNARE Complex: Correcting Single Molecule FRET Measurements for Hidden Events. *Biophysical Journal*, 93(6):2178–2187.

[Lieto et al., 2003] Lieto, A. M., Cush, R. C., and Thompson, N. L. (2003). Ligand-Receptor Kinetics Measured by Total Internal Reflection with Fluorescence Correlation Spectroscopy. *Biophysical Journal*, 85(5):3294–3302.

[Lieto and Thompson, 2004] Lieto, A. M. and Thompson, N. L. (2004). Total Internal Reflection with Fluorescence Correlation Spectroscopy: Nonfluorescent Competitors. *Biophysical Journal*, 87(2):1268–1278.

[Lim et al., 2013] Lim, K. H., Huang, H., Pralle, A., and Park, S. (2013). Stable, high-affinity streptavidin monomer for protein labeling and monovalent biotin detection. *Biotechnology and Bioengineering*, 110(1):57–67.

[Lin et al., 2010] Lin, W.-C., Yu, C.-H., Triffo, S., and Groves, J. T. (2010). Supported Membrane Formation, Characterization, Functionalization, and Patterning for Application in Biological Science and Technology. *Current Protocols in Chemical Biology*, 2(4):235–269.

[Linder and Deschenes, 2007] Linder, M. E. and Deschenes, R. J. (2007). Palmitoylation: policing protein stability and traffic. *Nature Reviews Molecular Cell Biology*, 8:74.

[Lingwood and Simons, 2010] Lingwood, D. and Simons, K. (2010). Lipid Rafts As a Membrane-Organizing Principle. *Science*, 327(5961):46 LP – 50.

[Liou and Storz, 2010] Liou, G.-Y. and Storz, P. (2010). Reactive oxygen species in cancer. *Free Radical Research*, 44(5):479–496.

[Liu and Fletcher, 2009] Liu, A. P. and Fletcher, D. A. (2009). Biology under construction: in vitro reconstitution of cellular function. *Nature Reviews Molecular Cell Biology*, 10:644.

[Liu et al., 2009] Liu, R., Garcia-Manyes, S., Sarkar, A., Badilla, C. L., and Fernández, J. M. (2009). Mechanical Characterization of Protein L in the Low-Force Regime by Electromagnetic Tweezers/Evanescent Nanometry. *Biophysical Journal*, 96(9):3810–3821.

[Liu et al., 2014] Liu, W., Tan, J., Mehryar, M. M., Teng, Z., and Zeng, Y. (2014). Peptide HIV fusion inhibitors: modifications and conjugations. *MedChemComm*, 5(10):1472–1482.

[Liu et al., 2015] Liu, Z., Lavis, L. D., and Betzig, E. (2015). Imaging Live-Cell Dynamics and Structure at the Single-Molecule Level. *Molecular Cell*, 58(4):644–659.

[Lomakina et al., 2014] Lomakina, E. B., Marsh, G., and Waugh, R. E. (2014). Cell Surface Topography Is a Regulator of Molecular Interactions during Chemokine-Induced Neutrophil Spreading. *Biophysical Journal*, 107(6):1302–1312.

[Loose et al., 2008] Loose, M., Fischer-Friedrich, E., Ries, J., Kruse, K., and Schwille, P. (2008). Spatial Regulators for Bacterial Cell Division Self-Organize into Surface Waves in Vitro. *Science*, 320(5877):789–792.

[Loose et al., 2011] Loose, M., Kruse, K., and Schwille, P. (2011). Protein Self-Organization: Lessons from the Min System. *Annual Review of Biophysics*, 40(1):315–336.

[Loose and Mitchison, 2013] Loose, M. and Mitchison, T. J. (2013). The bacterial cell division proteins FtsA and FtsZ self-organize into dynamic cytoskeletal patterns. *Nature Cell Biology*, 16:38.

[Loura et al., 2003] Loura, L. M. S., de Almeida, R. F. M., Coutinho, A., and Prieto, M. (2003). Interaction of peptides with binary phospholipid membranes: application of fluorescence methodologies. *Chemistry and Physics of Lipids*, 122(1):77–96.

[Lukosz, 1979] Lukosz, W. (1979). Light emission by magnetic and electric dipoles close to a plane dielectric interface. III. Radiation patterns of dipoles with arbitrary orientation. *Journal of the Optical Society of America*, 69(11):1495–1503.

[Ly et al., 2014] Ly, S., Bourguet, F., Fischer, N. O., Lau, E. Y., Coleman, M. A., and Laurence, T. A. (2014). Quantifying Interactions of a Membrane Protein Embedded in a Lipid Nanodisc using Fluorescence Correlation Spectroscopy. *Biophysical Journal*, 106(2):L05–L08.

[Macháň et al., 2016] Macháň, R., Foo, Y. H., and Wohland, T. (2016). On the Equivalence of FCS and FRAP: Simultaneous Lipid Membrane Measurements. *Biophysical Journal*, 111(1):152–161.

[Machán and Hof, 2010] Machán, R. and Hof, M. (2010). Lipid diffusion in planar membranes investigated by fluorescence correlation spectroscopy. *Biochimica et Biophysica Acta (BBA) - Biomembranes*, 1798(7):1377–1391.

[Machán and Wohland, 2014] Machán, R. and Wohland, T. (2014). Recent applications of fluorescence correlation spectroscopy in live systems. *FEBS Letters*, 588(19):3571–3584.

[Macrini, 2015] Macrini, C. (2015). *Bottom-up investigation of minimal membrane modules*. PhD thesis, University of Groningen and Max Planck Institute of Biochemistry.

[Magde et al., 1972] Magde, D., Elson, E., and Webb, W. W. (1972). Thermodynamic Fluctuations in a Reacting System—Measurement by Fluorescence Correlation Spectroscopy. *Physical Review Letters*, 29(11):705–708.

[Magde et al., 1974] Magde, D., Elson, E. L., and Webb, W. W. (1974). Fluorescence correlation spectroscopy. II. An experimental realization. *Biopolymers*, 13(1):29–61.

[Magde et al., 1978] Magde, D., Webb, W. W., and Elson, E. L. (1978). Fluorescence correlation spectroscopy. III. Uniform translation and laminar flow. *Biopolymers*, 17(2):361–376.

[Malins et al., 2018] Malins, D. C., Gunselman, S. J., Holmes, E. H., and Polissar, N. L. (2018). The etiology of breast cancer characteristic alterations in hydroxyl radical-induced dna base lesions during oncogenesis with potential for evaluating incidence risk. *Cancer*, 71(10):3036–3043.

[Manzo and Garcia-Parajo, 2015] Manzo, C. and Garcia-Parajo, M. F. (2015). A review of progress in single particle tracking: from methods to biophysical insights. *Reports on Progress in Physics*, 78(12):124601.

[Marnett, 2000] Marnett, L. J. (2000). Oxyradicals and DNA damage. *Carcinogenesis*, 21(3):361–370.

[Mashanov and Molloy, 2007] Mashanov, G. I. and Molloy, J. E. (2007). Automatic Detection of Single Fluorophores in Live Cells. *Biophysical Journal*, 92(6):2199–2211.

[Mashanov et al., 2004] Mashanov, G. I., Tacon, D., Peckham, M., and Molloy, J. E. (2004). The Spatial and Temporal Dynamics of Pleckstrin Homology Domain Binding at the Plasma Membrane Measured by Imaging Single Molecules in Live Mouse Myoblasts. *Journal of Biological Chemistry*, 279(15):15274–15280.

[Matos et al., 2010] Matos, P. M., Franquelim, H. G., Castanho, M. A. R. B., and Santos, N. C. (2010). Quantitative assessment of peptide-lipid interactions.: Ubiquitous fluorescence methodologies. *Biochimica et Biophysica Acta (BBA) - Biomembranes*, 1798(11):1999–2012.

[Matsumoto and Nishimura, 1998] Matsumoto, M. and Nishimura, T. (1998). Mersenne Twister: A 623-dimensionally Equidistributed Uniform Pseudo-random Number Generator. *ACM Trans. Model. Comput. Simul.*, 8(1):3–30.

[Matsuoka et al., 2006] Matsuoka, S., Iijima, M., Watanabe, T. M., Kuwayama, H., Yanagida, T., Devreotes, P. N., and Ueda, M. (2006). Single-molecule analysis of chemoattractant-stimulated membrane recruitment of a PH-domain-containing protein. *Journal of Cell Science*, 119(6):1071 LP – 1079.

[Matter et al., 2018] Matter, B., Seiler, C. L., Murphy, K., Ming, X., Zhao, J., Lindgren, B., Jones, R., and Tretyakova, N. (2018). Mapping three guanine oxidation products along DNA following exposure to three types of reactive oxygen species. *Free Radical Biology and Medicine*, 121:180–189.

[Mattheyses and Axelrod, 2006] Mattheyses, A. L. and Axelrod, D. (2006). Direct measurement of the evanescent field profile produced by objective-based total internal reflection fluorescence. *Journal of Biomedical Optics*, 11(1):14006–14007.

[McCain et al., 2004a] McCain, K. S., Schluesche, P., and Harris, J. M. (2004a). Modifying the Adsorption Behavior of Polyamidoamine Dendrimers at Silica Surfaces Investigated by Total Internal Reflection Fluorescence Correlation Spectroscopy. *Analytical Chemistry*, 76(4):930–938.

[McCain et al., 2004b] McCain, K. S., Schluesche, P., and Harris, J. M. (2004b). Poly(amidoamine) Dendrimers as Nanoscale Diffusion Probes in Sol-Gel Films Investigated by Total Internal Reflection Fluorescence Spectroscopy. *Analytical Chemistry*, 76(4):939–946.

[McElhaney, 1982] McElhaney, R. N. (1982). The use of differential scanning calorimetry and differential thermal analysis in studies of model and biological membranes. *Chemistry and Physics of Lipids*, 30(2):229–259.

[McMahon and Boucrot, 2015] McMahon, H. T. and Boucrot, E. (2015). Membrane curvature at a glance. *Journal of Cell Science*, 128(6):1065 LP – 1070.

[McMahon and Gallop, 2005] McMahon, H. T. and Gallop, J. L. (2005). Membrane curvature and mechanisms of dynamic cell membrane remodelling. *Nature*, 438(7068):590–596.

[Meier and Nauck, 2005] Meier, J. J. and Nauck, M. A. (2005). Glucagon-like peptide 1(GLP-1) in biology and pathology. *Diabetes/Metabolism Research and Reviews*, 21(2):91–117.

[Melo et al., 2011] Melo, A. M., Prieto, M., and Coutinho, A. (2011). The effect of variable liposome brightness on quantifying lipid-protein interactions using fluorescence correlation spectroscopy. *Biochimica et Biophysica Acta (BBA) - Biomembranes*, 1808(10):2559–2568.

[Melo et al., 2014] Melo, A. M., Prieto, M., and Coutinho, A. (2014). Quantifying Lipid-Protein Interaction by Fluorescence Correlation Spectroscopy (FCS). In Engelborghs, Y. and Visser, A. J. W. G., editors, *Fluorescence Spectroscopy and Microscopy: Methods and Protocols*, pages 575–595. Humana Press, Totowa, NJ.

[Melo et al., 2009] Melo, M. N., Ferre, R., and Castanho, M. A. R. B. (2009). Antimicrobial peptides: linking partition, activity and high membrane-bound concentrations. *Nature Reviews Microbiology*, 7:245.

[Merkel et al., 1989] Merkel, R., Sackmann, E., and Evans, E. (1989). Molecular friction and epitactic coupling between monolayers in supported bilayers. *J. Phys. France*, 50(12):1535–1555.

[Merrifield et al., 2002] Merrifield, C. J., Feldman, M. E., Wan, L., and Almers, W. (2002). Imaging actin and dynamin recruitment during invagination of single clathrin-coated pits. *Nature Cell Biology*, 4:691.

[Meseth et al., 1999] Meseth, U., Wohland, T., Rigler, R., and Vogel, H. (1999). Resolution of Fluorescence Correlation Measurements. *Biophysical Journal*, 76(3):1619–1631.

[Metzler et al., 2016] Metzler, R., Jeon, J.-H., and Cherstvy, A. G. (2016). Non-Brownian diffusion in lipid membranes: Experiments and simulations. *Biochimica et Biophysica Acta (BBA) - Biomembranes*, 1858(10):2451–2467.

[Michalet et al., 2007] Michalet, X., Siegmund, O. H. W., Vallerga, J. V., Jelinsky, P., Millaud, J. E., and Weiss, S. (2007). Detectors for single-molecule fluorescence imaging and spectroscopy. *Journal of Modern Optics*, 54(2-3):239–281.

[Michelman-Ribeiro et al., 2009] Michelman-Ribeiro, A., Mazza, D., Rosales, T., Stasevich, T. J., Boukari, H., Rishi, V., Vinson, C., Knutson, J. R., and McNally, J. G. (2009). Direct Measurement of Association and Dissociation Rates of DNA Binding in Live Cells by Fluorescence Correlation Spectroscopy. *Biophysical Journal*, 97(1):337–346.

[Midorikawa and Sakaba, 2015] Midorikawa, M. and Sakaba, T. (2015). Imaging Exocytosis of Single Synaptic Vesicles at a Fast CNS Presynaptic Terminal. *Neuron*, 88(3):492–498.

[Miles and Wallace, 2016] Miles, A. J. and Wallace, B. A. (2016). Circular dichroism spectroscopy of membrane proteins. *Chemical Society Reviews*, 45(18):4859–4872.

[Minton, 2001] Minton, A. P. (2001). The Influence of Macromolecular Crowding and Macromolecular Confinement on Biochemical Reactions in Physiological Media. *Journal of Biological Chemistry*, 276(14):10577–10580.

[Mitsuhashi, 1996] Mitsuhashi, M. (1996). Technical report: Part 1. Basic requirements for designing optimal oligonucleotide probe sequences. *Journal of Clinical Laboratory Analysis*, 10(5):277–284.

[Miyagi et al., 2017] Miyagi, A., Ramm, B., Schwille, P., and Scheuring, S. (2017). High-speed AFM reveals the inner workings of the MinDE protein oscillator. *Nano Letters*.

[Moerner, 2007] Moerner, W. E. (2007). New directions in single-molecule imaging and analysis. *Proceedings of the National Academy of Sciences*, 104(31):12596 LP – 12602.

[Moerner and Fromm, 2003] Moerner, W. E. and Fromm, D. P. (2003). Methods of single-molecule fluorescence spectroscopy and microscopy. *Review of Scientific Instruments*, 74(8):3597–3619.

[Montero et al., 2008] Montero, M., van Houten, N. E., Wang, X., and Scott, J. K. (2008). The Membrane-Proximal External Region of the Human Immunodeficiency Virus Type 1 Envelope: Dominant Site of Antibody Neutralization and Target for Vaccine Design. *Microbiology and Molecular Biology Reviews*, 72(1):54 LP – 84.

[Moraes et al., 2014] Moraes, I., Evans, G., Sanchez-Weatherby, J., Newstead, S., and Stewart, P. D. S. (2014). Membrane protein structure determination — The next generation. *Biochimica et Biophysica Acta (BBA) - Biomembranes*, 1838(1, Part A):78–87.

[Morrissey et al., 2008] Morrissey, J. H., Pureza, V., Davis-Harrison, R. L., Sligar, S. G., Ohkubo, Y. Z., and Tajkhorshid, E. (2008). Blood clotting reactions on nanoscale phospholipid bilayers. *Thrombosis Research*, 122:S23–S26.

[Mücksch, 2018] Mücksch, J. (2018). *Quantification of biomolecular binding dynamics by Fluorescence Correlation Spectroscopy*. PhD thesis, Ludwig-Maximilians-Universität München.

[Mücksch et al., 2018] Mücksch, J., Blumhardt, P., Strauss, M. T., Petrov, E. P., Jungmann, R., and Schwille, P. (2018). Quantifying Reversible Surface Binding via Surface-Integrated Fluorescence Correlation Spectroscopy. *Nano Letters*, 18(5):3185–3192.

[Müller et al., 1993] Müller, B., Zerwes, H. G., Tangemann, K., Peter, J., and Engel, J. (1993). Two-step binding mechanism of fibrinogen to alpha IIb beta 3 integrin reconstituted into planar lipid bilayers. *Journal of Biological Chemistry*, 268(9):6800–6808.

[Murray et al., 1997] Murray, D., Ben-Tal, N., Honig, B., and McLaughlin, S. (1997). Electrostatic interaction of myristoylated proteins with membranes: simple physics, complicated biology. *Structure*, 5(8):985–989.

[Myers et al., 2012] Myers, G. A., Gacek, D. A., Peterson, E. M., Fox, C. B., and Harris, J. M. (2012). Microscopic Rates of Peptide–Phospholipid Bilayer Interactions from Single-Molecule Residence Times. *Journal of the American Chemical Society*, 134(48):19652–19660.

[Nair et al., 2011] Nair, P. M., Salaita, K., Petit, R. S., and Groves, J. T. (2011). Using patterned supported lipid membranes to investigate the role of receptor organization in intercellular signaling. *Nature Protocols*, 6:523.

[Nath et al., 2007] Nath, A., Atkins, W. M., and Sligar, S. G. (2007). Applications of Phospholipid Bilayer Nanodiscs in the Study of Membranes and Membrane Proteins. *Biochemistry*, 46(8):2059–2069.

[Nath et al., 2008] Nath, A., Koo, P. K., Rhoades, E., and Atkins, W. M. (2008). Allosteric Effects on Substrate Dissociation from Cytochrome P450 3A4 in Nanodiscs Observed by Ensemble and Single-Molecule Fluorescence Spectroscopy. *Journal of the American Chemical Society*, 130(47):15746–15747.

[Nath et al., 2010] Nath, A., Trexler, A. J., Koo, P., Miranker, A. D., Atkins, W. M., and Rhoades, E. (2010). Chapter 6 - Single-Molecule Fluorescence Spectroscopy Using Phospholipid Bilayer Nanodiscs. In Walter, N. G. B. T. M. i. E., editor, *Single Molecule Tools: Fluorescence Based Approaches, Part A*, volume 472, pages 89–117. Academic Press.

[Nečas and Petr, 2012] Nečas, D. and Petr, K. (2012). Gwyddion: an open-source software for SPM data analysis.

[Neeley and Essigmann, 2006] Neeley, W. L. and Essigmann, J. M. (2006). Mechanisms of Formation, Genotoxicity, and Mutation of Guanine Oxidation Products. *Chemical Research in Toxicology*, 19(4):491–505.

[Nelson et al., 2007] Nelson, J. D., Brunel, F. M., Jensen, R., Crooks, E. T., Cardoso, R. M. F., Wang, M., Hessell, A., Wilson, I. A., Binley, J. M., Dawson, P. E., Burton, D. R., and Zwick, M. B. (2007). An Affinity-Enhanced Neutralizing Antibody against the

Membrane-Proximal External Region of Human Immunodeficiency Virus Type 1 gp41 Recognizes an Epitope between Those of 2F5 and 4E10. *Journal of Virology*, 81(8):4033 LP – 4043.

[Neumüller et al., 2010] Neumüller, K. G., Elsayad, K., Reisecker, J. M., Waxham, M. N., and Heinze, K. G. (2010). Photounbinding of Calmodulin from a Family of CaM Binding Peptides. *PLOS ONE*, 5(11):e14050.

[Nguyen et al., 2015] Nguyen, H. H., Park, J., Kang, S., and Kim, M. (2015). Surface Plasmon Resonance: A Versatile Technique for Biosensor Applications.

[Nguyen et al., 2012] Nguyen, T. T., Swift, J. L., and Cramb, D. T. (2012). Fluorescence Correlation Spectroscopy: The Measurement of Molecular Binding. In Geddes, C. D., editor, *Reviews in Fluorescence 2010*, pages 45–66. Springer New York, New York, NY.

[Nie et al., 1994] Nie, S., Chiu, D. T., and Zare, R. N. (1994). Probing individual molecules with confocal fluorescence microscopy. *Science*, 266(5187):1018 LP – 1021.

[Niederauer, 2018] Niederauer, C. (2018). *Direct Characterization of the Evanescent Field in Objective-Type Total Internal Reflection Microscopy*. Master's thesis, Ludwig-Maximilians-Universität München.

[Niederauer et al., 2018] Niederauer, C., Blumhardt, P., Mücksch, J., Heymann, M., Lambacher, A., and Schwille, P. (2018). Direct characterization of the evanescent field in objective-type total internal reflection fluorescence microscopy. *Optics Express*, 26(16):20492–20506.

[Nielsen et al., 2004] Nielsen, L. L., Young, A. A., and Parkes, D. G. (2004). Pharmacology of exenatide (synthetic exendin-4): a potential therapeutic for improved glycemic control of type 2 diabetes. *Regulatory Peptides*, 117(2):77–88.

[Nielsen and Otzen, 2013] Nielsen, S. B. and Otzen, D. E. (2013). Quartz Crystal Microbalances as Tools for Probing Protein–Membrane Interactions. In Kleinschmidt, J. H., editor, *Lipid-Protein Interactions: Methods and Protocols*, pages 1–21. Humana Press, Totowa, NJ.

[Ogilby, 2010] Ogilby, P. R. (2010). Singlet oxygen: there is indeed something new under the sun. *Chemical Society Reviews*, 39(8):3181.

[Oheim et al., 1998] Oheim, M., Loerke, D., Stühmer, W., and Chow, R. H. (1998). The last few milliseconds in the life of a secretory granule. *European Biophysics Journal*, 27(2):83–98.

[Ohsugi and Kinjo, 2009] Ohsugi, Y. and Kinjo, M. (2009). Multipoint fluorescence correlation spectroscopy with total internal reflection fluorescence microscope. *Journal of Biomedical Optics*, 14(1):14030–14034.

[Ohsugi et al., 2006] Ohsugi, Y., Saito, K., Tamura, M., and Kinjo, M. (2006). Lateral Mobility of Membrane-Binding Proteins in Living Cells Measured by Total Internal Reflection Fluorescence Correlation Spectroscopy. *Biophysical Journal*, 91(9):3456–3464.

[Oliphant, 2006] Oliphant, T. E. (2006). *A guide to NumPy*, volume 1. Trelgol Publishing USA.

[Oliver and Parikh, 2010] Oliver, A. E. and Parikh, A. N. (2010). Templating membrane assembly, structure, and dynamics using engineered interfaces. *Biochimica et Biophysica Acta (BBA) - Biomembranes*, 1798(4):839–850.

[Olveczky et al., 1997] Olveczky, B. P., Periasamy, N., and Verkman, A. S. (1997). Mapping fluorophore distributions in three dimensions by quantitative multiple angle-total internal reflection fluorescence microscopy. *Biophysical Journal*, 73(5):2836–2847.

[Oreopoulos and Yip, 2008] Oreopoulos, J. and Yip, C. M. (2008). Combined scanning probe and total internal reflection fluorescence microscopy. *Methods*, 46(1):2–10.

[Orth et al., 2003] Orth, R. N., Kameoka, J., Zipfel, W. R., Ilic, B., Webb, W. W., Clark, T. G., and Craighead, H. G. (2003). Creating Biological Membranes on the Micron Scale: Forming Patterned Lipid Bilayers Using a Polymer Lift-Off Technique. *Biophysical Journal*, 85(5):3066–3073.

[Otosu and Yamaguchi, 2018] Otosu, T. and Yamaguchi, S. (2018). Total Internal Reflection Two-Dimensional Fluorescence Lifetime Correlation Spectroscopy. *The Journal of Physical Chemistry B*, 122(22):5758–5764.

[Owczarzy et al., 2008] Owczarzy, R., Moreira, B. G., You, Y., Behlke, M. A., and Walder, J. A. (2008). Predicting Stability of DNA Duplexes in Solutions Containing Magnesium and Monovalent Cations. *Biochemistry*, 47(19):5336–5353.

[Paige et al., 2001] Paige, M. F., Bjerneld, E. J., and Moerner, W. E. (2001). A Comparison of Through-the-Objective Total Internal Reflection Microscopy and Epifluorescence Microscopy for Single-Molecule Fluorescence Imaging. *Single Molecules*, 2(3):191–201.

[Papadakis et al., 2014] Papadakis, C. M., Košovan, P., Richtering, W., and Wöll, D. (2014). Polymers in focus: fluorescence correlation spectroscopy. *Colloid and Polymer Science*, 292(10):2399–2411.

[Paszek et al., 2012] Paszek, M. J., DuFort, C. C., Rubashkin, M. G., Davidson, M. W., Thorn, K. S., Liphardt, J. T., and Weaver, V. M. (2012). Scanning angle interference microscopy reveals cell dynamics at the nanoscale. *Nature Methods*, 9:825.

[Patil and Ballou, 2000] Patil, P. V. and Ballou, D. P. (2000). The Use of Protocatechuate Dioxygenase for Maintaining Anaerobic Conditions in Biochemical Experiments. *Analytical Biochemistry*, 286(2):187–192.

[Pavani et al., 2009] Pavani, S. R. P., Thompson, M. A., Biteen, J. S., Lord, S. J., Liu, N., Twieg, R. J., Piestun, R., and Moerner, W. E. (2009). Three-dimensional, single-molecule fluorescence imaging beyond the diffraction limit by using a double-helix point spread function. *Proceedings of the National Academy of Sciences*, 106(9):2995 LP – 2999.

[Pawley, 2006] Pawley, J. B. (2006). *Handbook Of Biological Confocal Microscopy*. Springer, Boston, MA.

[Paz-Elizur et al., 2003] Paz-Elizur, T., Krupsky, M., Blumenstein, S., Elinger, D., Schechtman, E., and Livneh, Z. (2003). DNA Repair Activity for Oxidative Damage and Risk of Lung Cancer. *JNCI: Journal of the National Cancer Institute*, 95(17):1312–1319.

[Peisajovich et al., 2003] Peisajovich, S. G., Gallo, S. A., Blumenthal, R., and Shai, Y. (2003). C-terminal Octylation Rescues an Inactive T20 Mutant: IMPLICATIONS FOR THE MECHANISM OF HIV/SIMIAN IMMUNODEFICIENCY VIRUS-INDUCED MEMBRANE FUSION. *Journal of Biological Chemistry*, 278(23):21012–21017.

[Peng et al., 2018] Peng, S., Wang, W., and Chen, C. (2018). Surface Transient Binding-Based Fluorescence Correlation Spectroscopy (STB-FCS), a Simple and Easy-to-Implement Method to Extend the Upper Limit of the Time Window to Seconds. *The Journal of Physical Chemistry B*.

[Perez et al., 2006] Perez, J.-B., Martinez, K. L., Segura, J.-M., and Vogel, H. (2006). Supported Cell-Membrane Sheets for Functional Fluorescence Imaging of Membrane Proteins. *Advanced Functional Materials*, 16(2):306–312.

[Pero et al., 2006] Pero, J. K., Haas, E. M., and Thompson, N. L. (2006). Size Dependence of Protein Diffusion Very Close to Membrane Surfaces: Measurement by Total Internal Reflection with Fluorescence Correlation Spectroscopy. *The Journal of Physical Chemistry B*, 110(22):10910–10918.

[Pertsinidis et al., 2010] Pertsinidis, A., Zhang, Y., and Chu, S. (2010). Subnanometre single-molecule localization, registration and distance measurements. *Nature*.

[Petersen et al., 1993] Petersen, N. O., Höddelius, P. L., Wiseman, P. W., Seger, O., and Magnusson, K. E. (1993). Quantitation of membrane receptor distributions by image correlation spectroscopy: concept and application. *Biophysical Journal*, 65(3):1135–1146.

[Peterson et al., 2016] Peterson, E. M., Manhart, M. W., and Harris, J. M. (2016). Single-Molecule Fluorescence Imaging of Interfacial DNA Hybridization Kinetics at Selective Capture Surfaces. *Analytical Chemistry*, 88(2):1345–1354.

[Petrášek et al., 2011] Petrášek, Z., Derenko, S., and Schwille, P. (2011). Circular scanning fluorescence correlation spectroscopy on membranes. *Optics Express*, 19(25):25006–25021.

[Petrášek and Schwille, 2008] Petrášek, Z. and Schwille, P. (2008). Precise Measurement of Diffusion Coefficients using Scanning Fluorescence Correlation Spectroscopy. *Biophysical Journal*, 94(4):1437–1448.

[Petrášek and Schwille, 2009] Petrášek, Z. and Schwille, P. (2009). Fluctuations as a source of information in fluorescence microscopy. *Journal of The Royal Society Interface*, 6:S15–S25.

[Petrov and Schwille, 2008] Petrov, E. P. and Schwille, P. (2008). State of the Art and Novel Trends in Fluorescence Correlation Spectroscopy. In *Standardization and Quality Assurance in Fluorescence Measurements II*, pages 145–197. Springer Berlin Heidelberg, Berlin, Heidelberg.

[Pfeiffer and Höök, 2004] Pfeiffer, I. and Höök, F. (2004). Bivalent Cholesterol-Based Coupling of Oligonucletides to Lipid Membrane Assemblies. *Journal of the American Chemical Society*, 126(33):10224–10225.

[Pichoff and Lutkenhaus, 2005] Pichoff, S. and Lutkenhaus, J. (2005). Tethering the Z ring to the membrane through a conserved membrane targeting sequence in FtsA. *Molecular Microbiology*, 55(6):1722–1734.

[Pierce et al., 2002] Pierce, K. L., Premont, R. T., and Lefkowitz, R. J. (2002). Seven-transmembrane receptors. *Nature Reviews Molecular Cell Biology*, 3:639.

[Piliarik and Sandoghdar, 2014] Piliarik, M. and Sandoghdar, V. (2014). Direct optical sensing of single unlabelled proteins and super-resolution imaging of their binding sites. *Nature Communications*, 5:4495.

[Pisarchick and Thompson, 1990] Pisarchick, M. L. and Thompson, N. L. (1990). Binding of a monoclonal antibody and its Fab fragment to supported phospholipid monolayers measured by total internal reflection fluorescence microscopy. *Biophysical Journal*, 58(5):1235–1249.

[Posokhov et al., 2008] Posokhov, Y. O., Rodnin, M. V., Lu, L., and Ladokhin, A. S. (2008). Membrane Insertion Pathway of Annexin B12: Thermodynamic and Kinetic Characterization by Fluorescence Correlation Spectroscopy and Fluorescence Quenching. *Biochemistry*, 47(18):5078–5087.

[Poteser et al., 2016] Poteser, M., Leitinger, G., Pritz, E., Platzer, D., Frischauf, I., Romanin, C., and Groschner, K. (2016). Live-cell imaging of ER-PM contact architecture by a novel TIRFM approach reveals extension of junctions in response to store-operated Ca2+-entry. *Scientific Reports*, 6:35656.

[Pramanik, 2004] Pramanik, A. (2004). Ligand-receptor interactions in live cells by fluorescence correlation spectroscopy. *Current pharmaceutical biotechnology*, 5(2):205–212.

[Prat et al., 1998] Prat, F., Houk, K. N., and Foote, C. S. (1998). Effect of Guanine Stacking on the Oxidation of 8-Oxoguanine in B-DNA. *Journal of the American Chemical Society*, 120(4):845–846.

[Przybylo et al., 2006] Przybylo, M., Sýkora, J., Humpolíčková, J., Benda, A., Zan, A., and Hof, M. (2006). Lipid Diffusion in Giant Unilamellar Vesicles Is More than 2 Times

Faster than in Supported Phospholipid Bilayers under Identical Conditions. *Langmuir*, 22(22):9096–9099.

[Ramachandran et al., 2013] Ramachandran, S., Cohen, D. A., Quist, A. P., and Lal, R. (2013). High performance, LED powered, waveguide based total internal reflection microscopy. *Scientific Reports*, 3:2133.

[Ramirez-Diaz et al., 2018] Ramirez-Diaz, D. A., García-Soriano, D. A., Raso, A., Mücksch, J., Feingold, M., Rivas, G., and Schwille, P. (2018). Treadmilling analysis reveals new insights into dynamic FtsZ ring architecture. *PLOS Biology*, 16(5):e2004845.

[Ramm et al., 2018a] Ramm, B., Glock, P., Mücksch, J., Blumhardt, P., García-Soriano, D. A., Heymann, M., and Schwille, P. (2018a). The MinDE system is a generic spatial cue for membrane protein distribution in vitro. *Nature Communications*, 9(1):3942.

[Ramm et al., 2018b] Ramm, B., Glock, P., and Schwille, P. (2018b). In Vitro Reconstitution of Self-Organizing Protein Patterns on Supported Lipid Bilayers. *JoVE*, (137):e58139.

[Rasnik et al., 2006] Rasnik, I., McKinney, S. A., and Ha, T. (2006). Nonblinking and long-lasting single-molecule fluorescence imaging. *Nature Methods*, 3:891.

[Rauer et al., 1996] Rauer, B., Neumann, E., Widengren, J., and Rigler, R. (1996). Fluorescence correlation spectrometry of the interaction kinetics of tetramethylrhodamin α-bungarotoxin with Torpedo californica acetylcholine receptor. *Biophysical Chemistry*, 58(1):3–12.

[Raulin, 2002] Raulin, J. (2002). Human immunodeficiency virus and host cell lipids. Interesting pathways in research for a new HIV therapy. *Progress in Lipid Research*, 41(1):27–65.

[Redmond and Kochevar, 2007] Redmond, R. W. and Kochevar, I. E. (2007). Symposium-in-Print: Singlet Oxygen Invited Review. *Photochemistry and Photobiology*, 82(5):1178–1186.

[Renner et al., 2008] Renner, L., Osaki, T., Chiantia, S., Schwille, P., Pompe, T., and Werner, C. (2008). Supported Lipid Bilayers on Spacious and pH-Responsive Polymer Cushions with Varied Hydrophilicity. *The Journal of Physical Chemistry B*, 112(20):6373–6378.

[Resh, 2006] Resh, M. D. (2006). Trafficking and signaling by fatty-acylated and prenylated proteins. *Nature Chemical Biology*, 2(11):584–590.

[Rička and Binkert, 1989] Rička, J. and Binkert, T. (1989). Direct measurement of a distinct correlation function by fluorescence cross correlation. *Physical Review A*, 39(5):2646–2652.

[Ries et al., 2009a] Ries, J., Chiantia, S., and Schwille, P. (2009a). Accurate Determination of Membrane Dynamics with Line-Scan FCS. *Biophysical Journal*, 96(5):1999–2008.

[Ries et al., 2008a] Ries, J., Petrov, E. P., and Schwille, P. (2008a). Total Internal Reflection Fluorescence Correlation Spectroscopy: Effects of Lateral Diffusion and Surface-Generated Fluorescence. *Biophysical Journal*, 95:390–399.

[Ries et al., 2008b] Ries, J., Ruckstuhl, T., Verdes, D., and Schwille, P. (2008b). Supercritical Angle Fluorescence Correlation Spectroscopy. *Biophysical Journal*, 94(1):221–229.

[Ries and Schwille, 2006] Ries, J. and Schwille, P. (2006). Studying Slow Membrane Dynamics with Continuous Wave Scanning Fluorescence Correlation Spectroscopy. *Biophysical Journal*, 91(5):1915–1924.

[Ries and Schwille, 2008] Ries, J. and Schwille, P. (2008). New concepts for fluorescence correlation spectroscopy on membranes. *Physical Chemistry Chemical Physics*, 10(24):3487–3497.

[Ries et al., 2009b] Ries, J., Yu, S. R., Burkhardt, M., Brand, M., and Schwille, P. (2009b). Modular scanning FCS quantifies receptor-ligand interactions in living multicellular organisms. *Nature Methods*, 6:643.

[Rigler et al., 1993] Rigler, R., Mets, Ü., Widengren, J., and Kask, P. (1993). Fluorescence correlation spectroscopy with high count rate and low background: analysis of translational diffusion. *European Biophysics Journal*, 22(3):169–175.

[Rigler et al., 1999] Rigler, R., Pramanik, A., Jonasson, P., Kratz, G., Jansson, O. T., Nygren, P.-Å., Ståhl, S., Ekberg, K., Johansson, B.-L., Uhlén, S., Uhlén, M., Jörnvall, H., and Wahren, J. (1999). Specific binding of proinsulin C-peptide to human cell membranes. *Proceedings of the National Academy of Sciences*, 96(23):13318 LP – 13323.

[Rigler and Widengren, 2017] Rigler, R. and Widengren, J. (2017). Fluorescence-based monitoring of electronic state and ion exchange kinetics with FCS and related techniques: from T-jump measurements to fluorescence fluctuations. *European Biophysics Journal*.

[Rivas and Minton, 2016] Rivas, G. and Minton, A. P. (2016). Macromolecular Crowding In Vitro, In Vivo, and In Between. *Trends in Biochemical Sciences*, 41(11):970–981.

[Rivas and Minton, 2018] Rivas, G. and Minton, A. P. (2018). Toward an understanding of biochemical equilibria within living cells. *Biophysical Reviews*, 10(2):241–253.

[Roder et al., 2011] Roder, F., Waichman, S., Paterok, D., Schubert, R., Richter, C., Liedberg, B., and Piehler, J. (2011). Reconstitution of Membrane Proteins into Polymer-Supported Membranes for Probing Diffusion and Interactions by Single Molecule Techniques. *Analytical Chemistry*, 83(17):6792–6799.

[Roos et al., 2014] Roos, C., Kai, L., Haberstock, S., Proverbio, D., Ghoshdastider, U., Ma, Y., Filipek, S., Wang, X., Dötsch, V., and Bernhard, F. (2014). High-Level Cell-Free Production of Membrane Proteins with Nanodiscs. In Alexandrov, K. and Johnston, W. A., editors, *Cell-Free Protein Synthesis: Methods and Protocols*, pages 109–130. Humana Press, Totowa, NJ.

[Rothemund, 2006] Rothemund, P. W. K. (2006). Folding DNA to create nanoscale shapes and patterns. *Nature*, 440:297.

[Roy et al., 2008] Roy, R., Hohng, S., and Ha, T. (2008). A practical guide to single-molecule FRET. *Nature Methods*, 5:507.

[Rozovsky et al., 2012] Rozovsky, S., Forstner, M. B., Sondermann, H., and Groves, J. T. (2012). Single Molecule Kinetics of ENTH Binding to Lipid Membranes. *The Journal of Physical Chemistry B*, 116(17):5122–5131.

[Ruan et al., 2004] Ruan, Q., Cheng, M. A., Levi, M., Gratton, E., and Mantulin, W. W. (2004). Spatial-Temporal Studies of Membrane Dynamics: Scanning Fluorescence Correlation Spectroscopy (SFCS). *Biophysical Journal*, 87(2):1260–1267.

[Ruckstuhl et al., 2003] Ruckstuhl, T., Rankl, M., and Seeger, S. (2003). Highly sensitive biosensing using a supercritical angle fluorescence (SAF) instrument. *Biosensors and Bioelectronics*, 18(9):1193–1199.

[Ruckstuhl and Verdes, 2004] Ruckstuhl, T. and Verdes, D. (2004). Supercritical angle fluorescence (SAF) microscopy. *Optics Express*, 12(18):4246–4254.

[Rust et al., 2006] Rust, M. J., Bates, M., and Zhuang, X. (2006). Sub-diffraction-limit imaging by stochastic optical reconstruction microscopy (STORM). *Nature Methods*, 3(10):793.

[Rusu et al., 2004] Rusu, L., Gambhir, A., McLaughlin, S., and Rädler, J. (2004). Fluorescence Correlation Spectroscopy Studies of Peptide and Protein Binding to Phospholipid Vesicles. *Biophysical Journal*, 87(2):1044–1053.

[Saffarian and Elson, 2003] Saffarian, S. and Elson, E. L. (2003). Statistical Analysis of Fluorescence Correlation Spectroscopy: The Standard Deviation and Bias. *Biophysical Journal*, 84(3):2030–2042.

[Saffarian and Kirchhausen, 2008] Saffarian, S. and Kirchhausen, T. (2008). Differential Evanescence Nanometry: Live-Cell Fluorescence Measurements with 10-nm Axial Resolution on the Plasma Membrane. *Biophysical Journal*, 94(6):2333–2342.

[Sankaran et al., 2009] Sankaran, J., Manna, M., Guo, L., Kraut, R., and Wohland, T. (2009). Diffusion, Transport, and Cell Membrane Organization Investigated by Imaging Fluorescence Cross-Correlation Spectroscopy. *Biophysical Journal*, 97(9):2630–2639.

[SantaLucia, 1998] SantaLucia, J. (1998). A unified view of polymer, dumbbell, and oligonucleotide DNA nearest-neighbor thermodynamics. *Proceedings of the National Academy of Sciences*, 95(4):1460–1465.

[SantaLucia and Hicks, 2004] SantaLucia, J. and Hicks, D. (2004). The Thermodynamics of DNA Structural Motifs. *Annual Review of Biophysics and Biomolecular Structure*, 33(1):415–440.

[Santos et al., 2003] Santos, N. C., Prieto, M., and Castanho, M. A. (2003). Quantifying molecular partition into model systems of biomembranes: an emphasis on optical spectroscopic methods. *Biochimica et Biophysica Acta (BBA) - Biomembranes*, 1612(2):123–135.

[Sapra, 2013] Sapra, K. T. (2013). Atomic Force Microscopy and Spectroscopy to Probe Single Membrane Proteins in Lipid Bilayers. In Kleinschmidt, J. H., editor, *Lipid-Protein Interactions: Methods and Protocols*, pages 73–110. Humana Press, Totowa, NJ.

[Sarkar et al., 2004] Sarkar, A., Robertson, R. B., and Fernandez, J. M. (2004). Simultaneous atomic force microscope and fluorescence measurements of protein unfolding using a calibrated evanescent wave. *Proceedings of the National Academy of Sciences of the United States of America*, 101(35):12882–12886.

[Sauerbrey, 1959] Sauerbrey, G. (1959). Verwendung von Schwingquarzen zur Wägung dünner Schichten und zur Mikrowägung, Z. Physik, 155, 206–222.

[Saxton and Jacobson, 1997] Saxton, M. J. and Jacobson, K. (1997). Single-Particle Tracking: Applications to Membrane Dynamics. *Annual Review of Biophysics and Biomolecular Structure*, 26(1):373–399.

[Schätzel, 1986] Schätzel, K. (1986). Dead time correction of photon correlation functions. *Applied Physics B*, 41(2):95–102.

[Schätzel, 1987] Schätzel, K. (1987). Correlation techniques in dynamic light scattering. *Applied Physics B*, 42(4):193–213.

[Schätzel et al., 1988] Schätzel, K., Drewel, M., and Stimac, S. (1988). Photon Correlation Measurements at Large Lag Times: Improving Statistical Accuracy. *Journal of Modern Optics*, 35(4):711–718.

[Schmidt et al., 1996] Schmidt, T., Schütz, G. J., Baumgartner, W., Gruber, H. J., and Schindler, H. (1996). Imaging of single molecule diffusion. *Proceedings of the National Academy of Sciences*, 93(7):2926–2929.

[Schmitz et al., 2011] Schmitz, R., Yordanov, S., Butt, H. J., Koynov, K., and Dünweg, B. (2011). Studying flow close to an interface by total internal reflection fluorescence cross-correlation spectroscopy: Quantitative data analysis. *Phys. Rev. E*, 84(6):66306.

[Schneckenburger et al., 2012] Schneckenburger, H., Weber, P., Wagner, M., Schickinger, S., Richter, V., Bruns, T., Strauss, W., and Wittig, R. (2012). Light exposure and cell viability in fluorescence microscopy. *Journal of Microscopy*, 245(3):311–318.

[Schneider et al., 1988] Schneider, J., Rička, J., and Binkert, T. (1988). Improved fluorescence correlation apparatus for precise measurements of correlation functions. *Review of Scientific Instruments*, 59(4):588–590.

[Schnitzbauer et al., 2017] Schnitzbauer, J., Strauss, M. T., Schlichthaerle, T., Schueder, F., and Jungmann, R. (2017). Super-resolution microscopy with DNA-PAINT. *Nat. Protocols*, 12(6):1198–1228.

[Schwille et al., 1997] Schwille, P., Meyer-Almes, F. J., and Rigler, R. (1997). Dual-color fluorescence cross-correlation spectroscopy for multicomponent diffusional analysis in solution. *Biophysical Journal*, 72(4):1878–1886.

[Schwille et al., 1996] Schwille, P., Oehlenschläger, F., and Walter, N. G. (1996). Quantitative Hybridization Kinetics of DNA Probes to RNA in Solution Followed by Diffusional Fluorescence Correlation Analysis. *Biochemistry*, 35(31):10182–10193.

[Scomparin et al., 2009] Scomparin, C., Lecuyer, S., Ferreira, M., Charitat, T., and Tinland, B. (2009). Diffusion in supported lipid bilayers: Influence of substrate and preparation technique on the internal dynamics. *The European Physical Journal E*, 28(2):211–220.

[Seidler, 2017] Seidler, P. (2017). Optimized process for fabrication of free-standing silicon nanophotonic devices. *Journal of Vacuum Science & Technology B*, 35(3):31209.

[Senavirathne et al., 2015] Senavirathne, G., Liu, J., Lopez Jr, M. A., Hanne, J., Martin-Lopez, J., Lee, J.-B., Yoder, K. E., and Fishel, R. (2015). Widespread nuclease contamination in commonly used oxygen-scavenging systems. *Nature Methods*, 12:901.

[Seol and Neuman, 2018] Seol, Y. and Neuman, K. C. (2018). Combined Magnetic Tweezers and Micro-mirror Total Internal Reflection Fluorescence Microscope for Single-Molecule Manipulation and Visualization. In Peterman, E. J. G., editor, *Single Molecule Analysis: Methods and Protocols*, pages 297–316. Springer New York, New York, NY.

[Shai, 2013] Shai, Y. (2013). ATR-FTIR studies in pore forming and membrane induced fusion peptides. *Biochimica et Biophysica Acta (BBA) - Biomembranes*, 1828(10):2306–2313.

[Sharonov and Hochstrasser, 2006] Sharonov, A. and Hochstrasser, R. M. (2006). Wide-field subdiffraction imaging by accumulated binding of diffusing probes. *Proceedings of the National Academy of Sciences*, 103(50):18911 LP – 18916.

[Shaw et al., 2007] Shaw, A. W., Pureza, V. S., Sligar, S. G., and Morrissey, J. H. (2007). The Local Phospholipid Environment Modulates the Activation of Blood Clotting. *Journal of Biological Chemistry*, 282(9):6556–6563.

[Shechtman et al., 2015] Shechtman, Y., Weiss, L. E., Backer, A. S., Sahl, S. J., and Moerner, W. E. (2015). Precise Three-Dimensional Scan-Free Multiple-Particle Tracking over Large Axial Ranges with Tetrapod Point Spread Functions. *Nano Letters*, 15(6):4194–4199.

[Sheets et al., 1997] Sheets, E. D., Chen, L., and Thompson, N. L. (1997). Decreased IgG-FcγRII dissociation kinetics in the presence of a protein antigen. *Molecular Immunology*, 34(7):519–526.

[Shi et al., 2010] Shi, X., Lim, J., and Ha, T. (2010). Acidification of the Oxygen Scavenging System in Single-Molecule Fluorescence Studies: In Situ Sensing with a Ratiometric Dual-Emission Probe. *Analytical Chemistry*, 82(14):6132–6138.

[Shih et al., 2011] Shih, Y.-L., Huang, K.-F., Lai, H.-M., Liao, J.-H., Lee, C.-S., Chang, C.-M., Mak, H.-M., Hsieh, C.-W., and Lin, C.-C. (2011). The N-Terminal Amphipathic Helix of the Topological Specificity Factor MinE Is Associated with Shaping Membrane Curvature. *PLOS ONE*, 6(6):e21425.

[Sies and Menck, 1992] Sies, H. and Menck, C. F. (1992). Singlet oxygen induced DNA damage. *Mutation Research/DNAging*, 275(3-6):367–375.

[Simons and Gerl, 2010] Simons, K. and Gerl, M. J. (2010). Revitalizing membrane rafts: new tools and insights. *Nature Reviews Molecular Cell Biology*, 11:688.

[Simons and Ikonen, 1997] Simons, K. and Ikonen, E. (1997). Functional rafts in cell membranes. *Nature*, 387:569.

[Simons and Vaz, 2004] Simons, K. and Vaz, W. L. C. (2004). Model Systems, Lipid Rafts, and Cell Membranes. *Annual Review of Biophysics and Biomolecular Structure*, 33(1):269–295.

[Singh, 2016] Singh, P. (2016). SPR Biosensors: Historical Perspectives and Current Challenges.

[Smith et al., 2014] Smith, D. W., Iacono, S. T., and Iyer, S. S. (2014). *Handbook of fluoropolymer science and technology*. John Wiley & Sons.

[Sonal et al., 2019] Sonal, Ganzinger, K. A., Vogel, S. K., Mücksch, J., Blumhardt, P., and Schwille, P. (2019). Myosin-II activity generates a dynamic steady state with continuous actin turnover in a minimal actin cortex. *Journal of Cell Science*, 132(4):jcs219899.

[Sonesson et al., 2008] Sonesson, A. W., Blom, H., Hassler, K., Elofsson, U. M., Callisen, T. H., Widengren, J., and Brismar, H. (2008). Protein–surfactant interactions at hydrophobic interfaces studied with total internal reflection fluorescence correlation spectroscopy (TIR-FCS). *Journal of Colloid and Interface Science*, 317(2):449–457.

[Soumpasis, 1983] Soumpasis, D. M. (1983). Theoretical analysis of fluorescence photobleaching recovery experiments. *Biophysical Journal*, 41(1):95–97.

[Speight and Cooper, 2012] Speight, R. E. and Cooper, M. A. (2012). A Survey of the 2010 Quartz Crystal Microbalance Literature. *Journal of Molecular Recognition*, 25(9):451–473.

[Spindler et al., 2018] Spindler, S., Sibold, J., Gholami Mahmoodabadi, R., Steinem, C., and Sandoghdar, V. (2018). High-Speed Microscopy of Diffusion in Pore-Spanning Lipid Membranes. *Nano Letters*, 18(8):5262–5271.

[Spinke et al., 1992] Spinke, J., Yang, J., Wolf, H., Liley, M., Ringsdorf, H., and Knoll, W. (1992). Polymer-supported bilayer on a solid substrate. *Biophysical Journal*, 63(6):1667–1671.

[Sprague and McNally, 2005] Sprague, B. L. and McNally, J. G. (2005). FRAP analysis of binding: proper and fitting. *Trends in Cell Biology*, 15(2):84–91.

[Starr and Thompson, 2001] Starr, T. E. and Thompson, N. L. (2001). Total Internal Reflection with Fluorescence Correlation Spectroscopy: Combined Surface Reaction and Solution Diffusion. *Biophysical Journal*, 80(3):1575–1584.

[Starr and Thompson, 2002] Starr, T. E. and Thompson, N. L. (2002). Local Diffusion and Concentration of IgG near Planar Membranes: Measurement by Total Internal Reflection with Fluorescence Correlation Spectroscopy. *The Journal of Physical Chemistry B*, 106(9):2365–2371.

[Stellwagen et al., 2003] Stellwagen, E., Lu, Y., and Stellwagen, N. C. (2003). Unified Description of Electrophoresis and Diffusion for DNA and Other Polyions. *Biochemistry*, 42(40):11745–11750.

[Stenmark, 2009] Stenmark, H. (2009). Rab GTPases as coordinators of vesicle traffic. *Nature Reviews Molecular Cell Biology*, 10:513.

[Stewart, 2005] Stewart, G. C. (2005). Taking shape: control of bacterial cell wall biosynthesis. *Molecular Microbiology*, 57(5):1177–1181.

[Steyer and Almers, 1999] Steyer, J. A. and Almers, W. (1999). Tracking Single Secretory Granules in Live Chromaffin Cells by Evanescent-Field Fluorescence Microscopy. *Biophysical Journal*, 76(4):2262–2271.

[Steyer et al., 1997] Steyer, J. A., Horstmann, H., and Almers, W. (1997). Transport, docking and exocytosis of single secretory granules in live chromaffin cells. *Nature*, 388:474.

[Stillwell, 2016] Stillwell, W. (2016). Chapter 1 - Introduction to Biological Membranes. In Stillwell, W. B. T. A. I. t. B. M. S. E., editor, *Introduction to Biological Membranes*, pages 3–15. Elsevier.

[Stout and Axelrod, 1989] Stout, A. L. and Axelrod, D. (1989). Evanescent field excitation of fluorescence by epi-illumination microscopy. *Applied Optics*, 28(24):5237–5242.

[Strauss et al., 2018] Strauss, M. T., Schueder, F., Haas, D., Nickels, P. C., and Jungmann, R. (2018). Quantifying absolute addressability in DNA origami with molecular resolution. *Nature Communications*, 9(1):1600.

[Sun et al., 2008] Sun, Z.-Y. J., Oh, K. J., Kim, M., Yu, J., Brusic, V., Song, L., Qiao, Z., Wang, J.-h., Wagner, G., and Reinherz, E. L. (2008). HIV-1 Broadly Neutralizing Antibody Extracts Its Epitope from a Kinked gp41 Ectodomain Region on the Viral Membrane. *Immunity*, 28(1):52–63.

[Surovtsev and Jacobs-Wagner, 2018] Surovtsev, I. V. and Jacobs-Wagner, C. (2018). Subcellular Organization: A Critical Feature of Bacterial Cell Replication. *Cell*, 172(6):1271–1293.

[Sutherland, 1905] Sutherland, W. (1905). LXXV. A dynamical theory of diffusion for non-electrolytes and the molecular mass of albumin. *The London, Edinburgh, and Dublin Philosophical Magazine and Journal of Science*, 9(54):781–785.

[Swamy and Sankhala, 2013] Swamy, M. J. and Sankhala, R. S. (2013). Probing the Thermodynamics of Protein-Lipid Interactions by Isothermal Titration Calorimetry. In Kleinschmidt, J. H., editor, *Lipid-Protein Interactions: Methods and Protocols*, pages 37–53. Humana Press, Totowa, NJ.

[Swoboda et al., 2012] Swoboda, M., Henig, J., Cheng, H.-M. M., Brugger, D., Haltrich, D., Plumeré, N., and Schlierf, M. (2012). Enzymatic Oxygen Scavenging for Photostability without pH Drop in Single-Molecule Experiments. *ACS Nano*, 6(7):6364–6369.

[Swulius and Jensen, 2012] Swulius, M. T. and Jensen, G. J. (2012). The Helical MreB Cytoskeleton in Escherichia coli MC1000/pLE7 Is an Artifact of the N-Terminal Yellow Fluorescent Protein Tag. *Journal of Bacteriology*, 194(23):6382–6386.

[Szeto et al., 2004] Szeto, H. H., Schiller, P. W., Zhao, K., and Luo, G. (2004). Fluorescent dyes alter intracellular targeting and function of cell-penetrating tetrapeptides. *The FASEB Journal*, 19(1):118–120.

[Takahashi et al., 2005] Takahashi, Y., Sawada, R., Ishibashi, K., Mikuni, S., and Kinjo, M. (2005). Analysis of cellular functions by multipoint fluorescence correlation spectroscopy. *Current pharmaceutical biotechnology*, 6(2):159–165.

[Takakuwa et al., 1999] Takakuwa, Y., Pack, C.-G., An, X.-L., Manno, S., Ito, E., and Kinjo, M. (1999). Fluorescence correlation spectroscopy analysis of the hydrophobic interactions of protein 4.1 with phosphatidyl serine liposomes. *Biophysical Chemistry*, 82(2):149–155.

[Tamm and McConnell, 1985] Tamm, L. K. and McConnell, H. M. (1985). Supported phospholipid bilayers. *Biophysical Journal*, 47(1):105–113.

[Tanaka and Sackmann, 2005] Tanaka, M. and Sackmann, E. (2005). Polymer-supported membranes as models of the cell surface. *Nature*, 437:656.

[Tanaka et al., 2004] Tanaka, M., Wong, A. P., Rehfeldt, F., Tutus, M., and Kaufmann, S. (2004). Selective Deposition of Native Cell Membranes on Biocompatible Micropatterns. *Journal of the American Chemical Society*, 126(10):3257–3260.

[Tatulian, 2013] Tatulian, S. A. (2013). Structural Characterization of Membrane Proteins and Peptides by FTIR and ATR-FTIR Spectroscopy. In Kleinschmidt, J. H., edi-

tor, *Lipid-Protein Interactions: Methods and Protocols*, pages 177–218. Humana Press, Totowa, NJ.

[Teruel and Meyer, 2000] Teruel, M. N. and Meyer, T. (2000). Translocation and Reversible Localization of Signaling Proteins: A Dynamic Future for Signal Transduction. *Cell*, 103(2):181–184.

[Thomas et al., 2015a] Thomas, F. A., Visco, I., Petrášek, Z., Heinemann, F., and Schwille, P. (2015a). Diffusion coefficients and dissociation constants of enhanced green fluorescent protein binding to free standing membranes. *Data in Brief*, 5:537–541.

[Thomas et al., 2015b] Thomas, F. A., Visco, I., Petrášek, Z., Heinemann, F., and Schwille, P. (2015b). Introducing a fluorescence-based standard to quantify protein partitioning into membranes. *Biochimica et Biophysica Acta (BBA) - Biomembranes*, 1848(11, Part A):2932–2941.

[Thomas, 1999] Thomas, R. R. (1999). Material Properties of Fluoropolymers and Perfluoroalkyl-based Polymers. In Hougham, G., Cassidy, P. E., Johns, K., and Davidson, T., editors, *Fluoropolymers 2: Properties*, pages 47–67. Springer US, Boston, MA.

[Thompson, 1982] Thompson, N. L. (1982). Surface binding rates of nonfluorescent molecules may be obtained by total internal reflection with fluorescence correlation spectroscopy. *Biophysical Journal*, 38(3):327–329.

[Thompson, 1999] Thompson, N. L. (1999). Fluorescence Correlation Spectroscopy. In Lakowicz, J. R., editor, *Topics in Fluorescence Spectroscopy: Techniques*, pages 337–378. Springer US, Boston, MA.

[Thompson and Axelrod, 1983] Thompson, N. L. and Axelrod, D. (1983). Immunoglobulin surface-binding kinetics studied by total internal reflection with fluorescence correlation spectroscopy. *Biophysical Journal*, 43(1):103–114.

[Thompson et al., 1981] Thompson, N. L., Burghardt, T. P., and Axelrod, D. (1981). Measuring surface dynamics of biomolecules by total internal reflection fluorescence with photobleaching recovery or correlation spectroscopy. *Biophysical Journal*, 33(3):435–454.

[Thompson et al., 1997] Thompson, N. L., Drake, A. W., Chen, L., and Broek, W. V. (1997). Equilibrium, Kinetics, Diffusion and Self-Association of Proteins at Membrane

Surfaces: Measurement by Total Internal Reflection Fluorescence Microscopy. *Photochemistry and Photobiology*, 65(1):39–46.

[Thompson et al., 2011] Thompson, N. L., Navaratnarajah, P., and Wang, X. (2011). Measuring Surface Binding Thermodynamics and Kinetics by Using Total Internal Reflection with Fluorescence Correlation Spectroscopy: Practical Considerations. *The Journal of Physical Chemistry B*, 115(1):120–131.

[Thompson et al., 1993] Thompson, N. L., Pearce, K. H., and Hsieh, H. V. (1993). Total internal reflection fluorescence microscopy: application to substrate-supported planar membranes. *European biophysics journal*, 22(5):367–378.

[Thompson et al., 2002] Thompson, R. E., Larson, D. R., and Webb, W. W. (2002). Precise Nanometer Localization Analysis for Individual Fluorescent Probes. *Biophysical Journal*, 82(5):2775–2783.

[Toomre and Bewersdorf, 2010] Toomre, D. and Bewersdorf, J. (2010). A New Wave of Cellular Imaging. *Annual Review of Cell and Developmental Biology*, 26(1):285–314.

[Toomre and Manstein, 2001] Toomre, D. and Manstein, D. J. (2001). Lighting up the cell surface with evanescent wave microscopy. *Trends in Cell Biology*, 11(7):298–303.

[Torres and Levitus, 2007] Torres, T. and Levitus, M. (2007). Measuring Conformational Dynamics: A New FCS-FRET Approach. *The Journal of Physical Chemistry B*, 111(25):7392–7400.

[Tutkus et al., 2017] Tutkus, M., Marciulionis, T., Sasnauskas, G., and Rutkauskas, D. (2017). DNA-Endonuclease Complex Dynamics by Simultaneous FRET and Fluorophore Intensity in Evanescent Field. *Biophysical Journal*, 112(5):850–858.

[Uchida et al., 2016] Uchida, T., Yu, F., Nihei, M., and Taniguchi, J. (2016). Fabrication of antireflection structures on the surface of optical lenses by using a liquid transfer imprint technique. *Microelectronic Engineering*, 153:43–47.

[Unno et al., 2017] Unno, N., Kigami, H., Fujinami, T., Nakata, S., Satake, S.-i., and Taniguchi, J. (2017). Fabrication of calibration plate for total internal reflection fluorescence microscopy using roll-type liquid transfer imprint lithography. *Microelectronic Engineering*, 180:86–92.

[Unno et al., 2015] Unno, N., Maeda, A., Satake, S.-i., Tsuji, T., and Taniguchi, J. (2015). Fabrication of nanostep for total internal reflection fluorescence microscopy to calibrate in water. *Microelectronic Engineering*, 133:98–103.

[Valeur and Berberan-Santos, 2012] Valeur, B. and Berberan-Santos, M. N. (2012). *Molecular fluorescence: principles and applications*. John Wiley & Sons.

[Van Craenenbroeck and Engelborghs, 1999] Van Craenenbroeck, E. and Engelborghs, Y. (1999). Quantitative Characterization of the Binding of Fluorescently Labeled Colchicine to Tubulin in Vitro Using Fluorescence Correlation Spectroscopy. *Biochemistry*, 38(16):5082–5088.

[van der Velde et al., 2016] van der Velde, J. H. M., Oelerich, J., Huang, J., Smit, J. H., Aminian Jazi, A., Galiani, S., Kolmakov, K., Gouridis, G., Eggeling, C., Herrmann, A., Roelfes, G., and Cordes, T. (2016). A simple and versatile design concept for fluorophore derivatives with intramolecular photostabilization. *Nature Communications*, 7:10144.

[van der Walt et al., 2011] van der Walt, S., Colbert, S. C., and Varoquaux, G. (2011). The NumPy Array: A Structure for Efficient Numerical Computation. *Computing in Science & Engineering*, 13(2):22–30.

[Vanni et al., 2013] Vanni, S., Vamparys, L., Gautier, R., Drin, G., Etchebest, C., Fuchs, P. F., and Antonny, B. (2013). Amphipathic Lipid Packing Sensor Motifs: Probing Bilayer Defects with Hydrophobic Residues. *Biophysical Journal*, 104(3):575–584.

[Vaz et al., 1984] Vaz, W. L. C., Goodsaid-Zalduondo, F., and Jacobson, K. (1984). Lateral diffusion of lipids and proteins in bilayer membranes. *FEBS Letters*, 174(2):199–207.

[Vazquez et al., 2006] Vazquez, F., Matsuoka, S., Sellers, W. R., Yanagida, T., Ueda, M., and Devreotes, P. N. (2006). Tumor suppressor PTEN acts through dynamic interaction with the plasma membrane. *Proceedings of the National Academy of Sciences of the United States of America*, 103(10):3633 LP – 3638.

[Veerapathiran and Wohland, 2018] Veerapathiran, S. and Wohland, T. (2018). The imaging FCS diffusion law in the presence of multiple diffusive modes. *Methods*, 140-141:140–150.

[Veiga and Castanho, 2007] Veiga, A. S. and Castanho, M. A. R. B. (2007). The influence of cholesterol on the interaction of HIV gp41 membrane proximal region-derived peptides with lipid bilayers. *The FEBS Journal*, 274(19):5096–5104.

[Velazquez-Campoy and Freire, 2006] Velazquez-Campoy, A. and Freire, E. (2006). Isothermal titration calorimetry to determine association constants for high-affinity ligands. *Nature Protocols*, 1:186.

[Velazquez-Campoy et al., 2015] Velazquez-Campoy, A., Leavitt, S. A., and Freire, E. (2015). Characterization of Protein-Protein Interactions by Isothermal Titration Calorimetry. In Meyerkord, C. L. and Fu, H., editors, *Protein-Protein Interactions: Methods and Applications*, pages 183–204. Springer New York, New York, NY.

[Vincent et al., 2002] Vincent, N., Genin, C., and Malvoisin, E. (2002). Identification of a conserved domain of the HIV-1 transmembrane protein gp41 which interacts with cholesteryl groups. *Biochimica et Biophysica Acta (BBA) - Biomembranes*, 1567:157–164.

[Visco et al., 2016] Visco, I., Hoege, C., Hyman, A. A., and Schwille, P. (2016). In vitro Reconstitution of a Membrane Switch Mechanism for the Polarity Protein LGL. *Journal of Molecular Biology*, 428(24):4828–4842.

[Vogelsang et al., 2008] Vogelsang, J., Kasper, R., Steinhauer, C., Person, B., Heilemann, M., Sauer, M., and Tinnefeld, P. (2008). A Reducing and Oxidizing System Minimizes Photobleaching and Blinking of Fluorescent Dyes. *Angewandte Chemie International Edition*, 47(29):5465–5469.

[von Ahsen et al., 2001] von Ahsen, N., Wittwer, C. T., and Schütz, E. (2001). Oligonucleotide Melting Temperatures under PCR Conditions: Nearest-Neighbor Corrections for Mg2+, Deoxynucleotide Triphosphate, and Dimethyl Sulfoxide Concentrations with Comparison to Alternative Empirical Formulas. *Clinical Chemistry*, 47(11):1956–1961.

[von Smoluchowski, 1906] von Smoluchowski, M. (1906). Zur kinetischen Theorie der Brownschen Molekularbewegung und der Suspensionen. *Annalen der Physik*, 326(14):756–780.

[Wachsmuth et al., 2000] Wachsmuth, M., Waldeck, W., and Langowski, J. (2000). Anomalous diffusion of fluorescent probes inside living cell nuclei investigated by

spatially-resolved fluorescence correlation spectroscopy11Edited by W. Baumeister. *Journal of Molecular Biology*, 298(4):677–689.

[Wagner and Tamm, 2000] Wagner, M. L. and Tamm, L. K. (2000). Tethered Polymer-Supported Planar Lipid Bilayers for Reconstitution of Integral Membrane Proteins: Silane-Polyethyleneglycol-Lipid as a Cushion and Covalent Linker. *Biophysical Journal*, 79(3):1400–1414.

[Walder et al., 2012] Walder, R., Kastantin, M., and Schwartz, D. K. (2012). High throughput single molecule tracking for analysis of rare populations and events. *Analyst*, 137(13):2987–2996.

[Wallace and Janes, 2001] Wallace, B. A. and Janes, R. W. (2001). Synchrotron radiation circular dichroism spectroscopy of proteins: secondary structure, fold recognition and structural genomics. *Current Opinion in Chemical Biology*, 5(5):567–571.

[Wallace et al., 2003] Wallace, B. A., Lees, J. G., Orry, A. J. W., Lobley, A., and Janes, R. W. (2003). Analyses of circular dichroism spectra of membrane proteins. *Protein Science*, 12(4):875–884.

[Wallner et al., 2013] Wallner, J., Lhota, G., Jeschek, D., Mader, A., and Vorauer-Uhl, K. (2013). Application of Bio-Layer Interferometry for the analysis of protein/liposome interactions. *Journal of Pharmaceutical and Biomedical Analysis*, 72:150–154.

[Walter et al., 2008] Walter, N. G., Huang, C.-Y., Manzo, A. J., and Sobhy, M. A. (2008). Do-it-yourself guide: how to use the modern single-molecule toolkit. *Nature Methods*, 5:475.

[Wang and Axelrod, 1994] Wang, M. D. and Axelrod, D. (1994). Microclustering patterns of acetylcholine receptors on myotubes studied by spatial fluorescence autocorrelation. *Bioimaging*, 2(1):22–35.

[Wang et al., 2014] Wang, Y., Schnitzbauer, J., Hu, Z., Li, X., Cheng, Y., Huang, Z.-L., and Huang, B. (2014). Localization events-based sample drift correction for localization microscopy with redundant cross-correlation algorithm. *Optics Express*, 22(13):15982.

[Wawrezinieck et al., 2005] Wawrezinieck, L., Rigneault, H., Marguet, D., and Lenne, P.-F. (2005). Fluorescence Correlation Spectroscopy Diffusion Laws to Probe the Submicron Cell Membrane Organization. *Biophysical Journal*, 89(6):4029–4042.

[Webb, 2001] Webb, W. W. (2001). Fluorescence Correlation Spectroscopy: Genesis, Evolution, Maturation and Prognosis. In Rigler, R. and Elson, E. S., editors, *Fluorescence Correlation Spectroscopy: Theory and Applications*, pages 305–330. Springer Berlin Heidelberg, Berlin, Heidelberg.

[Weger and Hoffmann-Jacobsen, 2017] Weger, L. and Hoffmann-Jacobsen, K. (2017). A total internal reflection-fluorescence correlation spectroscopy setup with pulsed diode laser excitation. *Review of Scientific Instruments*, 88(9):93102.

[Weger et al., 2018] Weger, L., Weidmann, M., Ali, W., Hildebrandt, M., Gutmann, J. S., and Hoffmann-Jacobsen, K. (2018). Polymer Diffusion in the Interphase Between Surface and Solution. *Langmuir*, 34(24):7021–7027.

[Weidemann et al., 2014] Weidemann, T., Mücksch, J., and Schwille, P. (2014). Fluorescence fluctuation microscopy: a diversified arsenal of methods to investigate molecular dynamics inside cells. *Current Opinion in Structural Biology*, 28:69–76.

[Weidemann and Schwille, 2009] Weidemann, T. and Schwille, P. (2009). Fluorescence Correlation Spectroscopy in Living Cells. In Hinterdorfer, P. and Oijen, A., editors, *Handbook of Single-Molecule Biophysics*, pages 217–241. Springer US, New York, NY.

[Weiß et al., 2013] Weiß, K., Neef, A., Van, Q., Kramer, S., Gregor, I., and Enderlein, J. (2013). Quantifying the Diffusion of Membrane Proteins and Peptides in Black Lipid Membranes with 2-Focus Fluorescence Correlation Spectroscopy. *Biophysical Journal*, 105(2):455–462.

[Wexler-Cohen and Shai, 2007] Wexler-Cohen, Y. and Shai, Y. (2007). Demonstrating the C-terminal boundary of the HIV 1 fusion conformation in a dynamic ongoing fusion process and implication for fusion inhibition. *The FASEB Journal*, 21(13):3677–3684.

[White and Wimley, 1998] White, S. H. and Wimley, W. C. (1998). Hydrophobic interactions of peptides with membrane interfaces. *Biochimica et Biophysica Acta (BBA) - Reviews on Biomembranes*, 1376(3):339–352.

[Widengren, 2001] Widengren, J. (2001). Photophysical Aspects of FCS Measurements. In Rigler, R. and Elson, E. S., editors, *Fluorescence Correlation Spectroscopy: Theory and Applications*, pages 276–301. Springer Berlin Heidelberg, Berlin, Heidelberg.

[Widengren et al., 2007] Widengren, J., Chmyrov, A., Eggeling, C., Löfdahl, P.-Å., and Seidel, C. A. M. (2007). Strategies to Improve Photostabilities in Ultrasensitive Fluorescence Spectroscopy. *The Journal of Physical Chemistry A*, 111(3):429–440.

[Widengren et al., 1997] Widengren, J., Dapprich, J., and Rigler, R. (1997). Fast interactions between Rh6G and dGTP in water studied by fluorescence correlation spectroscopy. *Chemical Physics*, 216(3):417–426.

[Widengren et al., 1995] Widengren, J., Mets, U., and Rigler, R. (1995). Fluorescence correlation spectroscopy of triplet states in solution: a theoretical and experimental study. *The Journal of Physical Chemistry*, 99(36):13368–13379.

[Widengren and Rigler, 1996] Widengren, J. and Rigler, R. (1996). Mechanisms of photobleaching investigated by fluorescence correlation spectroscopy. *Bioimaging*, 4(3):149–157.

[Widengren et al., 1994] Widengren, J., Rigler, R., and Mets, Ü. (1994). Triplet-state monitoring by fluorescence correlation spectroscopy. *Journal of Fluorescence*, 4(3):255–258.

[Widengren and Schwille, 2000] Widengren, J. and Schwille, P. (2000). Characterization of Photoinduced Isomerization and Back-Isomerization of the Cyanine Dye Cy5 by Fluorescence Correlation Spectroscopy. *The Journal of Physical Chemistry A*, 104(27):6416–6428.

[Wienken et al., 2010] Wienken, C. J., Baaske, P., Rothbauer, U., Braun, D., and Duhr, S. (2010). Protein-binding assays in biological liquids using microscale thermophoresis. *Nature Communications*, 1:100.

[Wieprecht and Seelig, 2002] Wieprecht, T. and Seelig, J. B. T. C. T. i. M. (2002). Isothermal titration calorimetry for studying interactions between peptides and lipid membranes. In *Peptide-Lipid Interactions*, volume 52, pages 31–56. Academic Press.

[Wilkinson et al., 1994] Wilkinson, F., McGarvey, D. J., and Olea, A. F. (1994). Excited Triplet State Interactions with Molecular Oxygen: Influence of Charge Transfer on the Bimolecular Quenching Rate Constants and the Yields of Singlet Oxygen [O*2(1.DELTA.g)] for Substituted Naphthalenes in Various Solvents. *The Journal of Physical Chemistry*, 98(14):3762–3769.

[Williamson et al., 2011] Williamson, D. J., Owen, D. M., Rossy, J., Magenau, A., Wehrmann, M., Gooding, J. J., and Gaus, K. (2011). Pre-existing clusters of the adaptor Lat do not participate in early T cell signaling events. *Nature Immunology*, 12:655.

[Wimley et al., 1996] Wimley, W. C., Creamer, T. P., and White, S. H. (1996). Solvation Energies of Amino Acid Side Chains and Backbone in a Family of Host-Guest Pentapeptides. *Biochemistry*, 35(16):5109–5124.

[Wimley and White, 1996] Wimley, W. C. and White, S. H. (1996). Experimentally determined hydrophobicity scale for proteins at membrane interfaces. *Nature Structural Biology*, 3(10):842–848.

[Wiseman, 2013] Wiseman, P. W. (2013). Image Correlation Spectroscopy: Mapping Correlations in Space, Time, and Reciprocal Space. In Tetin, S., editor, *Fluorescence Fluctuation Spectroscopy (FFS), Part A*, volume 518, pages 245–267. Academic Press.

[Wiseman, 2015] Wiseman, P. W. (2015). Image Correlation Spectroscopy: Principles and Applications. *Cold Spring Harbor Protocols*, 2015(4):pdb.top086124.

[Wohland et al., 1999] Wohland, T., Friedrich, K., Hovius, R., and Vogel, H. (1999). Study of Ligand-Receptor Interactions by Fluorescence Correlation Spectroscopy with Different Fluorophores: Evidence That the Homopentameric 5-Hydroxytryptamine Type 3_{As} Receptor Binds Only One Ligand. *Biochemistry*, 38(27):8671–8681.

[Woll, 2014] Woll, D. (2014). Fluorescence correlation spectroscopy in polymer science. *RSC Advances*, 4(5):2447–2465.

[Woodson, 2005] Woodson, S. A. (2005). Metal ions and RNA folding: a highly charged topic with a dynamic future. *Current Opinion in Chemical Biology*, 9(2):104–109.

[Wu et al., 2012] Wu, H.-J., Henzie, J., Lin, W.-C., Rhodes, C., Li, Z., Sartorel, E., Thorner, J., Yang, P., and Groves, J. (2012). Membrane-protein binding measured with solution-phase plasmonic nanocube sensors. *Nature Methods*, 9(12):1189–1191.

[Xie, 1996] Xie, X. S. (1996). Single-Molecule Spectroscopy and Dynamics at Room Temperature. *Accounts of Chemical Research*, 29(12):598–606.

[Yamazaki et al., 2005] Yamazaki, V., Sirenko, O., Schafer, R. J., and Groves, J. T. (2005). Lipid Mobility and Molecular Binding in Fluid Lipid Membranes. *Journal of the American Chemical Society*, 127(9):2826–2827.

[Yang et al., 2004] Yang, W., Gelles, J., and Musser, S. M. (2004). Imaging of single-molecule translocation through nuclear pore complexes. *Proceedings of the National Academy of Sciences of the United States of America*, 101(35):12887–12892.

[Yıldırım et al., 2007] Yıldırım, M. A., Goh, K.-I., Cusick, M. E., Barabási, A.-L., and Vidal, M. (2007). Drug–target network. *Nature Biotechnology*, 25:1119.

[Yoon et al., 2006] Yoon, T.-Y., Okumus, B., Zhang, F., Shin, Y.-K., and Ha, T. (2006). Multiple intermediates in SNARE-induced membrane fusion. *Proceedings of the National Academy of Sciences*, 103(52):19731 LP – 19736.

[Yordanov et al., 2009] Yordanov, S., Best, A., Butt, H.-J., and Koynov, K. (2009). Direct studies of liquid flows near solid surfaces by total internal reflection fluorescence cross-correlation spectroscopy. *Opt. Express*, 17(23):21149–21158.

[Yordanov et al., 2011] Yordanov, S., Best, A., Weisshart, K., and Koynov, K. (2011). Note: An easy way to enable total internal reflection-fluorescence correlation spectroscopy (TIR-FCS) by combining commercial devices for FCS and TIR microscopy. *Review of Scientific Instruments*, 82(3):36105.

[Yun et al., 2007] Yun, B. H., Lee, Y. A., Kim, S. K., Kuzmin, V., Kolbanovskiy, A., Dedon, P. C., Geacintov, N. E., and Shafirovich, V. (2007). Photosensitized oxidative DNA damage: From hole injection to chemical product formation and strand cleavage. *Journal of the American Chemical Society*.

[Zadeh et al., 2011] Zadeh, J. N., Steenberg, C. D., Bois, J. S., Wolfe, B. R., Pierce, M. B., Khan, A. R., Dirks, R. M., and Pierce, N. A. (2011). NUPACK: Analysis and design of nucleic acid systems. *Journal of Computational Chemistry*, 32(1):170–173.

[Zalisko et al., 2017] Zalisko, B. E., Chan, C., Denic, V., Rock, R. S., and Keenan, R. J. (2017). Tail-Anchored Protein Insertion by a Single Get1/2 Heterodimer. *Cell Reports*, 20(10):2287–2293.

[Zerial and McBride, 2001] Zerial, M. and McBride, H. (2001). Rab proteins as membrane organizers. *Nature Reviews Molecular Cell Biology*, 2:107.

[Zhang et al., 2007] Zhang, B., Zerubia, J., and Olivo-Marin, J.-C. (2007). Gaussian approximations of fluorescence microscope point-spread function models. *Applied Optics*, 46(10):1819–1829.

[Zheng et al., 2014a] Zheng, Q., Jockusch, S., Zhou, Z., and Blanchard, S. C. (2014a). The contribution of reactive oxygen species to the photobleaching of organic fluorophores. *Photochemistry and Photobiology*, 90(2):448–454.

[Zheng et al., 2014b] Zheng, Q., Juette, M. F., Jockusch, S., Wasserman, M. R., Zhou, Z., Altman, R. B., and Blanchard, S. C. (2014b). Ultra-stable organic fluorophores for single-molecule research. *Chem. Soc. Rev.*, 43(4):1044–1056.

[Zhou et al., 2008] Zhou, H.-X., Rivas, G., and Minton, A. P. (2008). Macromolecular Crowding and Confinement: Biochemical, Biophysical, and Potential Physiological Consequences. *Annual Review of Biophysics*, 37(1):375–397.

[Zimmerberg and Kozlov, 2005] Zimmerberg, J. and Kozlov, M. M. (2005). How proteins produce cellular membrane curvature. *Nature Reviews Molecular Cell Biology*, 7:9.

A

APPENDIX TO CHAPTER II - QUANTIFYING REVERSIBLE SURFACE BINDING VIA SI-FCS

A.1 Supplementary Methods

Optical setup

Fluorescence images were recorded on a home-built custom-type TIRF microscope, which was constructed around a Nikon Ti-S microscope body with oil immersion objective (Nikon SR Apo TIRF, 100x magnification, 1.49 numerical aperture (NA)). Custom-built excitation and detection pathways (Supplementary Fig. A.1) extended the commercial body. Four laser lines (490 nm (Cobolt Calypso, 50 mW nominal), 532 nm (Cobolt Samba, 100 mW nominal), 561 nm (Cobolt Jive, 50 mW nominal) and 640 nm (Cobolt 06-MLD, 140 mW nominal)) were attenuated with an acousto-optical tunable filter (Gooch & Housego TF-525-250), which was interfaced through a PCI Express card (PCIe-6323 and BNC-2110) and controlled with a home-written LabView 2011 software (all National Instruments, Austin, USA). A polarization-maintaining single-mode fiber (kineFLEX-P-3-S-405.640-0.7-FCS-P0 and kineMATIX, Qioptiq, Hamble, UK) spatially filtered the excitation beams. At the fiber exit, the beam was collimated by an achromatic lens ($f = 25\,\mathrm{mm}$, Edmund Optics, Karlsruhe, Germany) and the polarization refiltered through a polarizing beam splitter (CCM1-PBS251/M, Thorlabs, Dachau. Germany). Achromatic doublets were employed for three-fold beam expansion ($f = -25, 75\,\mathrm{mm}$) and focusing the excitation in the objective's back focal plane ($f = 225\,\mathrm{mm}$, all purchased from Edmund Optics, Karlsruhe, Germany). A four-color notch beam splitter (zt405/488/561/640rpc flat, AHF Analysentechnik, Tübingen, Germany) directed the excitation laser beams towards the objective. A piezo-electric stage (Q545, Physikalische Instrumente, Karlsruhe, Germany) translated the excitation beam off-axis to switch between wide-field, HILO or TIRF imaging.

The emission light was directed towards the microscope side-port and spectrally band-

pass filtered (Semrock BrightLine 593/46, AHF Analysentechnik, Tübingen, Germany) in infinity space. The detection pathway comprised a $4f$ telescope ($f = 200\,\mathrm{mm}$, AC254-200-A-ML, Thorlabs, Dachau, Germany) and an electron-multiplying charge-coupled device (EMCCD) camera (iXon Ultra 897, Andor Technologies, Belfast, UK). The camera acquisition triggered the transmission of the acousto-optical tunable filter by TTL pulses. Images were recorded using the Andor Solis software (Andor Technologies, Version 4.28).

A custom-built focus stabilization eliminated the drift of the focus position: A near infrared laser (LP785-SF20, Thorlabs, Dachau, Germany) was back-reflected from the sample in TIRF configuration and focused on a CMOS camera (UI-3240CP-NIR-GL, Imaging Development Systems, Obersulm, Germany). A feedback control implemented in LabVIEW 2015 (National Instruments, Austin, USA) maximized the cross-correlation of the images of the laser spot and a reference image, respectively. The axial sample position was adjusted every 200 ms accordingly (P737.2SL and E-709.SRG, Physikalische Instrumente, Karlsruhe, Germany) to keep the sample in focus.

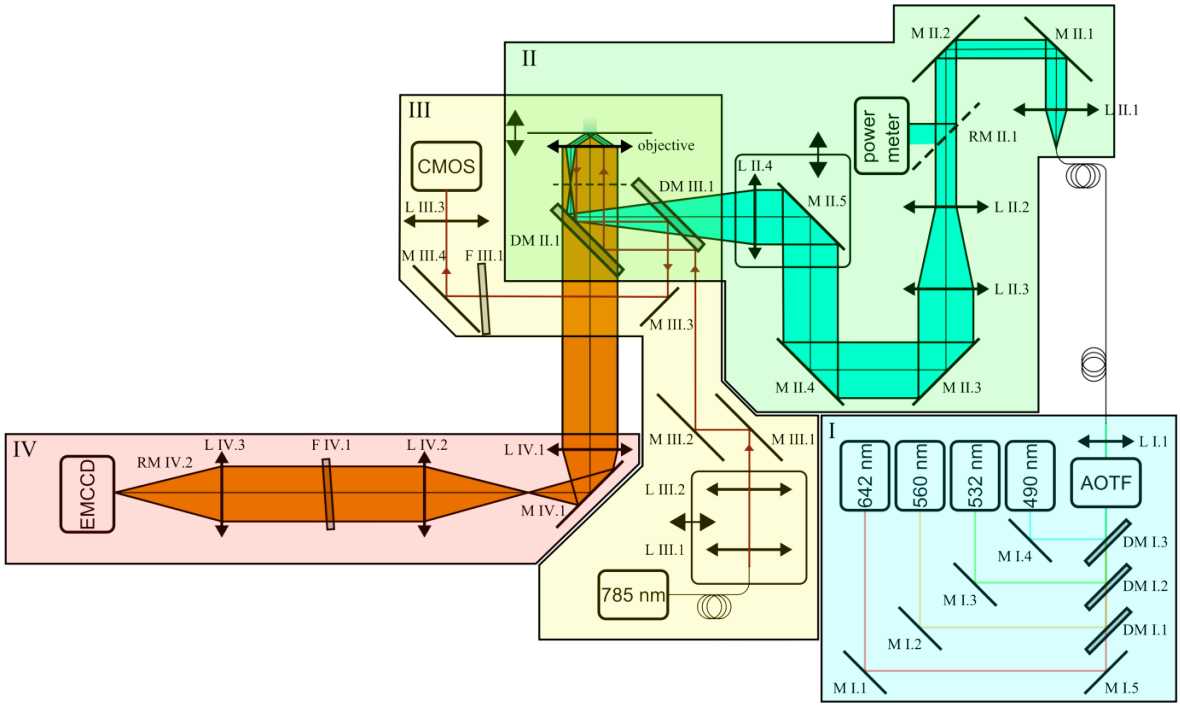

Figure A.1: Custom-built TIRF microscope.

SI-FCS image acquisition

Unless stated otherwise, SI-FCS analysis was performed on image sequences of 64×64 pixel (4×4 binning) and for comparable analysis resized to the camera resolution of 256×256 pixels. Image stacks were recorded for 1.5 million frames for 7 nt, 8 nt and 9 nt, and 150,000 frames for 10 nt, respectively. The exposure time was 10 ms and the camera frame rate 85 Hz for 7 nt, 8 nt, 9 nt, or 10 Hz 10 nt. The EM gain setting was varied, but does not influence the kinetics (data not shown). To exclude any effect of the EM gain, we varied this parameter systematically in an initial set of experiments, but observed no influence on the autocorrelation decay times obtained from SI-FCS measurements (data not shown).

SI-FCS data analysis

The autocorrelation curves were computed and analyzed using a custom-written Matlab 2017a (The MathWorks, Natick, USA) software: Each image was subdivided into 7×7 ROIs, each of them covering 31×31 pixels, spaced in a grid around the center of illumination. The effect of the choice of ROI size is discussed in Supplementary Fig. III.12 (p. 55). The signal in each ROI was integrated, yielding 49 intensity traces, which were bleach and drift-corrected by a single exponential, and individually correlated using the multiple-τ algorithm [Schätzel, 1987], in which we doubled the bin width after every sixteenth point in the autocorrelation curve. The obtained autocorrelation curves were fitted individually by a single exponential decay with an offset, from which the amplitude and the characteristic decay time were obtained. For samples containing two species, the autocorrelation curves were fitted by a sum of two exponentials with an offset. In the titration experiments, the biexponential fit accounted for a supposedly non-specific component appearing at high concentrations (10 nM for 10 nt, 100 nM for 9 nt).

Monte Carlo Simulations of SI-FCS measurements

If not mentioned otherwise, Monte Carlo Simulations were performed using a home-written MATLAB code (R2016a, MathWorks). The time step between two iterations was set to $dt = 1$ ms and the signal from 10 iterations was integrated to form one time point in the signal trace. This corresponds to a time resolution of the detector of 10 ms. For these simulations, we only considered fluctuations in signal originating from binding and unbinding events. Therefore, we initialized N_{surf} immobile binding sites at a surface and

had a fraction $\beta = \frac{1}{1+\frac{k_d}{k_a\langle A\rangle}}$ of them initially occupied. Moreover, we defined a probability of binding $P_{\text{binding}} = 1-e^{-k_a<A>dt}$ and unbinding $P_{\text{unbinding}} = 1-e^{-k_d dt}$. During each iteration, we treat occupied and unoccupied binding sites differently. For all bound sites we generated a uniformly distributed random number in the interval (0,1). If the random number was smaller than a threshold given by $P_{\text{unbinding}}$, the binding site was converted to an unoccupied state, otherwise it remained unchanged. The transitions from the unbound to bound state were simulated following an equivalent strategy. Each bound receptor contributed with the brightness 1 to the signal per iteration, each unoccupied binding site did not contribute to the signal. The described code does not simulate images, but only the integrated signal over a simulated area. Although it is straightforward to add the functionality of simulating images, all simulations with varying surface density (Supplementary Figure III.9, p. 51) were performed using the previously published Picasso tool [Schnitzbauer et al., 2017].

Fluorescently labeled complementary ssDNA in solution

Labeled imager strands with the sequence 5'-CTAGATGTAT-3'-Cy3B were purchased from Eurofins Genomics.

Buffers

For simplicity, we name the used buffers A+ and B+. Buffer A+ contains 10 mM Tris-HCl, 100 mM NaCl, 0.05 v% Tween20 and is adjusted to pH 8. Buffer B+ contains 5 mM Tris-HCl, 10 mM MgCl2, 1 mM EDTA, 0.05 v% Tween20 and is adjusted to pH 8.

Preparation of DNA origami samples

DNA origami structures were synthesized as previously described [Schnitzbauer et al., 2017]. In brief, structures were folded in a one-pot reaction with 40 µL total volume containing 10 nM scaffold (M13mp18), 10 nM biotinylated staples for surface attachment, 100 nM core staples and 1 µM extended staples in 1xTE buffer supplemented with 12.5 mM MgCl2. Structures were folded by first holding for 5 min at 80 °C, then going from 65 °C to 4 °C over the course of 3 hours. The assembly of the DNA origami structures was confirmed by super-resolution imaging with DNA-PAINT (see Supplementary Fig. III.11, p. 53).

Assembly of the Sample Chamber

Surfaces with immobilized DNA origami structures were prepared following a previously reported protocol [Schnitzbauer et al., 2017]. In brief, high precision #1.5 coverslips (Paul Marienfeld GmbH, Germany) were sonicated in acetone (chemical grade, Merck KGaA, Germany) for 10 minutes and then rinsed twice with ethanol (chemical grade, Merck Millipore, Germany) and water (milli-Q, Merck Millipore, Germany) and gently dried with pressurized air. The cleaning of the coverslip was completed by putting a drop of 2-propanol on it (Uvasol, Merck KGaA, Germany) and wiping with a paper tissue (Kimtech Science, Sigma Aldrich, Germany). The same procedure was performed on microscope slides ($76 \times 26\,\mathrm{mm}^2$, Menzel, Germany). The high precision coverslip and the microscope slide were assembled into a flow chamber by gluing them together with double-sided sticky-tape (Scotch, Conrad Electronic SE, Germany), yielding a roughly $5 \times 22 \times 0.08\,\mathrm{mm}^3$ large chamber. In a series of volume exchanges, the flow chamber was first incubated with 20 µL of 1 mg/mL albumin, biotin-labeled bovine (Sigma-Aldrich) in buffer A+ for two minutes, washed with 40 µL buffer A+, incubated with 20 µL of 0.5 mg streptavidin (Thermo Fisher Scientific) in buffer A+ for two minutes, washed with 40 µL buffer A+, washed with 40 µL buffer B+, incubated with 20 µL of 0.5 nM of the desired folded DNA origami structures, which were dissolved in buffer B+, for ten minutes, washed with 40 µL buffer B+ and finally loaded with 20 µL of imager strand in the required concentration. In a final step, the chamber was sealed using two-component epoxy glue (Toolcraft, Conrad Electronic SE, Germany). We verified the final concentration of fluorescently labeled ssDNA by confocal FCS measurements (see Supplementary Fig. A.1).

Measurement of the ligand concentration

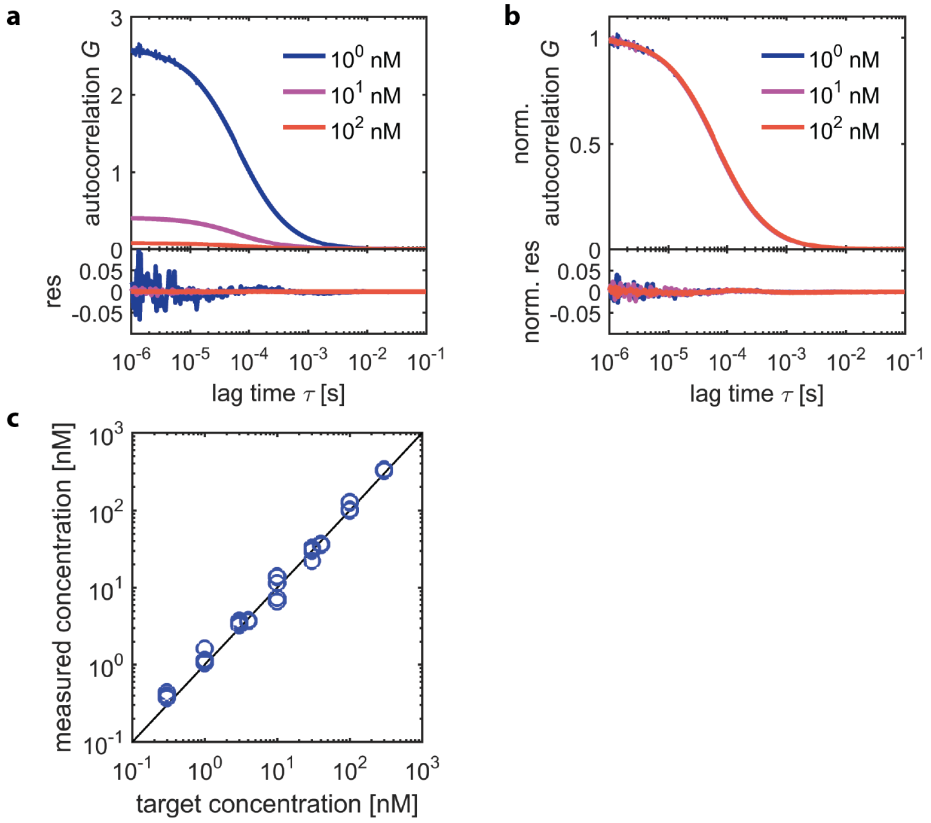

Figure A.1: caption on next page.

Figure A.1: Direct measurement of the ligand concentration. To validate that the target concentration of ligand is indeed reached in the sample, we performed confocal FCS measurements on a commercial LSM 780 Confocor3 system (Zeiss AG, Oberkochen, Germany). As we were interested in the concentration of imager strand in solution, we positioned the confocal volume 30 µm above the origami-coated surface. In an initial measurement, the confocal volume was calibrated using Alexa546NHS (ThermoFisher) and its reported diffusion coefficient $D = 341\,\mu m^2/s$ at 22.5 °C [Petrášek and Schwille, 2008]. As our experiments were carried out at 27 °C, we adjusted the diffusion coefficient using the well-known relation $D \sim \frac{T}{\eta(T)}$ and an empirical expression for the temperature dependence of the viscosity η of water [Kestin et al., 1978]. We ensured that the autocorrelations had no bleaching or triplet contributions by performing identical measurements at a wide range of irradiances (data not shown). Therefore, the correlation curves could be fitted by a simple 3D diffusion model function: $G(\tau) = N^{-1}\left(1+\frac{\tau}{\tau_D}\right)^{-1}\left(1+\frac{\tau}{S^2\tau_D}\right)^{-\frac{1}{2}}$. Here, N is the average number of particles in the detection volume and the diffusion time τ_D is defined as the ratio of the square of the e^{-2}-value of the Gaussian detection volume and the four-fold diffusion coefficient $\tau_D = \frac{w_{xy}^2}{4D}$. The structure parameter S represents the ratio of axial to lateral extension of the Gaussian-shaped detection function. The concentrations are directly obtained from the amplitude of the correlation curves: $c = N\left(\pi^{\frac{3}{2}} w_{xy}^3 S\right)^{-1}$. Fig. A.1a shows three representative correlation curves, their corresponding fits and the residuals. As expected, the amplitude scales with the concentration. Nonetheless, the investigated concentrations do not have an effect on the diffusion of ligand itself as the correlation curves become indistinguishable when normalized by the amplitude at zero lag time (Fig. A.1b). For the range of measured concentrations the target concentration and the measured concentration coincide within 10 % (Fig. A.1c). As a byproduct, we obtained the diffusion coefficient of the labeled 10 nt ssDNA strand in the specified buffer (B+) at 27 °C: $D = (205.2 \pm 7.9)\,\mu m^2/s$, which is in good agreement with a previously reported results [Stellwagen et al., 2003]. The presented numbers correspond to mean and standard deviation of 51 measurements, each of them at least 10 min long.

B

APPENDIX TO CHAPTER III - PHOTO-INDUCED DEPLETION OF BINDING SITES

B.1 Materials and Methods

Origami Purification

DNA origami nanostructures were synthesized as described previously [Schnitzbauer et al., 2017] and subsequently PEG purified. Folded DNA origami structures were mixed 1:1 (v/v) with 2x PEG purification buffer (PEG-8000 15 % (w/v), 500 mM NaCl, 1x TE buffer), centrifuged for 30 min at 17,900 rcf and 4 °C. The supernatant was removed and the DNA origami resuspended in folding buffer (12.5 mM $MgCl_2$, 10 mM Tris, 1 mM EDTA at pH 8.0) by shaking and heating for 5 min at 600 rpm and 30 °C. Previously described steps were repeated two times to increase the purification. Finally, DNA origami nanostructures were stored at −20 °C until use. The assembly of DNA origami nanostructures was confirmed using DNA-PAINT microscopy (Figure IV.2 and Figure IV.7). Origami structures exposed the docking sequence 5'-TTATACATCTA-3', consisting of a TT-spacer followed by nine nucleotides complementary to the imager sequence.

Buffers

For simplicity, we name the used buffers A+ and B+. Buffer A+ contains 10 mM Tris-HCl, 100 mM NaCl, 0.05 % (v/v) Tween20. Buffer B+ contains 5 mM Tris-HCl, 10 mM $MgCl_2$, 1 mM EDTA, 0.05 % (v/v) Tween20. Enyme buffer for the PO+C oxygen scavenging systems consists of 10 mM Tris pH 7.5, 50 mM KCl and 20 % glycerol for better stability

of the stock solutions.

Fluorescent Imager Solutions

Labeled imager strand solutions were used in varying target concentrations (10, 30, 100, 300 or 600 nM) in five conditions:

1. 'Conventional', as employed previously [Schnitzbauer et al., 2017, Mücksch et al., 2018] with the sequence 5'-CTAGATGTAT-3'-Cy3B (Eurofins SAM, Ebersberg, Germany) [Cooper et al., 2004];

2. 'Oxygen scavenger'

   (a) PO+C, as (1) but incubated for 1 hour prior to measurement with the PO+C oxygen scavenger system (1x PO, 1x C, 0.8 % Glucose as described in [Sonal et al., 2019]), with 1x Trolox added. Stock solutions: 100x PO solution consists of 26 mg of PO (P4234-250UN, Sigma-Aldrich Chemie GmbH, Taufkirchen, Germany), 684 µL of enzyme buffer; 100x C solution consists of 2 mg Catalase in 1 mL enzyme buffer. Both were centrifuge filtered (Ultrafree MC-GV, Merck KGaA, Darmstadt, Germany; 0.22 µm), flash frozen in liquid nitrogen and stored at −80 °C; 100x Trolox solution consists of 100 mg of Trolox (Sigma-Aldrich 238813-1G), 430 µL of methanol and 345 µL of NaOH (1 M) in 3.2 mL of H_2O, stored at −20 °C);

   (b) PCD+PCA, as (1) but incubated for 1 hour prior to measurement with the PCD+PCA oxygen scavenger system (1x PCD, 1x PCA, 1x Trolox), as described in [Schnitzbauer et al., 2017]. Stock solutions: 40x PCA solution consists of 154 mg of PCA (37580-25G-F, Sigma-Aldrich) in 10 mL of water, adjusted to pH 9.0 with NaOH; 100x PCD solution consists of 9.3 mg of PCD (P8279-25UN, Sigma-Aldrich) and 13.3 mL of buffer (50 % glycerol stock in 50 mM KCl, 1 mM EDTA and 100 mM Tris–HCl, pH 8.0), Trolox as above, all stored at −20 °C;

3. '18-mer spacer',

   (a) with the sequence Cy3B-5'-GTT ATG GGT GGT TTG GGG-CTAGATGTAT-3' (Eurofins SAM), where the hybridizing nucleotide sequence is identical to (1). Incubation 1:1 at identical concentration with 5'-CCC CAA ACC ACC CAT AAC-3' complementary unlabeled strands forms a stable duplex, increasing the

persistence length of the 18-mer spacer. The fluorescent dye is attached at 5' to maximize the distance of dye and hybridizing nucleotides. The sequence was checked to not form a secondary structure using the Nucleic Acid Package (NUPACK) [Zadeh et al., 2011];

(b) as in (3a) but with PO+C added as in (2a).

Sample Preparation

Sealed sample chambers were prepared as described previously [Schnitzbauer et al., 2017, Mücksch et al., 2018]. In brief, high precision #1.5 coverslips (Paul Marienfeld GmbH, Lauda Königshofen, Germany) were sonicated in acetone (chemical grade, Merck KGaA, Germany) for 10 min and then rinsed twice with ethanol (chemical grade, Merck Millipore, Germany) and water (milli-Q, Merck KGaA, Darmstadt, Germany) and gently dried with pressurized nitrogen. The cleaning of the coverslip was completed by putting a drop of 2-propanol on it (Uvasol, Merck KGaA, Darmstadt, Germany) and wiping with a paper tissue (Kimtech Science, Sigma Aldrich). The same procedure was performed on microscope slides ($76 \times 26\,\mathrm{mm}^2$, Menzel, Thermo Fisher Scientific, Waltham, MA, USA). The high precision coverslip and the microscope slide were assembled into a flow chamber by gluing them together with double-sided sticky-tape (Scotch, Conrad Electronic SE, Hirschau, Germany), yielding a roughly $5 \times 22 \times 0.08\,\mathrm{mm}^3$ large chamber. For DNA-PAINT unspecific binding between origami structures is easily detected in the final image and thus glass surfaces were used without prior cleaning. In a series of volume exchanges, the flow chamber was first incubated with 20 µL of 1 mg/mL albumin, biotin-labeled bovine (Sigma-Aldrich) in buffer A+ for two min, washed with 40 µL buffer A+, incubated with 20 µL of 0.5 mg/mL streptavidin (Thermo Fisher Scientific) in buffer A+ for two min, washed with 40 µL buffer A+ and washed with 40 µL buffer B+.

For DNA-PAINT imaging, 20 µL folded DNA origami solution, diluted 1:200 from PEG purified solution in B+ buffer, were incubated for five min. For SI-FCS, 20 µL folded DNA origami solution, diluted 1:20 from PEG purified solution in B+ buffer, were incubated for ten min. Chambers were washed with 40 µL buffer B+ and finally loaded with 20 µL of imager solution in the required condition (10 µM for DNA-PAINT imaging). In a final step, the chamber was sealed using two-component epoxy glue (Toolcraft, Conrad Electronic SE) or picodent twinsil 22 two component glue (picodent, Wipperfuerth, Germany). We verified the final concentration of fluorescently labeled ssDNA by confocal FCS measurements.

DNA-PAINT Microscopy Setup

DNA-PAINT imaging was carried out on an inverted custom-built microscope in an objective-type TIRF configuration with an oil-immersion objective (UAPON, 100x, NA 1.49, Olympus Europe, Hamburg, Germany). Fluorophores were excited with a DPSS laser with a wavelength of 561 nm (output power 1 W, DPSS-system, MPB Communications Inc., Montreal, QC, Canada). Laser power was adjusted by polarization rotation with a half-wave plate (WPH05M-561, Thorlabs, Dachau, Germany) before passing a polarizing beam-splitter cube (PBS101, Thorlabs). To spatially clean the beam-profile the laser light was coupled into a single-mode polarization-maintaining fiber (P3-488PM-FC-2, Thorlabs) using an aspheric lens (C610TME-A, Thorlabs). The coupling polarization into the fiber was adjusted using a zero-order half wave plate (WPH05M-561, Thorlabs). The laser light was collimated after the fiber using an achromatic doublet lens (AC254-050-A-ML, Thorlabs) resulting in a collimated beam of ∼6 mm full-width at half-maximum (FWHM). The laser beam was magnified by a factor of 2.5 using a telescope custom-built from two achromatic doublets (AC254-030-A-ML and AC508-075-A-ML, both Thorlabs). The excitation light was finally focused in the objective's back focal plane using an achromatic doublet lens (AC508-180-A-ML, Thorlabs). Fluorescence light was separated from the excitation by a dichroic beam splitter (F68-785, AHF Analysentechnik, Tübingen, Germany) directly below the objective, spectrally filtered with an emission filter (605/64, AHF Analysentechnik). The signal from the sample was finally imaged on a sCMOS camera (Zyla 4.2, Andor Technologies, Belfast, UK) without further magnification (TTL180-A, Thorlabs) resulting in an effective pixel size of 130 nm (after 2×2 binning). Microscopy samples were mounted on an x-y-z stage (S31121010FT and FTP2050, both Advanced Scientific Instrumentation, Eugene, OR, USA) used for focusing and laterally moving the sample with the microscope objective fixed in position.

DNA-PAINT Image Acquisition

DNA-PAINT super-resolution data was acquired with a sCMOS camera using µManager [Edelstein et al., 2010]. Acquisition parameters were: full chip 2×2 pixel binning, read out rate 200 MHz and dynamic range 16-bit. The exposure time was set to 200 ms, resulting in a camera frame rate of 5 Hz and in ∼83 min of total measurement time. The excitation power was set to 22 mW behind the objective with a Gaussian shaped illumination with a $1/e^2$-width of 84 µm, resulting in a peak irradiance of 0.2 kW/cm^2.

DNA-PAINT Data Analysis

Super-resolved DNA-PAINT images were computed with Picasso according to [Schnitzbauer et al., 2017]. Binding events were localized by Gaussian least-square fitting with a net gradient chosen to suppress localizations of noise. Localizations were drift corrected in a three-step process, first by redundant cross-correlation (RCC) [Schnitzbauer et al., 2017, Wang et al., 2014], subsequently based on picked DNA origami and finally based on picked individual docking sites. To generate subsets, the drift corrected localizations were split in subsets of 5000 frames each with a custom-written Python script and finally rendered individually. Super-resolved images were rendered blurring individual spots based on the global localization precision. To analyze bright and dark times, origami structures were picked (Picasso: 'pick similar') and further analyzed by a custom-written Python script (https://github.com/DerGoldeneReiter/qPAINT) acting on Picasso's 'Picked localization' files. Dark times of one frame were ignored to reduce artifacts caused by single missed localizations. For docking site analysis picked origami structures were averaged (translation and rotation) to a designed model structure using the 'average3' module of Picasso with a pixel oversampling of 40, setting a custom symmetry of 180 degrees [Strauss et al., 2018]. All individual docking sites were picked on the average image (Figure IV.8) in the render module of Picasso. 'Unfold' translates the picks of the average back to the individually picked structures and thus, picks of the individual docking sites on every origami structure are obtained. After counting the localizations of each picked single docking site, a lower cut-off value (three localizations) was used to identify active individual docking sites. Dividing the number of the active docking sites by the number of the originally picked origami structures used for averaging yields the average number of docking sites per origami.

SI-FCS TIRF Microscope

DNA-PAINT and SI-FCS time series were recorded on a custom-built TIRF microscope, constructed around a Nikon Eclipse Ti-S body as described previously [Mücksch et al., 2018]. Fluorescence was excited by 561 nm diode-pumped solid state (DPSS) laser (Cobolt Jive, 50 mW nominal, Hübner GmbH & Co. KG, Kassel Germany), spatially filtered by a single-mode fiber (kineFLEX-P-3-S-405.640-0.7-FCS-P0 and kineMATIX, Qioptiq, Hamble, UK), collimated ($f = 25\,\mathrm{mm}$, all standard achromats, Edmund Optics, Karlsruhe, Germany), linearly polarized (CCM1-PBS251/M, Thorlabs) and three-fold magnified ($f = -25,75\,\mathrm{mm}$). The TIRF angle was controlled by translating the focus ($f = 225\,\mathrm{mm}$) of

the excitation beam by means of a piezo-electric stage (Q545, Physikalische Instrumente, Karlsruhe, Germany) in the back focal plane of the objective (Nikon SR Apo TIRF, 100x magnification, 1.49 numerical aperture (NA), Nikon, Düsseldorf, Germany).

Fluorescence emission was separated from the excitation (zt405/488/561/640rpc flat, AHF Analysentechnik, Tübingen, Germany) before entering the microscope body. The image on the camera-port was relayed on an electron-multiplying charge-coupled device (EMCCD) camera (iXon Ultra 897, Andor Technologies) by an additional 4f telescope ($f = 200\,\mathrm{mm}$, AC254-200-A-ML, Thorlabs). Laser emission was attenuated and synchronized with the camera acquisition by an acousto-optical tunable filter (TF-525-250, Gooch & Housego, Torquay, UK), which was interfaced through a PCI Express card (PCIe-6323 and BNC-2110) and controlled with a custom LabView 2011 software (all National Instruments, Austin, TX, USA). The emission light was additionally band-pass filtered (593/46).

Drifting of the focus position was eliminated by a custom-built focus stabilization. A near-infrared laser (LP785-SF20, Thorlabs) was totally internally reflected from the glass-water interface of cover-slide and sample. The beam position was monitored on a CMOS camera (UI-3240CP-NIR-GL, Imaging Development Systems, Obersulm, Germany). A feedback control implemented in LabVIEW 2015 (National Instruments) maximized the cross-correlation of the images of the laser spot and a reference image, respectively. The axial sample position was adjusted every 200 ms accordingly (P737.2SL and E-709.SRG, Physikalische Instrumente). The sample and objective were temperature stabilized to 23 °C. (H101-CRYO-BL stabilization unit, with H101-MINI sample chamber and OKO-MOC objective stabilization, Okolab, Ottaviano, Italy).

SI-FCS Image Acquisition

Images were recorded using the Andor Solis software (Andor Technologies, Version 4.28) with 4×4 hardware binning as 64×64 pixel images for 1.5 million frames, as described previously [Mücksch et al., 2018], resulting in $\sim 5\,\mathrm{h}$ total measurement time. The exposure time was 10 ms, resulting in a camera frame rate of 85 Hz. The excitation power was set to 0.75 mW behind the objective, with a Gaussian shaped illumination with a $1/e^2$-width of 51 µm, resulting in a peak irradiance of $0.018\,\mathrm{kJ/cm^2}$. The EMCCD camera was used with electron multiplying gain, adapted according to the brightness of the sample.

SI-FCS Data Analysis

The autocorrelation curves were computed and analyzed using a custom-written Matlab 2017a (The MathWorks, Natick, MA, USA) software, described previously [Mücksch et al., 2018]. Intensity traces were generated by additional 8×8 software binning, resulting in 5.12 µm effective integrated area size, representing 32×32 native camera pixel. The signal in each pixel was integrated, yielding 64 intensity traces, which were bleach and drift-corrected by a single exponential, and individually correlated using the multiple-τ algorithm [Schätzel, 1987], in which we doubled the bin width after every sixteenth point in the autocorrelation curve. The obtained autocorrelation curves were fitted individually by a single exponential decay with an offset, from which the amplitude and the characteristic decay time were obtained. Similar to [Mücksch et al., 2018], concentrations above 100 nM were fitted with a bi-exponential to account for the second component originating from depletion of docking sites.

Direct Measurement of the Concentration of Imager Strands with Confocal FCS

We measured the solution concentrations of imager strands with confocal FCS, as described previously [Mücksch et al., 2018]. In brief, we used a commercial LSM 780 ConfoCor3 system (Zeiss AG, Oberkochen, Germany) with the confocal volume positioned 40 µm above the cover slide. We calibrated the confocal volume using Alexa546NHS (Thermo Fisher) and its reported diffusion coefficient $D = 341\,\mu m^2/s$ at 22.5 °C [Petrášek and Schwille, 2008]. We calculated the corresponding diffusion coefficient at the measurement temperature (26.5 °C to 27 °C) using the well-known relation $D \sim \frac{T}{\eta(T)}$ and an empirical expression for the temperature dependence of the viscosity η of water [Kestin et al., 1978]. We applied a simple 3D diffusion model function:

$$G(\tau) = N^{-1} \left(1 + \frac{\tau}{\tau_D}\right)^{-1} \left(1 + \frac{\tau}{S^2 \tau_D}\right)^{-\frac{1}{2}} , \tag{B.1}$$

as justified previously [Mücksch et al., 2018]. Here, N is the average number of particles in the detection volume, $\tau_D = \frac{w_{xy}^2}{4D}$ the diffusion time, with w_{xy} being the e^{-2}-value of the Gaussian detection volume and S the structure parameter. Concentrations are directly obtained from the amplitude of the correlation curves: $c = N \left(\pi^{\frac{3}{2}} w_{xy}^3 S\right)^{-1}$. As diffusion coefficient, we measured $D_{\text{conv}} = (201 \pm 5)\,\mu m^2/s$ ($n = 8$), in agreement with previously reported

results [Mücksch et al., 2018, Stellwagen et al., 2003] and $D_{18-\text{mer spacer}} = (120 \pm 20)\,\mu\text{m}^2/\text{s}$ ($n = 4$) for the 18-mer spacer. The presented numbers correspond to mean and standard deviation of the indicated n measurements, each of them at least 20 min long.

Simulation of Bright and Dark Times

Simulations of the bright and dark time distributions were generated with COPASI [Hoops et al., 2006]. Biochemical parameters for the simulation were: Mass action irreversible ($A + B \rightarrow C$, $C \rightarrow A + B$), $k_a = 1.5 \times 10^6/(\text{M}\,\text{s})$, $k_d = 0.3/\text{s}$ with varying number of initial species values ($B = 12, 10, 8, 6, 4$) corresponding to single dockings sites and fixed imager concentration of $\langle A \rangle = 10\,\text{nM}$. Time course simulations were performed with the same interval spacing (0.2 s) and total acquisition time (17 min per time segment) used in the DNA-PAINT image acquisitions. Obtained traces were analyzed analogous to experimental data using a custom-written Python script (`https://github.com/DerGoldeneReiter/qPAINT`).

Supplementary Materials

Raw data for DNA-PAINT, confocal FCS and SI-FCS experiments is available for download from: `https://dx.doi.org/10.17617/3.1v.`

C

APPENDIX TO CHAPTER V - DIRECT CHARACTERIZATION OF THE TIRF EXCITATION

C.1 Materials and Methods

Monte Carlo Simulation

Monte Carlo simulations for the combination of solution diffusion and binding were performed as previously described in [Mücksch, 2018,Ries et al., 2008a]. In brief, we performed simulations in Matlab (R2017a, The MathWorks, Natick, MA) with $\Delta t = 1\,\mathrm{ms}$ time steps, an integration time of $\Delta t_{\mathrm{cam}} = 10\,\mathrm{ms}$ and $N = 7.2 \times 10^6$ iterations. The box size of the simulation exceeded the lateral integration size by a factor 15 and the evanescent field by a factor of 20. In brief, particles were randomly displaced in every time step. Different from [Ries et al., 2008a], bound molecules were surface-immobilized ($D_{\mathrm{C}} \to 0$). Binding of molecules was simulated by evaluating the binding probability $P_{\mathrm{bind}} = 1 - \exp\left(\frac{k_a \langle B \rangle \Delta t}{d_{\mathrm{at}}}\right)$ for molecules with a distance to the surface smaller than $d_{\mathrm{at}} = \sqrt{2 D_{\mathrm{A}} \Delta t}$, with $\langle B \rangle$ being the mean concentration of unoccupied binding sites. If a random number $\in (0, 1)$ (Mesenne Twister, Matlab RandStream Class, [Matsumoto and Nishimura, 1998]) was smaller than P_{bind}, the molecule was converted in a bound molecule. Similarly, bound molecules were converted into freely diffusing molecules with the probability $P_{\mathrm{unbind}} = 1 - \exp(-k_d \Delta t)$. The molecule detection function including the effect of SAF was calculated as described in [Mücksch, 2018, Ries et al., 2008a].

Parameters of the simulation were: $\langle A \rangle = 10\,\mathrm{nM}$, $D_{\mathrm{C}} = 200\,\mu\mathrm{m}^2/\mathrm{s}$, $k_d = 10/\mathrm{s}$, $k_a = 5 \times 10^6/(\mathrm{M\,s})$, $d_{\mathrm{ev}} = 100\,\mathrm{nm}$, $a = 4.8\,\mu\mathrm{m}^2$, binding site density $S = 20.3/\mu\mathrm{m}^2$, NA = 1.46, $n_1 = 1.33$, $n_2 = 1.52$ and $\lambda_0 = 580\,\mathrm{nm}$.

C.2 Dip Coating Setup

Figure C.1 shows the custom-built setup used for dip coating coverslides with thin polymer layers. A motorized precision linear stage (1; LTM 45-50-HiSM, OWIS GmbH, Staufen, Germany) is mounted vertically on a solid base plate (2). A position control unit (3; PS10-32, OWIS GmbH, Staufen, Germany) drives the stage. Coverslides are placed into a custom 3D-printed mount (4) and dipped into a cuvette (5; Makro-Küvette 6030-OG, Hellma GmbH, Müllheim, Germany) containing the dip coating solution. CAD files of the 3D-printed parts are available upon request.

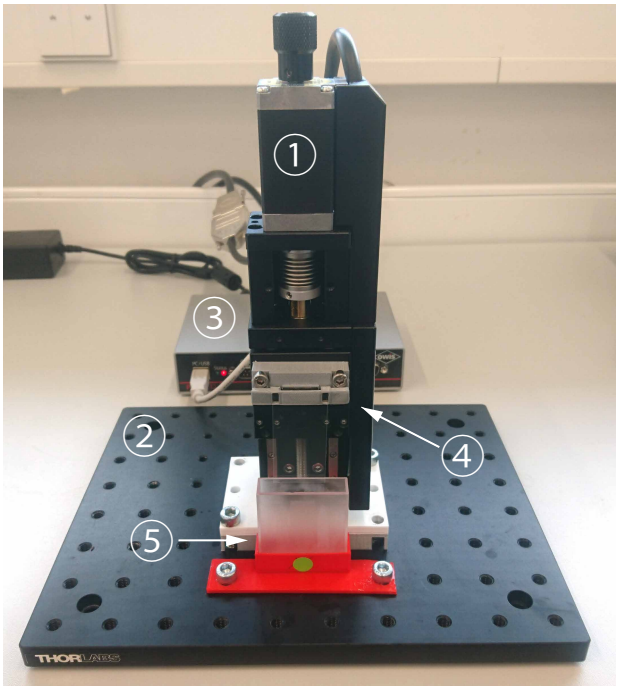

Figure C.1: Dip coating setup. A motorized precision linear stage (1) is mounted vertically on a solid base plate (2). A position control unit (3) drives the stage. Coverslides are placed into a custom 3D-printed mount (4) and dipped into a cuvette (5) containing the dip coating solution.

C.3 Supplementary Studies on Polymer Properties

Here, we present further studies on the physical properties of the thin polymer layers. Figure C.2a assesses the shelf-life of the calibration slides. AFM height distributions of the same slide recorded two months apart and with multiple washing steps in between show no change in the polymer layer thickness, with an initial thickness of 45.6 nm ± 2.3 nm, and a revisited slide thickness of 47.6 nm ± 2.1 nm, as determined by the distance of Gauss peak centers and their combined standard deviation. The absence of any signs of deterioration over time, and especially the chemical and mechanical stability against washing the calibration slides with commonly used solvents (e.g. isopropyl alcohol, ethanol, purified water) suggest a long shelf-life and the reusability of the calibration slides.

Access to the original glass surface for measuring the polymer layer thickness was created by scratching the polymer coating with a scalpel. In order to ensure the integrity of the glass surface, as well as the thorough removal of polymer in the scratched trench, an AFM image of the beginning of the scratch at the transition from coverslide surface to the coating was recorded (Figure C.2b). No signs of damage to the coverslide surface are observed. Furthermore, the complete removal of polymer material is inferred by equal height levels of the uncoated glass surface and the formerly coated surface in the trench. Conclusively, scratching the surface with a scalpel is a reliable method to uncover the glass surface.

Autofluorescence of the polymer was characterized by comparing the fluorescence intensity of a blank coverslide covered with pure water to the fluorescence intensities of a dip coated coverslide with a 200 nm thick polymer coating, covered with pure water, and covered with dye in aqueous solution (Figure C.2c). For the chosen laser settings with a peak irradiance of 15 W/cm^2 at an excitation wavelength of 491 nm), and a concentration of 5 µM Alexa Fluor 488 dye in aqueous solution, additional autofluorescence caused by the polymer coating is negligible compared to the fluorescence emission of the dye in aqueous solution.

Possible applications of the presented calibration slide may involve (single-molecule) experiments where the probed regions are small compared to the regions being probed in this work. Therefore, a representative high-resolution AFM image of a 2 µm × 2 µm area of the polymer surface, with a pixel size of 15.6 nm × 15.6 nm, and the associated probability density are shown in Figure C.3. A Gaussian fit to the probability density reveals a standard deviation of 0.22 nm around the mean height. The RMS surface roughness is

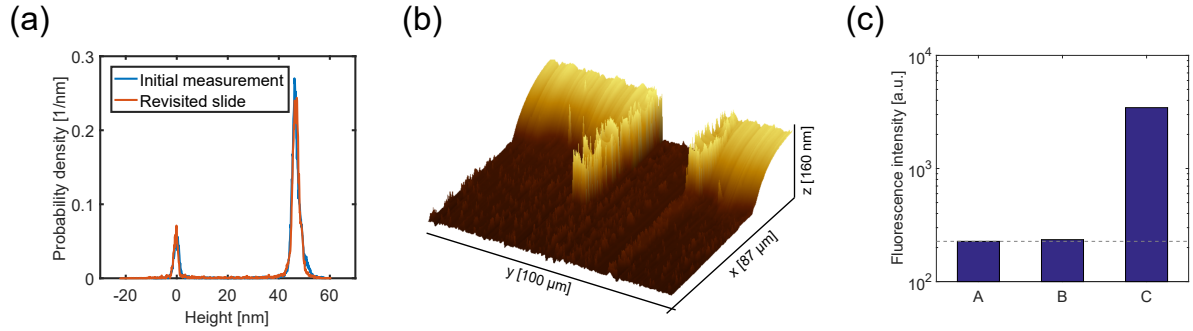

Figure C.2: (a) Shelf-life of the calibration slides. AFM height distributions of the same slide recorded two months apart and with multiple washing steps in between show no change in the polymer layer thickness, with the initial thickness determined as 45.6 nm ± 2.3 nm, and the revisited slide thickness of 47.6 nm ± 2.1 nm (distance of Gauss peak centers ± combined standard deviation). (b) Uncovering of the glass surface by scratching the coating. An AFM image of the beginning of the scratch at the transition from coverslide surface to the coating shows thorough removal of the polymer down to the glass surface. Furthermore, no signs of damage to the coverslide surface are observed. (c) Polymer autofluorescence. Background (dotted line) and (auto-)fluorescence intensities for a blank coverslide covered with pure water (A), and a coverslide with a 200 nm coating covered with pure water (B) and 5 µM Alexa Fluor 488 dye in aqueous solution (C). At a peak irradiance of 15 W/cm^2 at 491 nm and 5 µM Alexa Fluor 488, additional autofluorescence caused by the polymer coating is negligible compared to the dye's fluorescence.

0.34 nm. Both the local variability of the height, as well as the RMS surface roughness suggest excellent applicability of the calibration slide for experiments where highly-precise positioning in the axial dimension is required.

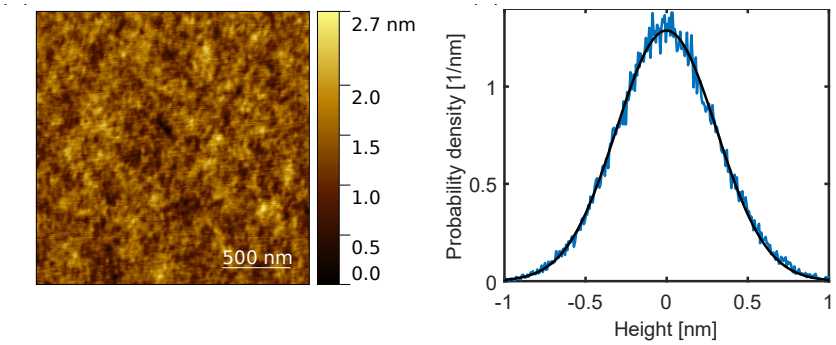

Figure C.3: High-resolution AFM image of the polymer surface. The pixel size of the AFM data is 15.6 nm × 15.6 nm. The probability density of height values around the mean polymer step height is fit with a Gaussian function with a standard deviation of 0.22 nm. The RMS surface roughness is 0.34 nm.

C.4 Lateral Displacement Method

The incident angle θ for a given TIR angle stage position x is determined based on a method shown in Figure C.4a, first presented by T.P. Burghardt [Burghardt, 2012]. A sample of free 5 µM Alexa Fluor 488 dye (Thermo Fisher Scientific Messtechnik GmbH, Munich, Germany) in aqueous solution is mounted on the objective. A series of images with the sample translated along the z-direction in steps of $\Delta z = 0.1$ µm is acquired ('z-stack'). The large incident angle θ of the excitation beam results in a measurable lateral displacement Δy of the fluorescence excitation spot when the sample is moved axially (Figure C.4b). Lateral displacements Δy_i of the illumination profile are extracted by the displacement of the center position of a 2D Gaussian fit to each image. To ensure reliable and precise fitting, no magnification telescope is used so that the excitation laser beam diameter fits well into the field of view. Figure C.4c shows the lateral displacement of the centroids in y-direction for different TIR angle stage positions x. A linear fit $f(z) = mz + c$ to the dependence of Δy on Δz directly gives the incident angle via $\theta = \arctan(m)$, as shown in Figure C.5.

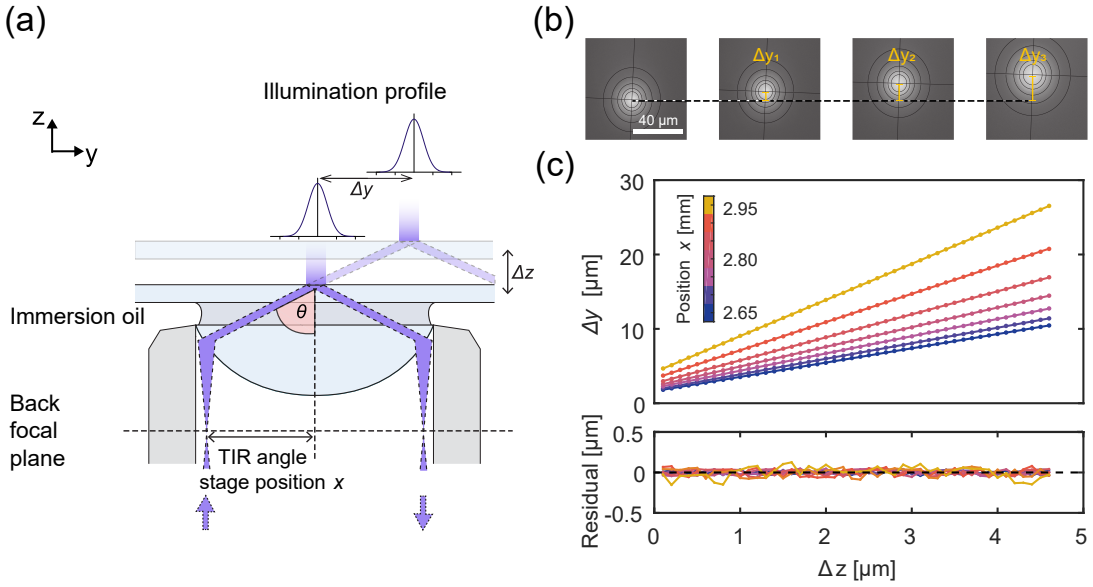

Figure C.4: (a) Lateral displacement method. A sample of free dye is mounted on the objective. The large incident angle θ results in a lateral displacement Δy of the fluorescence excitation spot when the sample is moved axially. (b) Displacement of the illumination profile. Lateral displacements Δy_i of the illumination profile are extracted by 2D Gaussian fits to each image during a z-stack. (c) Linear fit to lateral displacement data. The lateral displacement of the centroids in y-direction during a 4.5 µm z-stack with 0.1 µm step size is shown for different TIR angle stage positions x. Linear fits to the data directly give the incident angles.

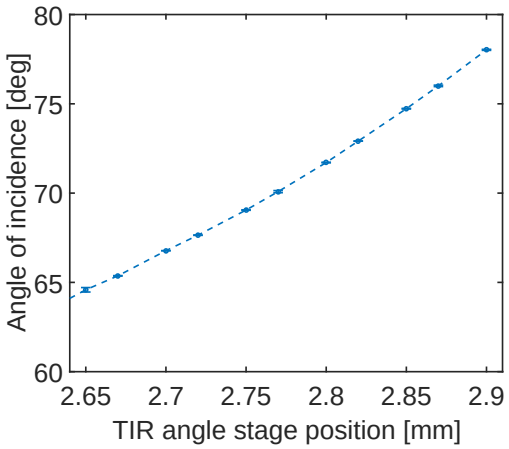

Figure C.5: Look-up-table for relating TIR angle stage positions x to the incident angle θ. Incident angles were determined with the lateral displacement method with an angular precision of 0.1°. Data correspond to mean and standard deviation of triplicate measurements.

C.5 Supplementary Studies on Evanescent and Non-evanescent Contributions

For excitation laser beam diameters small compared to the field of view of the TIRF microscope, a spatial separation of excitation field contributions with increasing polymer layer heights is observed (Figure C.6). 2D illumination profiles are fitted with 2D Gaussian functions $g_i(x,y) = A_i \exp\left(-\left[(x-x_{0,i})^2/2\sigma_{x,i}^2 + (y-y_{0,i})^2/2\sigma_{y,i}^2\right]\right)$, with coefficients A the amplitude, $x_{0,i}$, $y_{0,i}$ the center positions and $\sigma_{x,i}$, $\sigma_{y,i}$ the x and y widths. The fits are assisted by using the center positions and widths of a single 2D Gaussian fit to the TIRF image of free dye on an uncoated coverslide as the initial fit coefficients for the stationary field contribution. Figure C.6b and c show center positions and widths of the two 2D Gaussian fit functions. The center positions and widths of the two 2D Gaussian fits to the illumination profiles separate into two groups, with the one effectively stationary with constant widths for all step heights, and the other one being displaced laterally and becoming wider for increasing step heights. This behavior can be readily explained when identifying the two groups with evanescent and non-evanescent contributions. The evanescent field, with an imaginary k-vector in axial direction and zero lateral components, decays exponentially but otherwise remains unchanged for all sampled heights. Non-evanescent contributions, however, with non-zero real lateral k-vector components predominantly in one direction, produce increasingly laterally displaced fluorescence intensity profiles as the sampled height increases.

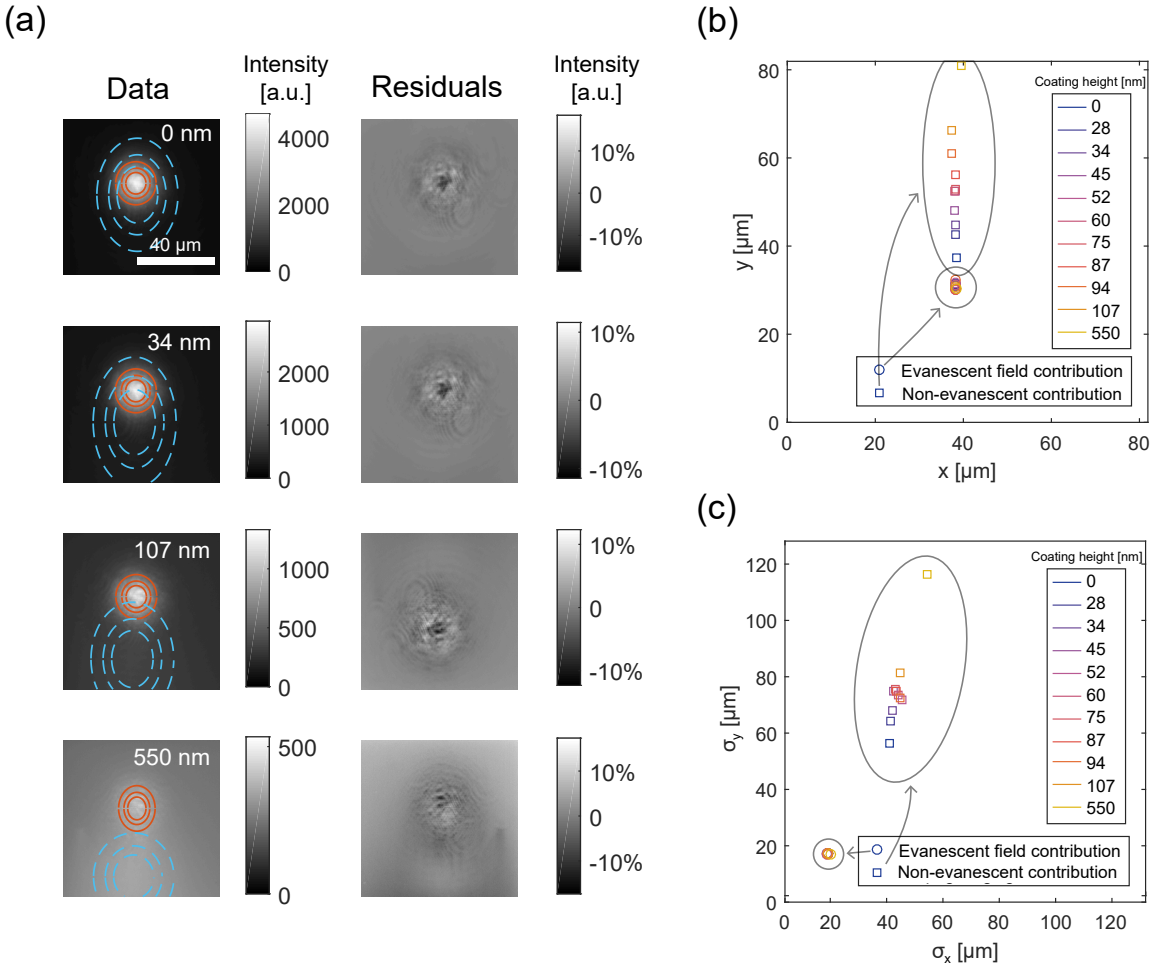

Figure C.6: (a) 2D Gaussians fits of spatially separating excitation field contributions. Left column: TIRF images of free dye above polymer layers of different height show a rapid decay as the step height increases. Illumination profiles were fit with two 2D Gaussian functions (solid orange and dotted blue rings, corresponding to 1/2, 1/4 and 1/8 of the 2D Gaussian fits' width). Right column: Residuals of the 2D Gaussian fits to the experimental data. Mean absolute residuals are below 5% of the respective amplitudes. (b – c) Center positions and widths of the two 2D Gaussian fit profiles. The center positions and widths of the two 2D Gaussian fits to the illumination profiles separate into two groups, with the one effectively stationary with constant widths regardless of the step height, and the other being displaced laterally and becoming wider for increasing step heights, suggesting evanescent and non-evanescent character respectively.

D

APPENDIX TO CHAPTER VI - QUANTIFICATION OF MEMBRANE BINDING

D.1 Materials and Methods to Section VI.2

D.1.1 Materials

Buffers

Origami Buffer B, same as B+ (Section B.1, p. 271), but without the addition of Tween-20. Buffer B contains 5 mM Tris-HCl, 10 mM $MgCl_2$, 1 mM EDTA and is adjusted to pH 8.

SLB buffer (Tris) contains 150 mM KCl and 25 mM Tris-HCl adjusted to pH 7.5.

Piranha solution, a mixture of seven drops sulfuric acid (98%) and two drops 50% hydrogen peroxide. The solution was mixed directly on the coverslip. Take precautions, as sulfuric acid is strongly acidic and sulfuric acid and hydrogen peroxide are corrosive. Work in a protected environment (fume cupboard) with proper protective equipment only.

Lipids

Lipid mixtures were prepared from stock solutions dissolved in chloroform. DOPC (Catalog No. 850375, Avanti Polar Lipids Inc., Alabaster, AL) was either used pure or doped with lipids with fluorescently labeled head groups to assess membrane quality in TIRF microscopy. Labeled phospholipds were Atto-488-DOPE or Atto-655-DOPE (AD 488-161 and AD 655-161, ATTO-TEC GmbH, Siegen, Germany) used at molar concentrations of 0.1 % or 0.05 %.

ssDNA imager strands

P1 imager strands were identical to Chapter B.1 (p. 272) with oxygen scavenger PO+C added.

TIRF and SI-FCS Microscopy Setup

For TIRF microscopy and SI-FCS we used the setup described above (Section A.1, p. 263 and B.1, p. 275). A detailed description can also be found in [Mücksch, 2018]. Additionally to the three-fold beam expansion ($f = -25,75\,\mathrm{mm}$) we implemented an exchangeable ten-fold beam expansion in order to offer a close to homogeneous illumination of the field of view ($f = -10,100\,\mathrm{mm}$, replaceable with kinematic mount: KB25/M, Thorlabs GmbH, Dachau, Germany). The resulting TIR excitation is characterized in Figure V.5 (p. 107) for both telescopes.

To check and optimize the setup stability, we monitored the excitation power (i) as back-reflected from the acousto optical tunable filter (AOTF) before fiber coupling (Area I, Figure A.1, p. 264), (ii) reflected from a polarizing beam splitter cube (CCM1-PBS251/M, Thorlabs) inserted in between lens L.II.1 and M.II.1 (Figure A.1), and (iii) totally internally reflected excitation from the glass-sample interface, passing back through the excitation optics until arriving with a lateral offset at mirror M.II.3 (Figure A.1) and being partially reflected from a pick-up mirror. In all three positions the power could be recorded simultaneous to the SI-FCS measurement.

Compared to Section B.1 (p. 275), the dectection pathway was extended with a two-color detection, allowing to image two separate spectral channels on one respective half of the camera chip [Mücksch, 2018]. In brief, mirrors on motorized stages (LTM 45-40-HiSM, controller PS10-32, OWIS GmbH, Staufen i. Br., Germany) directed the clipped excitation light (anodized razor blades) to a $4f$-telescope ($f = 300\,\mathrm{mm}$, AC254-300-A-M, Thorlabs). A dichroic beamsplitter (T550LPXR, Chroma, obtained from AHF Analysetechnik AG, Tübingen, Germany) separated the two channels. Both channels were individually band-pass filtered and projected with help of a right angle prism mirror (MRA25-P01, Thorlabs) alongside onto the EMCCD camera chip. Emission filters used with the excitation wavelengths 491 nm, 561 nm and 640 nm were 525/50, 593/46 (both Semrock BrightLine HC) and 670/30 ET (Chroma, all obtained from AHF Analysetechnik AG), respectively. For dual-channel detection we observed small reflections passing the excitation filters, that were additionally blocked by a quad-notch (NF03-405/488/561/635E-25, Semrock, obtained from AHF Analysetechnik AG) mounted directly on the camera C-mount. Optionally, a short-pass filter (775/SP Bightline HC, Semrock, obtained from AHF Analystechnik AG) additionally filtered remaining light from the focus stabilization ($\lambda_{\mathrm{stabilization}} = 785\,\mathrm{nm}$).

D.1.2 Preparation of Homogeneous SLBs from SUVs

Preparation of SLBs on microscopy glass coverslips by fusion of SUVs is described in detail in [Ramm et al., 2018b]. Here, we briefly summarize the preparation protocol.

Preparation of SUVs In brief, SUVs were formed from lipid mixtures dissolved in chloroform and dried first under N_2 flow and subsequently in vacuum for at least 30 min. The lipid film was rehydrated in SLB buffer to a lipid concentration of 4 mg/mL and subsequently vortexed. After 7-10 freeze-thaw cycles switching from liquid N_2 to water at 70 °C to 90 °C lipid aggregates and multilamellar structures are broken and the solution turns from opaque to clear. Vesicles were extruded 35-41 times through a membrane (50 µm pore size, Avanti mini extruder, Avanti Polar Lipids Inc.) and stored aliquoted (20 µL) at −20 °C until further use.

Preparation of SLB chambers Glass coverslips (#1.5 high precision, $22 \times 22\,\mathrm{mm}^2$, Paul Marienfeld, obtained from VWR International GmbH, Darmstadt, Germany) were either cleaned either with piranha solution or by means of an oxygen plasma.

For piranha cleaning, 7 drops of sulfuric acid and 2 drops of hydrogen peroxide were placed on the coverslip and incubated for at least 45 min. (Take precautions as piranha solution is strongly acidic and corrosive.) Piranha solution was subsequently washed off extensively with ultrapure water (Millipore, Merck Millipore) and dried under N_2 stream.

For plasma cleaning the coverslips were polished with a soft paper tissue (KIMB7552, Kimberley-Clark, obtained from VWR International GmbH), soaked with ethanol. Coverslips were further rinsed with ethanol and pure water to remove any remaining dust and dried under N_2 stream.

For the SLB chamber, we used the cylindrical part of a low-protein-binding 0.5 mL reaction tube (Protein LoBind Tubes, Eppendorf AG, Hamburg, Germany), cutting off the conical part and the lid. The remaining reaction cylinder was glued top-down on the pre-cleaned coverslip with uv-hardening glue (NOA68, Thorlabs GmbH) and cured under illumination at a wavelength of 360 nm for at least 5 min.

In the case of oxygen plasma cleaning, the assembled chamber was treated with an oxygen plasma (Zepto, Diener electronic GmbH & Co. KG, Ebhausen, Germany, settings: power 30-50%, oxygen pressure: 0.3 mbar, duration: 30-60 s) directly before SLB formation. Proper cleaning steps are crucial for mobile and homogeneous SLB formation (see [Ramm et al., 2018b] for troubleshooting).

SLB formation Thawed SUV solutions were sonicated until the solution appeared clear. SUV aliquots (20 µL at 4 mg/mL) were diluted with 130 µL SLB buffer to a working concentration of 0.53 mg/mL. If SUVs were frozen, they were sonicated again after dilution. Per chamber, 75 µL SUV solution were incubated on the coverslip for 3 min, before adding 200 µL SLB buffer and subsequently washing with additional 200 µL SLB buffer. Each chamber was washed eight more times, such that 2 mL of SLB buffer were used. Finally, the volume in the SLB chamber was adjusted.

D.1.3 Micropatterned SLB by Photolithography of Chromium on Microscopy Coverslides

Formation of Chromium Microarrays

Membrane corrals were formed on chromium patterns formed by metal evaporation and photolithography, as in parts described previously [Seidler, 2017]. Standard microscopy coverslips (#1.5 German Glass) were rinsed with 2-Propanol and water (Millipore, Merck Millipore) prior to oxygen plasma cleaning (Settings: pressure: 0.3 mbar, power: 30-50%, duration: 30-60 s). Bis(trimethylsilyl)amine (HDMS) was used as adhesion promoter and was vapor deposited on the cover slide for 2 min. Positive photo resist (AZ ECI 3027, MicroChemicals GmbH, Ulm, Germany) was spin coated onto the cover slide for 40 s at 4000 rpm with a start/stop acceleration of 2000 rpm/s, resulting in a roughly 3 µm thick layer of photo resist on the coverslip. Coverslips were further pre-baked for 90 s at 90 °C. The patterns were cured using UV lithography (µPG 101, Heidelberg Instruments, Heidelberg, Germany) with a 2 mm write head, 40 mW nominal output power at a wavelength of 375 nm, before passing a 20 % attenuation filter. Slides were subsequently post baked for 60 s at 110 °C before applying developer (AZ 351B, NaOH based, diluted 1:4 (v/v), MicroChemicals GmbH for 4 min. Finally, slides were rinsed with water (Millipore, Merck Millipore) and dried with N_2.

Chromium was evaporated at a rate of $1 - 2$ Å/s resulting in an approximately 30 nm thick chrome layer using an electron beam evaporator in a high vacuum coating plant.

The photoresist was lifted off in acetone with gentle agitation for 5 min in a sonicator (Model 1510, Branson) and rinsed with 2-Propanol.

Formation of Membrane Corrals on Chromium Microarrays

SLBs from DOPC were formed on chromium microarrays after oxygen plasma cleaning as described above (Section D.1.2). The lipid bilayer was labeled with 0.05 % Atto488-DOPE. We added chol-DNA at varying concentrations (Table D.1), by performing two additional washing steps with 150 µL of chol-DNA solution. We incubated chol-DNA staples for 2 min and subsequently washed two times with imaging buffer B. Finally, we added P1 imager strands and oxygen scavenger PO+C in buffer B to achieve the target concentration. The imager and PO+C are described in detail above (Section B.1).

Table D.1: Employed concentrations of cholesterol-DNA handles on chromium grids

Measurement	Cholesterol DNA concentration [nM]	Imager concentration [nM]
1	5	10
2	5	300
3	2	10
4	2	100
5	1	2000
6	1	600

FRAP

We recorded FRAP curves on membrane corrals, by (i) bleaching a 3 µm circular area or (ii) bleaching an entire membrane corral. SLBs were formed from DOPC as described above, with 0.05% Atto655-DOPE as fluorescent label. Fluorescence images were recorded on a commercial confocal laser scanning microscope (CLSM) (LSM 800, Carl Zeiss AG, Oberkochen, Germany) with an excitation and bleaching wavelength of 640 nm.

For the circular area, we recorded automatically 15 consecutive bleaching cycles. After bleaching correction with a linear fit to the fully recovered fluorescence intensity, we averaged all 15 bleaching cycles to obtain a FRAP trace. The resulting FRAP trace was fit with the model

$$F(t) = F_0 + C \exp\left(-\frac{\omega^2}{2Dt}\right)\left[I_0\left(-\frac{\omega^2}{2Dt}\right) + I_1\left(-\frac{\omega^2}{2Dt}\right)\right] \tag{D.1}$$

where $I_\nu\,(\nu = 1, 2)$ denotes the modified Bessel function of first kind [Soumpasis, 1983, Macháň et al., 2016].

For bleaching the entire membrane corral, we monitored the fluorescence of two neighboring membrane corrals and bleached a rectangular ROI covering one corral.

D.1.4 SI-FCS Acquisition and Analysis

SI-FCS Image Acquisition

We acquired SI-FCS image series as described above (Section A.1, p. 265 and Section B.1, p. 276). We recorded images, as before, with 4×4 hardware binning, but here at a resolution of 128×128 pixels, thus acquiring the whole camera chip (512×512 native camera pixels). To limit a spatial modulation of the fluorescence intensity of laterally diffusing molecules of interest, we used the 10x beam expansion of the excitation laser, leading to a width of $\omega_{\mathrm{FWHM}} \approx 150\,\mu\mathrm{m}$ of the illumination profile. We estimated the width based on the magnification compared to the previously characterized 3x beam expansion (B.1, p. 276). The field of view of the camera chip is $82 \times 82\,\mu\mathrm{m}^2$ and thus significantly smaller than the illumination profile.

SI-FCS Data Analysis

We obtained and analyzed fluorescence intensity traces, as described previously (Section A.1, p. 265 and Section B.1, p. 277). For Figures VI.5 and VI.6 we doubled the integrated ROI size from 2 to 128 pixels (corresponding to 8 to 512 native camera pixels or 1.3 µm to 82 µm), resulting in 4096, 1024, 256, 64, 16, 4 or 1 ROI(s). Intensity traces were obtained by integrating the fluorescence intensity within the ROIs.

For Figure VI.9 and VI.10 we generated binary masks to select the areas of surface integration. We time-averaged the image series and performed a thresholding to generate a binary image resembling the chromium grid. As areas covered by chromium appeared dark on the image, we used a thresholding that rather overestimated the size of the membrane corrals. A representative image of the generated binary masks is presented in Figure VI.8B. The thresholding step can be automated for higher throughput in the future. Based on the binary image, the further extraction of intensity traces, autocorrelation and fitting was automated as described above. Different from the monoexponential detrending employed in Chapters III and IV, we used a polynomial detrending before autocorrelation. While for chol-DNA samples with PO+C oxygen scavenging system the choice of the detrending model is of limited importance, we obtained improved results in the case of membrane binding of peptides (Section VI.3).

Polynomial Detrending

We performed a polynomial detrending of the intensity traces obtained from surface integration, as previously performed in TIR-FCS [Macháň et al., 2016]. We found a polynomial of 7th degree to account for minor long-term fluctuations of the intensity trace with unsystematic residuals.

$$I_{\text{corrected}}(t) = I_{\text{initial}}(t)/f(t) \tag{D.2a}$$

$$f(t) = p_1\,t^7 + p_2\,t^6 + p_3\,t^5 + p_4\,t^4 + p_5\,t^3 + p_6\,t^2 + p_7\,t + p_8 \tag{D.2b}$$

If traces showed strong intensity fluctuations, we truncated the traces to intervals with only small fluctuations or discarded them entirely, if the remaining intervals were shorter than 50 min. Corrected traces were checked to show no remaining apparent long-term fluctuations.

D.2 Materials and Methods to Section VI.3

D.2.1 Monte Carlo Simulations of Membrane Binding Without Surface Saturation Effects

Monte Carlo simulations were performed using Python 3.7 and custom-written code. Simulations were modified from previous simulations [Mücksch, 2018]. The time interval in between two simulation steps was $\Delta t = 0.1$ ms, the camera frame rate $\Delta t_{\text{cam}} = 1$ ms. Input parameters to the simulation were the total measurement time t_{tot} and the reaction rates k_{AB}, k_{BA}, k_{BC} and k_{CB} (Figure VI.12, 162). For the two-state system (Section VI.3.1, p. 156), the transition rates of state C, k_{BC} and k_{CB}, were set to zero. The probabilities of the transition were determined by

$$P_{ij} = 1 - \exp(-k_{ij}\,\Delta t)\,, \tag{D.3}$$

where k_{ij} is the transition from state i to j.

In states B and C, bound molecules contributed with the normalized brightness 1 to the total detected signal per iteration. Molecules in state A did not contribute to the signal. In the experimental system, at short lag times, molecules in solution (A) will contribute to the autocorrelation function by diffusion through the detection volume. For longer lag

times, solution diffusion can be assumed equilibrated. Here, we neglect solution diffusion and investigate only the contributions originating from binding.

To simulate molecules binding to the surface, the total number of binding molecules during the simulation was calculated as

$$N_{\mathrm{AB}} = \mathrm{round}\left(k_{\mathrm{AB}}\frac{t_{\mathrm{tot}}}{\Delta t}\right). \tag{D.4}$$

The appearance of the molecules was further randomly distributed over the iterations. As the reservoir of molecules in solution is assumed constant, the binding does only depend on the association rate k_{AB} and is independent of the development of the simulation. For randomization, we used NumPy [Oliphant, 2006, van der Walt et al., 2011] based on the Mersenne Twister pseudo-random number generator [Matsumoto and Nishimura, 1998]. States B and C were initialized as

$$N_{\mathrm{B}} = \frac{k_{\mathrm{AB}}}{k_{\mathrm{BA}}} \tag{D.5a}$$

$$N_{\mathrm{C}} = N_{\mathrm{B}}\frac{k_{\mathrm{BC}}}{k_{\mathrm{CB}}}, \tag{D.5b}$$

to accelerate reaching an equilibrium of binding and unbinding. For each condition, we simulated traces of $t_{\mathrm{tot}} = 6\,\mathrm{h}$ or 2.1×10^8 iterations.

In each time step Δt, we generated a random number $x \in [0, 1)$ for each molecule in state B. If $x < P_{\mathrm{BA}}$ or $x < P_{\mathrm{BC}}$, we transitioned the molecules into the states A or C, respectively. To avoid a bias for a transition to state A or C, we randomized the target state in the rare case that both inequalities were met. Similarly, we calculated the back-transitions from C to B with the probability P_{CB}. A transition to state A is equivalent to discarding the molecule, as the reservoir in solution is assumed infinite. Finally, we added the newly generated molecules from N_{AB} and calculated the number of molecules in each state at the end of the time step. The resulting intensity traces with the summed number of molecules in states B and C was autocorrelated with the multiple tau algorithm employed previously [Schätzel, 1987, Mücksch et al., 2018].

D.2.2 Materials

Lipids

As in Section D.1.1 (p. 289). For GUV formation, we used DOPC with 0.05 % Atto655-DOPE added. For nanodisc preparation, we used a 7:3 mixture of DOPC and DOPG (Avanti Polar Lipids Inc.).

Buffers

SLB buffer (Tris) contains 150 mM KCl and 25 mM Tris-HCl adjusted to pH 7.5.

Min buffer contains 150 mM KCl, 5 mM $MgCl_2$ and 25 mM Tris-HCl, adjusted to pH 7.5.

Peptides

Synthesis of MPER The fluorescently labeld MPER peptides, Atto488-C**ELDKWASLWNWF** and Cy3B-C**ELDKWASLWNWF** (bold sequence corresponds to amino acids 662–673 by HXBc2 numbering), were synthesized by the Biochemistry Core Facility of the Max Planck Insititute of Biochemistry. The purity was characterized as $> 90\,\%$.

MreB-mts-Atto655 The MTS from MreB was synthesized as MLKKFRGMFRGSGSSGK-Atto655-NH2 by the Biochemistry Core Facility of the Max Planck Institute of Biochemistry. The purity was characterized as $> 90\,\%$.

TIRF and SI-FCS Microscopy Setup

The microscopy setup is identical to Section D.1.1 (p. 290).

D.2.3 SLB Patches from Bursted GUVs

GUV electroformation on platinum wires: GUVs were electroformed in custom-made teflon chambers as described in [García-Sáez et al., 2010, Visco et al., 2016]. Electroformation chambers are reusable and sonicated for 30 min each, first in chloroform, then in ethanol, and dried with N_2 and finally in vacuum for 15 min to remove residual solvents. Cleaned chambers can be stored up to multiple weeks in closed glass vials until use. Two

platinum wires reach into the chamber and are connectable to a voltage source from outside. Lipid mixtures (3 µL at 2 mg/mL per electrode) were evaporated on the platinum wires and subsequently dried for 15 min under vacuum. Electroformation chambers were filled with 350 µL sucrose solution. The osmolarity of the sucrose solution is adapted to be roughly 5 % higher than the osmolarity of the final buffer, here 287 mOsm and 300 mOsm for SLB buffer and sucrose solution, respectively. Electroformation was performed at 2 V (AC) with a frequency of 10 Hz for one hour. GUVs were dispensed from the wires at 2 V (AC) with a frequency of 2 Hz for 30 min.

Formation of SLB patches: Patches of SLB were prepared by bursting GUVs in SLB chambers (for preparation of SLB chambers see Section D.1.2). Assembled chambers were plasma cleaned (power: 60%, air pressure: 0.3 mbar, duration: 10 min, plasma technology GmbH, Herrenberg-Gültstein, Germany) for 10 min immediately before adding 50 µL of GUVs diluted 1:5 (v/v) in SLB buffer to achieve well-separated patches. To avoid bursting of GUVs during sample transfer, pipette tips were cut to achieve an opening aperture exceeding 1 mm. SLB chambers were filled with additional 200 µL of SLB buffer and incubated for 30 min. After incubation, strong pipetting up and down bursts GUVs sedimented to the coverslip. Finally, chambers were washed 10x with 100 µL SLB buffer.

Surface Passivation For surface passivation we added three additional washing steps with 5 mg/ml β-caseine (C6905-250MG, Sigma Aldrich, Taufkirchen, Germany) dissolved in SLB buffer, such that the final concentration of β-caseine was 4.8 mg/ml. Subsequently we added peptide and oxygen scavenging buffers as in the case of non-passivated samples.

Oxygen Scavenger PO+C was prepared as described above (Section B.1, p. 272) and added to the final sample preparation at 1x concentration.

TIRF Microscopy was performed on the setup described above (Sections A.1, B.1 and D.1.1). For Figures VI.14 and VI.15C and D tile scans were recorded by acquiring a triggered time-series. A custom trigger logic combined with a custom-written xy-stage control software (LabVIEW 2015, National Instruments, Austin, TX) initiated frame recording at defined target positions. The focus stabilization automatically accounted for a tilt of the sample stage, keeping the sample in focus in all xy-positions. The kinetic cycle time in VI.15A and B was set to 6.8 ms.

D.2.4 Preparation of Homogeneous SLBs from SUVs

Homogeneous SLB were prepared as described above (Section D.1.2, p. 291).

Saturation Experiment For determining the saturation concentration of MPER on SLBs, we prepared a 3 µM MPER stock solution. We subsequently added 0.2 µL, 0.47 µL, 1.33 µL, 4.67 µL of MPER stock solution to 200 µL SLB buffer, in order to increase the MPER concentration to 3 nM, 10 nM, 30 nM, 100 nM, respectively. Further, we removed 106 µL sample and added additionally 6.7 µL and 23.3 µL to obtain MPER concentrations of 300 nM and 1 µM, respectively. Finally, we added 3.15 µL of the 94.6 µM master stock, to arrive at an MPER concentration of 3 µM. After each addition, we mixed the sample and acquired a tile scan consisting of 18 individual images, covering 82 × 41 µm each and evaluated the average fluorescence intensity.

The guide to the eye in Figure VI.16 (p. 177) is a Langmuir isotherm, described by

$$I(\langle A\rangle) = I_0 \frac{\langle A\rangle}{\langle A\rangle + K_d}\,. \tag{D.6}$$

Here, I is the fluorescence intensity, $\langle A\rangle$ the concentration of MPER, K_d the dissociation constant and I_0 normalization factor. The solution contribution in TIRF experiments can be accounted for by an additional linear term, as

$$I(\langle A\rangle) = I_0 \left(\frac{\langle A\rangle}{\langle A\rangle + K_d} + \frac{I_s}{I_0}\langle A\rangle \right)\,, \tag{D.7}$$

with I_s describing the solution contribution. Conventionally, the solution contribution is determined in a separate experiment in absence of surface binding sites [Thompson et al., 1997].

D.2.5 Lipid Bilayer Nanodiscs

Preparation of Nanodiscs

Lipid bilayer nanodiscs were prepared from MSP1E3 scaffold protein and a lipid mixture of 7:3 DOPC:DOPG as described in detail in [Roos et al., 2014] (courtesy of Philipp Glock, Tamara Heermann and Lei Kai). Two mixtures were prepared and stored aliquoted at −80 °C, doped with 1 % Atto488-DOPE and 1 % Atto655-DOPE, respectively.

Immobilization of Nanodiscs

To immobilize nanodiscs we built SLB chambers as described above (Section D.1.2) with coverslips cleaned with piranha solution and the chambers built from protein low-bind reaction tubes (0.5 mL, Protein LoBind Tubes, Eppendorf AG, Hamburg, Germany). We tested the surface attachment of nanodiscs for concentrations of 30 nM, 100 nM, 300 nM and 1 µM (Figure VI.20). In Figure VI.21, we used nanodiscs at at concentration of 100 nM. For SI-FCS autocorrelations, we increased the concentration of nanodiscs to 300 nM. To remove excess nanodiscs from solution, we washed three times with 200 µL Min buffer.

MPER Saturation We immobilized nanodiscs as described above at a concentration of 100 nM and recorded TIRF tile scans in absence of MPER and at MPER concentrations of 0.1 nM, 0.3 nM, 1 nM, 3 nM, 10 nM, 30 nM, 100 nM and 300 nM by addition of increasing amounts of MPER from a 100 nM stock solution (first 6 titration stepts) and a 94.6 µM stock solution (last 2 titration steps), respectively. Further, we calculated the mean intensity of 18 $82 \times 41\,\mu m^2$ tiles.

D.2.6 Membrane Corrals on Micropatterned Chromium Grids

Membrane corrals on micropatterned chromium grids were prepared as described above (Section D.1.3, p. 292).

D.2.7 SI-FCS Acqusition and Analysis

SI-FCS Image Acquisition We acquired SI-FCS image series as described above, at hardware binning $1 \times 1\,px^2$, $4 \times 4\,px^2$ or $8 \times 8\,px^2$.

SI-FCS Data Analysis We performed a polynomial detrending of the intensity traces as described above (Section D.1.4). Here, the instabilities of the fluorescence intensity traces were non-monotonous and supposedly a complex combination of unspecific binding, excitation laser instabilities, mechanical or thermal drift or photo-induced immobilization of the labeled peptide. As the average fluorescence intensity (in particular on SLB patches) is high compared to the observed fluctuations, even minimal instabilities in the sub-percent regime can affect the whole image and dominate the autocorrelation function. We found the polynomial fit model for detrending described above (Equation D.2) to eliminate fluctuations reliably. Employing a polynomial model, however, it needs to be ensured that

the detrending does not effect the fluorescence intensity traces on the time scale of the autocorrelation times of interest.

Segementation of SLB Patches

For generating binary integration masks covering the SLB patches, we temporally averaged the complete time series. We performed a thresholding on the resulting average image and checked by eye that the recorded patch is fully covered by the binary mask. Further, we isolated individual patches, saving a binary mask for each patch within the field of view. Only SLB patches fully within the field of view were further analyzed. Integration was finally performed within the areas defined by the binary masks individually. Except for the generation of the binary masks and the quality control of the thresholding, the analysis is automated to optimize throughput.

D.3 Supplementary Figures

D.3.1 Binding Kinetics of MPER to Nanodiscs Are Independent of the ROI Size

To show that lateral diffusion is confined to lipid bilayer nanodiscs in Figure VI.22 (p. 189), we reanalyzed the data with different integration ROI sizes. Within the uncertainty of the measurement, we find no dependence of the decay times τ_1 or τ_2 on the ROI size (Figure D.1). Binding to lipid bilayer nanodiscs thus resembles the case of surface-immobilized binding sites (Figure III.12, p. 55).

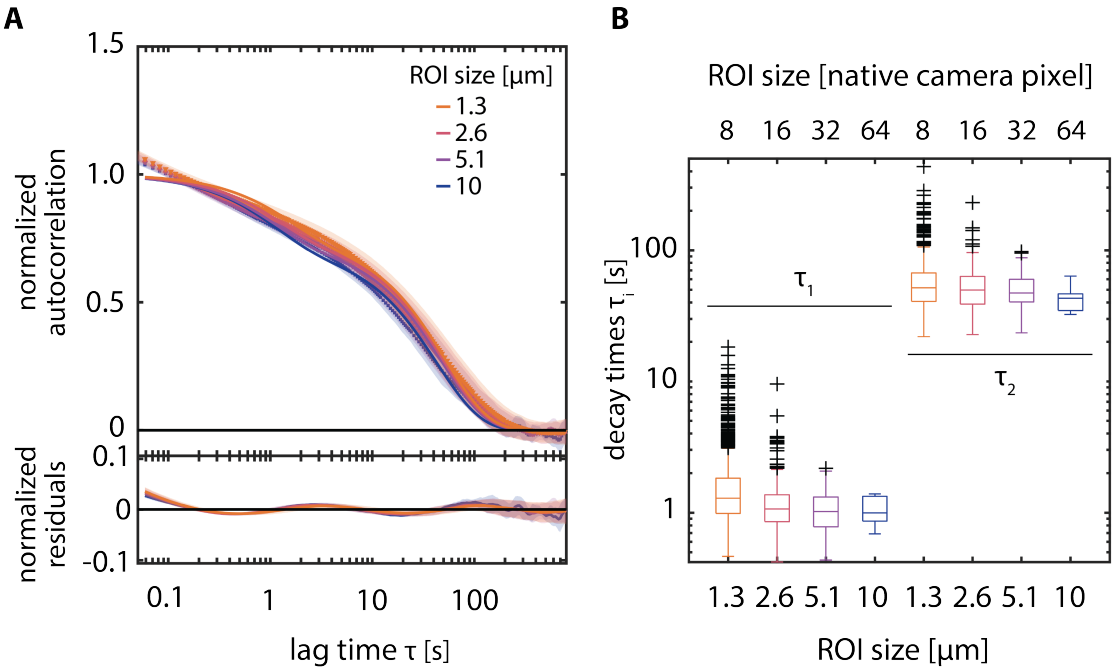

Figure D.1: Dependence of MPER binding to nanodiscs on the ROI size. (A) Normalized SI-FCS autocorrelation curves for the binding of MPER to surface-immobilized nanodiscs (MSP1E3) for different ROI sizes. Data reanalyzed from Figure VI.22 (p. 189). **(B)** Characteristic decay times τ_1 and τ_2 from the fits in (A) for the different ROI sizes. Nanodisc composition 7:3 DOPC:DOPG with 1 mol % Atto655-DOPE, 5 nM Atto488-MPER in SLB buffer.

D.3.2 Binding Kinetics of MPER to Nanodiscs Are Unaltered by Addition of TCEP

The improved SNR obtained for the autocorrelation curves on nanodiscs enables us to test for changes of the obtained binding kinetics depending on the system under investigation. Our purified MPER construct contains one cysteine and is therefore prone to dimerization by disulfide bonds in conventional SLB buffer. We therefore investigated the influence of the reducing reagent TCEP, which prevents cysteine-cysteine binding. Interestingly, we do not observe changes in binding kinetics upon addition of TCEP (Figure D.2). The normalized autocorrelation curves are indistinguishable in absence or presence of TCEP, as are the decay times τ_1, τ_2 and the amplitude ratio $G_1/(G_1+G_2)$ (Figure D.2). Only for the absolute values of the amplitudes G_1 and G_2 we find lower values in presence of TCEP. The difference within the two identical measurements with TCEP, however, is on the same order as is the the difference in between the two conditions. As observed previously on SLB patches (Section VI.3.4, pp. 170ff.), the amplitude is less reproducible than the amplitude ratio and the decay times.

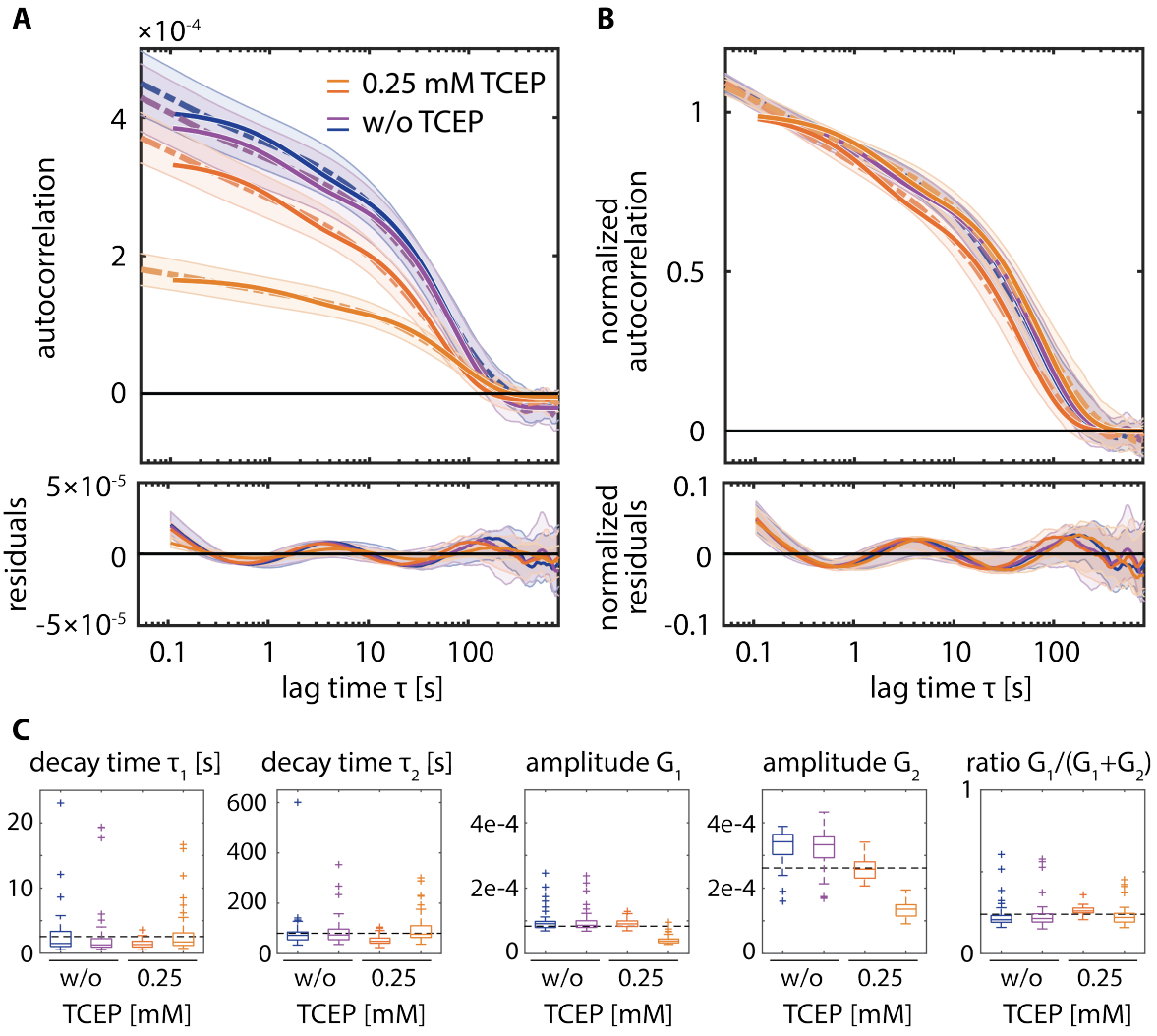

Figure D.2: Addition of TCEP does not alter the binding kinetics to nanodiscs. **(A)** SI-FCS autocorrelation curves for the binding of MPER to surface-immobilized nanodiscs (MSP1E3) in absence (blue-purple) and presence (orange) of 0.25 mM TCEP. Results from one experiment are presented as: upper panel: average of 49 ROIs (dashed line), the standard deviation of the ROIs (shaded area) and the fit of Equation VI.32 to the average; lower panel: residuals to the fit to the average (solid line) and standard deviation of the residuals of the fits to the individual ROIs (shaded area). **(B)** Normalized autocorrelation curves, displayed as in (A). **(C)** Box plots of fit parameters of the individual ROIs. Lines within the box indicate the median; bottom and top edges of the box indicate the 25th and 75th percentiles, respectively. The whiskers extend to the data points not considered outliers; outliers are marked individually as plus signs. The dashed black line marks the average over all sample ROIs. Nanodisc composition 7:3 DOPC:DOPG with 1 mol % Atto655-DOPE, 5 nM Atto488-MPER in SLB buffer.

D.3.3 Bacterial Membrane Targeting Sequences

In particular in the context of synthetic biology, it is important to not only understand, but also fine tune membrane binding. We previously studied the pattern formation of peripheral membrane proteins induced by the binding of the MinDE system to SLBs [Ramm et al., 2018a]. In particular, we found that the modulation depends on the strength of membrane binding. To estimate the binding strength, we used a simple characterization by acquiring a series of sections along the optical axis with a confocal laser scanning microscope and evaluating the change in the average intensity from glass over the membrane to solution (Figure D.3). We applied this method to a set fluorescence fusion proteins with and without MTS. The individual MTS are described in detail in [Ramm et al., 2018a]. The fluorescent protein mCherry with an N-terminal His-tag shows no partitioning to the SLB and thus the fluorescence intensity increases around the glass-membrane-solution interface only because of the increasing overlap of the detection volume with the solution. In contrast, we find an increase of the fluorescent signal localized at the membrane for the fusions of mCherry with MTS. The increase at the plane of the membrane further depends on the binding strength of the MTS, such as the single MTS of MreB (1xMreB) shows the lowest partitioning to the membrane, whereas the MTS of FtsA and two consecutive MreB MTSs (2xMreB) show a high partitioning to the SLB. For the MTS of FtsY and BsD, we find intermediate values.

To facilitate SI-FCS measurements with the bacterial MTS, we prepared lipid bilayer nanodiscs with a 7:3 mixture of DOPC:DOPG as described above (Section D.2.5). The mCh-MTS fusions showed fast photo-bleaching when investigated over longer periods in TIRF microscopy. We therefore synthesized the weakest binding MTS (1xMreB) with a synthetic dye (MreB-MTS-Atto655) to increase photo-stability.

We recorded SI-FCS autocorrelation curves (Figure D.4) as in the case of MPER binding to nanodiscs (Figure VI.22, p. 189). The obtained curves, however, show a decay of the autocorrelation curve over a wide time range that is not well described by the bi-exponential fit model. Future studies will need to investigate the origin of this complex decay, to extract kinetic rates from the autocorrelation function.

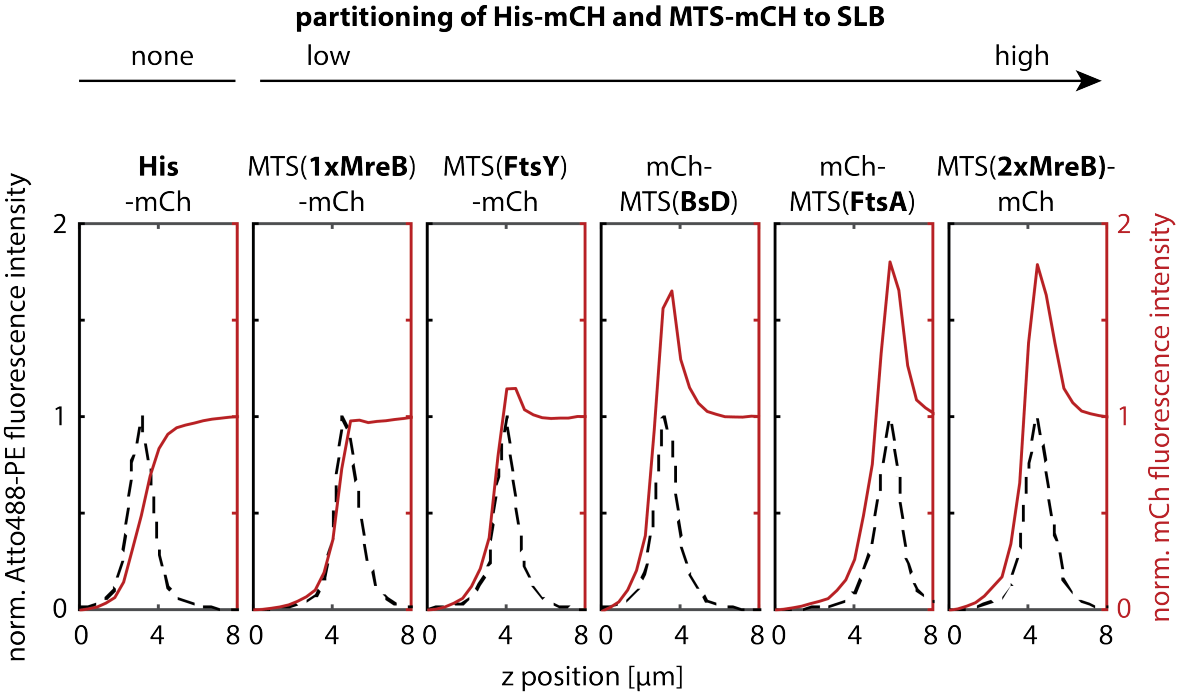

Figure D.3: Partitioning of MTS constructs. Confocal fluorescence microscopy z-stacks of the membrane staining (black, dashed) and different mCherry(mCh) fusion proteins (red, solution concentration: 1 µM) with an MTS on the N- or C-terminus, or without MTS (His-mCh). Displayed are the z-dependent fluorescence intensities normalized to the maximum and the solution value for the membrane and the partitioning protein, respectively. SLB composition: 70 mol % DOPC, 30 mol % DOPG, 0.05 mol % Atto488-PE. Figure adapted from [Ramm et al., 2018a].

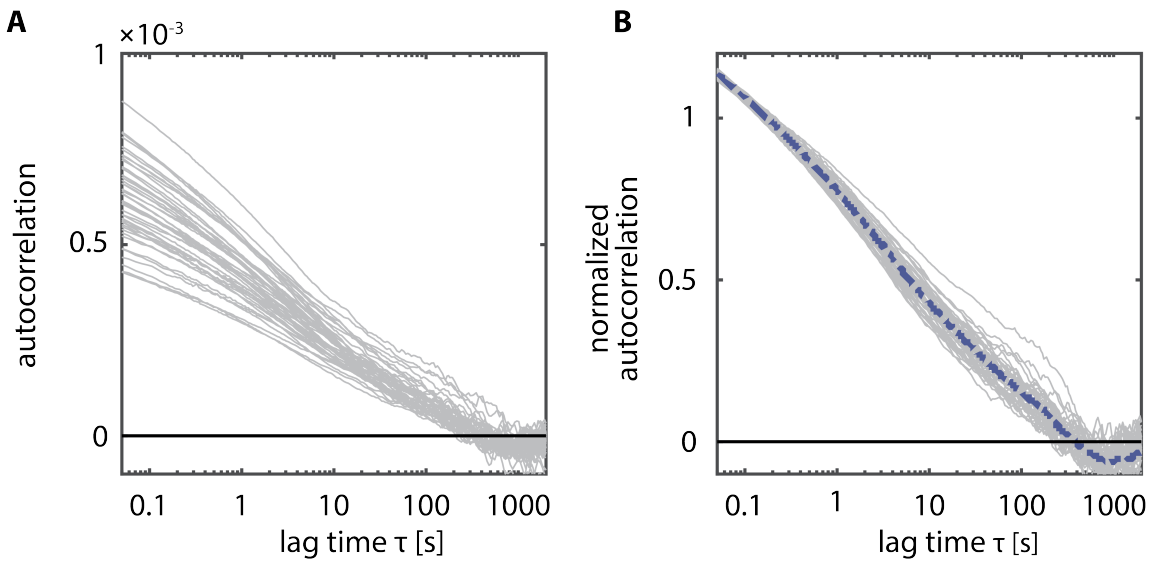

Figure D.4: SI-FCS autocorrelation curves for MreB binding to surface-immobilized nanodiscs (MSP1E3). **(A)** SI-FCS autocorrelation curves (gray) obtained from integration of 49 ROI. **(B)** Normalized autocorrelation curves, displayed as in (A), but with the average of the normalized autocorrelation curves (blue dash-dot line). Nanodisc composition 7:3 DOPC:DOPG with 1 mol % Atto488-DOPE, 10 nM Atto655-MreB-MTS in SLB buffer.

PUBLICATIONS

Publications related to this thesis

* denotes equal contributions.

1) Jonas Mücksch*, **Philipp Blumhardt***, Maximilian T. Strauss, Eugene P. Petrov, Ralf Jungmann, Petra Schwille (2018), Quantifying reversible surface binding via surface-integrated FCS. *Nano Lett.*, 18(5): 3185-3192, doi: 10.1021/acs.nanolett.8b00875

2) Christian Niederauer, **Philipp Blumhardt**, Jonas Mücksch, Michael Heymann, Armin Lambacher, Petra Schwille (2018), Direct characterization of the evanescent field in objective-type total internal reflection fluorescence microscopy. *Opt. Express*, 26: 20492-20506, doi: 10.1364/OE.26.020492

3) **Philipp Blumhardt**, Johannes Stein, Jonas Mücksch, Florian Stehr, Julian Bauer, Ralf Jungmann and Petra Schwille (2018), Photo-induced Depletion of Binding Sites in DNA-PAINT Microscopy. *Molecules* 23 (12), 3165, doi: 10.3390/molecules23123165

4) Beatrice Ramm, Philipp Glock, Jonas Mücksch, **Philipp Blumhardt**, Michael Heymann, Petra Schwille (2018), The MinDE system is a generic spatial cue for membrane protein distribution in vitro. *Nature communications*, 9.1 (2018): 3942., doi: 10.1038/s41467-018-06310-1

5) Philipp Glock, Johannes Broichhagen, Simon Kretschmer, **Philipp Blumhardt**, Jonas Mücksch, Dirk Trauner, Petra Schwille (2018), Optical control of a biological reaction-diffusion system. *Angew. Chem. Int. Ed.*, 57(9): 2362-2366. doi: 10.1002/ange.201712002

6) Sonal, Kristina Anne Ganzinger, Sven Kenjiro Vogel, Jonas Mücksch, **Philipp Blumhardt**, Petra Schwille (2019), Myosin-II activity generates a dynamic steady state with continuous actin turnover in a minimal actin cortex. *J. Cell. Sci.* 2019 : jcs.219899, doi: 10.1242/jcs.219899

Other publications

1) Martin Tomas, **Philipp Blumhardt**, Anja Deutzmann, Tobias Schwarz, Dimitri Kromm, Alfred Leitenstorfer, Elisa Ferrando-May (2013), Imaging of the DNA damage-induced dynamics of nuclear proteins via nonlinear photoperturbation. *J. Biophoton*, 6: 645-655. doi: 10.1002/jbio.201200170

2) Elisa Ferrando-May, Martin Tomas, **Philipp Blumhardt**, Martin Stöckl, Matthias Fuchs, Alfred Leitenstorfer (2013), Highlighting the DNA damage response with ultrashort laser pulses in the near infrared and kinetic modeling. *Frontiers in Genetics*, 4: 135. doi: 10.3389/fgene.2013.00135

3) Ruslan Batulin, Peter Moroshkin, Dmitrii Tayurskii, **Philipp Blumhardt**, Paul Leiderer, Kimotoshi Kono (2014), Laser Spectroscopy of Ba^+ ions in liquid He: Towards the detection of Majorana fermion surface state in superfluid ^{3}He-B, , 175: 63, doi: 10.1007/s10909-013-0910-x

ACKNOWLEDGMENTS

I am deeply grateful for the way I was allowed to experience science – free, with plenty of opportunities and many wonderful and supportive people. It certainly became an inspiring, valuable and informative experience.

Prof. Petra Schwille: Petra, thank you for all the trust, freedom and support you gave me over the years. The level of independence you granted us while equipping us with the best tools, fruitful ideas and always maintaining an open door is probably a unique research experience.

Prof. Ralf Jungmann: Ralf, it has been a real pleasure to work with you. Discussions with you were not only pleasant, but also full of insights and inspiration.

Prof. Don Lamb and *Prof. Tobias Bonhoeffer*: Thank you for being part of my TAC, for the personal and for the the scientific advices.

Jonas Mücksch: Thank you for being something like my PhD brother. Throughout all the years, I could always count on you. Working with you was fun, inspiration and a safe harbor in case of storm. I am grateful that we shared all the good and bad times and became friends for life.

Philipp Glock: There are not many people like you, with such good intentions, pleasant character and inspiring intellect. It was always nice to work with you and I will never forget all the scientific help, but more importantly I appreciate all the out-of-work hours and all the personal advice you gave me. I am glad the MPI brought me amazing friends like you.

Beatrice Ramm: So inspiring, so full of ideas. Even in tougher times, you never stopped to be thrilled about science. Thank you for sharing your inspiration with me and the pleasant team work on multiple projects. You always seem full of energy and I am grateful that even in times when you were actually not, you still invested some of it to support me. Everybody should be happy who can count you as team mate and friend – I certainly am!

Henri Franquelim: The expert on membranes and many more. What Wikipedia is for the internet, you have been for the lab – including the availability of many languages and the fun article/fact of the day. Thank you for all your help on membrane- and DNA-related issues. It was a pleasure to work with you.

Alena Khmelinskia: Frisbee, LSM night sessions, drinks, origami, harassment boxes,

office discussions, star wars, pink presentations and unicorns - the constant attempt to keep work and fun in balance. It was great to have you in the office, have you as a person to rely on and share all those crazy years with you.

Christian Niederauer: I am happy you did you Master's thesis with us and even more happy that it became a success – thanks to you! Your soft skills, efficiency and goal orientation made it a pleasure to work with you. I am grateful for the time we shared inside and out of the lab.

Araceli Sebastian: It was a pleasure to have you as a student – always nice, honest and hard working. It is a pity that I did not manage to bring your project to a publishable level. Nonetheless, you did excellent work and I am happy we also had a lot of fun on the way.

Magnus Carsten-Huppertz: Your project was probably the emotionally toughest of the three Master's theses, as nothing seemed to work in the beginning. And yet we labeled the ring in the end, also because you pushed it! Thank you for all the efforts you put into the project!

Sonal: The wise lady of the office: smart, helpful, funny and always a sharp tongue. Thank you for all the nice chats and the nice working atmosphere.

Kristina Ganzinger: The wise lady from the other office. I am happy you managed to stay in science, as I have seen few people maintaining your level of self-reflection, expertise and constant support for a large fraction of their environment. I am glad we worked together.

Maximilian T. Strauss: Thank you for all your help on getting started with DNA origami and DNA-PAINT. Your contribution was vital for the success we had with the DNA hybridization as a proof-of-concept system.

Eugene Petrov: Eugene, you are inspiring in your work ethics, your expertise and your willingness to teach. I am grateful for everything I learned from you, even if I realized too late it could have been even much more.

Hiro Eto and *Tamara Heermann*: Thank you for contributing to a very pleasant lab atmosphere, all your help, the climbing, all the nice breaks and chats.

Johannes Stein and *Florian Stehr*: Thank you for the nice team work and your contributions to the photo-depletion story that gained in quality from your PAINT analysis.

Thomas Weidemann: You were always willing to share your extensive experience and gave me many helpful comments. Thank you for all your maintenance work and your constant efforts for a positive impact.

Sigrid Bauer: The GUV lab was always a pleasure to work in. Thank you for your great maintenance efforts and all your help with sample preparations. *Bea Scheffer*: Thank you for all your help in the north of the lab, especially with everything bacteria related.

Silke Leuze-Bütün: You support us on so many, often hidden levels, that are essential for us to focus on science. Thank you for all your daily efforts and the always pleasant interaction.

Frank Siedler and Helge Vogl: You took a lot off our shoulders. Thank you, Frank and Helge, for maintaining the lab and all the efforts you put to create a safe, organized and functioning working environment.

Brigitte Hartl: Du warst wahrhaft die gute Seele des Labors! So viele kleine und große Dinge, um die du dich gekümmert hast, immer heiter und jedem wohlgesonnen. Das Labor hat durch dich viel Menschlichkeit gewonnen.

Gosia, Leon, Matias, Peter: Thank you for adding to the lab being a nice place to work in. I always enjoyed having you around! *Marc Bramkramp*: Thank you for helpful discussions on everything bacteria related that did not make it into the thesis in the end.

Kathrin Lang: Thank you for the collaboration and all the samples for the non-natural amino acid labeling project. It is a pity the story is not out there yet.

German Rivas: Discussions with you were always motivating and insightful. Thank you!

Christian Eggeling, *Erdinc Sezgin*, *Silvia Galiani*: I am grateful for all the help you offered around anything STED related. It is a pity it never became a solid project.

Michael Heymann: Maybe I should have printed something... Thank you Micha, for being full of ideas and actually sharing them. I enjoyed our chats and if things would have turned out a bit different, maybe we would have done nice science together.

Armin Lambacher: In the end, we at least managed to work on one publication together. If the circumstances would have been different, we probably could have had nice common projects. Thank you for all the nice discussions and chats.

Florian Schüder and *Thomas Schlichthärle*: Thank you for several nice and helpful discussions.

HiWis and Internships: *Christopher Jockisch, Wilhelm Frisch, Emre Eren.* Thank you for all your efforts and the pleasant team work. I apologize for all the chaos we were in after the move and most importantly, for every single time we forgot one of you for lunch. *Laura Kacenauskaite*, thank you for getting the scanning-FCS project started with us. You have been a talented student and a pleasure to work with.

IMPRS and *CeNS* did not offer only a list of inspiring activities, but also expanded my professional and personal network. A special thank you therefore goes to *Hans-Jörg Schaeffer*, *Ingrid Wolf*, *Maximiliane Reif*, *Susanne Hennig* and *Claudia Leonhardt* for all the organizational efforts.

I have to thank all the Schwille lab for all the help and fun I found there.

Many wonderful friends accompanied me during this time, who I could share all the nice moments with, but also found escape and support whenever needed. I can not appreciate enough to have you wonderful people in my life. Vielen Dank, lieber Cornelius, für mein erstes zu Hause in München, in das ich jeden Tag gerne heim gekommen bin. Und ein ebenso großer Dank geht an Alex, Caro, Diego, Erkan, Fabian, Gregor, Irene, Jan, Julia, Lena, Lydia, Mandy, Martin, Michi, Nele, Peter, Richi, Sara, Silvia, Vera, Willi & Wilma.

Meine liebe Familie, liebe Eltern, lieber Jan. Seit über 30 Jahren ist jeden einzelnen Tag auf euch Verlass! Ich bin unglaublich dankbar für die Umstände unter denen ich aufwachsen durfte. Euch Dreien verdanke ich unglaublich viel.

Finally, *Caterina*, I have to thank you for a lot of patience, understanding, joy, distraction, uplifting, perspective and comfort. Thank you for your love! I will always look forward to come home to you!